A Spectroscopic Study on Nanosensors and Porphyrins for Bioimaging

ROSSER, GERALDINE,ANN

How to cite:

ROSSER, GERALDINE,ANN (2015) *A Spectroscopic Study on Nanosensors and Porphyrins for Bioimaging*, Durham theses, Durham University. Available at Durham E-Theses Online: http://etheses.dur.ac.uk/11308/

A Spectroscopic Study on Nanosensors and Porphyrins for Bioimaging

---

Geraldine Ann Rosser

A thesis presented for the degree of
Doctor of Philosophy

Supervised by Professor Andrew Beeby
Department of Chemistry
University of Durham
March 2015

A Spectroscopic Study on Nanosensors and Porphyrins for Bioimaging

Abstract

Luminescence imaging has grown in development and research over recent years and the desire to expand within the area has increased with it.

The development of PEBBLEs (Probes Encapsulated By Biologically Localised Embedding), luminescent optical nanosensors, presents a new possibility for cellular imaging due to their nanoscale nature. Derivatives of this system have shown great potential in the field of biological imaging as non-invasive probes. Investigations into the photophysical properties of various dyes incorporated into PEBBLEs have been reported in the recent literature, in an attempt to characterise and better understand the system.

This thesis contains the photophysical properties of a series of PEBBLE based optical nanosensors. The work has been presented in sections according to their application or prioritised characteristic.

The first results chapter, Chapter 3, details the photophysical characteristics of a ratiometric pH sensing nanoparticle and the various development steps achieved, looking at how the fluorophores change on entrapement within the polyacrylamide matrix.

Chapter 4 describes the calcium sensing nanoparticles developed, specifically with and without photosensitising porphyrins conjugated to the exterior of the PEBBLE, making probes capable of reporting changes in calcium flux with reactive oxygen species.

Chapter 5 discusses the ability to incorporate hydrophobic fluorophores within the polyacrylamide nanoparticles, and thus introducing their solubility within aqueous solutions.

The more general topic of the luminescence emission properties of porphyrins is covered within Chapter 6 looking at the trication derivative of two well-known porphyrins, TMPyP and ZnTMPyP, and any changes they exhibit in different environments. These form the basis

for the porphyrins that were initially introduced to nanoparticles as they are commonly used as examples of the complex structure of porphyrins today.

Finally the results in Chapter 7 detail the photophysical properties of four platinum and palladium porphyrins and their respective nanoconjugates that were synthesised with the application of oxygen sensing in mind.

Chapters 1, 2, 8 and 9 detail a general overview or introduction to the topics discussed, any experimental methods used within, the overall conclusions drawn with an emphasis on future work and an experimental section, respectively.

Acknowledgements

Over the last five years I have been lucky enough to work with so many great people that have helped me through the last five years. I would like to first and foremost extend my thanks to my supervisor Prof.Andrew Beeby who has provided me with so much support and guidance and the odd coffee in his office. I truly appreciate the time and effort that went in to supervising me, In addition I am also grateful for all the members of the Beeby group, both past and present, namely Ben, Bob, Vale and Andy and not to mention the many fourth years I have seen come and go. I cannot end this list without extending my thanks to the honorary members of the lab – Robek and Kate.

Alongside the Beeby research group I would like to extend my thanks to the collaborators of this project. Namely Prof. Ross Boyle and Dr Francesca Giuntini from the University of Hull and Dr Jon Aylott and his student Andrea Lavado from the University of Nottngham. Especially to Francesca for the time and effort she has put into the helping me throughout and for putting up with me visiting her laboratory on more than one occasion.

As well as my direct colleagues within the chemistry I have also had the pleasure of working with and getting to know a number of other people in the Durham Chemistry Department that have provided me with support and fun times. Specifically I would like to thank Elaine, Casey, Massey, Gemma and Beth. I would also like to say a huge thank you to all the technicians, support staff and lab attendants – the department would not be the same without you! Outside the chemistry department I owe a large amount of gratitude to my friends who have helped make Durham my home, specifically people from King’s, and despite no longer living in Durham it will always be a home to me. Over the past year I have been lucky enough to work with some amazing people at the Royal Society of Chemistry who have all helped to motivate me through this last step – thank you!

On a more personal note I am so grateful to the support my family has given to me, to my mum and dad, my sister and her family and my grandparents.

Finally, to my husband Jon, who has supported me in so many ways, thank you for making it all bearable and supporting me to the end - I never would have got through this without you!

Declaration

The work in thesis is based on research carried out under the supervision of Prof. Andrew Beeby, in the Department of Chemistry, University of Durham, England. No part of this thesis has been submitted elsewhere for any other degree or qualification and it is all my own work unless referenced to the contrary.

Table of contents

List of figures

List of tables

Abbreviations

CG	Calcium Green-1
CG-dextran	Calcium Green-1 dextran conjugate
C3CA	Coumarin-3-carboxylic acid
CoumDex	Coumarin dextran conjugate
CoumDNP	Nanoparticles containing coumarin dextran conjugate
CTAB	Cetyltrimethyl ammonium bromide
DCM	Dichloromethane
DMSO	Dimethyl sulfoxide
EDC	1-Ethyl-3-(3-dimethylaminopropyl)carbodiimide
EGTA	Ethylene glycol tetraacetic acid
EtOH	Ethanol
FITC	Fluorescein Isothiocyanate
HOMO	Highest occupied orbital
IC	Internal conversion
ISC	Intersystem crossing
LUMO	Lowest unoccupied orbital
O.D.	Optical Density
MeOH	Methanol
PAA	Polyacrylamide
PBA	Pyrene-1-butyric acid
PBS	Phosphate buffered saline
PEBBLE	Probes Encapsulated by Biologically Localised Embedding
PdTMPyP	5-(4-Methoxycarbonylphenyl)-10,15,20-tris(4-methylpyridinium)porphyrinato palladium (II) trichloride
PdTMPyP-NP	Nanoparticles containing 5-(4-Methoxycarbonylphenyl)-10,15,20-tris(4-methylpyridinium)porphyrinato palladium (II) trichloride

PdTSP	5-(4-Carboxyphenyl)-10,15,20-tris(sulfonatophenyl) porphyrinato palladium (II) trisodium
PdTSP-NP	Nanoparticles containing5-(4-Carboxyphenyl)-10,15,20-tris(sulfonatophenyl) porphyrinato palladium (II) trisodium
PDT	Photodynamic Therapy
PLQY	Photoluminescent quantum yield
PtTMPyP	5-(4-Methoxycarbonylphenyl)-10,15,20-tris(4-methylpyridinium)porphyrinato platinum (II) trichloride
PtTMPyP-NP	Nanoparticles containing 5-(4-Methoxycarbonylphenyl)-10,15,20-tris(4-methylpyridinium)porphyrinato platinum (II) trichloride
PtTSPP	5-(4-Carboxyphenyl)-10,15,20-tris(sulfonatophenyl) porphyrinato platinum (II) trisodium
PtTSP-NP	Nanoparticles containing5-(4-Carboxyphenyl)-10,15,20-tris(sulfonatophenyl) porphyrinato platinum (II) trisodium
PyDex	Pyrene dextran conjugate
PyDNP	Nanoparticles containing pyrene dextran conjugate
ROS	Reactive Oxygen Species
SDS	Sodium dodecyl sulfate
SV	Stern-Volmer
TAMRA	5(6)-Carboxytetramethylrhodamine N-succinimidylester
TCPC	Time correlated photon counting
TCSPC	Time correlated single photon counting
TMPyP	5,10,15,20-Tetrakis(1-methyl-4-pyridinio)porphyrin
TMPyPHSE	TMPyP hydroxyl succinimide ester
ZnTMPyP	5,10,15,20-Tetrakis(1-methyl-4-pyridinio)porphyrin zinc
ZnTMPyPHSE	ZnTMPyP hydroxyl succinimide ester

Non SI units and symbols

A	Amplitude or pre-exponential factor
a.u.	Arbitrary units
d_{2h}	Symmetry group of free base porphyrins
d_{4h}	Symmetry group of metalloporphyrins
F	Fluorescence
I	Intensity of emission
K_d	Dissociation constant
k_Q	Bimolecular quenching constant
K_SV	Stern-Volmer constant
ppb	Parts per billion
$p\mathrm{O}_2$	Partial pressure of oxygen
Q	Quencher
S	Total spin quantum number
S_0	Ground singlet excited state
S_n	n^{th} singlet (excited) state
T_n	n^{th} triplet (excited) state
$^1\Delta_\mathrm{g}$	Singlet oxygen
λ_em	Emission wavelength, nm
λ_ex	Excitation wavelength, nm
Φ_Δ	Singlet oxygen quantum yield
Φ_f	Fluorescence quantum yield
τ	Lifetime
τ_f	Lifetime of fluorescence

1. Introduction

Optical imaging is a technique that exploits the use of light to image systems and their responses. Over the years there has been an increase in the development and research of different optical imaging techniques for detection within cellular environments. One of the main attractions for this is that more modern optical approaches are less invasive than previous devices or technologies e.g. physical probes.

The use of fluorescence within cellular imaging has gained and maintained a lot of interest over the years. One of the benefits being that, by using different molecules that emit fluorescence, fluorophores, the sensor or sensing system can be adapted for different conditions or requirements.

Another area which has gained more attention within mainstream research over recent years is the combination of nanotechnology with optical sensors. The idea here being the development of nanoscale optical sensors for bioimaging working to minimise current limitations on optical imaging e.g. localised concentration, leaching and toxicity.

1.1. General overview on photophysics

Luminescence, the light emission from electronically excited states, is a well-known phenomenon that has been an area of interest within research for many years. [1] The uses and applications have been exploited and developed over the years, ranging from lighting (e.g. the fluorescent lamp) and UV lighting to analytical chemistry as a means to detect the presence of particular species.

Photo-luminescence occurs by means of a molecule absorbing a photon, changing the electronic configuration of the molecule, creating an excited electronic state. These excited states can relax back to the ground electronic configuration emitting light. The luminescence process is generally described as either fluorescence or phosphorescence according to the change in the spin of the ground and excited states. The multiplicity of the excited state can be either singlet or triplet depending on the overall spin of the electrons within the molecule. In a singlet state the electrons are antiparallel (↑↓, $S = 0$) whereas electrons in a triplet state are parallel (↑↑, $S = 1$); when an electron is in the excited singlet state it is of opposite spin to the corresponding second electron in the ground state, whereas when an electron is in the excited triplet state it is of the same spin as the corresponding electron in the ground state.

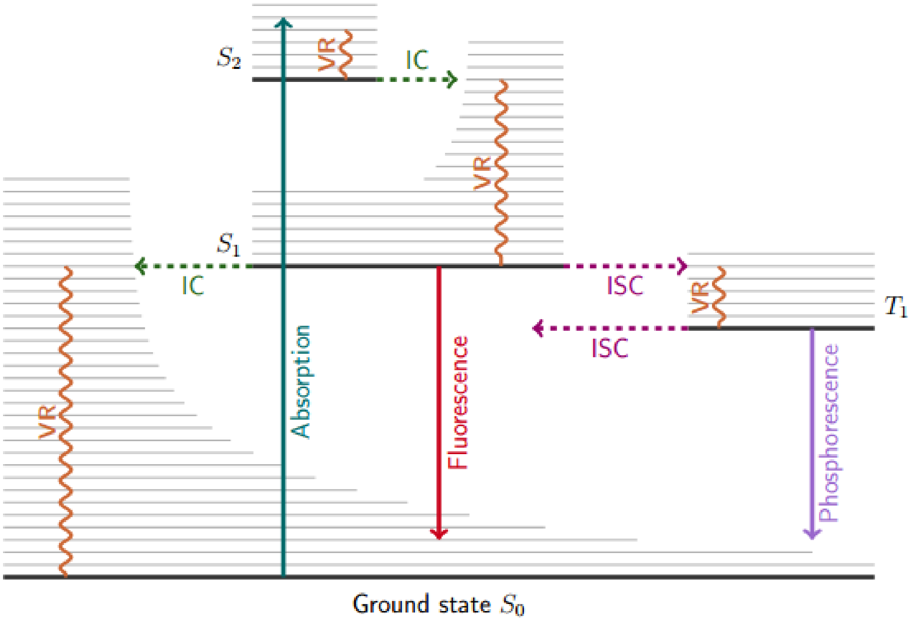

Figure 1.1 Jablonski diagram, emphasizing the spins of the electrons in each state to the side of the spin level (e.g. S_0).(modified)

The Jablonski diagram (Figure 1.1) shows in more detail what happens, at the vibrational level, to a molecule during the processes of fluorescence, phosphorescence and also non-radiative decay. When a photon is initially absorbed by the molecule, it can result in the promotion of an electron from the HOMO of the ground singlet state (S_0) molecule into a higher lying orbital or LUMO to generate an electronic excited state (S_n). The subscript '*n*' denotes the fact that there are a number of higher energy levels that the electron can potentially reach by excitation; corresponding to each of these there are a number of vibrational energy levels. The two electronic excited states seen in Figure 1.1 are the first, S_1, and the second, S_2.

The excited molecule loses excess vibrational energy by means of vibrational relaxation, losing the energy to the solvent bath until it reaches the lowest vibrational level of the electronic state. At this point the vibrationally relaxed S_n state converts into an isoenergetic vibrationally excited state of the S_{n-1} state a process known as 'internal conversion' (IC) which is a non-radiative process. The rate of internal conversion is inversely proportional to the enegy gap between the electronic states, hence in a typical molecule the process is rapid until the lowest vibrational state of the S_1 state is reached. It is this state that undergoes fluorescence or intersystem crossing (ISC). If the excited molecule relaxes directly back down from S_1 to S_0 radiatively, this is a fluorescence event; these are short lived processes ($\tau \approx 10^{-9}$ seconds) due to the fact that the process is an '*allowed*' transition between states of the same spin. The spin selection rule dictates the restrictions that apply for the possibility of an electron to transition between states of different multiplicity (i.e. singlet to triplet).

The lowest excited singlet state can undergo the process of intersytstem crossing, whereupon there is a change in the spin of the excited state: effectively the two unpaired electrons become parallel spin in the triplet state (↑↓ to ↑↑). Phosphorescence arises from the relaxation of an excited triplet state back to the singlet ground state, $T_1 \rightarrow S_0$. They are lower in energy than their corresponding singlet states owing to electron-electron repulsions, a stipulation from Hund's first rule. Transitions from this triplet state back to the ground singlet state ($T_1 \rightarrow S_0$) are forbidden and are, therefore, slow (giving longer lifetimes, typically 10^3 to 10^0 s^{-1})[2].

Photophysical processes are covered in more detail within the Experimental Methods section in 2.1.

1.2. Fluorescent molecules

A fluorophore is the section of a compound which causes it to fluoresce or to be fluorescent. Intrinsic fluorophores are naturally occurring materials that act as fluorophores whereas extrinsic fluorophores are molecules that have been specifically designed and synthesised in order to express the desired fluorescence that are added to a system to act as probes.[2]

Fluorophores are generally known to be composed with elements of aromaticity e.g. aromatic rings or conjugation. Extrinsic fluorophores are commonly useful where labelling is required, e.g. protein or DNA labelling, where the molecule of interest is totally devoid of fluorescence at the start.

This also introduces the phenomenon of autofluorescence. Autofluorescence is essentially background signal due to emission from endogenous fluorophores and can be observed from all biological samples, particularly under UV excitation. Labelling DNA or proteins is not always necessary as they tend to exhibit characteristic fluorescence, however, as this is weak and considered as background then the ability to label the components with extrinsic fluorophores is essential.

A range of fluorescent dyes have been developed and are commercially available for a multitude of applications. For example, dyes to monitor the change in pH, monitor the change in concentration of a specific ion, and monitor fluctuations in temperature or for general microscopy. Examples of fluorescent dyes or molecules used commonly within commercial applications are:

- Fluorescein, not only used a standard in research labs but also within health care e.g. optometry;
- Rhodamine dyes are commonly used as laser dyes and also in fluorescence microscopy;
- Ninhydrin and its fluorescent properties are used for fingerprinting imaging.

Fluorescence has a multitude of uses in a variety of areas, as discussed, and one of the areas that have become more prevalent in scientific research is combining fluorescence with nanotechnology. The 2014 Nobel Prize in Chemistry was awarded to Eric Betzig, William E. Moerner and Stefan W. Hell for imaging using fluorescent dyes and bypassing the diffraction limit stipulated by Ernest Abbe in 1873.[3]

1.3. Nanoparticles for optical sensing

There has been a growing interest in the development of nanotechnology for a variety of applications with an emphasis on biomedical applications, for example biosensing, targeted drug delivery and bioimaging (acquiring biological images by using fluorescence probes or detection of fluorescence). The potential for sensitive nanodevices is greatly improved by combining the use of nanotechnology with luminescence from its proven use as an indicator or sensor of its environment. Bioimaging can be broken down into 3 techniques; (1) simply to make cells fluoresce for imaging, (2) targeting cells or specific cell areas and (3) to use fluorescent sensors for specific species.

Research into using nanoparticles for optical sensing (optical nanosensors) has increased over the past decade, developing and designing systems that utilise the sensitivity that fluorescence offers for measurements in intracellular environments. Nanosensors offer two main advantages over standard fluorescent dyes; (1) protection of the fluorescent sensing component from the intracellular environment and (2) protection of the intracellular environment from potential toxic effects of the fluorescent probe that might otherwise have been encountered from such effects as leaching. Optical nanosensors convert signals derived from their environments (e.g. a change in the concentration of a specific ion) into an optical response (e.g. a change in the intensity of the fluorescent signal) and a wide variety of different nanosensing systems have been developed over recent years based on different matrices.

There is a range of ‘types’ of nanomaterials used or currently being researched for bioimaging. These include nanomaterials made from fluorescent dyes doped into silica, hydrophilic polymers, hydrophobic polymers and semi-conducting polymers, metallic particles, and quantum dots among others.

The nanomaterials used throughout the work presented in this thesis are hydrophilic polyacrylamide nanomaterials. Sasaki *et al.* reported the first optical nanosensor in 1996, consisting of a polyacrylamide nanoparticle with the fluorescent dye, fluorescein, entrapped within it, therefore, designing the first pH responsive optical nanosensor.[4] In 1998 Kopelman then introduced the idea of a PEBBLE (Probes Encapsulated By Biologically Localised Embedding) as an optical nanosensor specifically designed for intracellular measurements.[5]

1.4. Probes Encapsulated By Biologically Localised Embedding

As mentioned above, Probes Encapsulated By Biologically Localised Embedding (PEBBLEs) are a subcategory of nanoparticles. They are optical sensors of the nanoscale dimension that are specifically designed to meet the desire and need for a non-invasive imaging method for real-time measurements inside cells i.e. the method does not rupture the cell or render it inoperable. The PEBBLE nanosensor is a term that includes and describes a whole group of particles made of an external, inert matrix with a core containing dyes or the sensing mechanism.[5] The matrix provides a protection component both from and for the cell or the monitored environment.

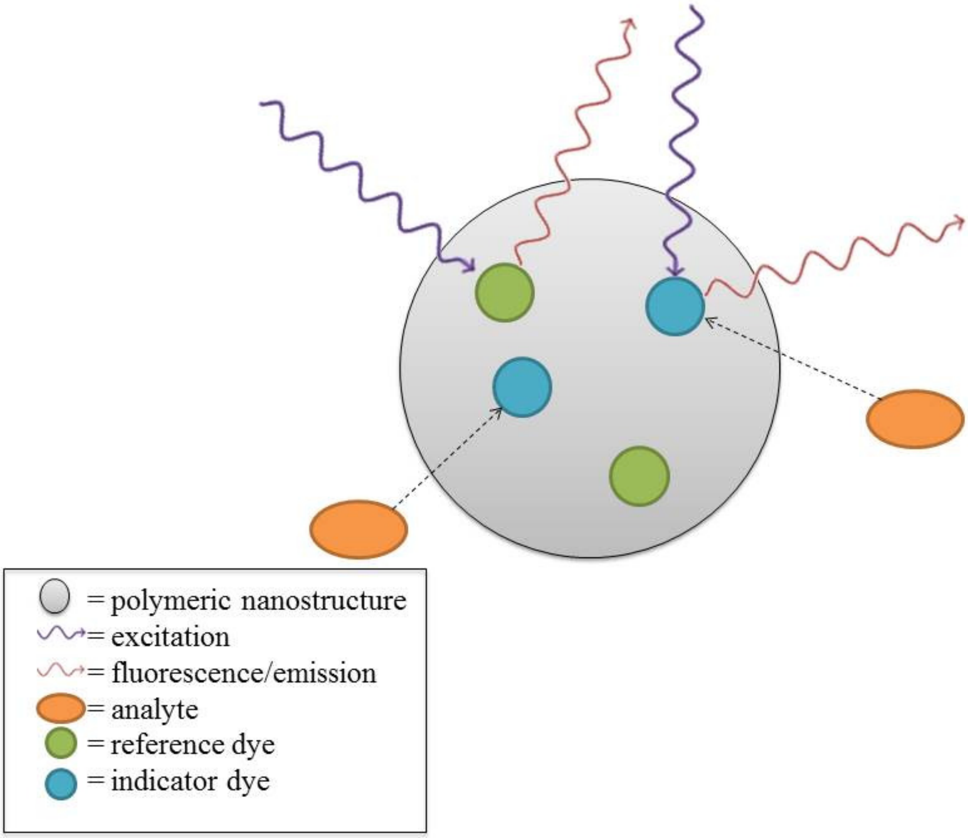

Figure 1.2 Diagram showing the general schematic idea of a ratiometric optical sensing PEBBLE

The dyes are trapped inside the matrix and are therefore incapable of leaching out into and proving potentially cytotoxic. Also the protection of the matrix prevents or delays the process of photobleaching and/or an alteration in the chemical structure or behaviour due to the absence of larger molecules, e.g. proteins or heavy metals.[5, 6] If the chemical structure of the dye went through a chemical change then this would inhibit their use in the first place. This therefore leads to the suggestion that they are potentially suitable for intracellular measurements due to their non-disruptive nature.[7] The typical size of a PEBBLE (20-100 nm and even up to 600 nm)[6, 8] will also provide minimal physical damage to the cell in that the penetration of a 60 nm PEBBLE leads to a penetration volume of 1 ppb of the cell’s volume which is insignificant in comparison to a typical optode (e.g. fibre optic sensor), which would have a penetration volume of more than 1% of the cell volume.[5, 8]

Previous work on PEBBLEs has led to nanosensors (ranging in size) for calcium,[9, 10] magnesium,[11] potassium,[12] sodium,[12] copper,[13] chloride[14] and zinc[15] monitoring that are clearly beginning to make way for a new generation of intracellular measurements.[7, 8] They have been found to be reversible and the dyes do not appear to leach from the PEBBLE. The dyes that are used in PEBBLE work tend to be conjugated dyes. To eliminate the possibility of the dye leaching out of the polymeric matrix it can be attached to a dextran sugar. [7]

1.5. Porphyrins

Porphyrins are a group of brightly coloured compounds involved in a number of biological processes such as oxygen transport (e.g. haemoglobin), light harvesting and electron transfer and transport (e.g. chlorophyll).[16, 17] Due to their distinctive properties they have applications in a number of fields including fluorescence imaging and photosensitisation.[18, 19]

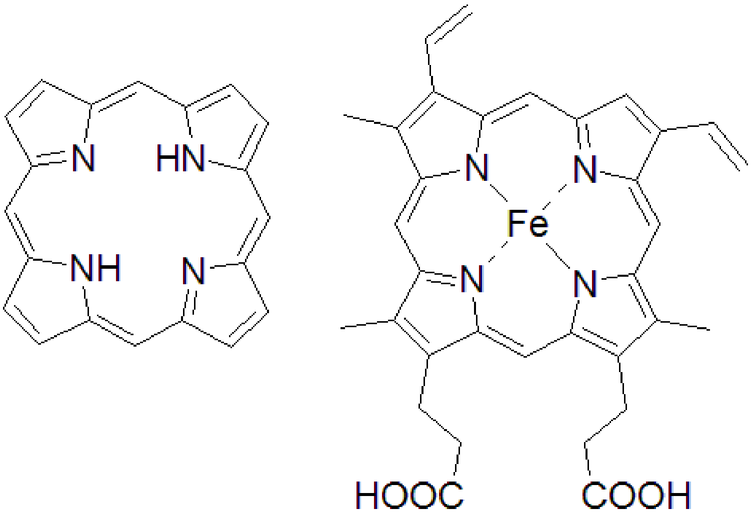

Figure 1.3 Chemical structures of porphine (left) and haemoglobin (right)

They are a class of compounds that are intensely coloured and are all built upon the framework of the macrocycle known as porphine (Figure 1.3 left-hand structure). One of the most common naturally occurring porphyrins is the red blood cell pigmentation molecule, haemoglobin (Figure 1.3 right-hand structure). These two molecules represent examples of the two types of porphyrins found, these being free-base porphyrins (like porphine) and metalloporphyrins (like haemoglobin), with their 'simplified' represenations shown in Figure 1.4.

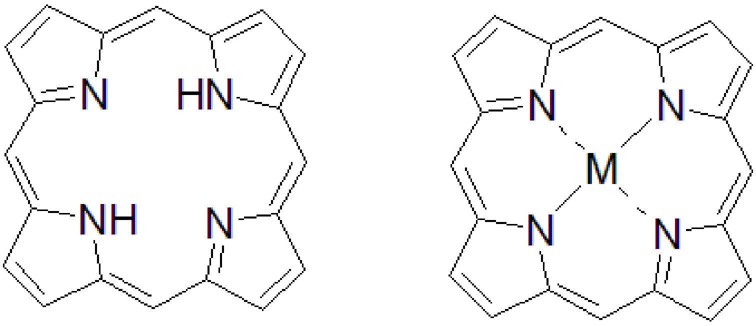

Figure 1.4 Simplified molecular structures of a free-base porphyrin (left) and metalloporphyrin (right).

They are a group of molecules, that in obeying Hückels rule ($4n + 2$), are aromatic and have a system of delocalised π-electrons which alters the chemistry depending upon whether they are free porphyrins or metalloporphyrins. Previous research has shown that the delocalisation of metalloporphyrins follows a 16 atom pathway whilst free base porphyrins follow an 18 atom pathway, highlighted in Figure 1.5.[20, 21] This is explained by the two central N-H bonds and the steric effect which forces the hydrogen atoms out of the plane resulting in the less symmetric 18 atom pathway being favoured.[16]

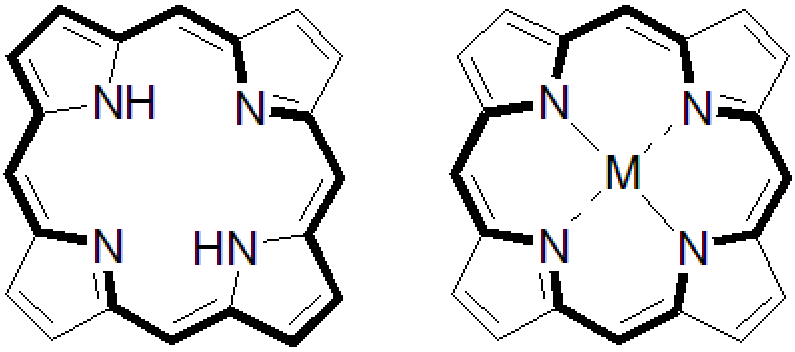

Figure 1.5 Delocalised porphyrin pathways consisting of 18 atom (left) and 16 atoms (right)

The aromatic property of porphyrins leads to the distinct characteristics that are observed in their UV-vis spectra as can be seen in Figure 1.6. This tends to take the form of having an intense band approximately in the region of 400 nm that corresponds to what is known as the

Soret band. This is due to the strong transition from the ground state of the porphyrin to the second excited singlet state ($S_0 \rightarrow S_2$). The significantly weaker absorption bands that extend towards the red region of the spectrum are known as the Q-bands. These absorption bands arise from the much weaker electronic transition to the first excited singlet state from the ground state ($S_0 \rightarrow S_1$).

However, fluorescence is only observed from the first excited singlet state due to rapid internal conversion occurring between S_2 and S_1. The number of Q bands seen in the spectrum is attributable to what type of porphyrin the molecule is; e.g. metalloporphyrin or free-base porphyrins (Figure 1.4). This is therefore due to symmetry in the molecule. A metalloporphyrin has 4-fold symmetry whilst a free-base porphyrin has only 2-fold symmetry elements, approximating to D_{4h} and D_{2h} respectively.[22] A free-base porphyrin such as that shown in in Figure 1.4 has only two of its inner nitrogen atoms protonated which results in two close lying transition dipole moments for the Q-bands, referred to as the 0_x and 0_y bands, whereas a metalloporphyrin has symmetrical central nitrogens bound to the metal centre which would exhibit only a single Q-band. The additional structure of the bands arises from vibrational fine structure. So, the difference in the energy gap between each of the Q-band absorptions is due to the slight differences in the vibrational components along the axis of the molecule for the same electronic transition.

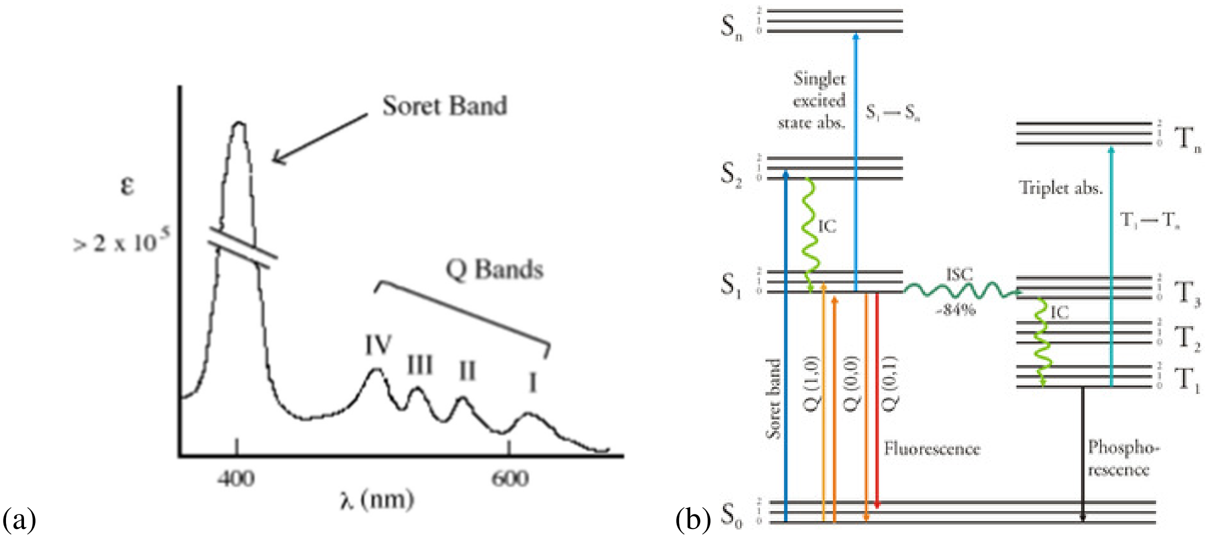

Figure 1.6 (a) Diagram of Soret and Q-bands seen in the porphyrins absorption spectrum [23] (note – this shows four Q-bands, indicative of a metalloporphyrin) and (b) a Jablonski diagram indicating the various transitions responsible for absorption and emission in porphyrins [24(modified)]

Porphyrins are well known for their ability to generate reactive oxygen species (ROS) and so are used commonly as photosensitisers within photodynamic therapy (PDT).[25] When the porphyrin is in an excited state, is when it is capable of interacting with molecular oxygen to generate singlet oxygen, $O_2\ {}^1\Delta_g$, a highly reactive oxygen species. This occurs by energy transfer from the lowest excited triplet level of the porphyrin to molecular oxygen in its triplet ground state. Reactive oxygen species are responsible for oxidative stress, a process with serious implications to cellular based systems and thought to be involved in the process and development of a number of medical conditions including ageing, heart disease and carcinogenesis.[26, 25] Excited state metalloporphyrins, containing closed-shell metal ions, are known for undergoing intersystem crossing which leads to a longer lifetime and phosphorescence emission.

Water-soluble, cationic porphyrins have received much topical interest over the years due to their bioactivity and hence potential application in anti-cancer research or as sensitisers in photodynamic therapy, PDT.[27-29] However, porphyrins themselves are a very complex family of molecules where a greater understanding is sought; they represent simple models of complex structures.[22, 30]

Porphyrins are one of the major families of molecules that are used as photosensitisers in PDT due to their high efficiency for producing singlet oxygen, and a brief overview on PDT is covered further in section 1.6.

1.6. Photodynamic Therapy

Treatment of disease by means of light can be traced back in origin many centuries. The skin disease vitiligo is known to have been managed by oral ingestion of the plant Amni Majus followed by exposure to sunlight.[31] The active ingredient in this plant is psoralen and is now commonly used in the treatment for the skin disease of psoriasis. This is a form of photochemotherapy, a treatment that employs the use of light to initiate a series of photochemical processes. A form of photochemotherapy developed that is commonly used to target and kill malignant cells is known as photodynamic therapy (PDT), a term first coined by von Tappeiner in the early 20th century.[32] PDT exploits the use of a chemical, known as a photosensitiser, in conjunction with molecular oxygen to stimulate cell death.[33, 34] A photosensitiser is a molecule that upon absorption of light, is promoted to an excited state and can undergo intersystem crossing with molecular oxygen to produce singlet oxygen (Type II) or undergo electron transfer to generate other reactive oxygen species (Type I), see Figure 1.7.

PDT is used for the treatment of conditions such as certain types of cancers.[35] It is recognised that a greater variety of photosensitizers are required within the field that offer a wider range of both optical and targeting properties. Whilst it is renowned in medicine, a greater understanding of the mechanism is still sought in order to harness its full potential over a range of applications. Research and applications for PDT has widened over the years to include work within dermatology (e.g. psoriasis – similar to that of vitiligo), tissue repairs (e.g. wounds) and microbiology (e.g. gum disease).[35]

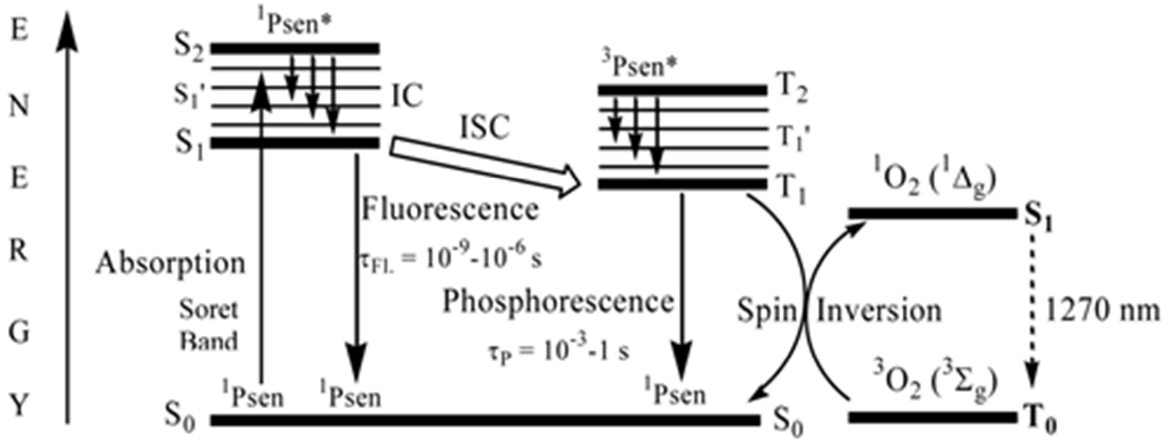

Figure 1.7 Jablonski diagram showing the energy transitions that occur in Type II PDT; exciting a photosensitiser and the formation of singlet oxygen when the energy is transferred to molecular oxygen. [36]

Photodynamic therapy requries:

- A photosensitiser
- A light source appropriate for exciting the photosensitiser
- Tissue oxygen

The mechanism of PDT follows the same principles as that of luminescent transitions. Upon absorption of a photon the photosensitizer molecule is excited and raised from its lower singlet ground state (S_0) to a higher excited singlet state (S_n), undergoing vibrational relaxation to reach its lowest excited singlet state (S_1). From here the molecule can undergo a number of different transitions to other energy levels to eventually return to its ground state, these are depicted in Figure 1.7. There are two types of photodynamic reactions defined[37]; Type I generates free radicals by the transfer of electrons whilst Type II reacts with molecular oxygen to form singlet oxygen. Figure 1.7 illustrates the mechanism of Type II PDT as that is the application route of concern within this text. The efficiency of this process can be monitored by means of luminescence from singlet oxygen at 1270 nm.

1.7. Reactive oxygen species

In the simplest of terms, like the name states, these are reactive species or molecules that contain an oxygen atom, some examples of them being singlet oxygen ($^1O_2$, the lowest excited electronic state of O_2), hydroxyl radical ($^\bullet OH$), and superoxide (O_2^-/HO_2^-, both anion and radical). They are all highly reactive species as a result of having unpaired electrons in their valence shell. An imbalance or increase of ROS in a biological system is known as oxidative stress which is a process that is strongly linked to many medical conditions e.g. ageing, heart disease and cancer.[26, 38]

It is currently not possible to measure the relationship between ROS and the molecular response of oxidative stress on a system, and due to the possible medical consequences it is a desired topic of understanding. There are, currently, some fluorescent probes that can measure intracellular O_2 and ROS levels[39] but they tend to have the drawback of toxicity against them (as previously mentioned chemical and physical interference).[40] Also, due to their high reactivity and short lived existence, a method to monitor them would need to be an immediate response measurement in order to see the impact that ROS have and what cellular response is generated. There has been work on the relationship between intracellular oxygen concentrations and the generation of ROS but these have not yet reached a conclusive level of understanding.[38, 41]

1.8. Singlet oxygen generation and calcium

The generation of singlet oxygen was covered briefly in Section 1.6 on photodynamic therapy. Figure 1.8 is a simplified Jablonski diagram but shows in more detail the process for the production of photsensitized singlet oxygen.

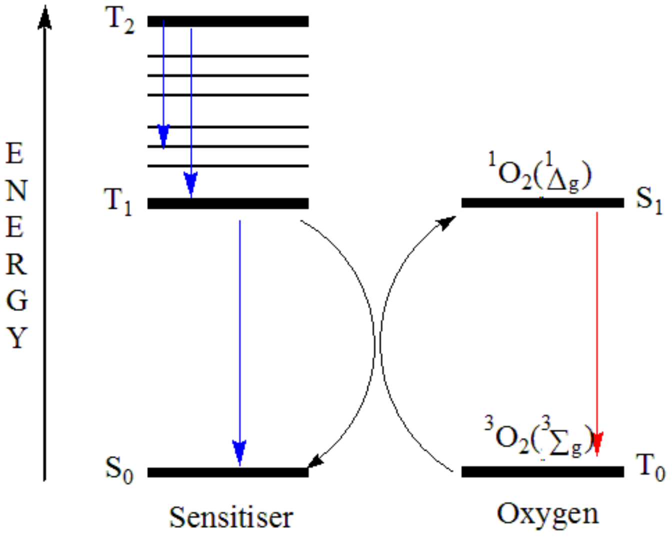

Figure 1.8 Simplified Jablonski diagram indicating the generation singlet oxygen from a sensitizer (e.g. porphyrin). **Blue** arrows indicate the internal conversion and phosphorescence from the sensitizer on returning to its ground state; **black** arrows represent the process of spin inversion or energy transfer from the sensitizer to the oxygen molecule; **red** arrow represents the phosphorescence emitted from singlet oxygen at 1270 nm as it returns to its triplet ground state.

The lowest lying electronic state for molecular oxygen is a triplet state, $^3\Sigma_g^-$, having two unpaired electrons in its highest occupied molecular orbital. Above this it has two low-lying singlet states; $^1\Delta_g$ and $^1\Sigma_g^+$. The former is the lower of the two, with both electrons paired in one orbital. The latter is slightly higher in energy having two spin-paired electrons in separate orbitals, (see Figure 1.9).

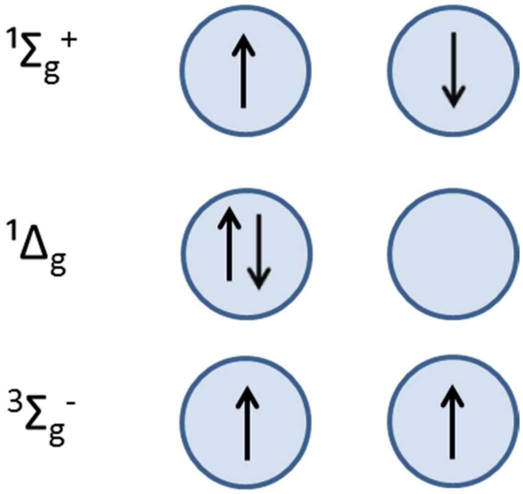

Figure 1.9 Diagram to represent the electronic states of molecular oxygen and the electron spins in the p_x and p_y orbitals

The $^1\Sigma_g^+$ state has a much shorter lifetime than that of $^1\Delta_g$ so rapidly relaxes or decays to the lowest excited singlet state. This singlet state, being the lowest excited state and spin forbidden in relation to the triplet ground state, has a relatively long lifetime. The transition from $^1\Delta_g$ to $^3\Sigma_g^-$ can be observed by its phosphorescence at 1270 nm. The lifetime of singlet oxygen differs depending on the solvent used, for example in water it has a lifetime of 3.5 μs whilst in D_2O the lifetime is easier to observe with a lifetime of 67 μs.[42]

As previously discussed, singlet oxygen is implicated in the mechanism or process of cell death and associated with various diseases or conditions e.g. cancer. Previous research has shown how calcium is an important intracellular signalling ion used as a stress indicator, specifically within the mitochondria of a cell.[43]

A novel route to monitoring the effects of singlet oxygen present or generated would be to measure the levels of Ca^{2+}, in response to the generation of singlet oxygen in the same local environment. Calcium is essential to the body and plays an important part in the monitoring and maintenance within areas such as cell biochemistry (signalling), muscular activity and cell metabolism. Using molecular probes sensitive towards calcium bound to nanoparticles it should be possible to monitor specific cellular of Ca^{2+} in response to ROS stimuli.[10]

As previously stated, the porphyrin family is a class of molecules that are known for their ability to produce singlet oxygen and are a popular choice of sensitisers for use in photodynamic therapy.[44] They are also known to accumulate in the mitochondrial region of a cell.[45] By using the aforementioned porphyrin molecules in conjunction with a calcium sensitive fluorophore, both bound to the same nanoparticles it would be possible to design a system that generates singlet oxygen and can also monitor the local cellular response to the species by means of the Ca^{2+} flux change.

1.9. Aims and objectives

The aim of this chapter has been to provide a brief overview and introduction to some of the fundamentals behind the research detailed in this thesis. Each of the results sections contain, where appropriate, further background information to the sub-topic in question.

All the work discussed throughout this thesis lies under the umbrella category of developing various labelled polyacrylamide PEBBLEs, and building up experience and control data. Each separate section details a different area that is of current interest in both nanomaterial and photophysical research. The majority of the species synthesised, unless stated, were done so by collaborators and the main emphasis at Durham University was to characterise their photophysical properties. The separate chapters each have a different focus of the photophysical properties that are of interest to those species e.g. for oxygen sensitive species the interest was mainly in how sensitive the probes' luminescence was to the concentration of oxygen.

The overall objectives for this project were to characterise the photophysical properties of the designed and synthesised PEBBLEs (see Figure 1.10 for generic schematic), determining the effectiveness of species entrapped in nanoparticles for a variety of applications. This required the design of various systems incorporating both fluorophores and porphyrins into/onto the polyacrylamide matrix. The sections below detail the specific applications or objectives for the nanoparticles discussed in this thesis.

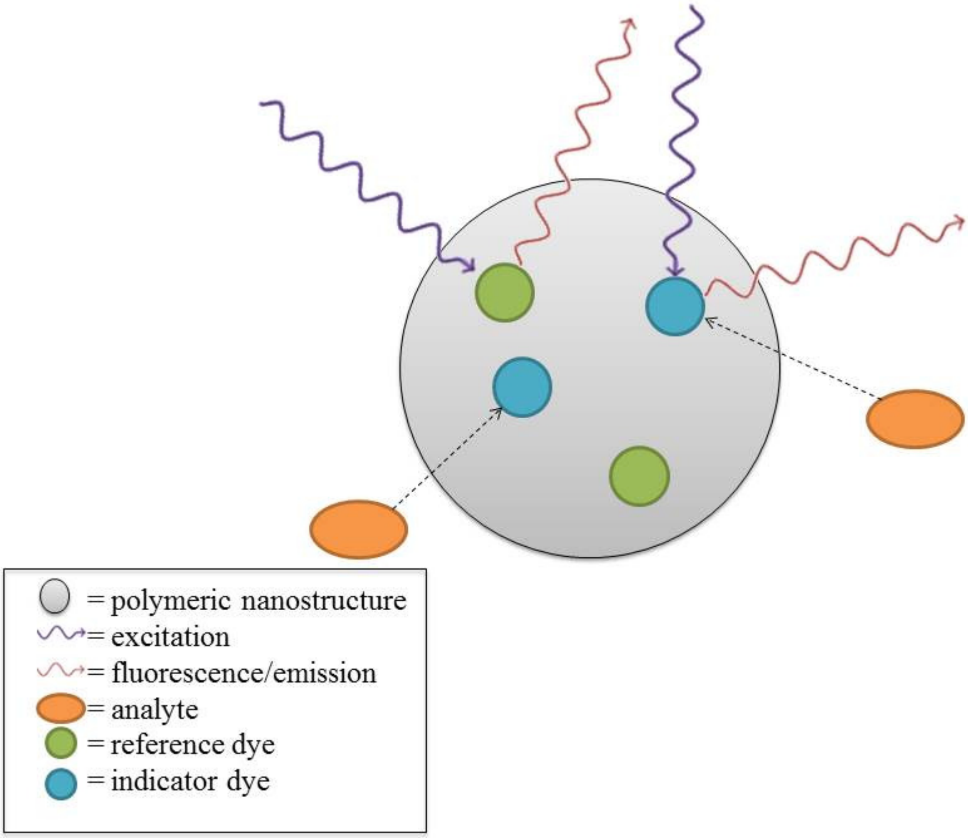

Figure 1.10 Generic schematic diagram of the proposed PEBBLE design

1.9.1. Nanoparticles sensitive to pH

A number of fluorescent dyes have been developed to monitor the changes/alterations in the pH of an environment. These dyes are often toxic for use in bioimaging and as dyes alone cannot be used due to the toxicity implications. Designing and characterizing a nanosensor for monitoring cellular pH could lead to a new type of probe for bioimaging and pH sensing. Such a pH sensing system was also selected as a simple starting point to develop and characterize probes of this type.

1.9.2. Nanoparticles incorporating hydrophobic fluorophores

Many fluorescent dyes exhibit useful and interesting photophyscial properties but due to their lack of solubility in aqueous media their applications are often hindered or limited. Developing nanoparticles which have hydrophobic dyes encapsulated within their matrix could be a valuable development for the future of other fluorescent dyes.

1.9.3. Nanoparticles for calcium sensing

As previously discussed, calcium ions are often released or their concentration within a cell changes when it is undergoing stress or inhibiting effects. Being able to understand these changes in the calcium flux or monitor it is beneficial to further understand mechanisms such as cell death. Incorporating a calcium sensitive dye within the nanoparticles could enable a non-invasive imaging method for monitoring the concentration of calcium within cells.

1.9.4. Nanoparticles for oxygen sensing

Being able to monitor and measure the concentration of oxygen, pO_2, in various environments has a wide variety of applications. Developing a nanoparticle that acts as an oxygen sensor will be beneficial to the current work of oxygen sensing, e.g. hypoxic cells, offering a new approach and greater understanding.

1.9.5. Conjugating porphyrins to the nanoparticle surface

As previously discussed porphyrin molecules play an important role in a number of biological applications, such as PDT. By conjugating the porphyrins to the exterior of the polymer nanoparticle matrix, it will offer new approaches for their current applications and their properties will play an important role in the development of other nanoparticles.

As mentioned, singlet oxygen is in a short lived and highly reactive excited state and it does not travel far before it either reacts or relaxes back to its ground state. Therefore, an important aspect of the nanoparticle design is that it is capable of specific direction towards the required subcellular location. As previously mentioned, mitochondria have been found to be a popular target for previous photodynamic therapy agents. Therefore, it is of great interest to design a system that is able to essentially ‘drive’ the nanoparticles to this location of this organelle. This is possible and has been demonstrated using porphyrins, as mentioned previously.

2. Experimental methods and general information

The focus of the work in this thesis is on the determination of photophysical characteristics exhibited by the nanosensors and porphyrins. The following chapter describes in more detail the processes involved and how they are measured/recorded.

The basic principles of molecular photophysics can be explained with the aid of the simplified Jablonski diagram in Figure 2.1. The Jablonski diagram illustrates the different electronic states of a molecule and the different radiative transitions observed in the processes of absorption and emission.

2.1. Photophysical processes and spectra

Luminescence spectroscopy is a technique that allows the excited electronic states of molecules to be probed; this provides information regarding the electronic structure e.g. the HOMO and LUMO energy levels of the molecule.

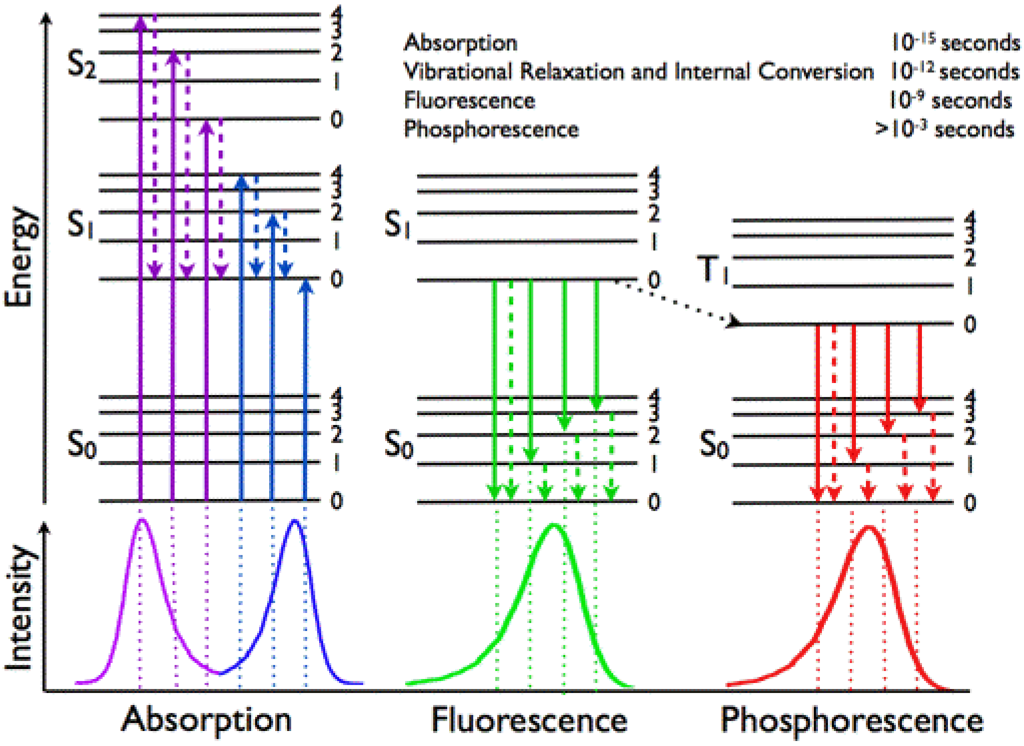

Figure 2.1 Jablonski diagram illustrating energy levels in relation to the spectra produced for each process. The dotted arrows show various pathways of non-radiative transitions.[46]

2.1.1. Absorption

The process of electronic absorption is where a molecule absorbs a photon of an appropriate or specific energy which corresponds to the excitation of electrons. This results in the promotion of a valence electron from its ground state to a vibrational level in an excited singlet state. This is shown by the blue and violet arrows on the Jablonski diagram in Figure 2.1. An absorption spectrum of a molecule can be recorded depicting the intensity of absorption at a given wavelength.

2.1.2. Fluorescence

The process of fluorescence is when a molecule emits the photon which it absorbed in the process of absorption, relaxing back down to its ground state and in doing so giving off energy in the form of light. This is shown on the Jablonski diagram in Figure 2.1 by the green arrows and spectrum. The fluorescence spectrum of a molecule can be recorded through monitoring the light given off by exciting it with a specific amount of energy. This then typically generates a spectrum of the fluorescence intensity at each wavelength; this is called an emission spectrum. It is also possible to record an excitation spectrum, where the $S_0 \leftarrow S_1$

process is recorded, which is normally identical to the absorption spectrum because the fluorescence intensity is proportional to the absorption. It is the dependence of emission intensity which is recorded at a single emission wavelength scanning the excitation wavelength, in this way it is measured in the opposite way to the emission spectrum.

2.1.3. Phosphorescence

The process of phosphorescence is the same as that for fluorescence but the emission of light is from the triplet state, whereas the emission of light in fluorescence is from the singlet state. In order for a molecule to phosphoresce it must undergo intersystem crossing. This process is depicted by the red arrows and spectrum in Figure 2.1.

2.1.4. Quenching

This refers to any process which decreases the resulting luminescence intensity of a given molecule or substance. The most common pathway for quenching is collisional quenching where the fluorophore, in its excited state, is deactivated by a quencher (another molecule in solution). For example, oxygen is a known quencher so phosphorescence is measured in the absence of oxygen. The process for collisional quenching can be described by the well-known Stern-Volmer (SV) equation:

$$\frac{F_0}{F} = 1 + K[\mathrm{Q}] = 1 + k_q \tau_0 [\mathrm{Q}]$$

Equation 2.1 Stern-volmer equation describing the process of collisional quenching; K is the Stern-Volmer quenching constant, k_q is the bimolecular quenching constant, τ_0 is the lifetime unquenched and $[Q]$ is the concentration of the quencher

A fluorophore that is sensitive to the quencher Q has a high Stern-Volmer constant K. This implies that the product of bimolecular rate and lifetime is high. Whereas, if this value is low, it implies that the quencher is not in an accessible range to the fluorophore e.g. it is shielded.

2.2. General layout of spectra throughout

The standard layout, unless specified, for a set of absorption, excitation and emission spectra for one molecule consists of the absorption in blue offset above the excitation spectrum which is below that in red, with the emission spectrum on the same level as the excitation spectrum in green. See Figure 2.2. The excitation and emission wavelengths used are enclosed in the figure captions alongside the solvents in which the samples were recorded.

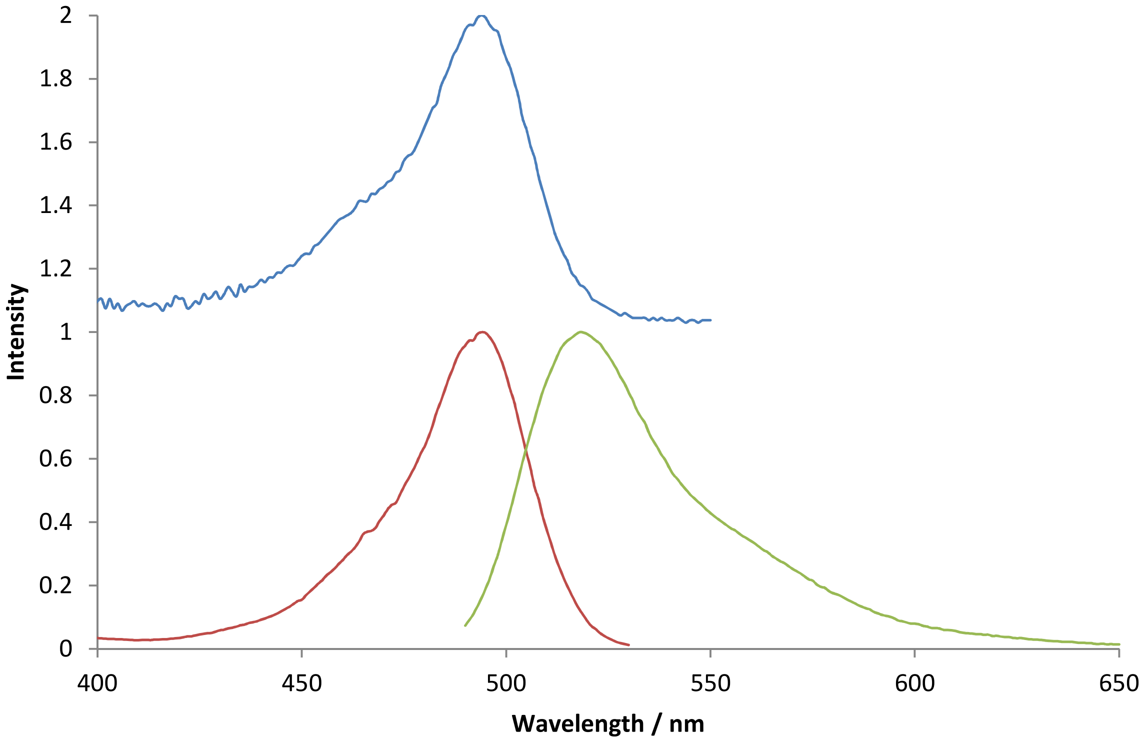

Figure 2.2 Absorption, excitation and emission spectra to illustrate 'standard specta layout'. Normalised absorption (blue), excitation (red) and emission (green) spectra for FITC-dextran in PBS, λ_{ex} = 480 nm and λ_{em} = 540 nm.

Spectra of nanoparticle samples contain only excitation and emission spectra as the absorption of the fluorophores incorporated were hidden by the absorption of the polyacrylamide matrix. The solutions of the nanoparticles tend to be scattering and hence absorption spectra are misleading.

2.3. Collaborators: synthesis and chemicals

This project has been carried out in collaboration with Prof. Ross Boyle and Dr Francesca Giuntini from University of Hull and Dr Jon Aylott and Andrea Lavado from Nottingham University.

The nanoparticles were sized by dynamic light scattering (DLS) and particles without any other molecules conjugated to the surface yielded particles with a mean size of 45 ± 10 nm whilst those with porphyrins attached to the exterior of the surface were in the size range 95 ± 10 nm. This was carried out in the Nottingham and Hull laboratories.

Collaborators from the University of Hull provided and synthesised all the porphyrins discussed in this thesis as well as synthesising the oxygen sensitive nanosensors described in Section 7. They also synthesised the nanoparticles for calcium sensing described in Sections 3.3 and 4. The Calcium Green-1 dextran conjugate was purchased from Life Technologies™ and incorporated into nanoparticles by Dr Giuntini.

The nanoparticles for pH sensing described in Sections 3.1 and 3.2 were synthesised in the laboratory at Nottingham University. The dextran conjugate of FITC was purchased from Sigma Aldrich. The dextran conjugate of TAMRA was synthesised in Nottingham.

Research visits to the laboratories in both Hull and Nottingham were undertaken for practice and understanding of the various synthetic methods and procedures.

The nanoparticles containing hydrophobic molecule derivatives were synthesised in Durham as well as the dextran conjugates involved, these are described within Section 5.

All reagents were purchased from Sigma-Aldrich, Alfa Aesar and Life Technologies unless otherwise stated. Solvents were obtained in house; D_2O was purchased from Goss Scientific. All water used was deionised.

The aminodextran used throughout was purchased from Life Technologies™. It was 10,000 MW and on average contained 2.5 moles of amine to every mole of dextran but is known to vary from lot to lot.[47]

With thanks to Dr Robek Pal for providing the PBS pellets for use throughout this study.

2.4. Experimental techniques

2.4.1. Absorption/Ultraviolet-visible Spectroscopy (UV/Vis)

Absorption spectra were carried out using an ATI Unicam UV-2 spectrometer. Samples were measured in two-sided quartz cuvettes and background spectra of the corresponding solvent were subtracted. The wavelength range recorded is specified for each spectrum and all were run at a scan speed of 10 nm/s with a resolution of 1 nm unless stated.

2.4.2. Luminescence spectroscopy

Luminescence spectroscopy measurements were recorded using a Jobin-Yvon Horiba Fluorolog 3-22 Tau-3 spectrofluorimeter with right angle (90°) detection in relation to the illumination source (Figure 2.3). Dilute solutions with ≈ 0.1 O.D. in a 10 mm quartz cuvette were recorded in order to avoid inner-filter effects.[2] All recorded spectra were corrected for the spectral response of the machine. Samples were recorded in four-sided quartz cuvettes.

Fluorescence emission spectra were obtained as a plot of fluorescence intensity against emission wavelength (nm). Fluorescence excitation spectra were obtained by measuring the intensity of the emission as a function of the excitation wavelength (nm). The excitation spectrum produces a profile which is normally identical to that of the absorption spectrum of the sample and determines or identifies the wavelengths necessary to produce emission as opposed to simply recording the absorption spectrum. Any differences between the excitation and absorption spectra potentially indicate impurities or more complex behaviour and require further investigation.

The same process was used for obtaining the phosphorescence excitation and emission spectra. These were recorded in cuvettes equipped with degassing limbs and grease-free Youngs taps. Samples were degassed using the freeze-pump-thaw method.

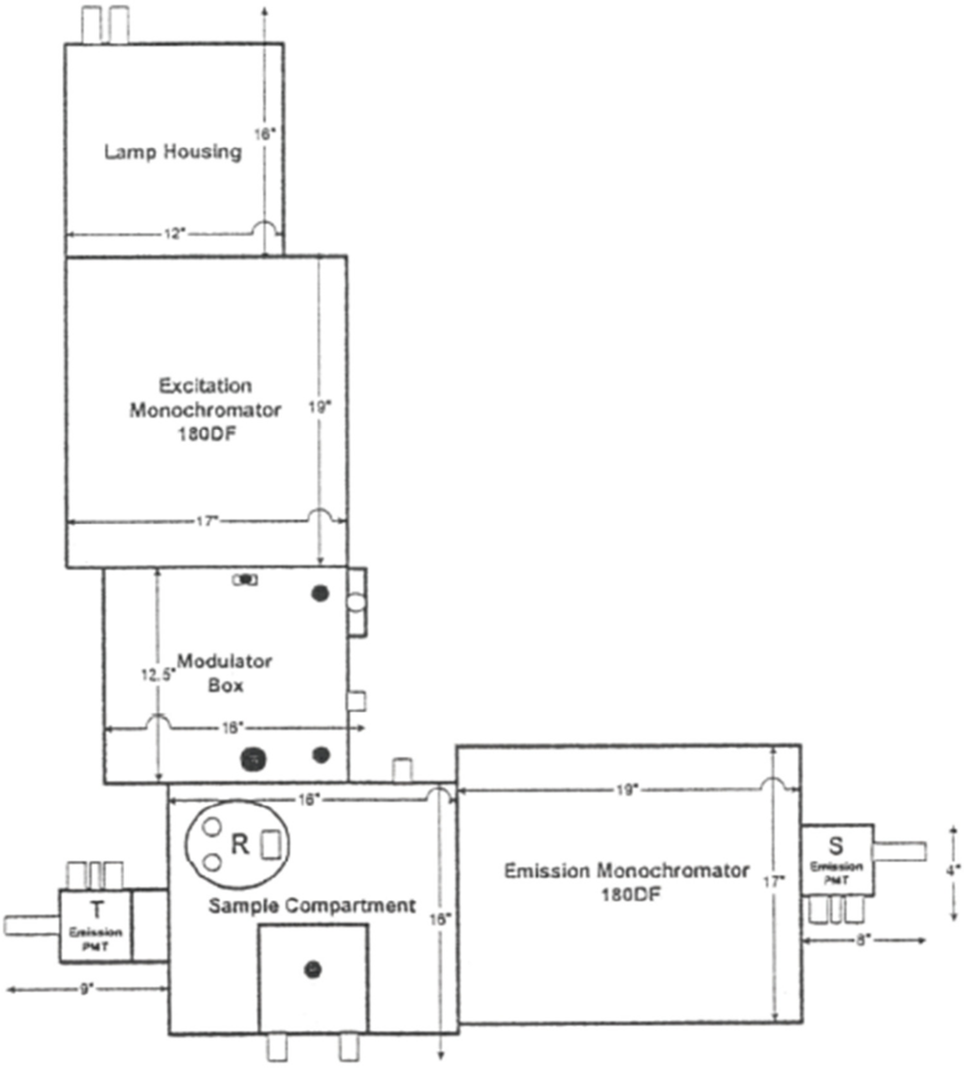

Figure 2.3 Schematic of the Fluorolog 3-22 Tau-3 spectrofluorimeter (Image from the JY Horiba Fluorolog manual).

2.4.3. Luminescence lifetimes

Time-Correlated Single Photon Counting (TCSPC)

Fluorescence lifetime measurements were, in most cases, obtained via the time-correlated single photon counting technique (TCSPC), a description of this method can be found in Lakowicz[2] and Becker[48]. The method described by Beeby *et al.* was used.[49]

Samples were excited by either a pulsed IBH NanoLED diode (371 or 396 nm) or the third harmonic of a cavity-dumped, mode-locked Coherent Verdi-pumped MIRA-D Titanium-Sapphire Laser (300 nm). Emission was collected at 90° to the source of excitation. The emission wavelength was selected by a Jobin Yvon Triax 190 monochromator. Fluorescence was recorded over a minimum of 10,000 counts in the peak channel of the pulse height analyser. A dilute suspension of Ludox® silica in water was used to obtain an instrument response function at the excitation wavelength. Depending on the sample the time per channel was altered to record the best fit in the window. The data was then extracted and analysed using the method of iterative-reconvolution and non-linear least squares fitting using a spreadsheet written in Microsoft Excel. Data was fitted to a sum of two exponentials and the quality of fit assessed by examining the reduced chi-squared, the randomness of residuals and of the random auto-correlation function.

All measurements were recorded in a four-sided cuvette using an absorbance value of 0.10 (± 0.03), which was measured and checked using an ATI Unicam UV-2 spectrophotometer.

Time-Correlated Photon Counting (TCPC)

Phosphorescence lifetimes were recorded using a time-correlated photon counting spectrometer. The samples were held in a four-sided quartz cuvette equipped with a degassing bulb. The samples were excited using the output of a pulsed nitrogen laser (VSL-337i OEM), which provided a 10 Hz pulse train of pulse duration <5 ns at 337 nm, with a pulse energy of ca. 5 μJ. Emission was collected at 90° to the excitation source and the emission wavelength was selected using a monochromator (Bentham TM300) and the selected light detected using a red-sensitive photon counting photomultiplier module (Hamamatsu H10682-1). The arrival times of multiple photons were recorded from each laser shot using a multi-channel scaler, and the data from a minimum of 10,000 laser shots was acquired to furnish the emission decay. For phosphorescent and oxygen sensitive species, prior to measurements the sample was completely degassed by a series of freeze–pump–thaw cycles. Once degassed the concentration of oxygen in the sample cell was adjusted by back-filling the cell with a known pressure of air and according to Henry's Law, $[O_2] \propto p_{air}$. In this way the concentration of dissolved oxygen could be varied from 0–0.27 mM.

Phosphorescence lifetimes for species in section 7 were recorded using the above protocol.

The fluorescence lifetime measurements obtained in section 5.1, 5.3.1 and 5.3.2 for the pyrene derivatives were recorded using the same system as described above as they were too long to measure for the aforementioned TCSPC set up. However, these were not degassed;

they were recorded in a simple four-sided quartz cuvette without recording the concentration of oxygen present.

All measurements were recorded with an absorbance value of 0.10 (± 0.03) at the excitation wavelength, which was measured and checked using the Unicam spectrometer.

2.4.4. Titration: pH

The pH was carefully controlled by additions of acid (2 M HCl) or alkali (2 M NaOH) and the pH was monitored using a calibrated Jenway 3320 pH meter.

The absorbance, excitation and emission spectra were then recorded at specific pH values.

2.4.5. Titration: calcium

The calcium titrations described in this thesis were based on the method and buffer in the protocol provided by Life Technologies^{TM}.[50] Titrations of nanoparticles were recorded via front face collection on the Fluorolog whilst fluorophores in solution were recorded via right angle collection.

2.4.6. Singlet oxygen quantum yields (ΦΔ)

The singlet oxygen quantum yield, Φ_Δ, was determined by time-resolved phosphorescence measurements. Samples were dissolved in D_2O, allowed to equilibrate with air and excited using the third harmonic of a Q-switched Nd:YAG laser (355 nm). A $CuSO_4$ filter was used upstream of the solution to remove residual 1064 nm radiation in the pump beam. Typical pulse energies used were in the range 0.1–1 mJ per pulse. A North Coast E0-817P Ge photodiode/amplifier combination detected the singlet oxygen phosphorescence at right angles to the incident laser beam. The sample was placed in a fluorescence cuvette with a 10 mm path length close to the detector. The singlet oxygen luminescence was selected with a 1270 nm silicon interference filter (bandpass, 30 nm) placed close to the detector. Singlet oxygen quantum yields were determined relative to rose Bengal ($\Phi_\Delta = 0.76$).

3. Nanoparticles for chemical sensing

Chemical sensing is part of a process where a signal is acquired that contains information about the chemical composition of an environment or system in real time. Chemical sensors for different environments have been a subject of research in the chemistry community and exist as a number of different systems. A chemical sensor is a self-contained analyte that has the properties to somehow provide information on its current location or environment.[51]

The initial aim for the project was to develop a ratiometric system for pH sensing using fluorescence of commercial probes to explore the potential effect the polyacrylamide matrix could have on prospective fluorophores. Acrylamide itself is a known fluorescence quencher, therefore, it is important to know whether there is a quenching effect from the nanoparticle matrix or not.[52, 53] Therefore, developing a system where the fluorescence properties are maintained was an essential first step.

An obvious choice for a pH sensitive fluorescent probe was fluorescein (Figure 3.1) due to its current usage as a pH probe in cell microscopy. Conjugation to amino-dextran is achieved by reacting it with fluorescein isothiocyanate (FITC). This fluorescein dextran conjugate is commercially available and purchased from Sigma Aldrich. The next step was to develop a system that had potential for monitoring cell activity and death. Based on the knowledge that one of the proposed mechanisms for response to stress of a cell is in the change in the flux of, or release of calcium ions, we decided to use Calcium Green, a commercially available probe for calcium sensing, within the nanoparticles.

In this section FITC and Calcium Green were purchased as their dextran conjugates from Sigma Aldrich and Life Technologies^{TM} respectively. 5(6)-Carboxytetramethylrhodamine dextran was synthesised by reacting *N*-succinimidyl ester of the rhodamine with aminodextran to form its dextran conjugate (see experimental Section 9).

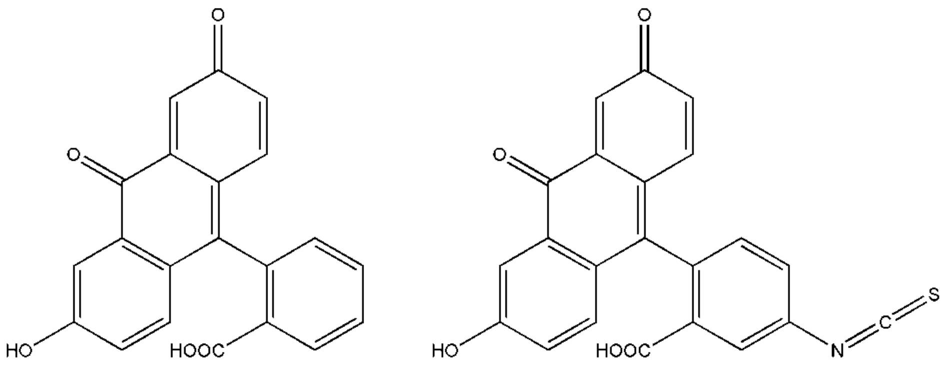

Fluorescein

Fluorescein Isothiocyante (FITC)

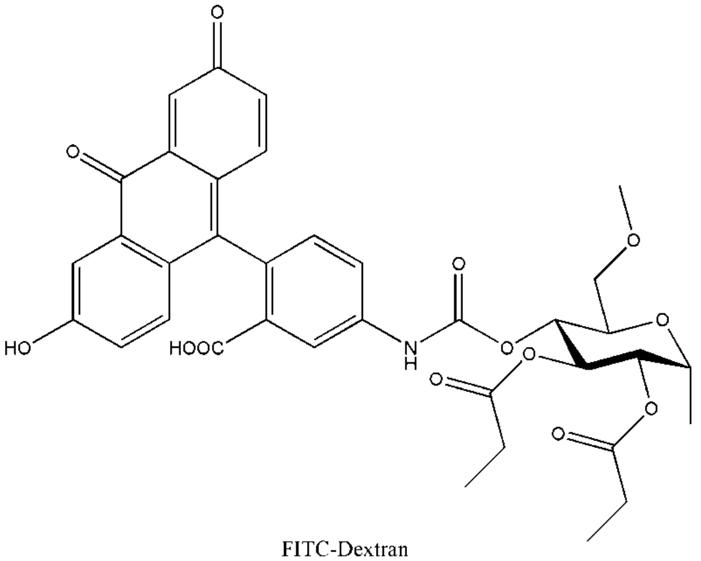

FITC-Dextran

Figure 3.1 Molecular structures of fluorescein (top left), its derivative fluorescein isothicyanate (top right) and the dextran conjugate of fluorescein isothiocyanate (bottom).

3.1. Nanoparticles for pH sensing

Throughout this section the photophysical properties for the development of a system for pH sensing on the nanoscale are discussed. Firstly, a pH sensitive dye is introduced in solution and then incorporated within the polyacrylamide matrix and the sensitivity of the system to pH is analysed.

This idea is then carried forward with the potential for a ratiometric pH nanosensor. A ratiometric system is one that is based on the ratio of two different fluorescent intensities. In this instance two dyes are used, one which has a sensitive response to the signal being monitored and one which is insensitive and so provided an internal reference or calibration for the measurement. The advantage of this type of system is that it allows the correction of artefacts due to changes in laser focus, excitation, background or autofluorescence. By calibrating the system, the ratio of the observed fluorescence intensities from the two fluorophores, are used to eliminate these artefacts.

3.1.1. Fluorescein isothiocyanate (FITC)

FITC-Dextran is a commercially available material containing multiple molecules of the pH sensitive dye conjugated to a polymeric dextran sugar backbone. FITC is a derivative of fluorescein which is a common fluorescent dye that is regularly used as a fluorescent standard due to its high quantum yield (literature value = 0.90)[54]. The difference between the structure of fluorescein and that of FITC is that the latter has a reactive isothiocyanate (N=C=S) group attached, replacing a regular hydrogen atom, which can be used to form the dextran conjugate. The effects of this substitution on the electronic structure, and hence photophysical properties of the fluorescence, is minimal and the conjugates retain their high fluorescence quantum yield.

Due to its high quantum yield, good water solubility and moderate photochemical stability fluorescein and its derivatives have been used as an important fluorophore for confocal laser-scanning microscopy and flow cytometry applications.[55] The fluorescence properties of FITC-dextran were characterised and calibrated to ensure a comparison could be made to the case when the dye-dextran conjugate is entrapped in a nanoparticle to determine whether its fluorescence properties were maintained.

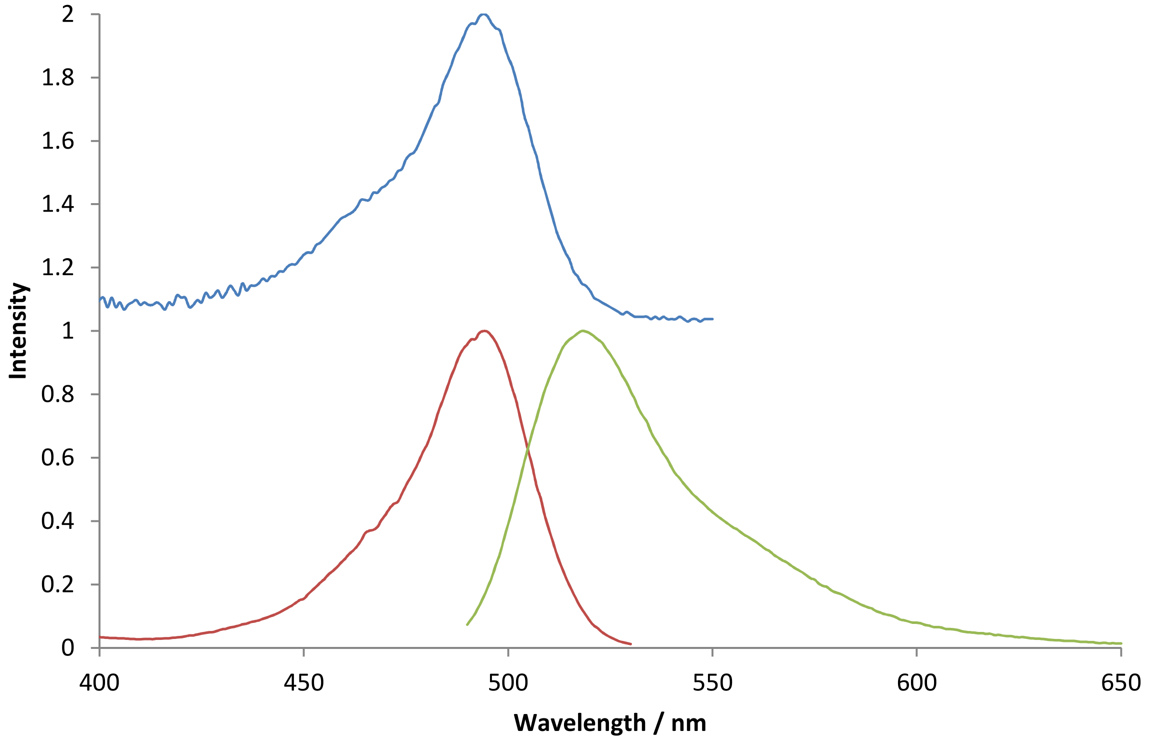

Figure 3.2 Normalised absorption (blue), excitation (red) and emission (green) spectra for FITC-dextran in PBS, λ_{ex} = 480 nm and λ_{em} = 540 nm.

The absorption and emission maxima for FITC-dextran (as shown in Figure 3.2) are 495 nm and 520 nm respectively. This data shows that FITC-dextran has a Stokes shift of approx. 25 nm. The absorption and excitation spectra present the same profile which suggests there are no impurities or effects of aggregation upon the conjugation to dextran.

The PLQY recorded at 495 nm of 0.92 corresponds to the high value characteristic of any dye derivative of fluorescein, a further indication that the fluorophore maintains its photophyscial properties after conjugation to amino dextran. The molar extinction coefficient calculated at 492 nm was 74,000 M^{-1} cm^{-1} correlating well with the literature value of 76,900 M^{-1} cm^{-1} of the parent molecule, fluorescein.[56]

Titration demonstrating pH sensitivity

Titrations with acid and alkali were performed in order to characterize the pH sensitivity of the dye. The data is shown by means of both the emission, and absorbance data obtained and also a titration curve to further exemplify this. The concentration of FITC within the FITC-dextran sample used for the pH titrations was 1.75×10^{-6} mol dm^{-3}; this was calculated from the absorbance of 0.13 at pH 7.4, prior to any pH change.

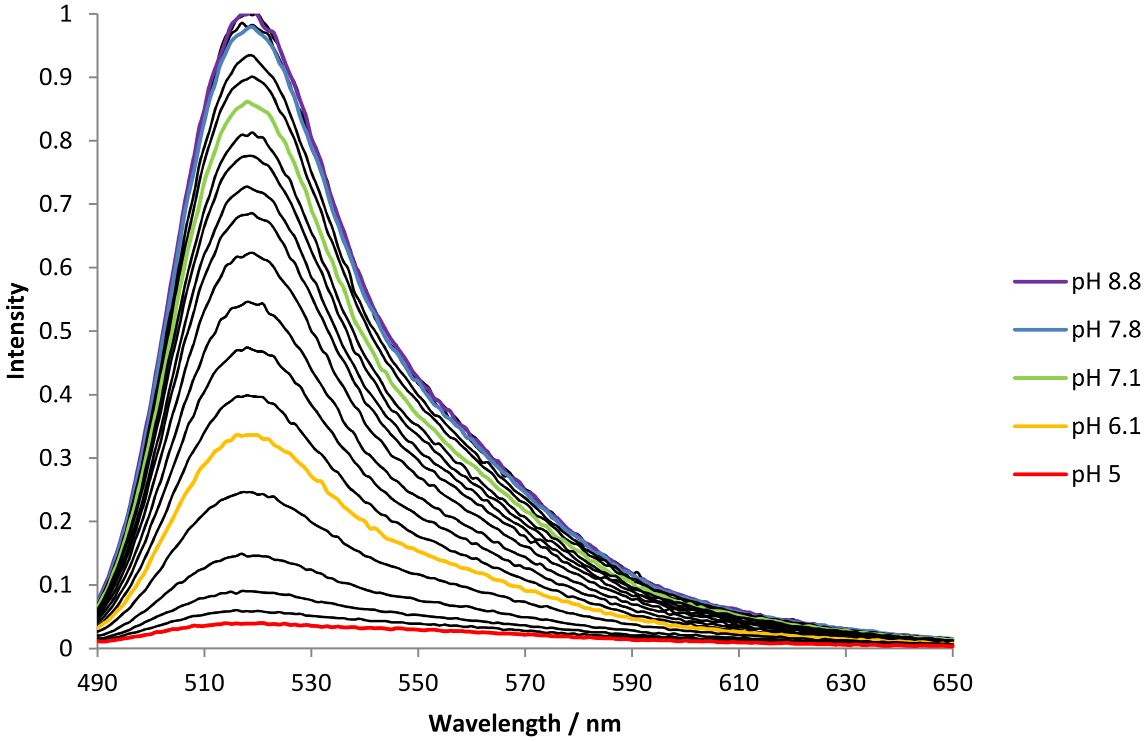

Figure 3.3 Normalised emission spectra for pH titration of FITC-dextran measured in distilled water ranging between pH 5-9, λ_{ex} = 480 nm.

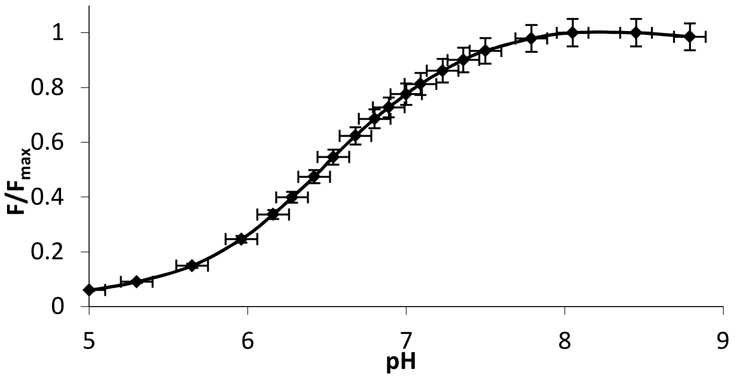

Figure 3.4 Titration curve extrapolated from data in Figure 3.3 using the fluorescence intensity values from the emission maximum at 520 nm (F) relative to the emission from the most intense sample (F_{max}) as a function of pH.

FITC entrapped in nanoparticle

The next step was to incorporate FITC-dextran within the polyacrylamide matrix, and determine any differences in the photophysical properties of the naked FITC-dextran and the nanoparticle entrapped dye.

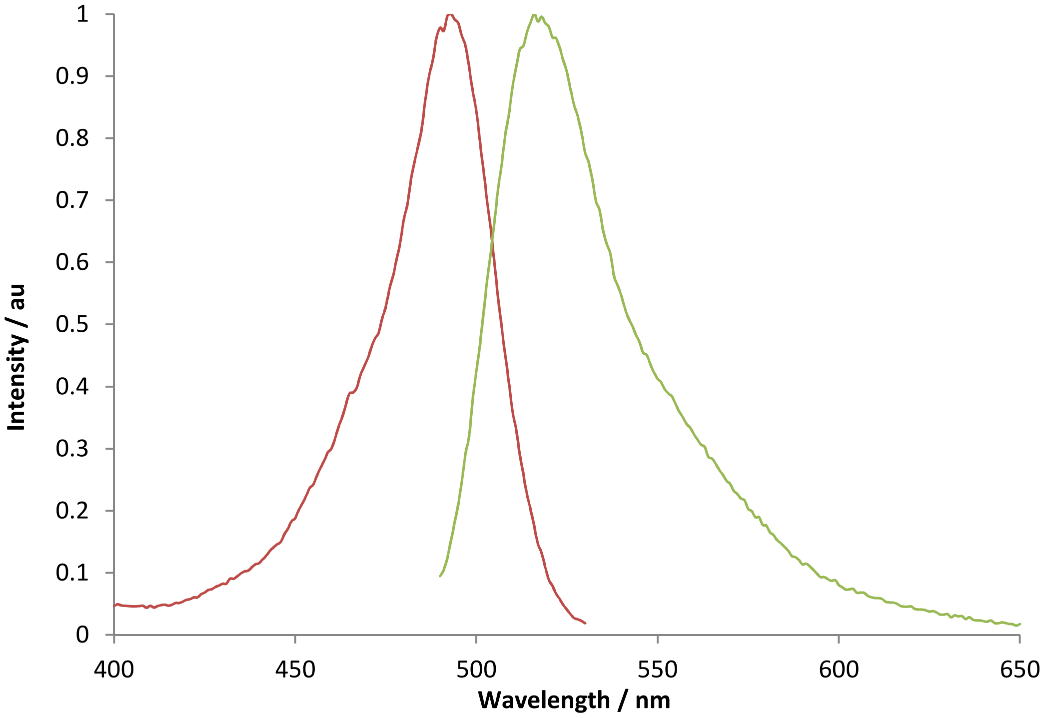

Figure 3.5 Normalised excitation and emission spectra of FITC-dextran entrapped in dye measured in PBS, λ_{ex} = 480 nm and λ_{em} = 540 nm.

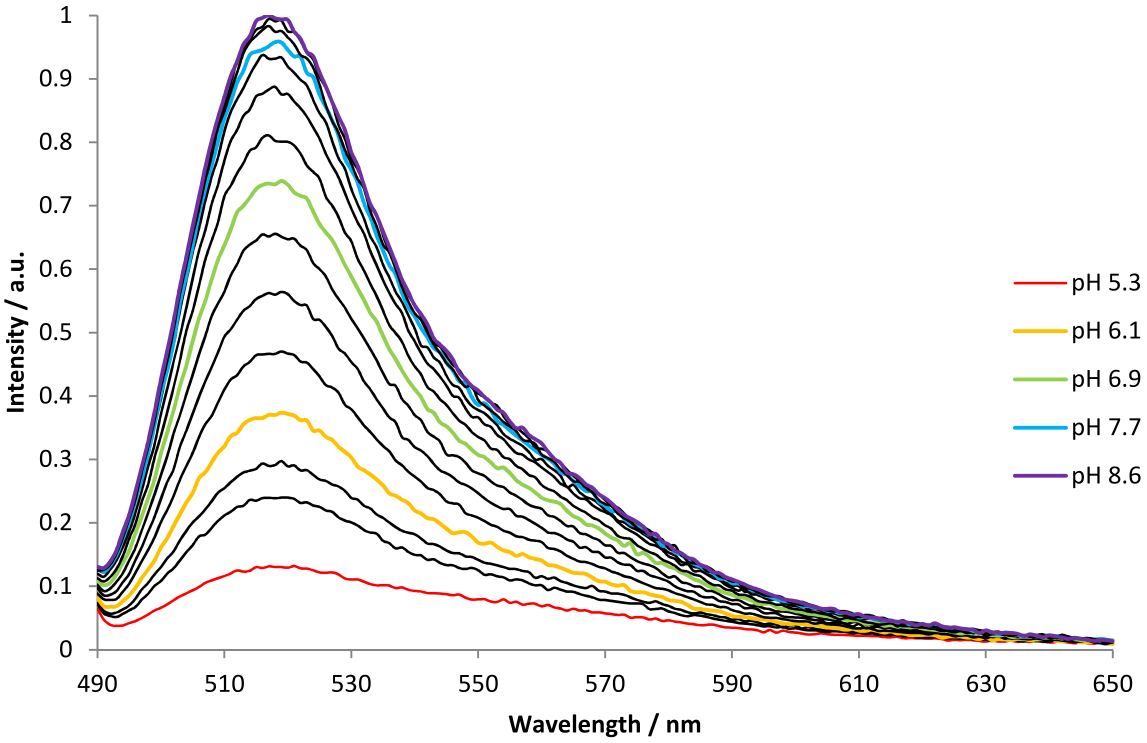

Figure 3.6 Normalised emission spectra for pH titration of FITC-dextran entrapped in PEBBLE, measured in PBS, $\lambda_{ex} = 480$ nm.

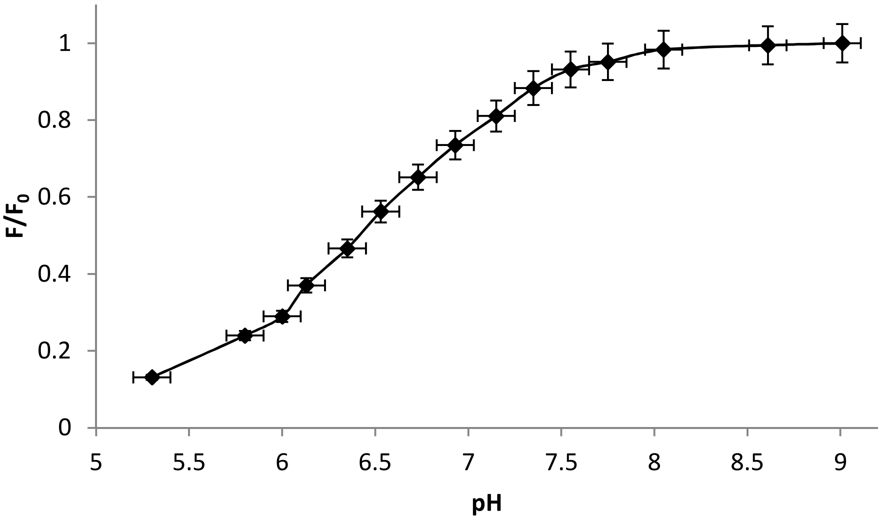

Figure 3.7 Emission pH titration curve extrapolated from data in Figure 3.6 using the fluorescence emission maximum of 519 nm.

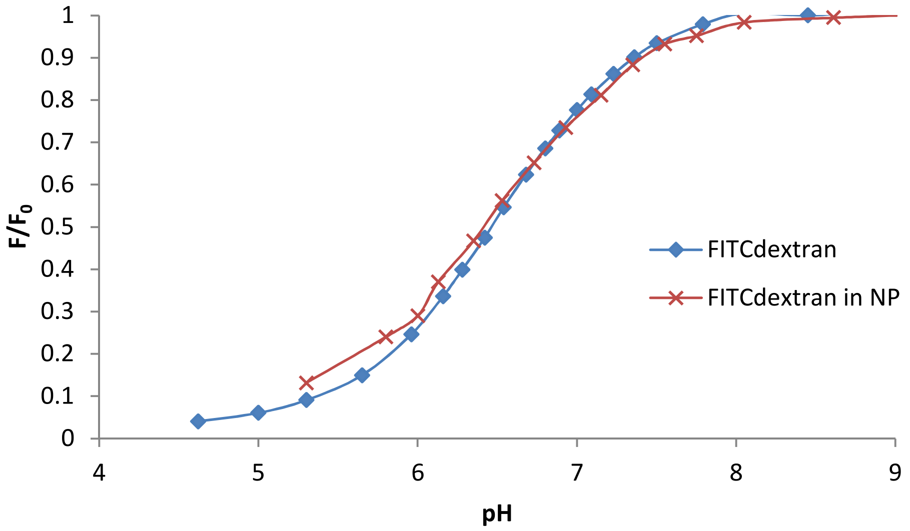

Figure 3.8 Overlaid emission pH titration curve of FITCdextran and FITCdextran entrapped in polyacrylamide nanoparticle at 519 nm, measured in PBS, λ_{ex} 480 nm.

Table 3.1 Comparison of photophysical properties of FITCdextran in solution and in nanoparticle

FITC-dextran	Abs max / nm	Em max / nm	Fluorescence lifetime / ns
In solution	493	520	3.8 (± 0.1)
Inside Particle	492	519	3.7 (± 0.1)

The above results confirm the ability to incorporate fluorophores within the polyacrylamide matrix of nanoparticles by means of dextran-dye conjugation. The pH nanosensors also confirm similar sensitivity to pH change as the dye in solution and that, within error, the incorporation within the matrix has no effect on the fluorescence lifetime of the fluorophore.

3.2. Ratiometric sensing

The benefit of being able to anchor labels into the polymer matrix is that at the point of synthesis it would be possible to anchor more than one probe and hence develop a system that could respond to multiple stimuli or environmental changes. Using this technique, the next stage was to develop a ratiometric pH sensor using FITC (pH sensitive) and a complimentary pH insensitive dye.

3.2.1. 5(6)-Carboxytetramethylrhodamine N-succinimidylester (TAMRA)

The dye chosen for ratiometric sensing was the *N*-succinimidyl ester of 5(6)-carboxytetramethylrhodamine, TAMRA, which is a derivative of rhodamine and related to the fluorescein family of molecules, but importantly it does not undergo changes in its fluorescence characteristics when exposed to pH change making it a pH insensitive fluorescent dye.

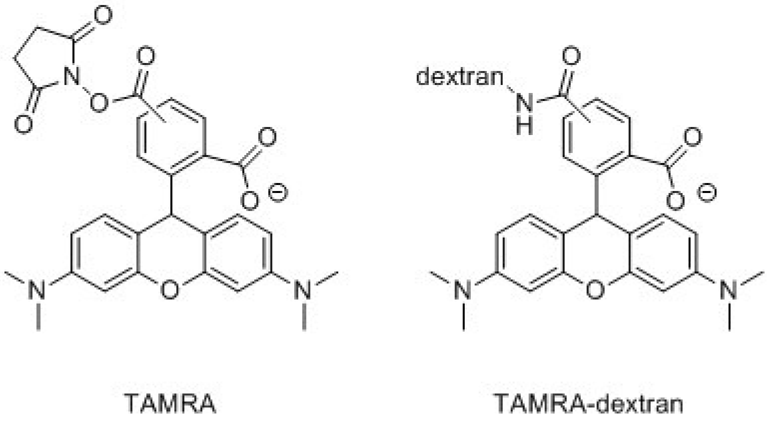

Figure 3.9 Molecular structures of TAMRA and its dextran conjugate

The photophysical properties of TAMRA are well established, being again a commercially available dye, and the emission maxima for both TAMRA and FITC are 60 nm apart but the absorption spectra overlap and so is a useful starting point for a ratiometric pH sensor. Also, by choosing the *N*-succinimidyl ester, it was straightforward for the dextran conjugation, which was undertaken by collaborators in the Nottingham laboratory.

This section displays the observed photophysical properties and characteristics of the dye TAMRA in solution and as the dextran conjugate. Figure 3.10 and Figure 3.11 display the absorption, excitation and emission spectra for both TAMRA and TAMRA-destran respectively.

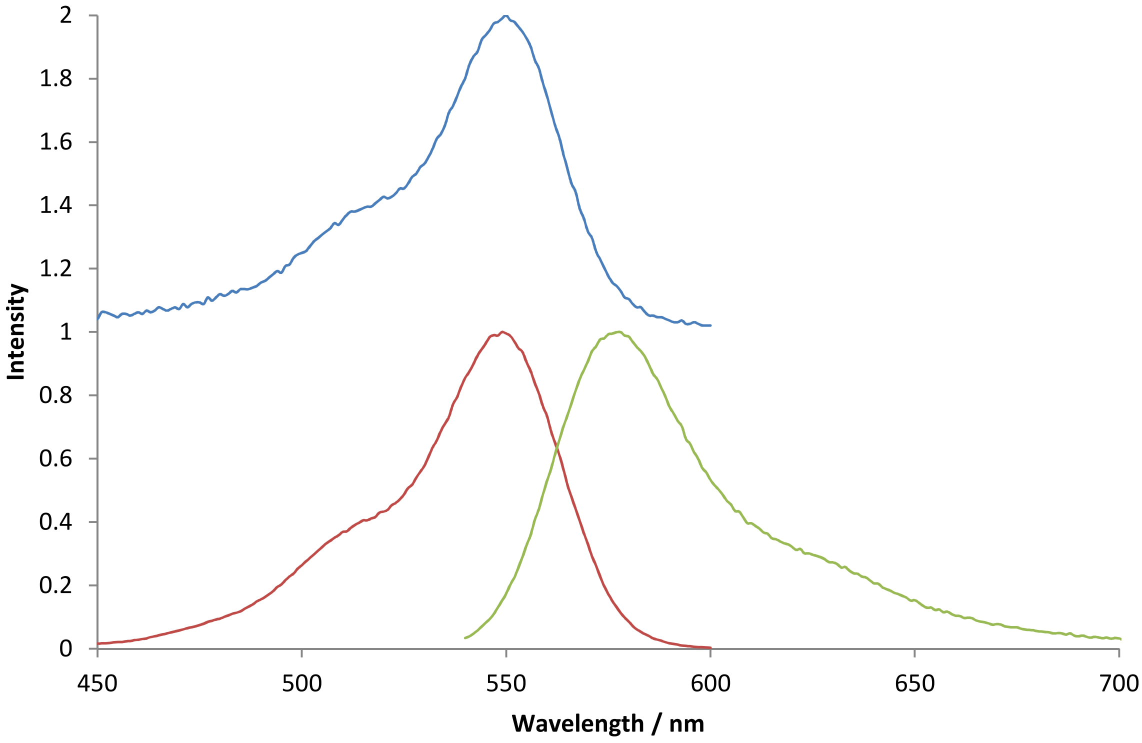

Figure 3.10 Normalised absorption, excitation and emission spectra of TAMRA measured in PBS, λ_{ex} = 530 nm and λ_{em} = 610 nm.

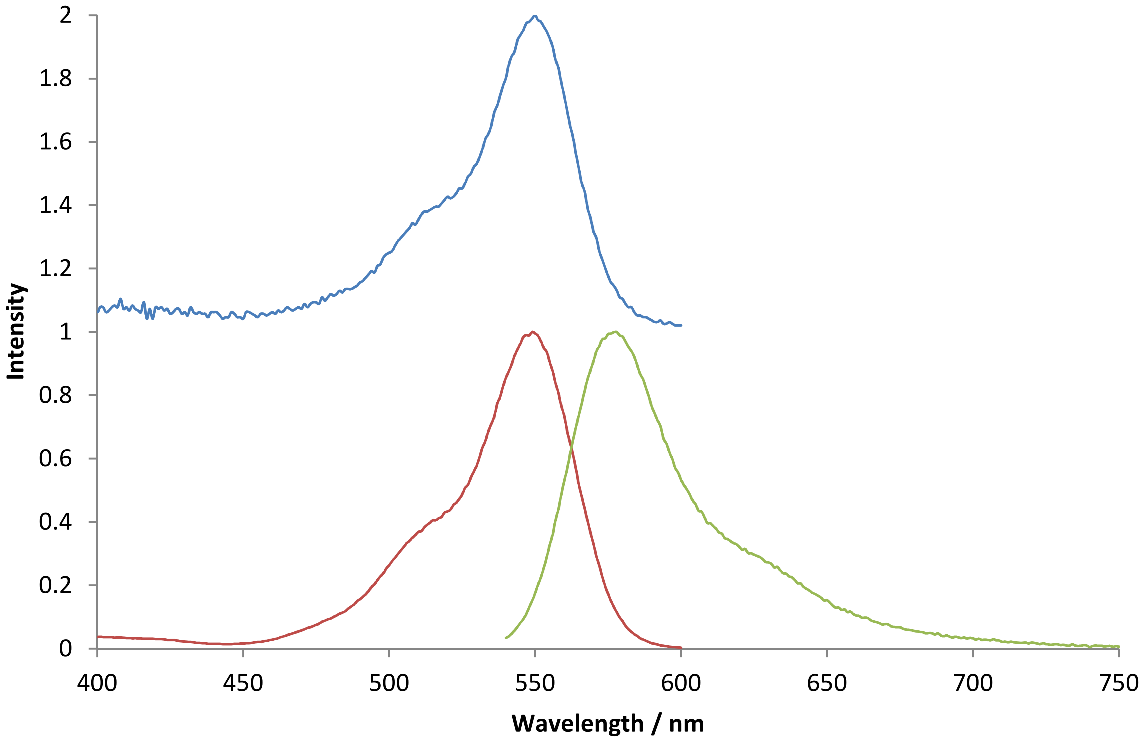

Figure 3.11 Normalised absorption, excitation and emission spectra of TAMRAdextran in PBS, λ_{ex} = 520 nm and λ_{em} = 600 nm

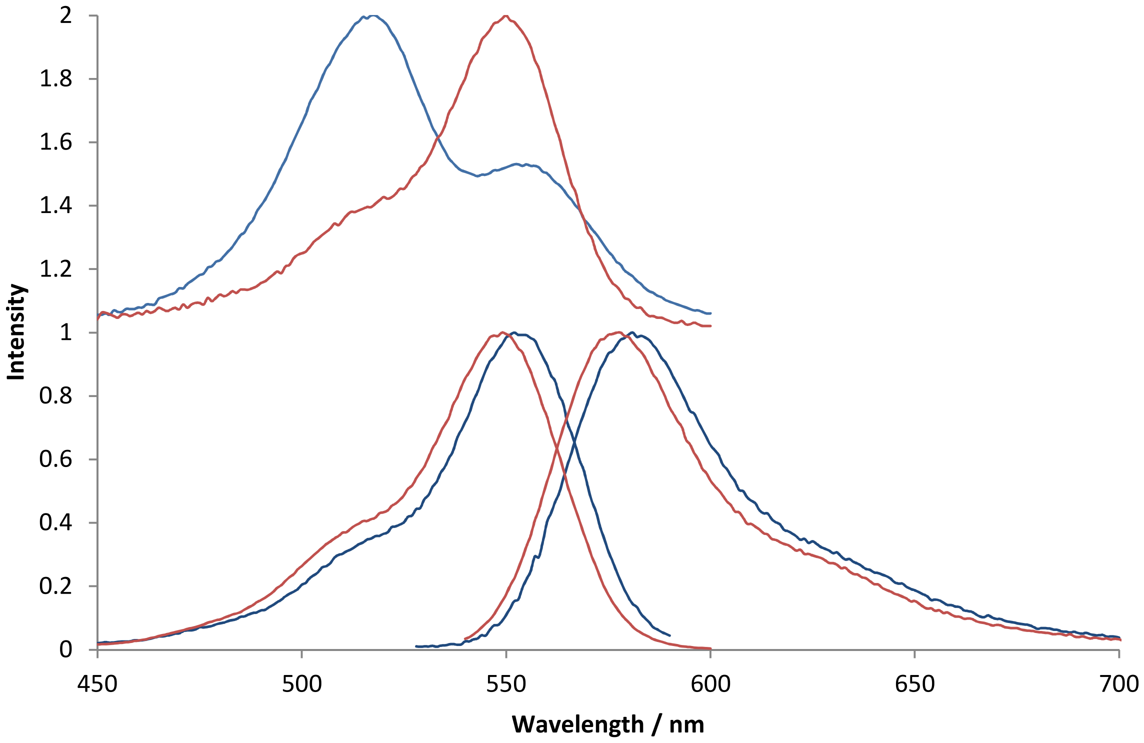

Figure 3.12 Overlaid normalised absorption, excitation and emission spectra of TAMRA (red) and TAMRAdextran (blue) in PBS, λ_{ex} = 530 nm and λ_{em} = 610 nm

Table 3.2 Data comparing TAMRA and TAMRA dextran in PBS

Sample	Absorption / nm	Emission / nm	Lifetime / ns
TAMRA	517, 550	578	2.3 (± 0.1)
TAMRAdextran	517, 552	580	2.2 (± 0.1)

As shown from Figure 3.12 and Table 3.2, the fluorescence emission from TAMRAdextran shows similar peak positions as that of TAMRA with a shift of 2 nm from the emission maximum. This can be attributed to the slight difference the functionality of the isothiocyanate group to the aminodextran. This also confirms that the dextran conjugation does not have a large impact on the fluorescence of the dye as it does not alter the structure of the emission, which if there was any effect on the fluorescence from the dextran sugar, a greater change than a 2 nm shift would be seen. For example, a change in the overall structure of shape of the emission spectrum of the dye would be seen.

However, there is a noticeable change in the absorption spectra between TAMRA and TAMRA-dextran. For TAMRA, the absorption spectrum is an approximate mirror image of the emission. The ratio of the intensities of these two peaks is seen to invert when conjugated to dextran. As mentioned before, the excitation spectra should be a replica of the absorption peak confirming the wavelengths that correspond to the fluorescent activity seen in the emission spectrum. Here, the absorption and excitation spectra do not match; in fact the excitation spectrum matches that of TAMRA not conjugated to dextran. This feature in the absorption is clear evidence of a non-fluorescent aggregate of TAMRA-dextran. Aggregation of the fluorophore is not a surprise as the possibility of several molecules being held closer together in solution as the dextran strand essentially curls up is quite high. This aggregation can be explained by the exciton theory developed by Kasha in the 1950s in which describes the splitting of excited states in molecular aggregates.[57, 58]

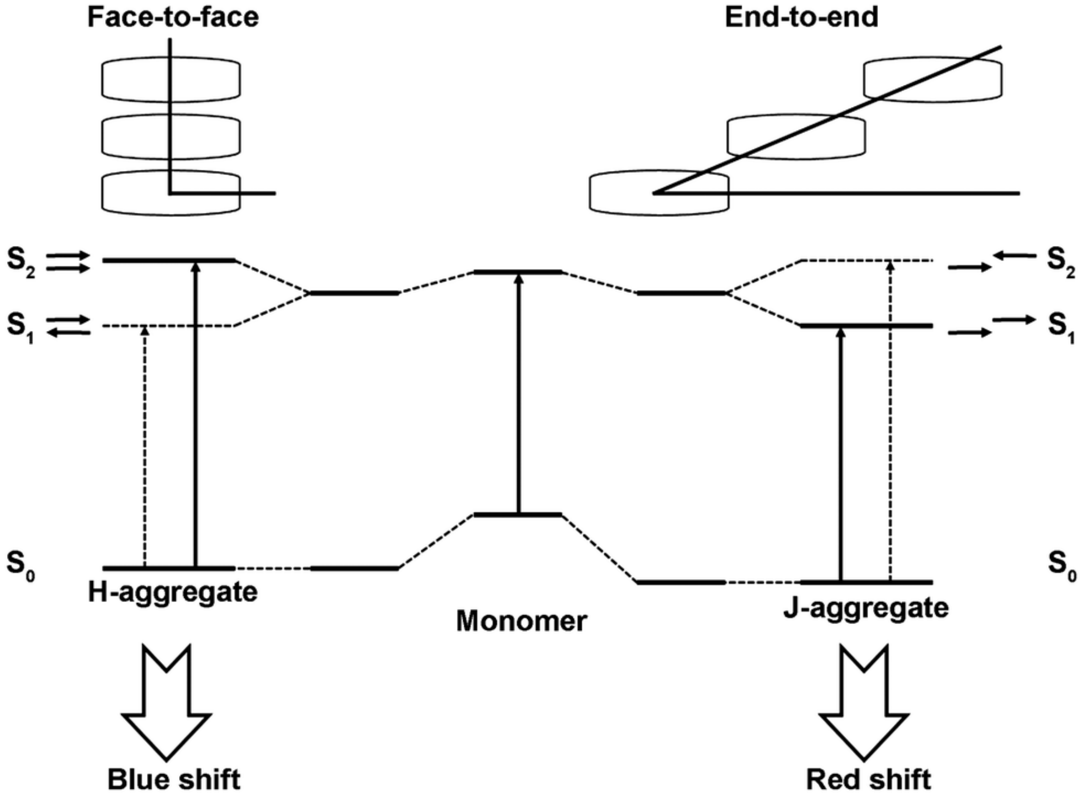

Figure 3.13 Simplified energy diagram explaining the exciton theory for aggregates[59]

It can be seen from the simplified energy diagram in Figure 3.13 the aggregates of TAMRA-dextran in solution fit the model of an H-dimer as the shift in energy seen in the absorption spectrum is towards the higher energy, lower wavelength. However, the fact that the aggregation of the fluorophore dextran molecule is not present in the excitation spectrum suggests that the aggregate is non-fluorescent. Due to the presence of fluorescence still within the sample it can be assumed that there is a mixture of monomers and aggregates within the dextran conjugate.

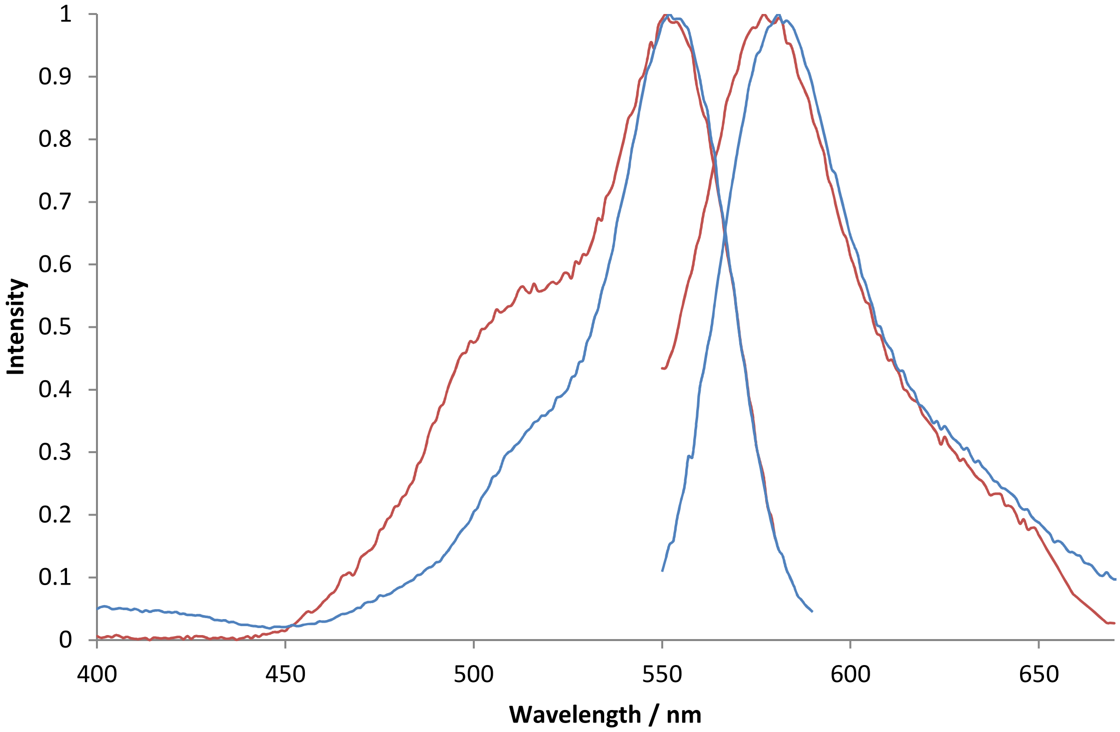

Figure 3.14 Overlaid normalised excitation and emission spectra of TAMRAdextran (red) incorporated within polyacrylamide nanoparticles and TAMRAdextran (blue), both recorded in PBS, λ_{ex} = 535 nm and λ_{em} = 595 nm

Due to the nature of the nanoparticle, the excitation and emission spectra wavelengths used were close to the maximum (less than 10 nm either side of the maximum), and the same wavelengths were used for TAMRAdextran for comparison value. As seen from Figure 3.14, when incorporated into the polyacrylamide matrix, the TAMRAdextran dye appears to maintain its photophysical characteristics. A slight rise in the shoulder peak of the excitation peak is seen at 515 nm which can be attributed to the inner filter effect. Due to the nature of the nanoparticles, the polyacrylamide matrix increases the absorption and potential for scattering of the sample. For this reason the fluorescence spectra are measured using front face detection on the spectrometer but in the excitation spectrum this may still be a factor as the detection is not by front face collection. The comparison and overview of the photophysical properties of TAMRA-dextran in solution and TAMRA-dextran in the nanoparticles can be seen in Table 3.3.

Table 3.3 Data comparing photophysical properties of TAMRA-dextran in solution and in nanoparticle, all measurements recorded in PBS

TAMRA-dextran	Absorption / nm	Emission Max / nm	Lifetime / ns
In solution	515, 555	580	2.2 (± 0.1)
Inside Particle	-	578	2.3 (± 0.1)

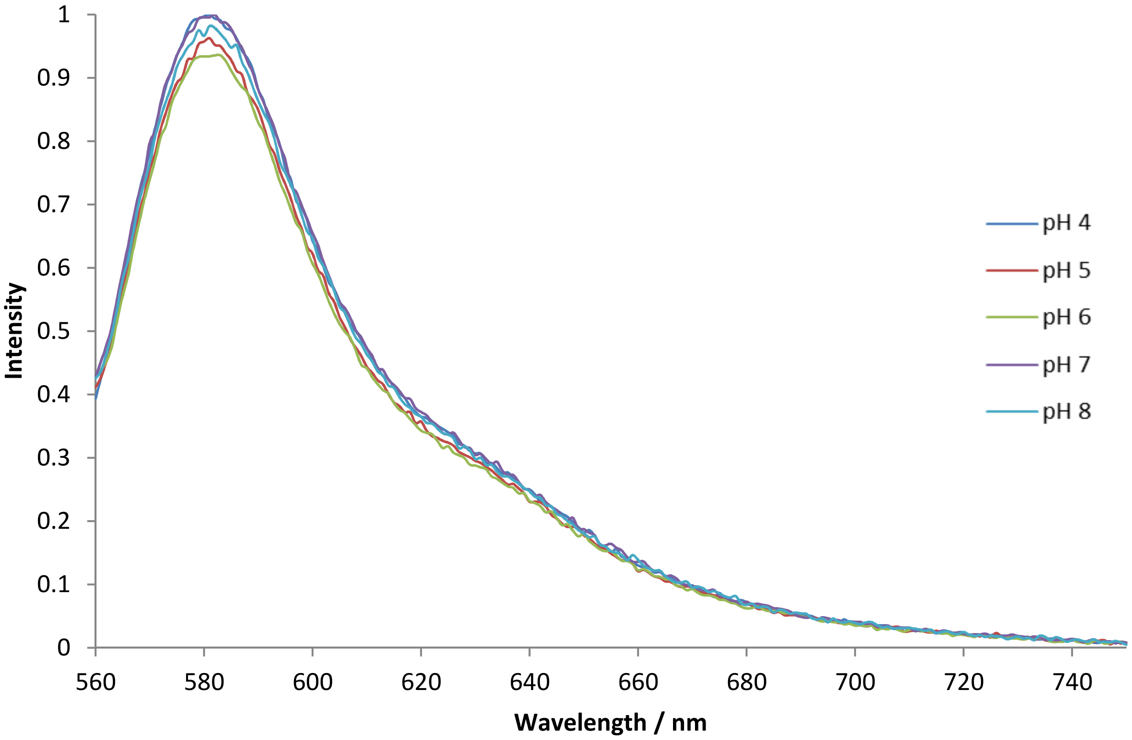

Figure 3.15 Normalised emission spectra of TAMRA-dextran recorded in PBS ranging from pH 4 – 8, λ_{ex} = 555 nm.

Figure 3.15 illustrates the use of TAMRA as a pH insensitive dye as the emission intensity remains essentially unchanged under acidic and alkaline conditions.

The next step was to prepare and characterise the dyes entrapped together within polyacrylamide nanoparticles.

3.2.2. Nanosensors with FITC and TAMRA entrapped

The previous work has shown that the TAMRA dye is inert to alterations in the pH of the environment whilst the FITC dye has a strong on-off emission sensitive to pH. Thus a particle containing both dyes would have the potential for being a ratiometric pH nanosensor.

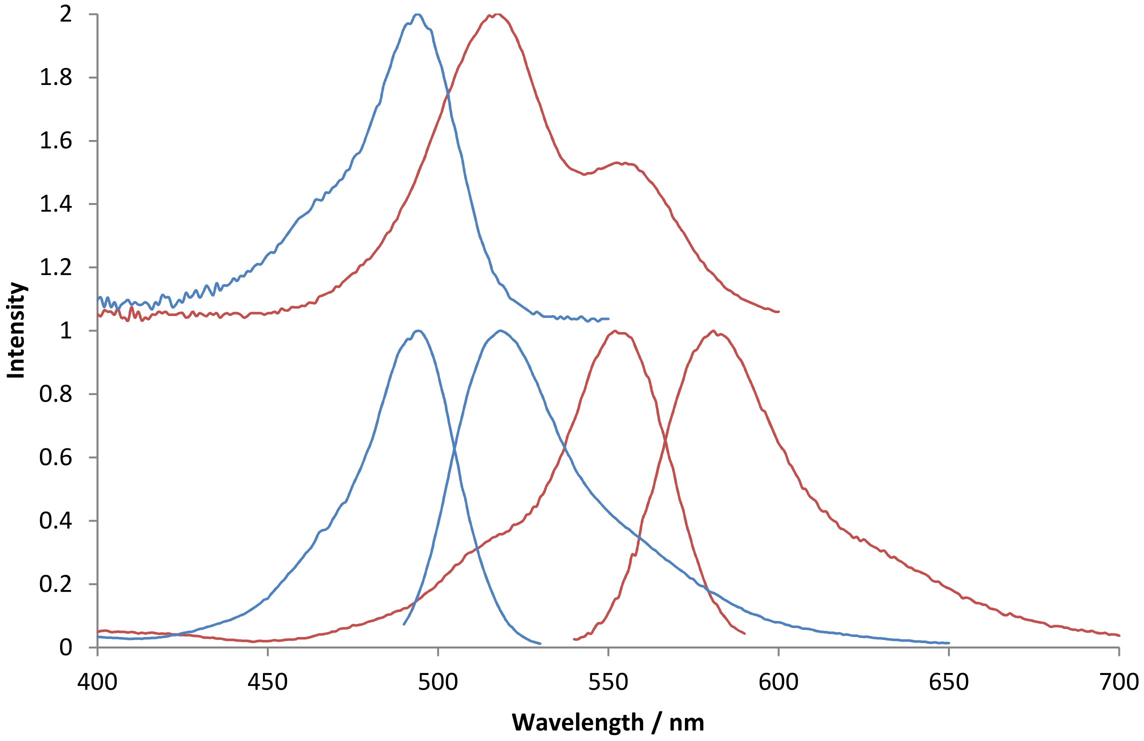

Figure 3.16 Normalised absorption, excitation and emission spectra of FITC-dextran (blue spectra, λ_{ex} = 480 nm and λ_{em} = 540 nm) and TAMRA-dextran (red spectra, λ_{ex} = 530 nm and λ_{em} = 600 nm) in PBS.

The fluorescence emission spectra of both TAMRA and FITC within the polyacrylamide nanoparticle are clearly visible. Figure 3.16 shows fluorescence spectra of FITC-dextran and TAMRA-dextran in alkaline, neutral and acidic conditions where the fluorophores are excited together and therefore recorded together. Because the tail of the emission from FITC overlaps with that of TAMRA, the intensity of the rhodamine fluorophore is affected by the pH change. Therefore, spectra were taken by exciting the dyes within areas of their absorption to ensure reduced overlap and hence co-excitation with the other dye.

For this reason, using doubly-labelled particles with dextran conjugates, the TAMRA fluorophore was excited at 535 nm and FITC at 480 nm in order to obtain separate spectra from the two fluorophores. The fluorescence spectra in Figure 3.17 and Figure 3.18 show how the fluorescence intensity of each fluorophore responds to the level of pH when entrapped together within the polyacrylamide matrix. As can be seen from these data the fluorescence of the individual fluorophores can easily be monitored when entrapped together as doubly-labelled nanoparticles by wavelengths specific to their absorption spectrum.

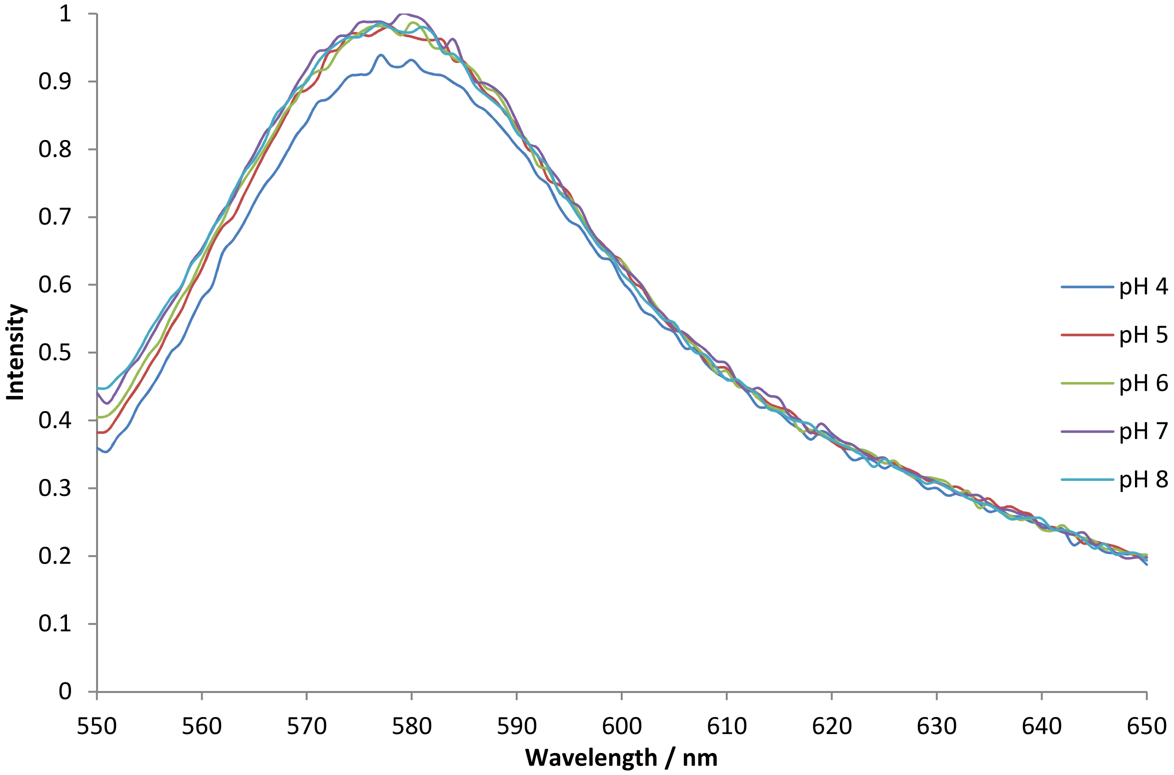

Figure 3.17 Normalised, with relative intensities, emission spectra of TAMRA-dextran in doubly-labelled nanoparticles measured over pH range 4 - 8 in distilled water, λ_{ex} = 540 nm.

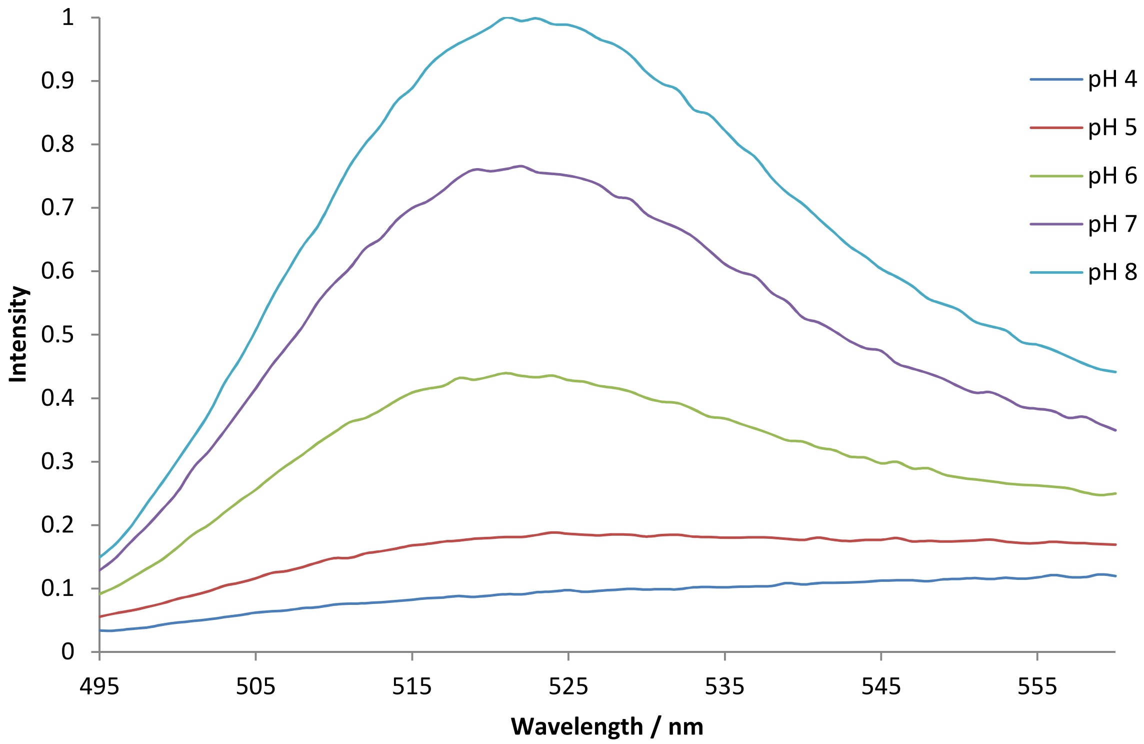

Figure 3.18 Normalised, with relative intensites, emission spectra of FITC-dextran in double labelled nanoparticles measured over pH range 4 – 8 in distilled water, λ_{ex} = 480 nm.

By extracting the data from the fluorescence spectra plots in Figure 3.17 and Figure 3.18, F/F_{max}, which is the fluorescence emission relative to the maximum emission from the pH titration of FITC, was plotted as a function of pH (Figure 3.19) demonstrating that for a system where FITC-dextran and TAMRA-dextran are co-incorporated into polyacrylamide nanoparticles at a ratio of 2:3 (FITC:TAMRA), the relative fluorescence emission spectra can be used to monitor local pH. The relative intensity of fluorescence of TAMRA was approximately a third greater than the fluorescence monitored for FITC at pH 8 and approximately three times greater than the fluorescence measured for FITC at pH 4.

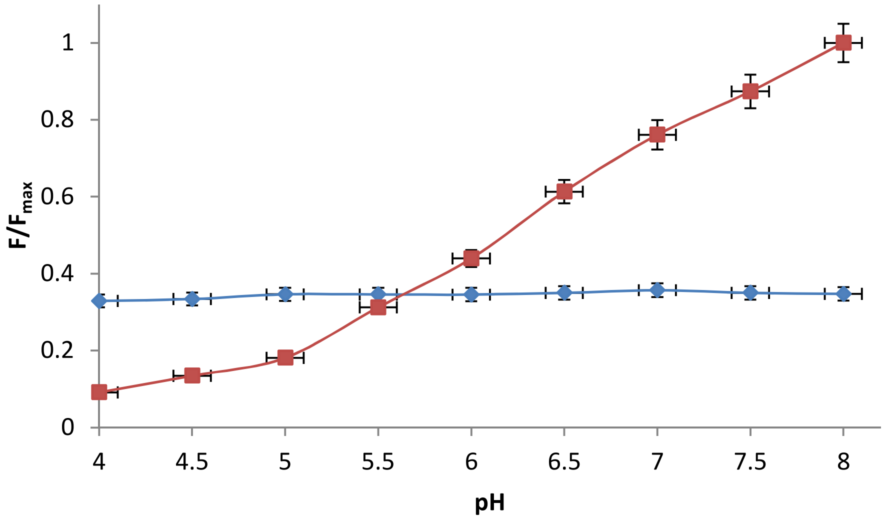

Figure 3.19 Fluorescence intensity for pH calibration of FITC-dextran (red data points λ_{ex} 480 nm) and TAMRA-dextran (blue data points λ_{ex} 555 nm) excited within polyacrylamide nanoparticle. Titration carried out in PBS with pH ranging from 4 to 8. The dyes were excited separately to ensure the emission collected was from the individual fluorophores.

The ratio of the two dyes incorporated in the nanoparticles determined by research with collaborators at Nottingham University to ensure the fluorescence of both TAMRA and FITC were visible and of comparable intensities.

The calibration of the pH sensitive dye, FITC, in nanoparticles indicates that the synthesised nanosensors have the same sensitivity to the level of pH as the dye, FITC, on its own in solution. When recording the data the only noted difference between the two batches was in the intensity but this can be attributed to the absorption of the polyacylamide matrix and, therefore, the absorbance of the dye at the wavelength of excitation will be lower.

3.3. Calcium sensing nanoparticles

One of the project aims was to be able to monitor the changes in cellular biochemistry by the change in calcium ion flux. A common dye for calcium sensing is Calcium Green-1 (Figure 3.20) which is commercially available.[60] The ability to monitor the intracellular concentration of calcium ions is important because, as mentioned previously, research has linked an association in cells between the change in the concentration of calcium ions present and stress that the cells exhibit e.g. oxidative stress. The idea for developing and characterising a nanosensing system for calcium would be to monitor the change of calcium concentration in a cell in order to attempt to understand the mechanism of cell death. The molecular probe employed would need to still be sensitive towards calcium ions in the environment through the PAA matrix of the nanoparticle and therefore initial experiments investigated the photophysical properties of the commercially available dye Calcium Green-1 compared with those of the dye incorporated within polyacrylamide nanoparticles.

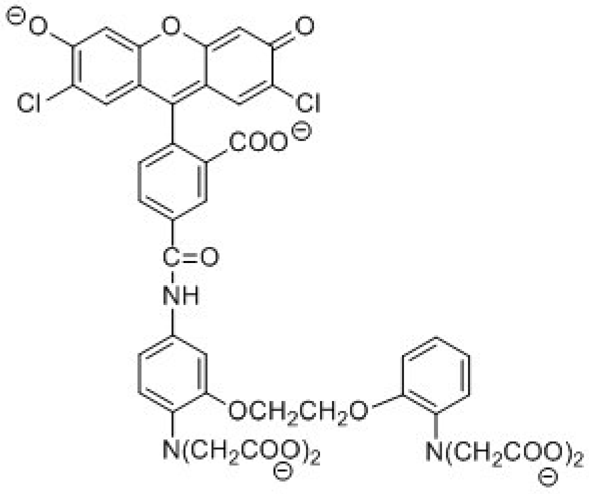

Calcium Green-1

Figure 3.20 Molecular structure of CalciumGreen-1

3.3.1. Calcium Green

There are a number of commercial dyes for calcium sensing that either increase or decrease in emission intensity with varying ranges of sensitivity.[61] The fluorophore chosen for this project was Calcium Green-1 (Figure 3.20), which is a derivative containing the fluorescein fluorophore. This commercially available probe was chosen over some of the more common calcium sensors, e.g. Fluo-3 and Fura-4-F, due to the fact that Calcium Green-1 is known for being capable of detecting $[Ca^{2+}]_{free}$ over a wider concentration range and with increased brightness at saturation (Φ_f for Calcium Green-1 = 0.75 and Φ_f for Fluo-3 = 0.14, both at saturation).[61] The dye also exhibits two fluorescent lifetimes depending on the species present; one being the Ca^{2+} bound and the other being Ca^{2+} free.[62]

Despite not being the most common of the commercial fluorescent calcium sensors, Calcium Green-1 is still widely chosen for biological observations e.g. in observing calcium dynamics on brain slice preparations or imaging the intracellular concentration of Ca^{2+} in neurons.[63, 64] This is due to its excitation and emission spectral ranges falling in the visible spectrum as opposed to some of the other calcium probes which have albeit high quantum yields but require excitation in the UV region.

Table 3.4 Literature reported values for working detection range of $[Ca^{2+}]_{free}$, excitation wavelengths and K_d values.[50, 61]

Calcium Sensor	Working range / µM	Abs maximum / nm	K_d / nM
Calcium Green-1	0 – 39	515	190
Fura-2	0 – 39.8	363	140
Indo-1	0 – 43.5	346	230

Excitation using visible light is a desirable property for potential molecules for cell imaging as visible light is less damaging to cells than UV and also minimises autofluorescence. Table 3.4 shows the fluorescence data from two other common calcium sensors that have similar working ranges to that of Calcium Green-1 but being excited in the UV limits their potential for cell imaging. Calcium Green-1 is commercially available from Life Technologies™ as its dextran conjugate, CG-dextran, which is the material used within this section.

The normalised spectra in Figure 3.21 show the fingerprint wavelengths of absorption and emission for the commercial probe. The probe was purchased as its dextran conjugate, hence all measurements relate to the dextran conjugate.

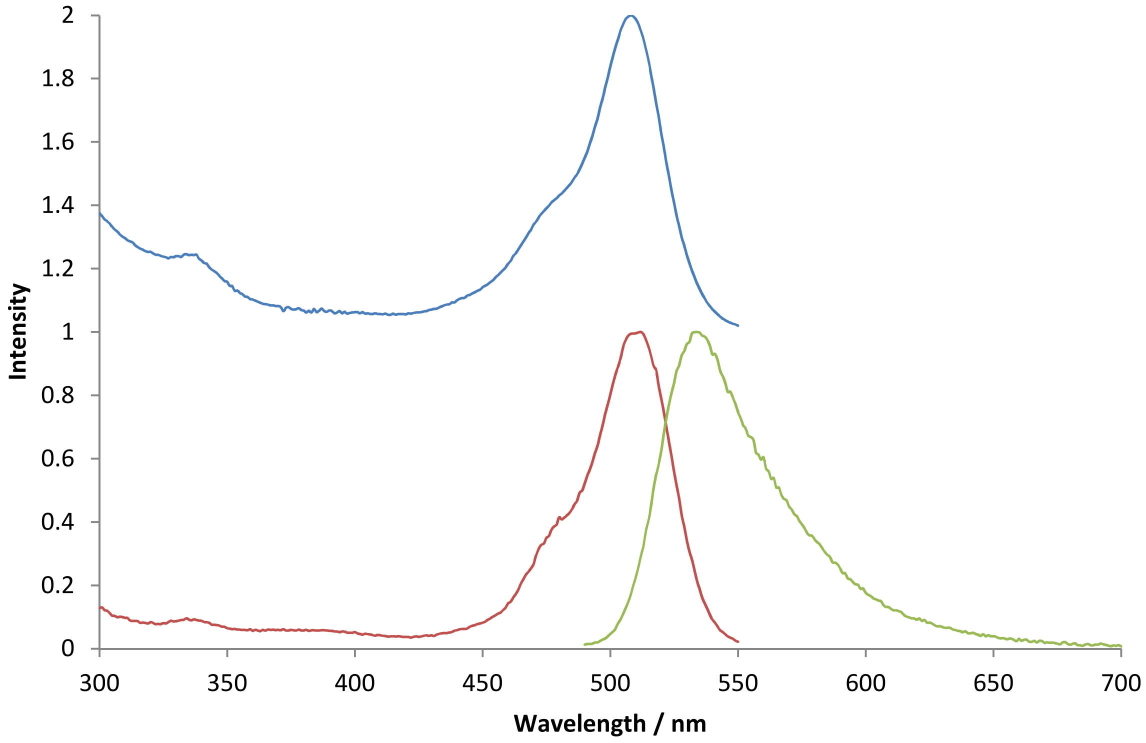

Figure 3.21 Normalised absorption, excitation and emission spectra for Calcium Green-1 dextran in water, λ_{ex} = 480 nm and λ_{em} = 560 nm.

In distilled water, the commercially available probe CG-dextran exhibits strong fluorescence easily detectable within the visible range (Figure 3.21)

Table 3.5 Data for fluorescence lifetime, amplitude for τ_f' (A) and quantum yield measurements recorded for Calcium Green-1 dextran compared with comparative literature values. All measurements carried out in distilled water. (The amplitude factors for τ_f can be calculated by 1 - A′).

	τ_f / ns	**τ_f' / ns**	***A′* $[Ca^{2+}]_{zero}$**	***A′* $[Ca^{2+}]_{saturated}$**	**Φ_f**	**Em max / nm**
Recorded	0.65 (± 0.03)	3.63 (± 0.06)	0.10 (0.02)	0.67 (0.06)	0.73 (± 0.10)	533
Literature[65, 66, 61, 62]	0.7	3.70	0.05	0.62	0.75	530

The fluorescence lifetime measurements obtained yielded two values, which is consistent with the literature for the dye. The long-lived component of 3.63 ns is attributed to the Ca^{2+} bound species whilst the short-lived component corresponds to the Ca^{2+} free specie. The amplitude factors for these illustrate the increase of the Ca^{2+} bound species as $[Ca^{2+}]_{free}$ increases.

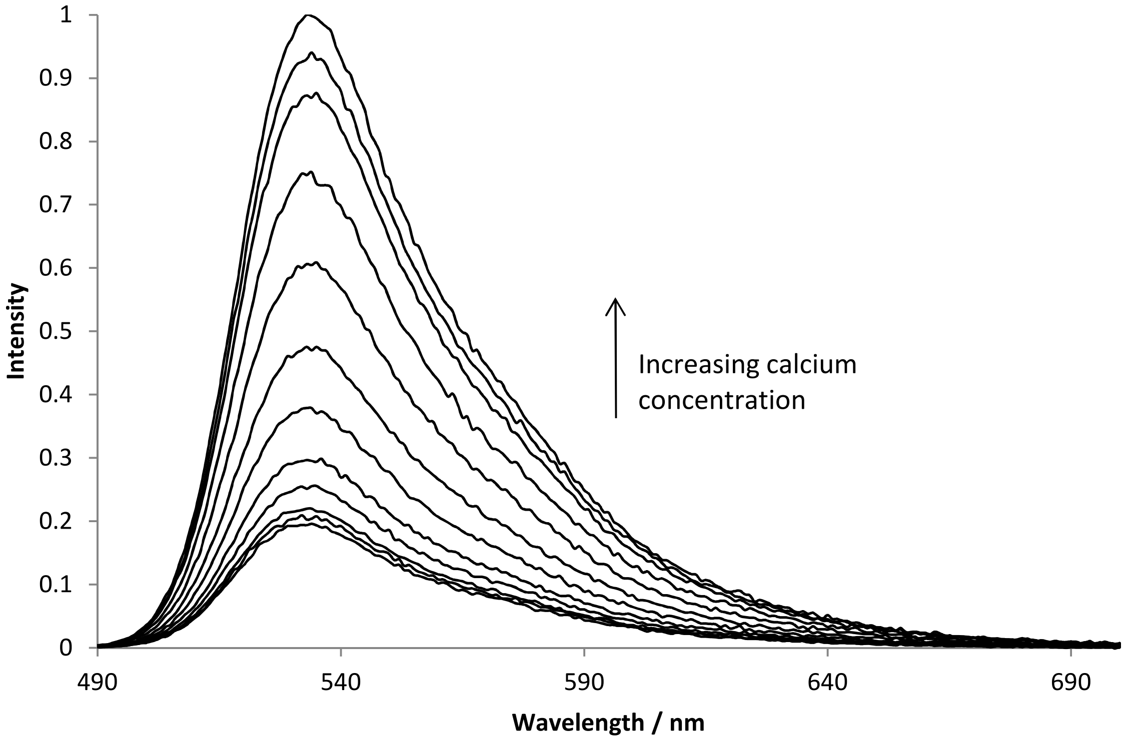

Figure 3.22 Normalised emission spectra of Calcium Green-1 in EGTA buffer upon addition of CaEGTA, λ_{ex} = 480 nm.

As Calcium Green-1 is a commercially available probe, the titration method for calibration published by Life Technologies™,[50] was used as the protocol for work in this section. In this method Calcium Green-1 dextran was titrated in a buffer solution of 10mM EGTA with a known concentration of calcium in 10mM EGTA. Figure 3.22 shows the emission spectral profiles throughout the titration, demonstrating the fluorescence intensity increase with the addition of calcium. The plot of the F/F_0 vs $[Ca^{2+}]_{free}$ in figure represents the calibration of the fluorophore and together these correspond to the information given by Life Technologies™ in their protocol and information data.

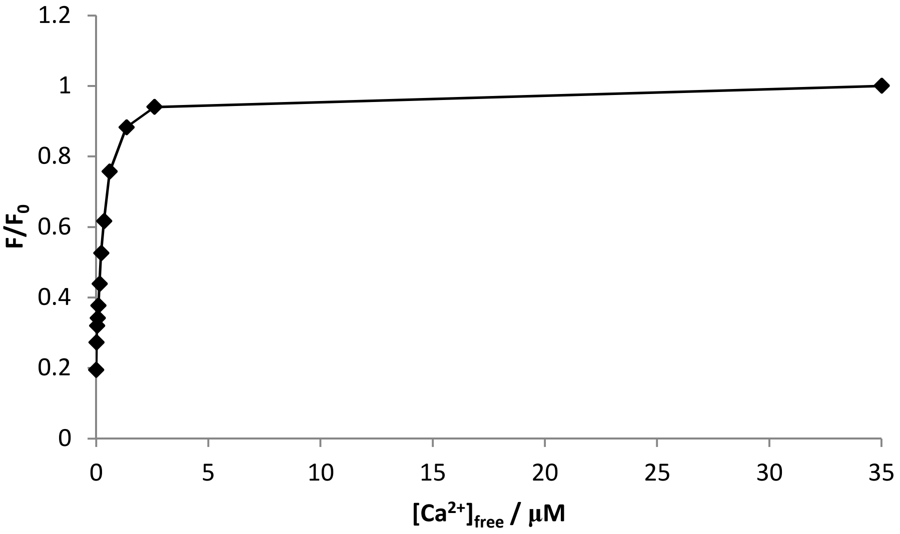

Figure 3.23 Titration curve of Calcium Green upon addition of calcium, data extrapolated from Figure 3.22 using the emission maximum of 533 nm.

The titration curve obtained for the calcium titration of Calcium Green-1 dextran corresponds to data from Life Technologies^{TM} indicating possible replication of the data. This also confirms the working range being from 0 – 40 µM with a greater responsivity for lower concentrations.

The double log plot in Figure 3.24 further confirms the fluorophores ability as a calcium sensor and agrees with the data published by Life Technologies^{TM}. The gradient of the calibration plot confirms and indicates towards a 1:1 binding of Calcium Green-1 to free calcium ions. The x-intercept was extrapolated to be -6.5619, which correlates directly to the log $K_d^{\text{indicator}}$. This yields a value for K_d of 274 nM ± 5nM in comparison with the literature value of 190 nM.[50]

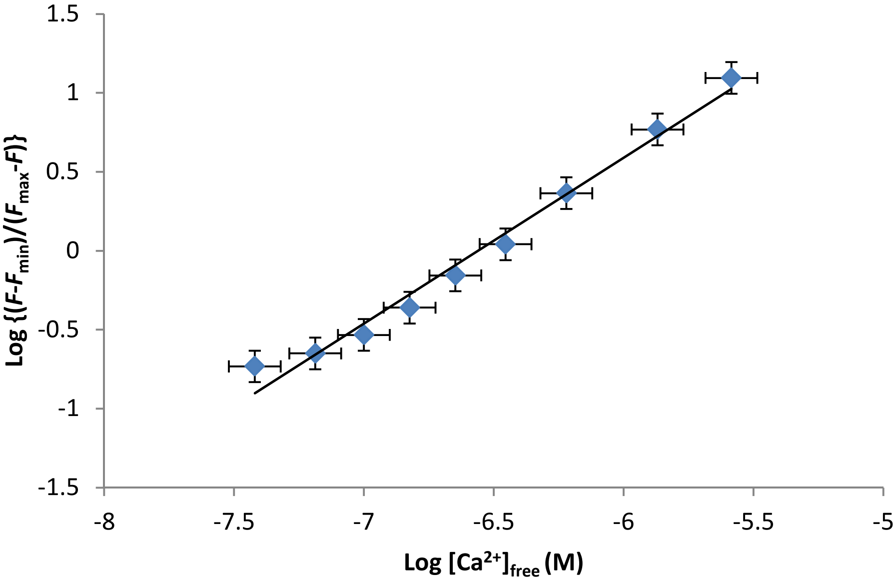

Figure 3.24 Calibration of Calcium Green-1 dextran in EGTA buffer solution, data extrapolated from Figure 3.23. As a double log plot the Ca^{2+} response of the indicator is linear with the *x*-intercept being equal to the log of the $K_d^{indicator}$. The sample was excited at 470 nm and the emission intensity taken from 533 nm for the calibration. [log{(*F*-*F*min)/(*F*max-*F*)} = 1.1 (log[Ca^{2+}]) + 6.90].

As with the pH sensing system, the next step on analysing the dye was to trap it in nanoparticles and monitor its response to calcium in the surrounding medium.

3.3.2. Calcium Green nanosensors

It was important to ensure that the sensing capabilities of the dye remained unchanged or were calibrated for the presence of the polyacrylamide matrix.

Calcium Green was entrapped inside the nanoparticle in the same method as before by entrapment of the dextran conjugate inside the polymer nanoparticle.

The nanosensors were then subjected to the same photophysical measurements, calibration and characterisation as with the CG-dextran in solution.

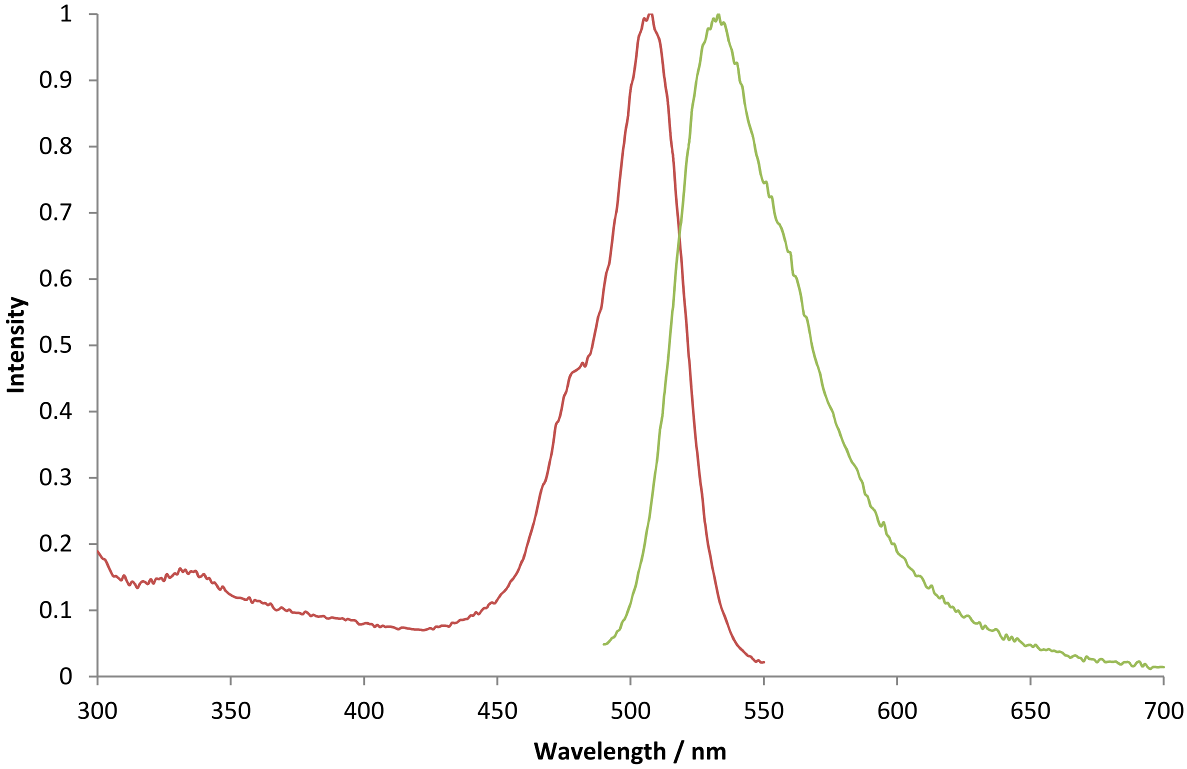

Figure 3.25 Normalised excitation and emission spectra for CG nanosensors in PBS, λ_{ex} = 480 nm and λ_{em} = 560 nm

The normalised excitation and emission spectra (Figure 3.25) for the CG nanosensors in PBS indicate that the probe as a calcium detector is still active from within the matrix.

As with the pH sensitive nanosensors, the next questions after incorporating the dye was whether the spectral properties were maintained after the nanosensor synthesis. It can be seen in Figure 3.25 and Figure 3.26 that the spectral properties are maintained after nanosensor synthesis. The same emission and excitation bands can clearly be seen with collection using the same excitation and emission wavelengths.

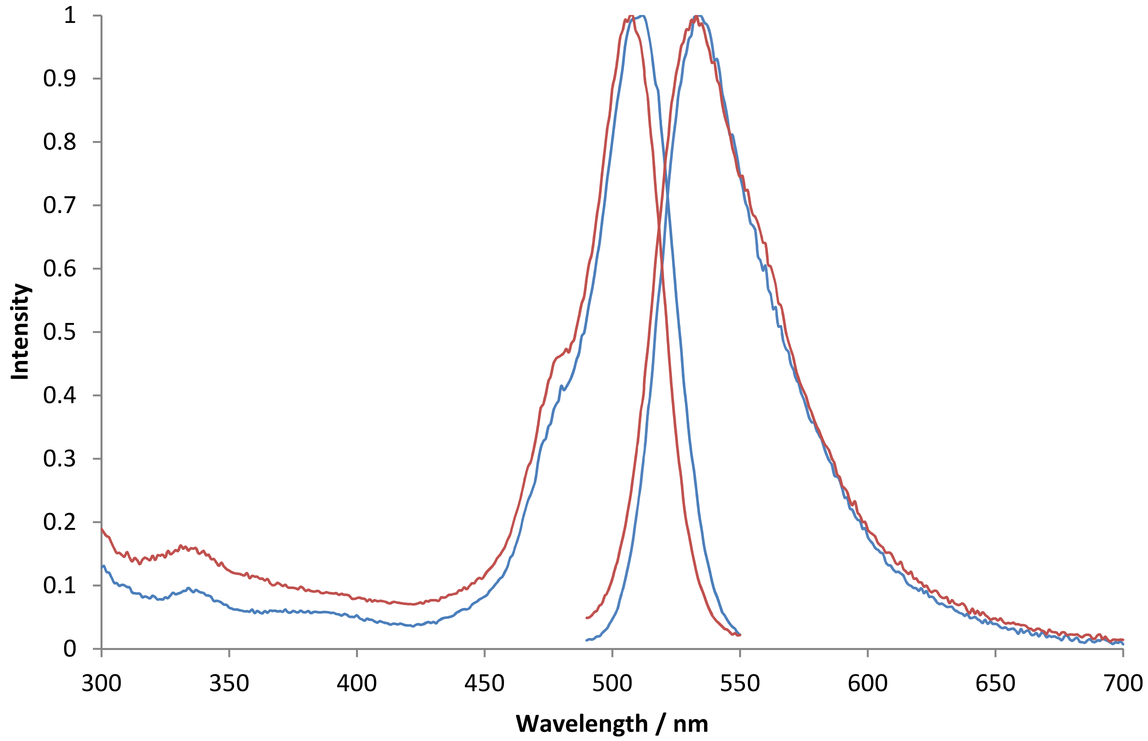

Figure 3.26 Normalised excitation and emission spectra for CG dye (blue) and CG nanosensor (red) in PBS, λ_{ex} = 480 nm and λ_{em} = 560 nm.

Table 3.6 Data recorded for fluorescence lifetimes of CG in solution and in nanosensor, measured in water. (The amplitude factors for τ_f can be calculated by 1 - A′).

	τ / ns	τ' / ns	*A'* $[Ca^{2+}]_{zero}$	*A'* $[Ca^{2+}]_{saturated}$	Abs max / nm	Em max / nm
CGdextran in solution	0.65 (± 0.03)	3.63 (± 0.06)	0.10 (0.02)	0.67 (0.06)	515	533
CGdextran nanosensor	0.59 (± 0.02)	3.52 (± 0.05)	0.15 (0.05)	0.58 (0.10)	513	532

The data recorded for both CGdextran in solution and CGdextran in the nanoparticles that can be seen in Table 3.6 shows that the fluorescence lifetime of the fluorophore is still detected within the same range and characteristic of the dye in comparison to the literature values.[65, 66]

The CG entrapped nanosensors were then titrated with known amounts of free calcium to record and calibrate its sensitivity. The same method and protocol was used as with the commercial probe in solution.

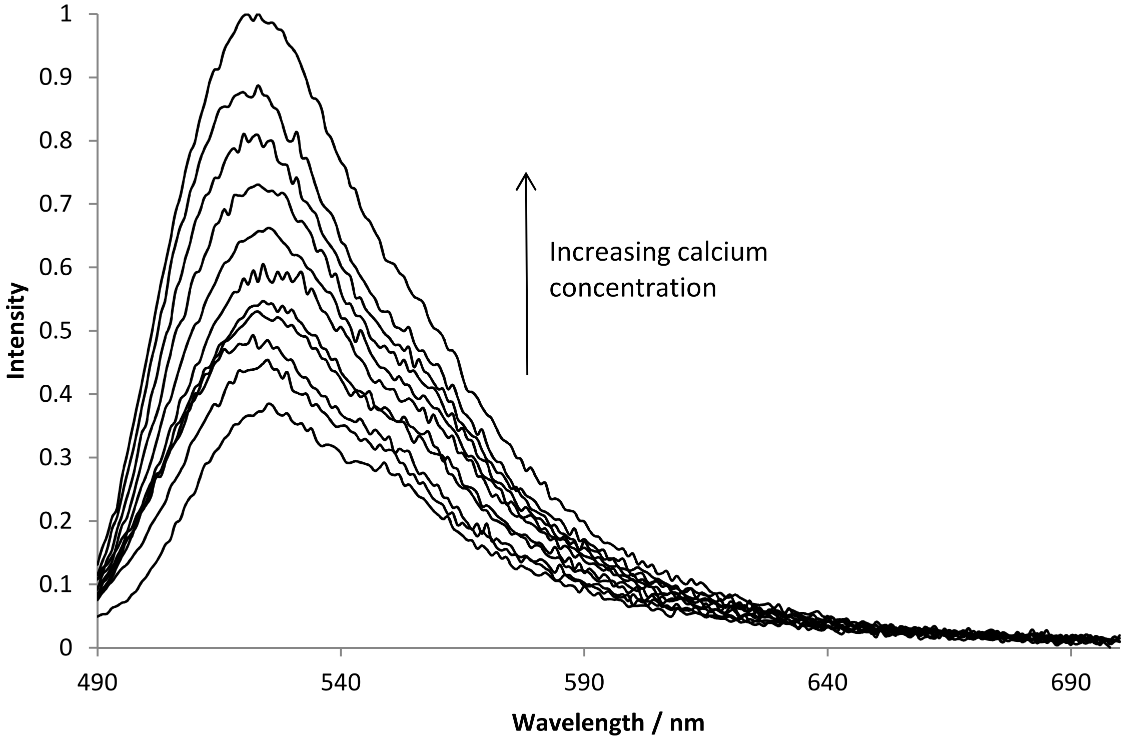

Figure 3.27 Normalised emission spectra from calcium titration of CG nanosensors in EGTA buffer on addition of CaEGTA, λ_{ex} = 480 nm.

The emission spectra (Figure 3.27) recorded from the calcium titration of the CG nanosensors mimic the trend observed for the probe in solution, outside of the polyacrylamide matrix.

The points extrapolated for calculation were, therefore, always taken at 533 nm which is the maximum for the emission of the Calcium Green-1 dextran probe as well as the Calcium Green nanosensors.

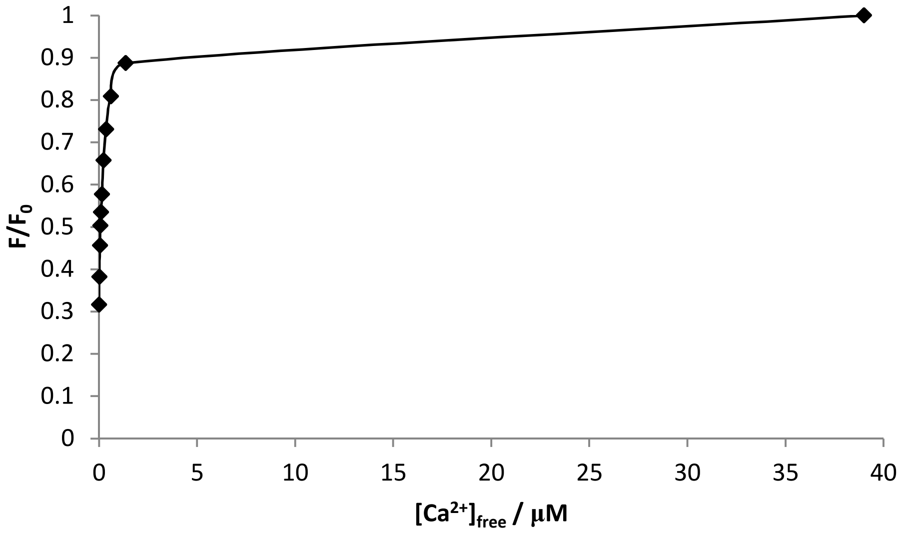

Figure 3.28 Titration curve of CG nanosensors upon addition of calcium, data extrapolated from Figure 3.27 using the emission maximum of 533 nm.

The titration curve (Figure 3.28) obtained from the calcium titration of CG containing nanoparticles indicates there is no detrimental effect on the fluorophores' sensing abilities when entrapped in the nanoparticle. The working range is still up to 39 µM with a greater sensing affinity for the lower concentrations.

The double log plot (Figure 3.29) also confirms that the binding ratio is still 1:1 with a slope of 0.9493. The *x*-intercept was calculated as -6.5864 giving a value for K_d as 259 nM which correlates well with that observed for the probe in solution (274 nM).

As stated for both the probe and the nanosensor the calculations for K_d were calculated within 15 nM of each other and were calculated to be in close proximity with literature values. The difference of literature values could be down to variations in pH and temperature to which the calculations for the K_d of the probe is known to be very sensitive to both of these factors.

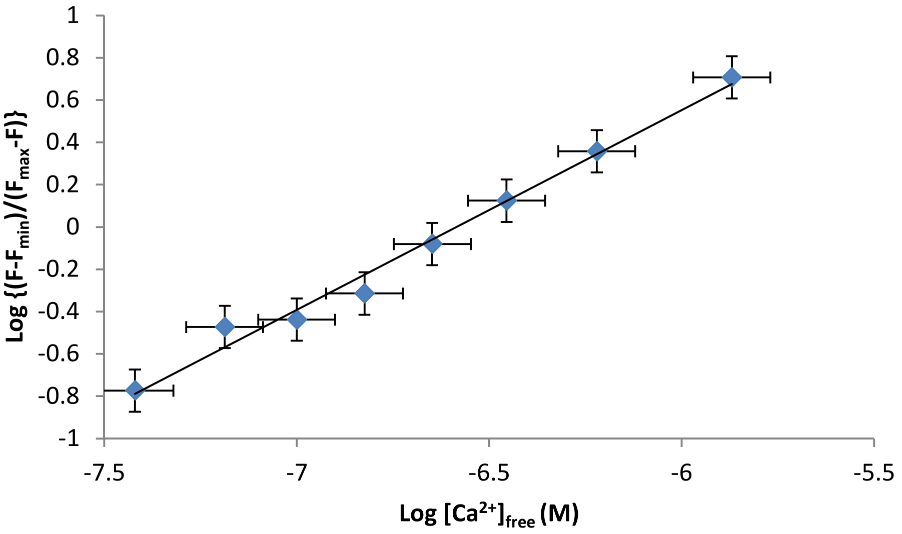

Figure 3.29 Calibration of CG nanosensors in EGTA buffer solution, data extrapolated from Figure 3.28. As a double log plot the Ca^{2+} response of the indicator is linear with the x-intercept being equal to the log of the $K_d^{indicator}$. The sample was excited at 470 nm and the emission intensity taken from 533 nm for the calibration. [$\log\{(F-F_{min})/(F_{max}-F)\} = 1.0 (\log[Ca^{2+}]) + 6.22$].

3.4. Concluding remarks

The data discussed in this chapter clearly indicate the potential for polyacrylamide nanosensors to entrap different responsive fluorescent probes within the matrix and hence to act as individual nanoscopic reporter particles.

The sensing abilities for both the pH and calcium nanosensors remained intact in comparison with that of their naked dyes in solution. It has also been shown possible to synthesise ratiometric nanosensors using one insensitive dye in relation to the sensing component.

The benefit of the ratiometric nanosensor is that the non-responsive dye acts as an internal calibration for the responsive dye, and that due to the nature of the host matrix the dyes will remain anchored within the same location – the interior of the nanoparticle. This reduces the possibility of the dye leaching out of the nanoparticle, maintaining the performance of the nanoparticle and prolonging it’s use.

4. Calcium porphyrin nanosensors

After demonstrating the successful entrapment of fluorophore dextran conjugates into the polyacrylamide matrix of the nanoparticles and retaining the response of the molecular probes, and the ability to effectively conjugate photosensitising porphyrins to the outside of the nanoparticle matrix, the next step was to combine these two principles in one nanoparticle.

This section displays the results from the synthesised calcium-porphyrin nanoparticles. The idea being that if the nanoparticles were placed into a cell, the porphyrin could be excited and would generate singlet oxygen within the cell. The cell would then undergo oxidative stress and the change in calcium flux could be monitored by the calcium sensitive dye within the nanosensor. Singlet oxygen has a relatively short lifetime so by attaching the porphyrin to the outside of the nanoparticle the singlet oxygen is released into the local environment and not within the nanoparticle.

This chapter discusses the photophysical properties of nanoparticles with Calcium Green dextran entrapped and zinc tetramethylpyridinium porphyrin (ZnTMPyP) conjugated to the surface.

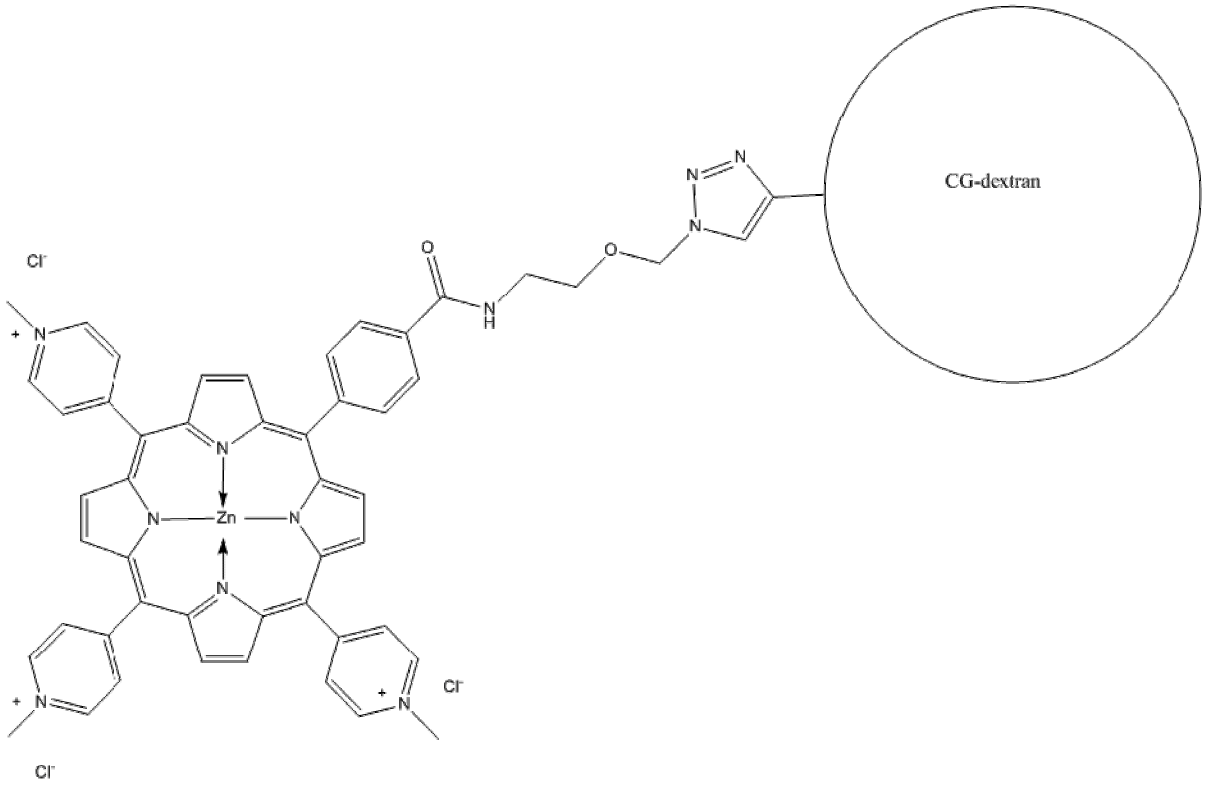

Figure 4.1 Diagram to show how zinc tetramethylpyridinium porphyrin is attached to the nanoparticle matrix

The diagram in Figure 4.1 illustrates the general idea of the porphyrin attached to a nanoparticle. However, in practice, there would be numerous porphyrins attached to the cross-linked polyacrylamide surface and, as previously discussed, the nanoparticle itself is unlikely to be perfectly round or circular. Nanoparticles with porphyrins attached to the exterior of the nanoparticle surface yielded particles with an average diameter of 100 nm. Those synthesized without porphyrins attached yielded particles with an average diameter of 40 nm.

The sensitivity of the nanoparticles system show in Figure 4.1 to calcium ions was monitored by means of titration using the same method as for the CG-nanosensor described in section 3.3.

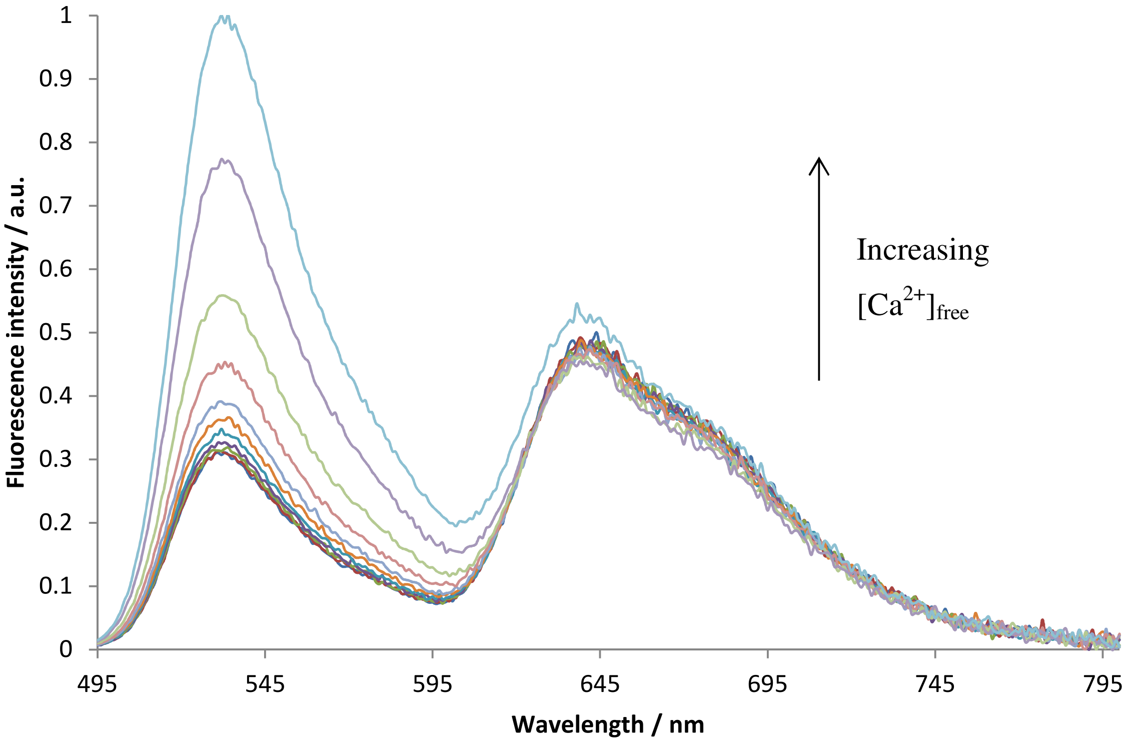

Figure 4.2 Normalized emission spectra of calcium porphyrin nanoparticles recorded in EGTA buffer titrated with CaEGTA, λ_{ex} = 485 nm.

The spectra in Figure 4.2 show that the calcium titration of the nanoparticles yielded a comparable calibration to that of the calcium dye in solution as well as the calcium dye in nanoparticles without the porphyrin present. This suggests that the presence of the porphyrin does not affect the response of Calcium Green to the sensitivity of calcium in its environment.

Another notable observation from the emission spectra is the minimal change in intensity of the porphyrin emission band. The small changes observed can be attributed to the rise in fluorescence seen in the tail end of the calcium dye's emission that overlaps with the porphyrin emission from 600 nm towards the red end of the spectrum.

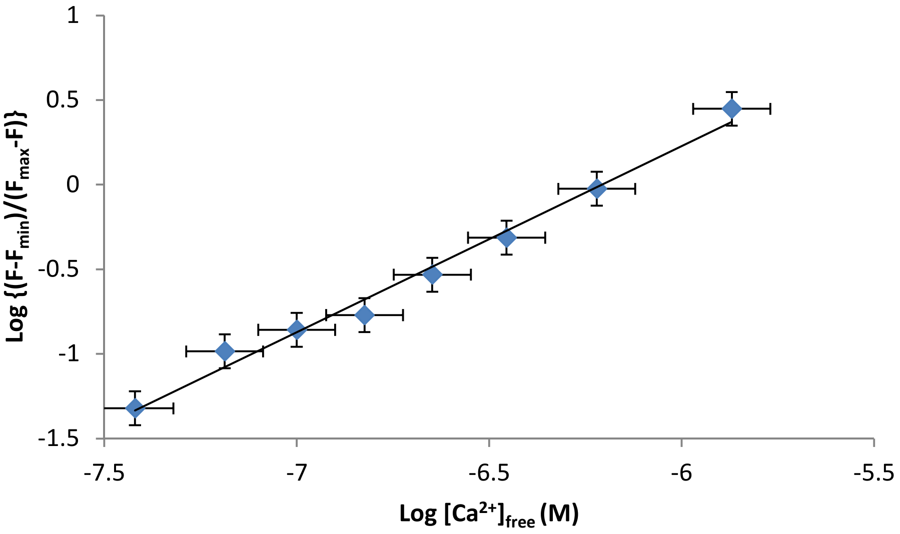

Figure 4.3 Calibration of CG-porphyrin nanoparticles in EGTA buffer solution, data extrapolated from Figure 4.2. As a double log plot the Ca^{2+} response of the indicator is linear with the x-intercept being equal to the log of the $K_d^{indicator}$. The sample was excited at 470 nm and the emission intensity taken from 533 nm for the calibration. [log $\{(F\text{-}F_{min})/(F_{max}\text{-}F)\}$ = 1.1 (log[Ca^{2+}]) + 6.83].

The calibration for the calcium titration in Figure 4.3 has a gradient of 1.1, which is in good agreement with the dye in solution and the dye in the nanoparticle in the absence of the porphyrin. This also again confirms the 1:1 binding of the dye to calcium ions. The *x*-intercept again is equal to the log of the $K_d^{indicator}$ and yields a value of 609 nM ± 5 nM. This is larger than the value calculated for the calibration of the dye in solution and in nanoparticles in the absence of porphyrins. This change in the K_d is attributed to fluctuations in the pH and temperature of the sample.

5. Nanoparticles incorporating hydrophobic fluorophores

Another direction of the project was to attempt either the entrapment or conjugation of hydrophobic fluorescent molecules to the interior of the nanoparticles.

An interest in the development of the PEBBLE nanoparticle technology was to be able to use functionalised fluorescent dyes that were hydrophobic or had low solubility in water. By this method we could exploit the use once again of an amide bond between amino dextran and a carboxylic acid group to allow the entrapment or anchoring of the dye within the polyacrylamide nanoparticle matrix preventing its loss through leaching.

Pyrene is hydrophobic fluorophore widely used as a fluorescent standard and known for its high fluorescent quantum yield and interesting photophysical properties, one of which is its solvochromatic properties that lend itself to a probe for environment sensing.[2, 67]

It has also been reported that a limitation of the pyrene molecule is its ability form aggregates or excimers. This leads to an additional emission band towards the red part of the visible spectrum as well as quenching of the fluorescence resulting in lower quantum yields.[68, 69]

Pyrene is a well-known example of a molecule that forms excimers, or excited-state dimers, at high concentrations resulting in a large, broad blue emission band centred around 470 nm appearing in the emission spectrum. Whilst, at low concentrations only the typically well-structured emission bands of the molecule are visible with just the tail of the monomer fluorescence extending into the 500 nm region with no emission band at 470 nm. Excimers are formed when a molecule in an excited state interacts with a molecule of the same composition in the ground state (see below in Equation 5.1 and Figure 5.1 for the formation of excimer and the energy diagram).

$P(S_o) + h\nu \rightarrow P(S_1)$	Absorption
$P(S_1) \rightarrow P(S_o) + h\nu$	Normal fluorescence
$P(S_1) + P(S_o) \rightarrow P(S_1){:}P(S_o)$	Excimer formation
$P(S_1){:}P(S_o) \rightarrow P(S_o) + P(S_o) + h\nu$	Excimer fluorescence

Equation 5.1 Mechanisms to show the formation of excimers

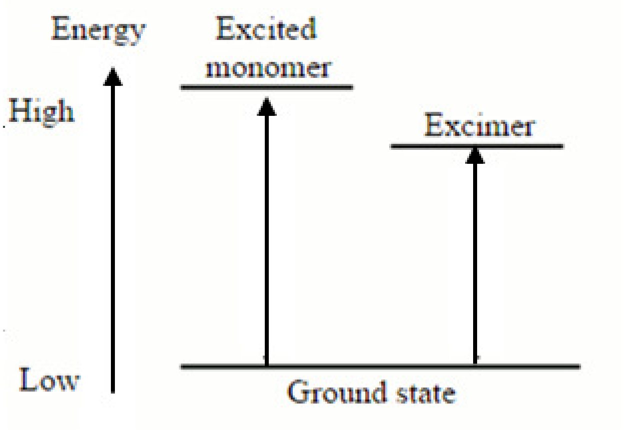

Figure 5.1 Simplified excimer energy diagram

Figure 5.2 shows in detail the energy transitions involved in the formation of an excimer including the energy levels for pyrene and its excimer.

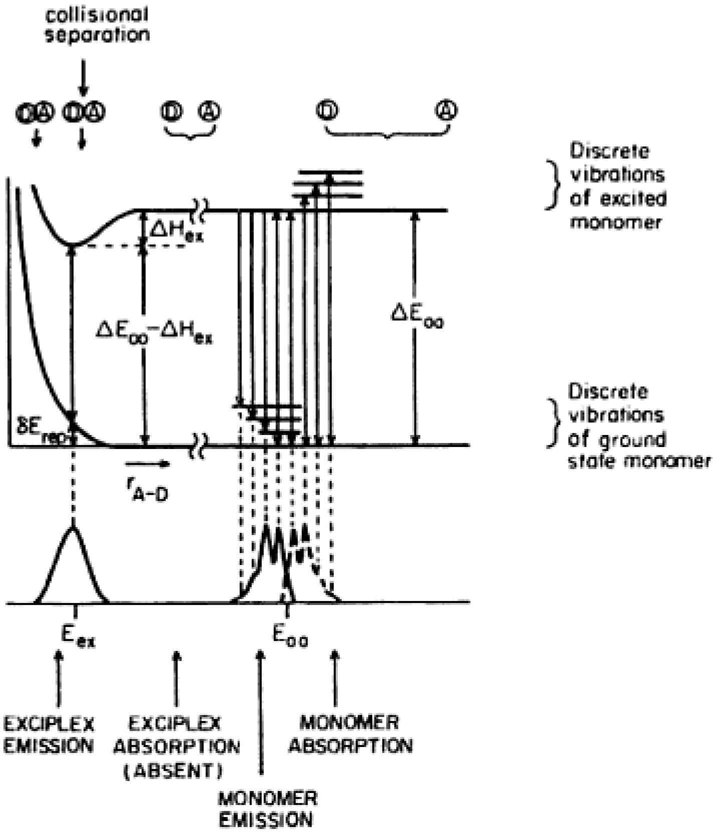

(a)

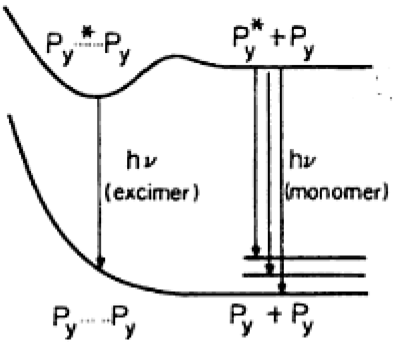

(b)

Figure 5.2 Two diagrams illustrating the excimer fluorescence with respect to the excited state and ground state, (a) showing the surface interpretation of excimer emission and (b) pyrene excimer energy level diagram.[70]

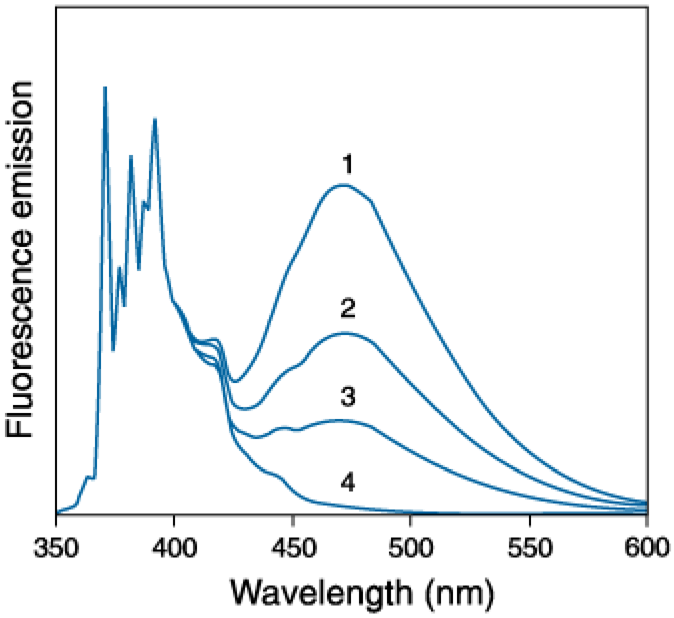

Figure 5.3 Fluorescence emission spectra of pyrene excimer formation in ethanol, taken from Life Technologies™ [47]

The interest here was to incorporate a pyrene derivative into the polyacrylamide matrix and thus forming a hydrophilic pyrene containing nanoparticle with the aim to develop its applications in areas such as fluorescence microscopy, and in so doing, developing the use of pyrene in aqueous environments.

Coumarin is another hydrophobic fluorophore which is widely used in bioimaging, being a highly fluorescent class of compound.[71-73] Coumarin derivatives have been widely researched and developed within the areas of biology, medicine and fluorescent dyes (e.g. laser dyes). Coumarin derivatives have also been developed as fluorescent reporters in pH probes for detection of a range of compounds and monitoring fluctuations in the pH of an environment.

As with molecules of the pyrene family, the fluorescence emission of coumarins is extremely sensitive to the local conditions or environment of the molecule e.g. polarity and viscosity. The research on coumarins has, therefore, lent itself towards fluorescent probes for heterogenous environments, e.g. polymers and solids.

The two molecules employed in this section were pyrene-1-butyric acid and coumarin-3-carboxylic acid; both these molecules contain a free carboxylic acid to react with the amino group of aminodextran for the formation of the dye conjugates.

5.1. Pyrene butyric acid

Pyrene-1-butyric acid (PBA) is a commercially available fluorescent derivative of pyrene with a carboxylic acid attached to an alkyl chain, shown in Figure 5.4. It is soluble in DMSO and DMF as well as alcohols (e.g. methanol and ethanol) but here the solubility is low. Due to the large lipophilic pyrene group it has poor water solubility so cannot be used in aqueous environments easily. Previous research has explored and developed its use as an oxygen sensor due to its long lived excited state giving a fluorescence lifetime of 220 ns in degassed and 30.6 ns in aerated ethanol solutions.[74] However, due to its low solubility its potential has been limited for biological use as it needs to be incorporated with another (non-aqueous) medium.[75, 76] By conjugating the fluorophore to dextran, the molecule's solubility in water should increase and hence facilitate the use of this conjugate as a pyrene based nanosensor for oxygen. The first step was to measure the photophysical properties of PBA in a variety of organic solvents and then attempt conjugation of the dye to dextran followed by entrapment into polyacrylamide nanoparticles.

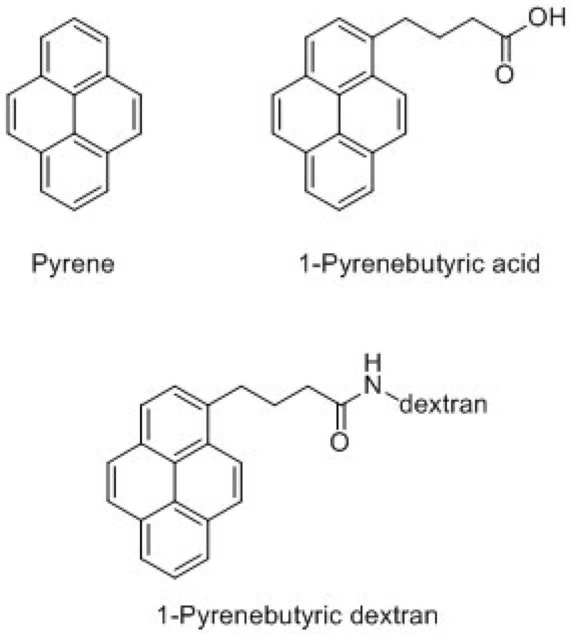

Figure 5.4 Molecule structures of pyrene (top left), 1-pyrenebutyric acid (top right) and 1-pyrenebutyric dextran (bottom)

The fluorescence properties of PBA were initially measured in a variety or organic solvents before any conjugation in order to determine its behaviour before conjugation to dextran and entrapment into the nanoparticle matrix. These properties were then compared to the dextran conjugated water soluble derivatives and any changes in the fluorescence characteristics were observed.

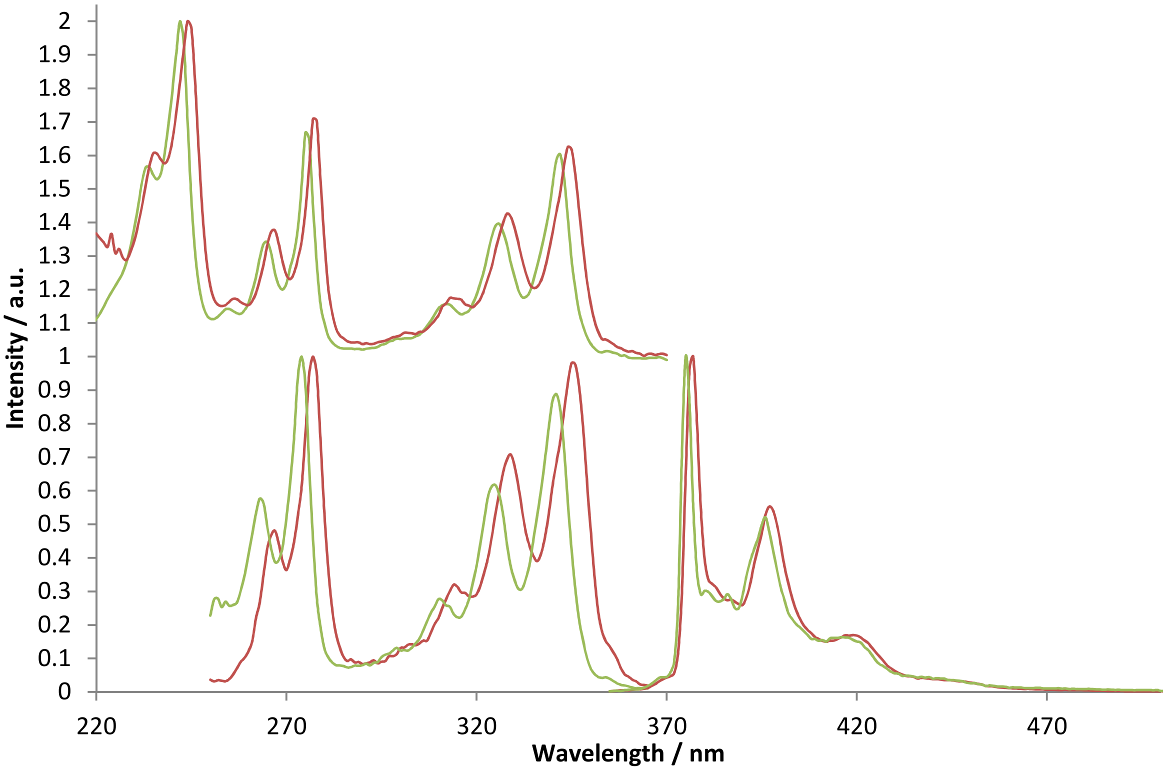

Figure 5.5 Normalized absorption, excitation and emission spectra of pyrene butyric acid in DCM and DMSO (red) and ethanol and methanol (green), λ_{ex} = 345 nm and λ_{em} = 375 nm.

Table 5.1 Absorption and emission spectral peak data for PyBut in various organic solvents extrapolated from Figure 5.5

Solvent	Absorption / nm	Emission / nm
DCM and DMSO,	(235,245) 267, 277 315, 328, 345	377, 397, 417
EtOH and MeOH	(233, 243) 265, 275 312, 325, 342	375, 396, 415

For both the emission and absorption of PyBut in DCM, DMSO and ethanol the characteristic sharp fluorescence peaks of the parent pyrene molecule are observed.

Table 5.2 Fluorescence lifetime values for PBA recorded in aerated solutions of various solvents, λ_{ex} = 337 nm and λ_{em} = 375 nm (decays shown in Figure 5.6)

Solvent	Fluorescence Lifetime / ns
DCM	30
DMSO	95
Ethanol (Literature)[74]	33 (30.6)
Methanol	32

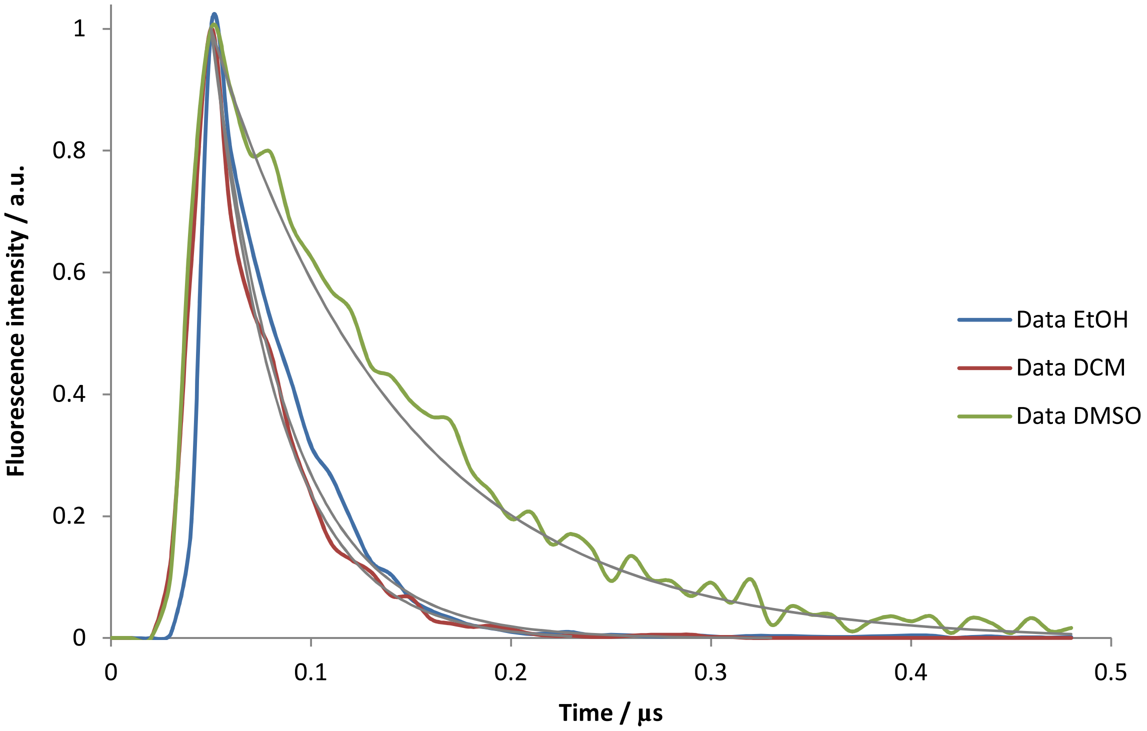

Figure 5.6 Fluorescence lifetime data and fit decays for PBA in aerated solutions of EtOH, DCM and DMSO using TCPC excited at 337 nm with emission collected at 375 nm.

The fluorescence lifetimes recorded demonstrate the molecule’s sensitivity to its environment. The data shown in Table 5.2 and Figure 5.6 were both recorded in aerated solutions of the solvents. The recorded values for the lifetimes of PBA in ethanol correlate well with that found in literature.[74]

As mentioned previously, PBA is known to be an oxygen sensitive molecule and the data in Figure 5.14 in Section 5.1.1 shows the lifetimes recorded for PBA in MeOH at varying concentrations of oxygen illustrating the oxygen sensitivity.

The conjugation of PBA to aminodextran was made using a standard amide linking protocol using EDC as the coupling agent yielding pyrene dextran conjugates (PyDex). The initial conjugation, PyDex2, was done in a 1:2:1 ratio by weight of dye : amino dextran (MW 10,000) : EDC, giving a molar ratio of 4:70 of the aminodextran : dye. According to the supplier, Life Technologies ™, the aminodextran of 10,000 MW has an average of 2.5 moles of amino groups per dextran (according to the general Certificate of Analysis)[77]. The initial conjugations were done using an excess of PBA to ensure conjugation. The resulting solid was washed with DCM to remove excess or non-conjugated PBA yielding a product that was soluble in water. The photophysical properties of this water soluble conjugate were measured. The initial conjugation was done with a large excess of the fluorescent dye to ensure multiple labelling of the polymeric aminodextran.

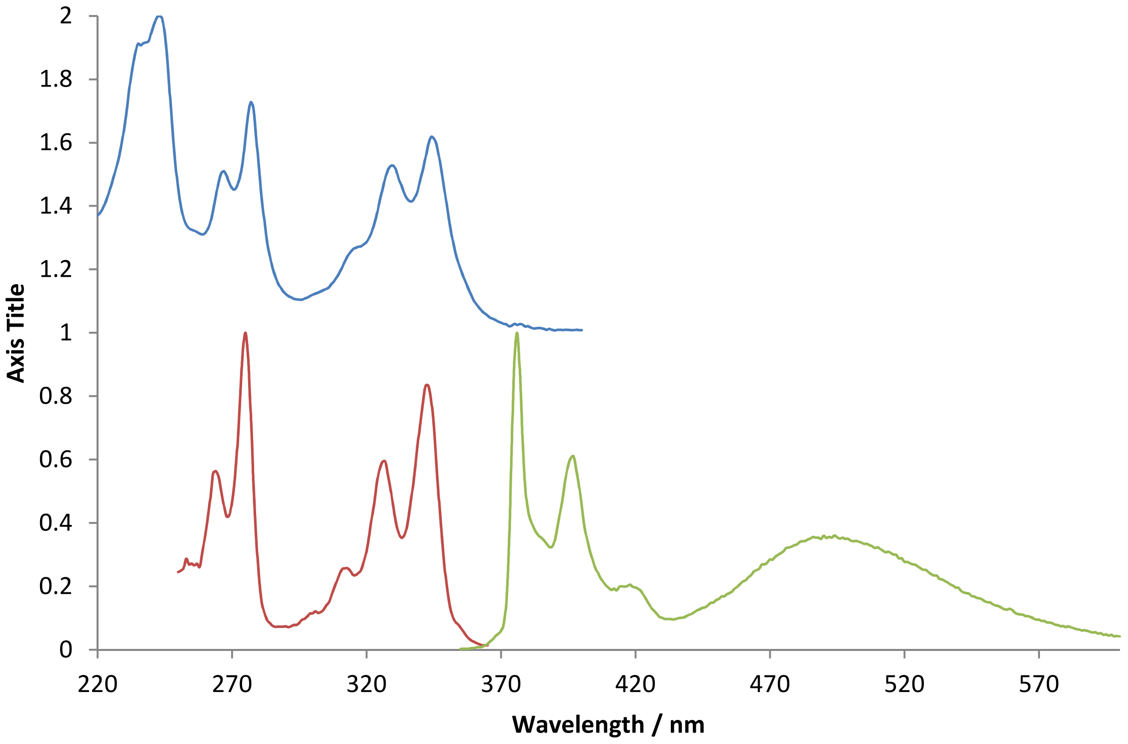

Figure 5.7 Normalized absorption, excitation and emission spectra of PyDex2 recorded in an aerated solution of PBS, λ_{ex} = 345 nm and λ_{em} = 375 nm.

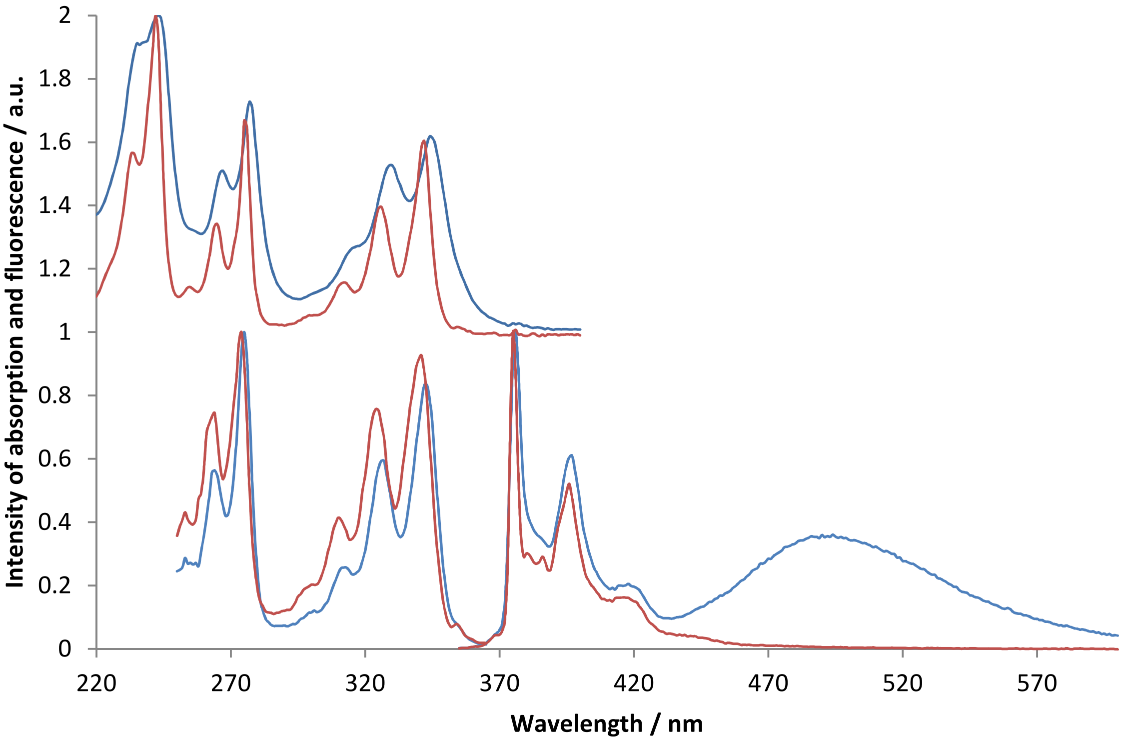

Figure 5.8 Normalized absorption, excitation and emission spectra of PBA recorded in methanol (red) and PyDex2 recorded in PBS (blue), λ_{ex} = 345 nm and λ_{em} = 375 nm.

The overlaid spectra in Figure 5.8 illustrate that the spectral changes of the sharp emission peaks that arise for the pyrene-1-butyric acid dextran conjugate recorded in an aqueous environment, are minimal giving a shift of 1-2 nm towards the red. The more noticeable difference consists of a broad peak from the edge of the last sharp emission peak at ≈ 430 nm with an emission maximum of 495 nm and extending into the red at 600 nm. According to the literature of pyrene fluorescence it is well documented that this type of emission peak arises as a result of pyrene excimer formation.[69, 70, 78]

Table 5.3 Absorption and emission data points for PBA in MeOH and PyDex2 in water, λ_{ex} = 345 nm.

	Absorption / nm	Emission / nm
PyDex2 in water	235, 245 267, 277 316, 328, 345	376, 396, 414 (495)
PBA in MeOH	233, 243 265, 275 312, 325, 342	375, 396, 415

The sharp peaks observed in the absorption and emission spectra of PyDex2 in Figure 5.8 correlate well with the spectral peaks observed for PBA in organic solvents and those described in the literature.[79-82] The broad band at 495 nm can be attributed to the formation of pyrene excimer. As discussed previously, the formation of an excimer occurs when a molecule in an excited state interacts with a molecule of the same species in the ground state, and is well-known for pyrene derivatives. The molecules of pyrene also have to be close together in order to form an excimer and with this in mind the diagram in Figure 5.9 indicates the possibilities for how the PBA molecule bound to the amino dextran might reside in solution.

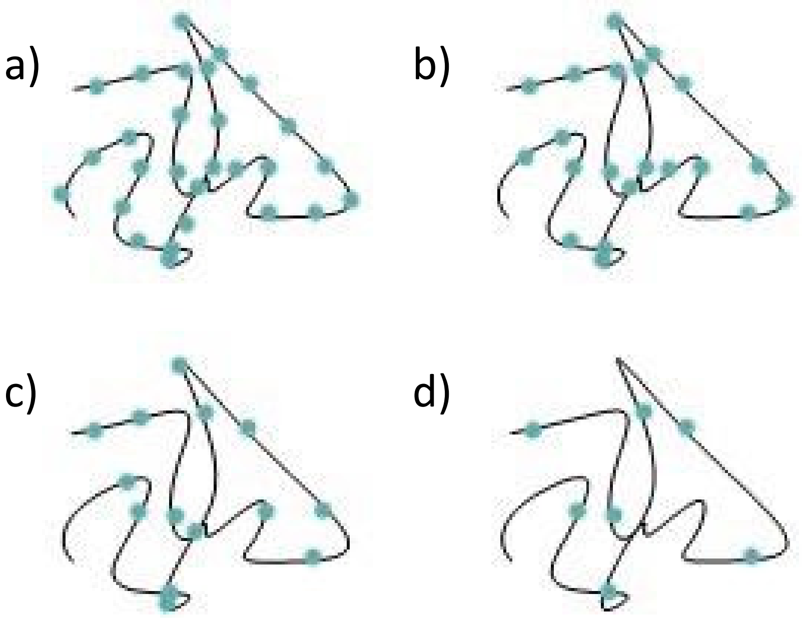

Figure 5.9 Diagram illustrating possibilities for how various concentrations of pyrene could bind to strands of aminodextran, showing high to low concentrations (a – d).

At high ratios of dye : dextran, the pyrenes bound to dextran would have a higher chance of being in close proximity and hence interacting with molecules of its own species providing the opportunity for excimer formation. As the concentrations of PBA within the dextran polymer decrease, the probability for such an encounter and thus excimer formation also decreases as the likelihood of its being next to or close to other molecules of PBA is much lower, i.e the PBA molecules would be isolated from each other.

For all samples made, there was an excess of PBA molecules present in the reaction mixture with respect to aminodextran to accommodate for the multiple amino groups present on one strand of dextran. This excess suggests that there could be aggregation of the pyrene monomer forming or inclusion of PBA into the dextran strand, particularly for samples with the highest concentration of PBA present. The close proximity of PBA molecules increases the potential for the excimer to form.[83, 84] However, there is no evidence of aggregation in the absorption spectrum. Due to the hydrophobic nature of pyrene it would also be expected for hydrophobic interactions to push the pyrenes together increasing the likelihood of excimer formation. A single strand of dextran in water will naturally curl up, along with others, as opposed to being open and accessible to the solvent which has the potential to bring more pyrene molecules into close proximity with each other which is a well-known argument for pyrene excimer formation.[69] The other possibility is that due to the fact that the dextran molecules intertwine as well as the excess of PBA within the conjugation process, there could be residual PBA molecules included within the dextran coils that are not conjugated but are physically entrapped. Due to hydrophobic interactions with other pyrene molecules these could associate with PBA molecules that are bound or form excimers. The latter argument is less favoured as the reaction mixture was thoroughly washed and agitated throughout washings which would limit the possibility for this.

This was explored further by synthesising a number of conjugations with varying ratios of the quantity of PBA in relation to that of aminodextran in order to attempt a conjugation either limiting or completely eradicating the presence of the excimer formation.

The different quantities used in the conjugations are shown in Table 5.4. The quantity of aminodextran was kept constant with the amount of PBA being the variable. It is important to note that as the molar ratio increased, for PyDex samples 1 and 2 excess PBA was seen both to the naked eye and by monitoring the fluorescence of the washings. PyDex samples 3 – 6 showed no presence of PBA in the washings indicating all the PBA in the reaction mixture had reacted with the aminodextran. Fluorescence peaks of PBA were evident in the washings from PyDex 3, monitored by fluorescence spectroscopy in MeOH. These were recorded and were consistent with the emission peaks seen for PBA in MeOH.

Table 5.4 Quantities used for various conjugations of aminodextran (10,000 MW) with PBA.

Sample	Aminodextran / mg (moles/µmol)	PBA / mg (moles/ µmol)
PyDex 1	40 (4)	40 (139)
PyDex 2	40 (4)	20 (70)
PyDex 3	40 (4)	10 (35)
PyDex 4	40 (4)	2 (7)
PyDex 5	40 (4)	1 (3.5)
PyDex 6	40 (4)	0.5(1.7)

The spectra in Figure 5.10 show that the positions of both the sharp monomer peaks in the emission as well as the broad excimer peak remain the same. However, the relative intensity of the excimer increases with the quantity of PBA used in the reaction. From this, it can be seen that the degree of excimer formation shows a good correlation with the number of conjugated pyrene butyric acid molecules per dextran chain. The broad peak associated with the excimer only changes in intensity and remains a broad peak centralised with its maximum at 492 nm, extending from the tail end of the pyrene fluorescence peaks at 430 nm to 600 nm.

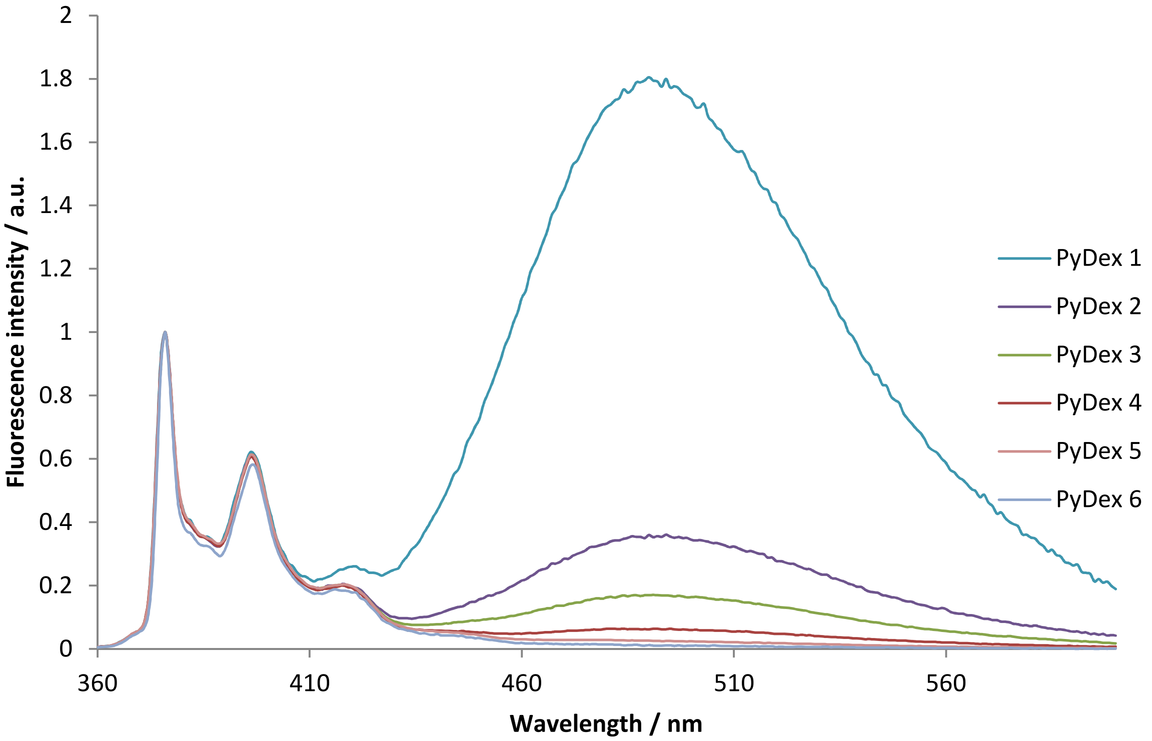

Figure 5.10 Emission spectra of PyDex samples 1-6 recorded in PBS, normalised to the emission intensity at 375 nm, λ_{ex} = 345 nm.

The conjugations show that as the amount of PBA present at the point of conjugation decreases, the extent of the excimer that forms decreases. Another observation to note is that at lower concentrations it can be assumed that all the pyrene butyric acid present was incorporated or conjugated to the dextran molecule, whilst as the concentrations of PBA in the reaction mixture increased, not all the PBA was incorporated into the product. This is known due to the fact that PBA was present in washings of the conjugate product which was monitored by recording the absorption and fluorescence but also in the more concentrated samples it could be seen by the naked eye in the yellow colour of the washings. The dextran samples were washed thoroughly until the resulting washings were free of unreacted PBA.

The positions of the sharp, characteristic pyrene monomer fluorescence emission peaks remain unchanged throughout each dextran conjugated derivative. The positions are also consistent with PBA suggesting that, except for the excimer formation, there is little change in the excited state occurring after conjugation and as seen in Table 5.5, the fluorescence lifetime recorded for the monomer fluorescence remains consistent, within error.

Table 5.5 Fluorescence lifetime data for pyrene butyric acid and the synthesised dextran conjugates, τ_f recorded at 375 nm and τ_f' recorded at 500 nm in aerated solutions of PBS or MeOH.

	τ_f / ns (monomer)	τ_f' / ns (excimer)
PBA in MeOH	38 (±4)	41 (±4)
PyDex 1	142 (±8)	78 (±6)
PyDex 2	146 (±8)	81 (±6)
PyDex 3	144 (±8)	80 (±6)
PyDex 4	136 (±8)	85 (±6)
PyDex 5	132 (±8)	88 (±6)
PyDex 6	130(±7)	127 (±7)

The fluorescence lifetime decays for PBA in MeOH and PyDex 1 in PBS can be seen in Figure 5.11 and Figure 5.12 respectively.

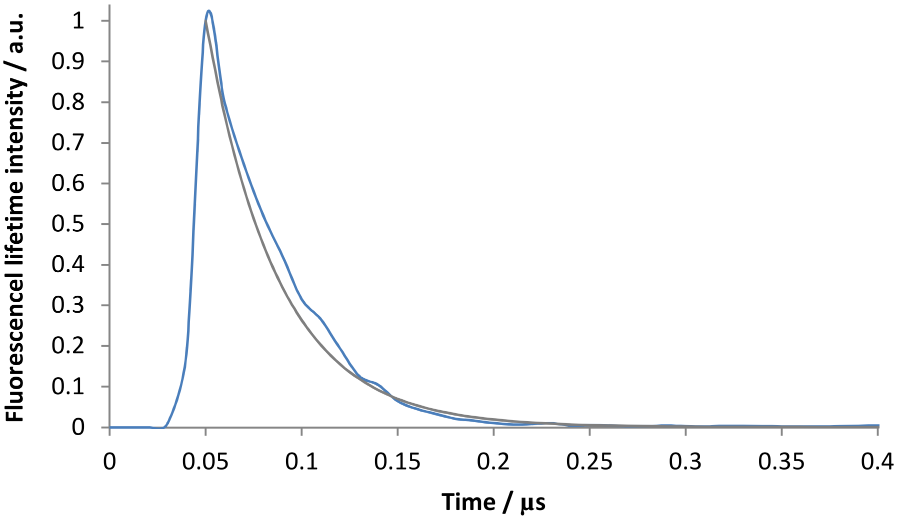

Figure 5.11 Fluorescence lifetime data (blue) and fit (grey) for PBA in MeOH, excited at 337 nm with fluorescence collected at 375 nm.

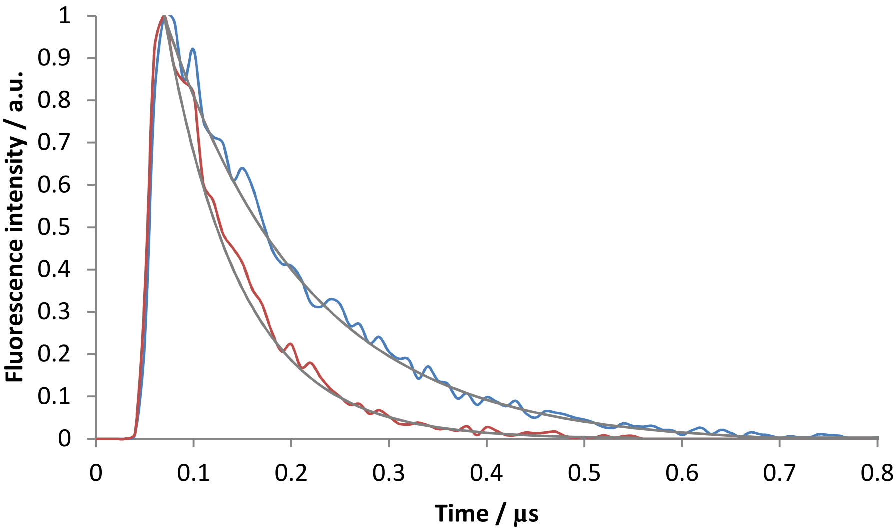

Figure 5.12 Fluorescence lifetime data and fit (in grey) for PyDex1 in PBS, excited at 337 nm with fluorescence collected at 375 nm (blue spectrum) and 500 nm (red spectrum).

The lifetime of PBA in organic solvents is significantly shorter than in aqueous environments due to greater solubility of oxygen in organic solvents, typically 0.1 mM in water and 1 mM in MeOH, which fits with previous research defining it as a probe for measuring the concentration of oxygen.[74] The recorded lifetimes of the various PyDex conjugates all suggest the fluorescence lifetime of the monomer in an aerated aqueous environment of PBS to be ≈ 140 ns (± 10 ns); an example is shown in Figure 5.12 with the fluorescence lifetime data of PyDex1. The lifetime recorded for the fluorescence of the broad fluorescence band at 500 nm resulted in lifetimes that were significantly shorter, giving a value for τ_f' of ≈ 81 ns. This result further confirms the presence of the pyrene excimer fluorescence here, corresponding to what is shown in the literature.[68, 85, 86]

In the data collected there is no ‘rise-time’ observed which indicates that the excimer is formed in solution immediately as it does not take any time to form which also suggests that the pyrene molecules are already held in close proximity enabling the rapid formation of the excimer. As the decay is also mono-exponential, i.e. no significant rise time, it suggests this is the case throughout the whole sample confirming that the excimer is formed by the close proximity of two bound pyrene molecules as opposed to via inclusion of some residual PBA molecules.

The important point to highlight here is that the rise time of the excimer band is rapid, for pyrene on its own in solution the excimer has a rise time that matches the decay of the monomer emission. This shows that excimer formation is a dynamic process and takes time to occur. In the system discussed here this is not the case, the rise time is fast and not related to the monomer decay. This information suggests that there are two types of site for pyrenes in these conjugates. One where the pyrene is isolated and has no chance of meeting another pyrene and a second where the pyrene has a close neighbour where they interact strongly and rapidly.

The fluorescence lifetime was also recorded for PBA in methanol at 500 nm where the pyrene excimer band is seen which gave a fluorescence lifetime value of 43 ns which is consistent with the fluorescence lifetime recorded of the same sample at 375 nm confirming that no excimer is present along with the absence of a broad emission peak.

The excimer fluorescence for PyDex6 gave a fluorescence lifetime of 127 ns which can be attributed to the tail end of the monomer fluorescence suggesting the absence of the excimer within that sample. This also confirms it is possible to synthesise PyDex with a sufficiently low pyrene loading to prevent excimer formation. If the excimer was forming due to inclusion of PBA in the dextran solution then it would be more likely to see a rise time as the pyrene butyric acid would be free to move about within the solution. In the model where the PBA is bound to the dextran and held in place then its interaction with another molecule of PBA would be instantaneous as they are next to each other. However, if the PBA was present by ‘inclusion’ within the dextran, as opposed to bound to it, then the possibility of its interacting with another molecule is not certain and might not happen instantaneously after the point of excitation.

5.1.1. Oxygen sensitivity

The fluorescence intensity of pyrene-1-butyric acid is known to be oxygen sensitive which has previously led to its use as an oxygen probe. The long lived fluorescence lifetime of pyrene derivatives means that diffusion limited quenching by oxygen at concentration of µM – mM has a significant impact upon the observed lifetime and emission intensity, *vide infra*.

Oxygen sensitive measurements were carried out on PBA in MeOH and PyDex6 by studying the fluorescence properties of both at varying concentrations of oxygen..

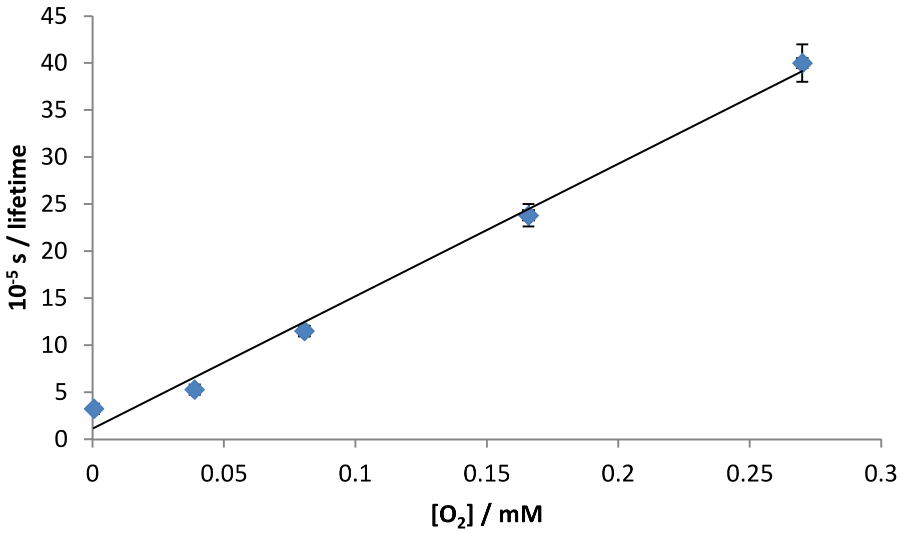

Figure 5.13 Stern-Volmer plot of PBA in MeOH, excited at 337 nm with fluorescence emission monitored at 375 nm, data used from Figure 5.14. 10^{-5}/lifetime = $142[O_2] + 0.85$.

Figure 5.13 shows PBA has a quenching constant of 1.4×10^{10} dm^{-3} mol^{-1} s^{-1} in MeOH, with fluorescence lifetimes extending between 25 and 273 ns in aerated and degassed solutions respectively. These correlate well with previous findings of PBA in EtOH that gave a value for k_q of 1.3×10^{10} dm^{-3} mol^{-1} s^{-1}, with fluorescence lifetimes extending between 30.6 and 220 ns in aerated and degassed solutions respectively.[74]

The fluorescence lifetime decays for the data of PBA in MeOH are shown in Figure 5.14 with the fitted data overlaid on the raw data.

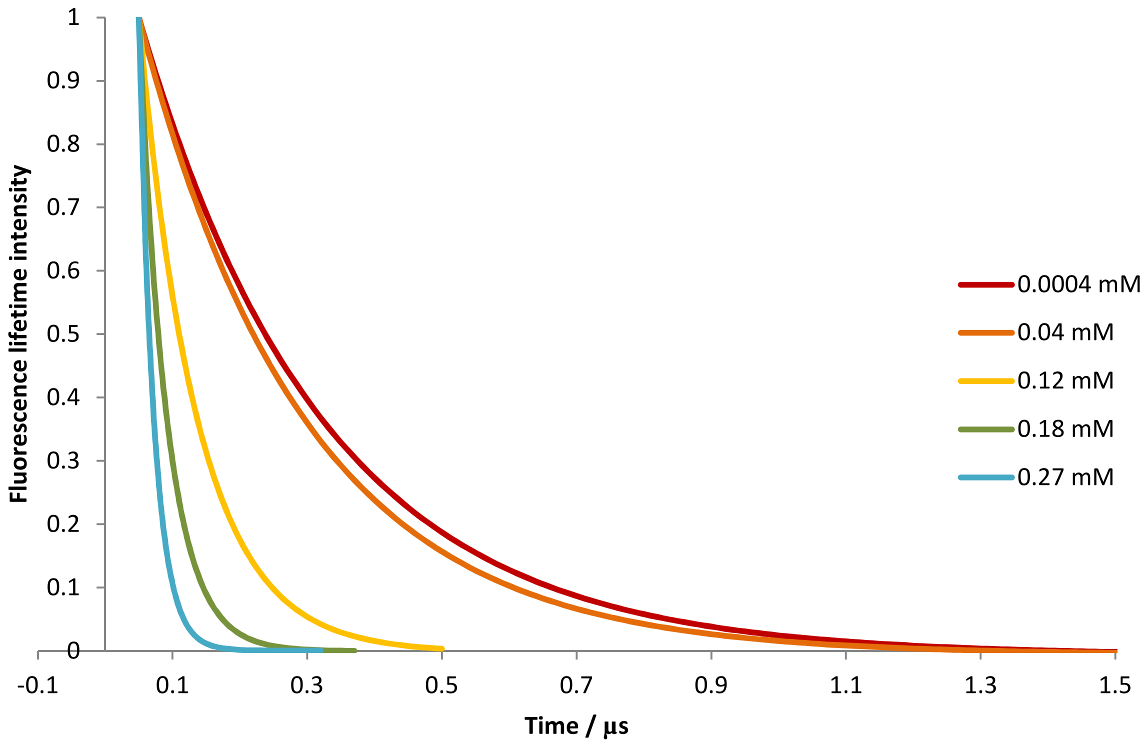

Figure 5.14 Fitted fluorescence lifetime decays for PBA in MeOH for aerated solutions (blue) to degassed solutions (red), excited at 337 nm with fluorescence collected at 375 nm, $[O_2]$ shown in legend.

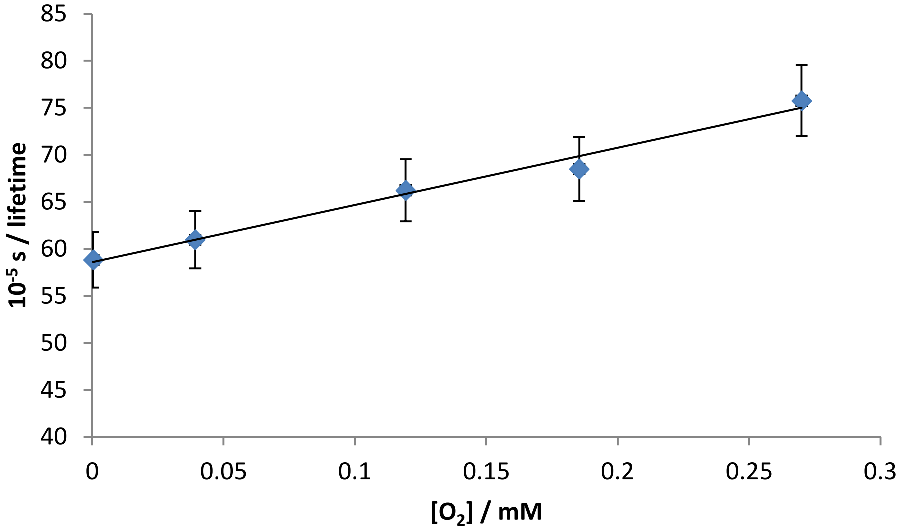

Figure 5.15 Stern-Volmer plot of PyDex6 in H_2O, excited at 337 nm with fluorescence emission collected at 375 nm. 10^{-5}/lifetime = $60.8[O_2] + 58.6$

Previous work has shown that PBA dissolved in an aqueous medium is sensitive to the concentration of oxygen present but results in a lower value for k_Q due to the slight difference in the viscosity of the two solvents. In the literature, values for k_Q of PBA in water have been calculated as 8.0×10^9 dm^{-3} mol^{-1} s^{-1}, with fluorescence lifetimes recorded as 106 to 138 ns in aerated and degassed aqueous solutions respectively. This is consistent with the findings of the studies of the oxygen sensitive properties of PyDex6 in water, where a quenching constant of 6.1×10^9 dm^{-3} mol^{-1} s^{-1} in water was measured with fluorescence lifetimes extending between 132 and 170 ns in aerated and degassed solutions respectively. The Stern-Volmer plot showing the data for the PyDex sample can be seen in Figure 5.15. The decays measured from both aerated and degassed solutions of water are shown in Figure 5.16.

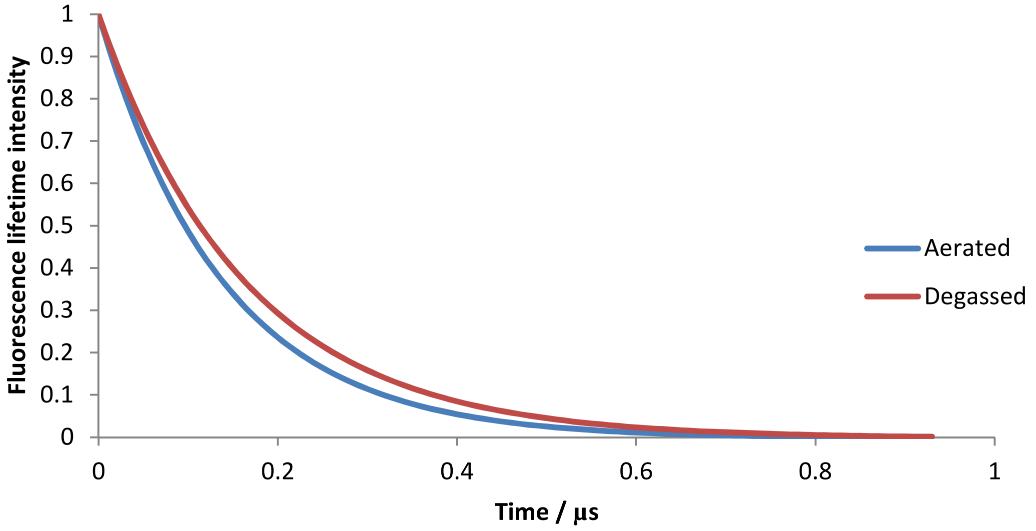

Figure 5.16 Fitted fluorescence lifetime decays for PyDex in H_2O for an aerated solution (blue) and a degassed solution (red), excited at 337 nm with fluorescence collected at 375 nm.

For the oxygen sensitive measurements of PyDex6, the fluorescence emission was collected at 375 nm and 500 nm in order to determine the presence of excimer fluorescence. The recordings found at 500 nm yielded, within error, the same values of oxygen concentration as those found at 375 nm. This further indicates the absence of excimer formation in the PyDex6 sample.

5.2. Coumarin-3-carboxylic acid

Research into coumarin derivatives has led to potential uses in fluorescence spectroscopy, e.g. fluorescent probes.[71, 72] Coumarin is a hydrophobic fluorescent dye (Figure 5.17) which given its possible applications would be interesting to incorporate into a hydrophilic medium to see if, like pyrene, its photophysical properties remain the same when the molecule is embedded in a nanoparticle. Commercially available coumarin-3-carboxylic acid was used in the work described in this next section as it can readily form a covalent amide bond with aminodextran. [87, 88]

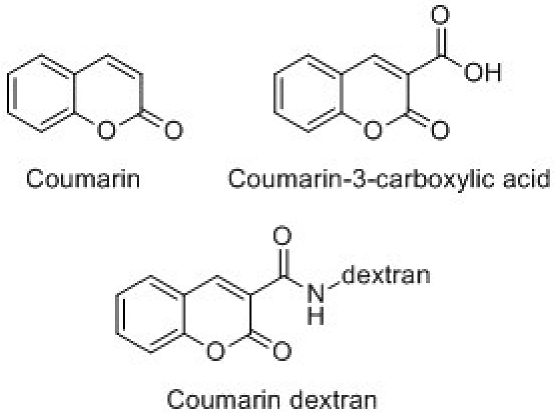

Coumarin Coumarin-3-carboxylic acid

Coumarin dextran

Figure 5.17 Molecular structures of Coumarin and its derivatives Coumarin-3-carboxylic acid and Coumarin dextran

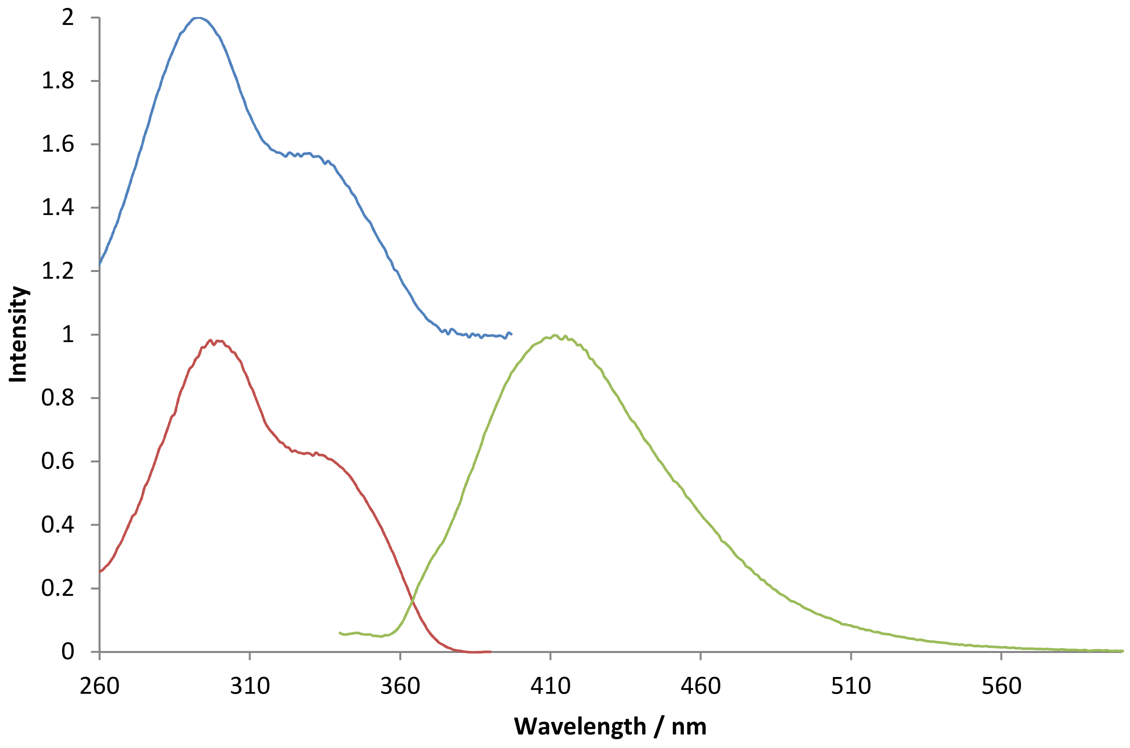

Figure 5.18 Normalized absorption, excitation and emission spectra of Coumarin-3-carboxylic acid recorded in EtOH, λ_{ex} = 330 nm and λ_{em} = 460 nm.

The fluorescence spectra of coumarin-3-carboxylic acid were recorded in separate solutions of DMSO, EtOH (shown in Figure 5.18) and DCM.

The same conjugation method used for making PyDex, EDC coupling, was used to attach the coumarin-3-carboxylic acid to aminodextran (MW 10,000). The product obtained was washed thoroughly with DCM and resulted in a water soluble product: the photophysical properties of this conjugated material are discussed here and compared with the dye in organic solvents.

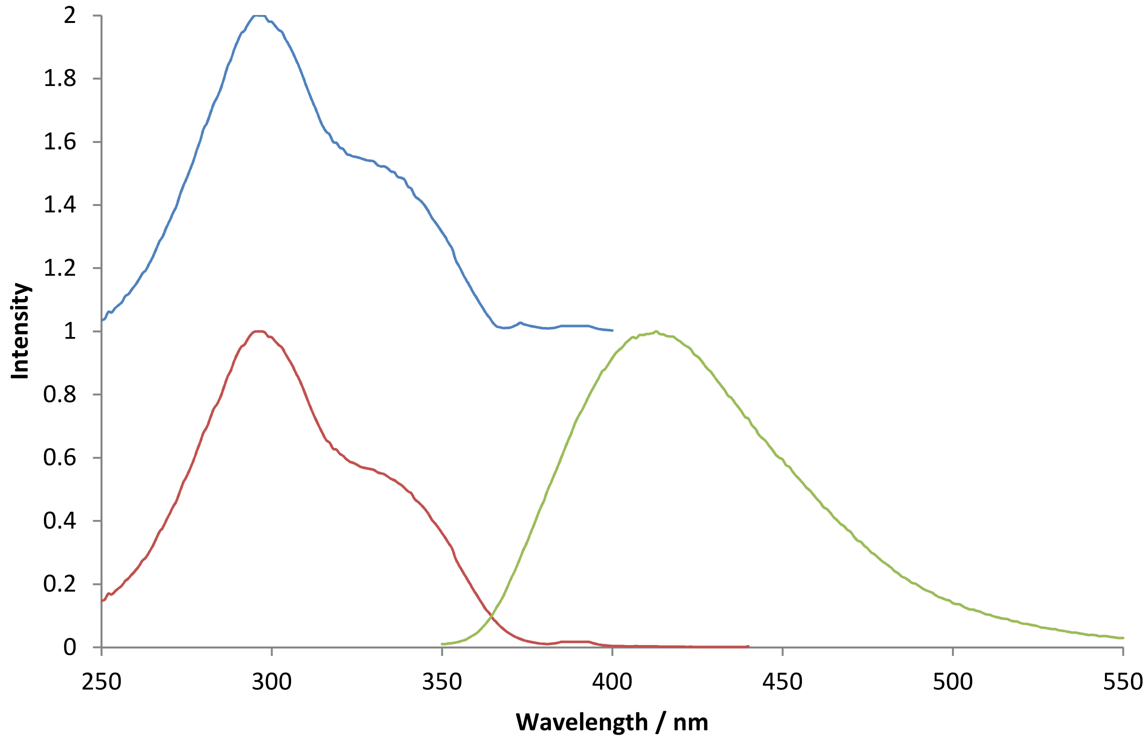

Figure 5.19 Normalized absorption, excitation and emission spectra of Coumarin-3-dextran recorded in PBS, λ_{ex} = 300 nm and λ_{em} = 460 nm.

Figure 5.19 shows the normalised fluorescence spectra of CoumDex which largely resemble that of the coumarin-3-carboxylic acid fluorophore.

The comparison of the fluorescence spectra of the two samples are further shown in the overlaid spectra in Figure 5.20 which highlights a slight red shift in the absorption for the CoumDex sample in comparison with C3CA in ethanol. This shift is not seen in the excitation spectrum and can again be attributed to the presence of a non-fluorescent aggregate seen in the ground state. The excitation as seen in Figure 5.20 bears no distinct change between the two samples indicating that the electronic structure of the molecules in their excited state are comparable.

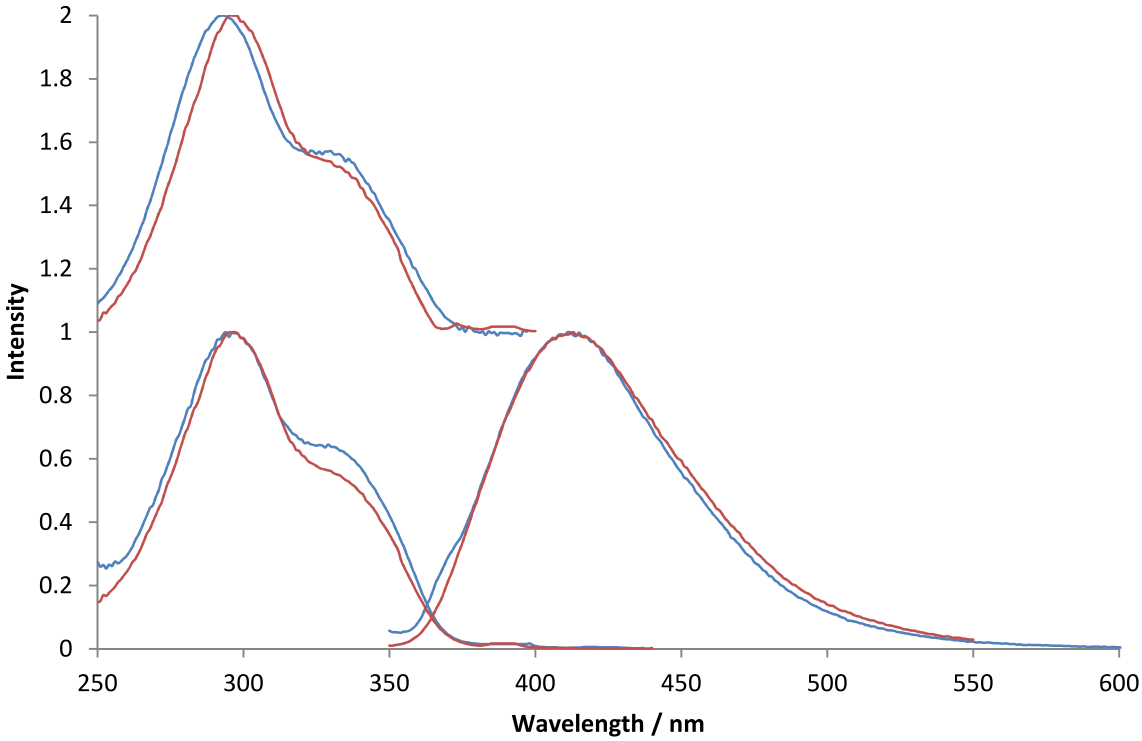

Figure 5.20 Normalized absorption, excitation and emission spectra for C3CA (blue spectra) recorded in EtOH overlaid with Coumarin-dextran (red spectra) recorded in water, λ_{ex} = 300 nm and λ_{em} = 460 nm.

Table 5.6 Fluorescence spectra and absorption peak data extrapolated from Figure 5.20 and fluorescence lifetime for C3CA recorded in EtOH and CoumDex recorded in water. Peaks in round brackets indicate aggregate peak, square brackets indicate small discernable shoulder.

	Absorption / nm	**Emission / nm**	**Fluorescence lifetime / ns**
C3CA in EtOH	293, [330]	412	0.34 (± 0.05)
CoumDex in water	300, (332)	413	0.33 (± 0.05)

CoumDex was synthesised at two different concentrations of coumarin:aminodextran by weight, the first being 1:4 and the second being 1:8. The molar calculations are shown below in Table 5.7.

Table 5.7 Quantities used for various conjugations of aminodextran (10,000 MW) with C3CA

Sample	**Aminodextran / mg (moles/µmol)**	**C3CA / mg (moles/ µmol)**
CoumDex1	40 (4)	10 (53)
CoumDex2	40 (4)	5 (26)

5.3. Incorporation of pyrene and coumarin dextran conjugates into nanoparticles

Following attachment of coumarin and pyrene derivatives to aminodextran, the incorporation of the conjugates into polyacrylamide nanoparticles was attempted. These were synthesised using the same method as for the synthesis of polyacrylamide nanoparticles with the fluorescent dyes in chapter 3 (e.g. FITC-dextran).

5.3.1. Pyrene butyric dextran in nanoparticles

Initially, to ensure incorporating the dextran conjugates into the polyacrylamide matrix was possible, PyDex3 was used for the nanoparticle synthesis (generating nanosensor 3 or PyDNP3). An important question in the experiment was to see if the pyrene excimer was still observed and if so whether the amount of the excimer emission observed for the nanoparticles differed from that of the dextran conjugate in solution.

The spectra in Figure 5.21 show the fluorescence spectra for the new PyDex nanoparticles (PyDNP3). The overlaid spectra in Figure 5.22 show that the fluorescence emission and absorption profile for nanoparticles containing PyDex (PyDNP) is consistent with that of the corresponding PyDex sample.

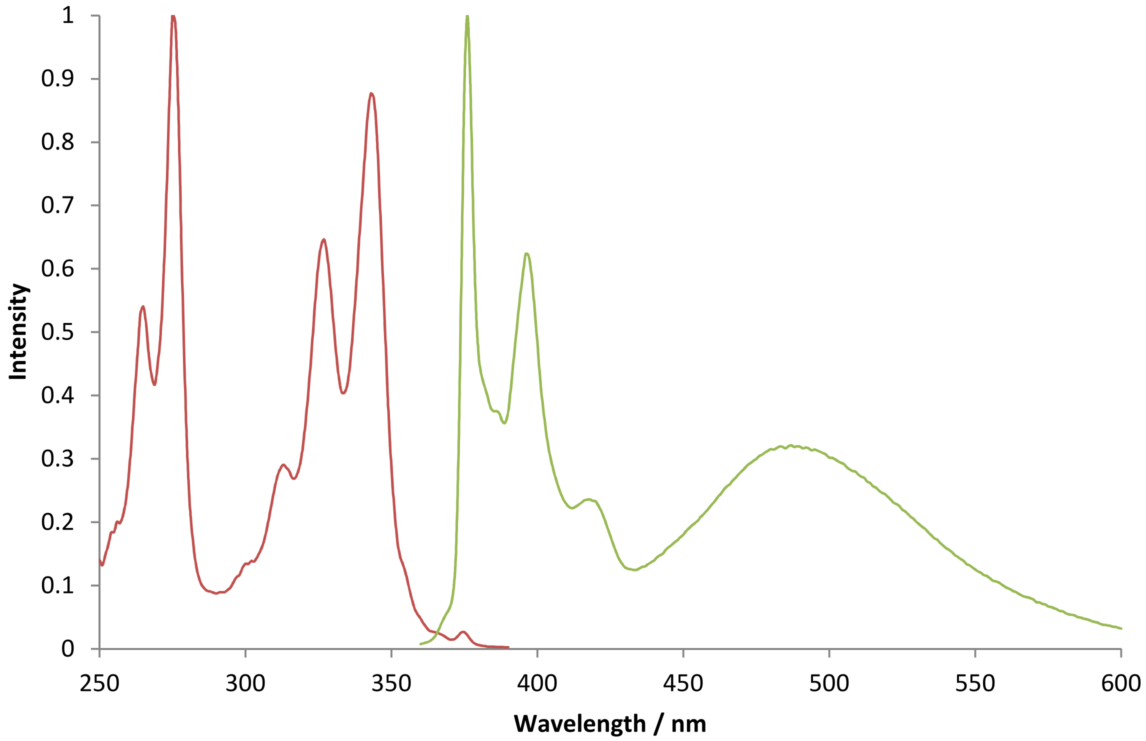

Figure 5.21 Normalized excitation and emission spectra of PyDNP3 in PBS, λ_{ex} = 350 nm and λ_{em} = 400 nm.

Table 5.8 Fluoresence spectra and absorption peak data for PyDNP1 recorded in PBS extrapolated from Figure 5.21

	Absorption	**Emission**
PyDNP3	265, 276 (316), 328, 345	376, 396, 414 (488)

PyDNP3 were synthesised from sample PyDex3 (4:35 molar ratio of aminodextran:PBA). Looking at the emission spectra of the dextran conjugate and the entrapped conjugate dye in Figure 5.22 we see that entrapping the dye-conjugate does not appear to affect the fluorescence emission of the fluorophore. Pyrene and its derivatives are known for their intense fluorescence properties: these are retained by incorporating them into the polyacrylamide nanoparticles.

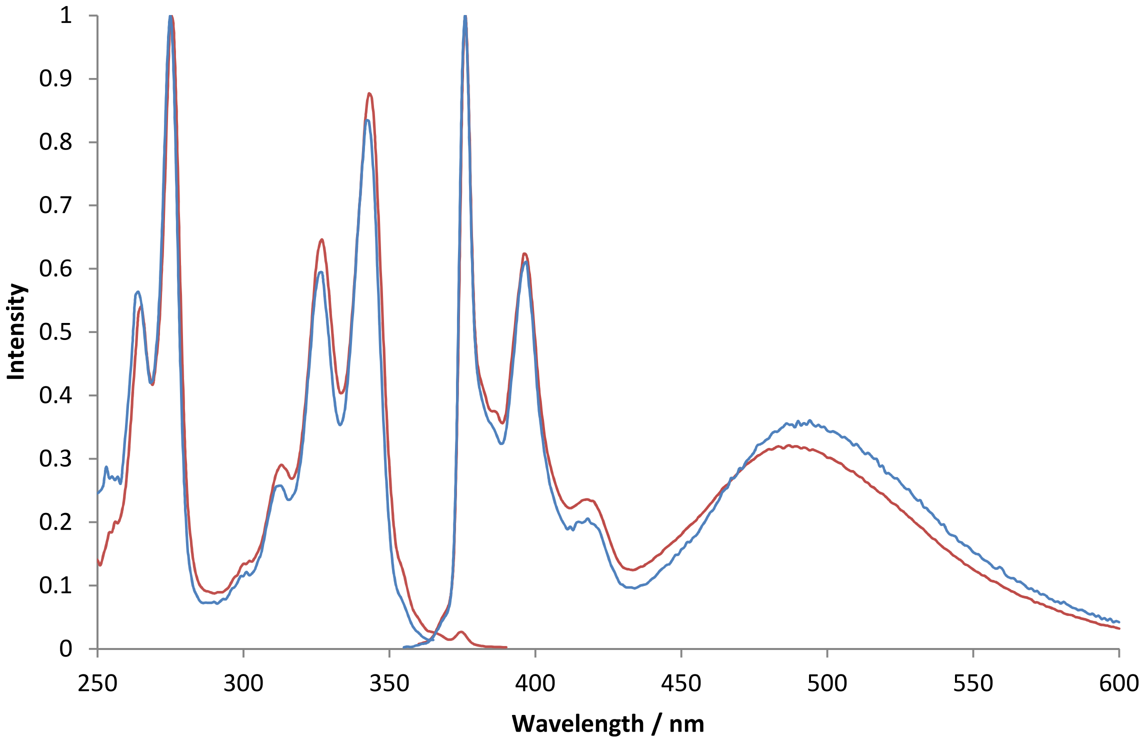

Figure 5.22 Normalized excitation and emission spectra of PyDex3 in PBS(blue) and incorporated into nanoparticle PyDNP3 (red), λ_{ex} = 350 nm and λ_{em} = 400 nm.

Polyacrylamide nanoparticles were synthesised incorporating the various synthesised PyDex samples. The fluorescence spectra of the resultant nanosensors resembled that of the PyDex samples in solution. The overlaid spectra shown in Figure 5.22 demonstrate how the photophysical properties were maintained, and a similar degree of excimer emission is observed as for the dextran conjugate alone, albeit with a small shift in the emission wavelength. This also suggests that it is possible to generate nanosensors limiting the presence of the excimer and that the pyrene derivative does not further aggregate within the nanoparticle. This was confirmed in the synthesis of polyacrylamide nanoparticles containing PyDex6 (4:1.7 molar ratio of aminodextran:PBA).

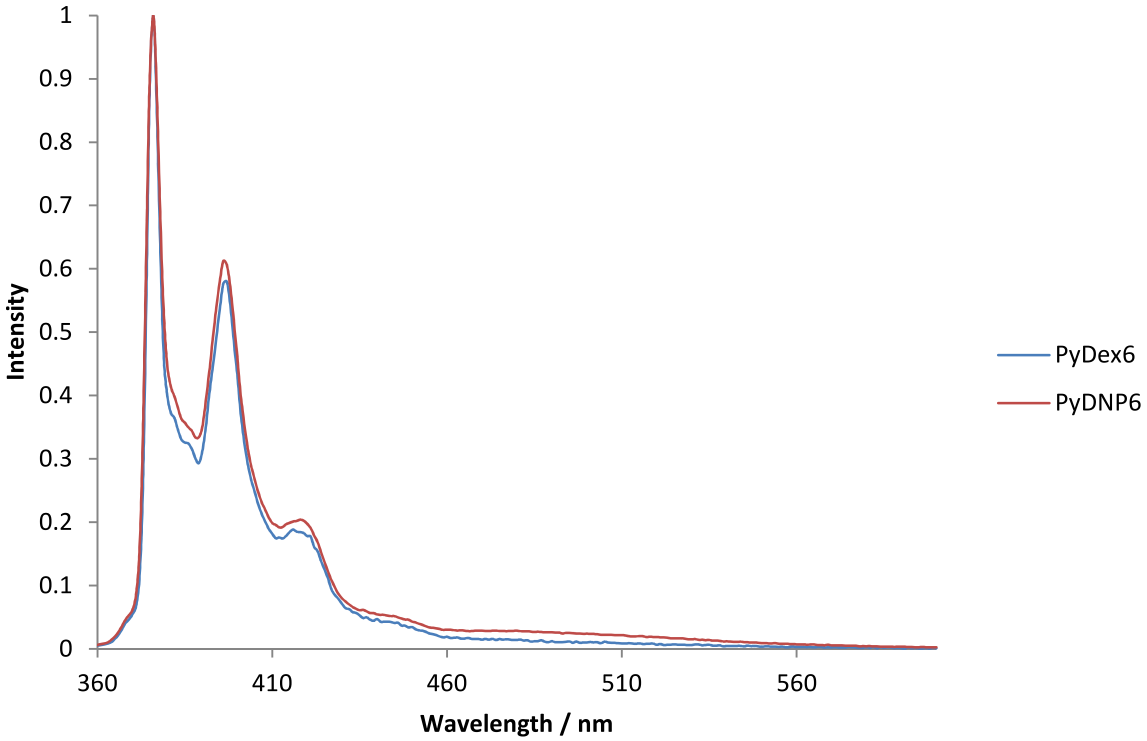

Figure 5.23 Normalized emission spectra of PyDex6 and PyDNP6, λ_{em} = 400 nm.

The emission spectrum of PyDNP6 fitted with its corresponding PyDex sample in solution is shown in Figure 5.23. The similarity indicates that it is possible to synthesise a pyrene based nanosensor without the presence of the pyrene excimer present.

Table 5.9 Fluorescence lifetimes of nanosensors containing various PyDex samples. τ_f collected at 375 nm and τ_f' collected at 500 nm.

Nanosensor	PyDex sample	τ_f / ns	τ_f' / ns
PyDNP 1	PyDex1	110 (± 9)	85 (± 7)
PyDNP 2	PyDex2	115 (± 9)	82 (± 7)
PyDNP 3	PyDex3	117 (± 9)	83 (± 7)
PyDNP 4	PyDex4	113 (± 9)	90 (± 8)
PyDNP 5	PyDex5	117 (± 9)	87 (± 8)
PyDNP 6	PyDex6	118 (± 9)	115 (± 9)

5.3.2. Oxygen sensitivity

As with PBA and PyDex in section 5.1.1, oxygen sensitive measurements were carried out on nanoparticles containing PyDex in order to determine whether after incorporation, the fluorescent signal of the dye remains sensitive towards oxygen or not. The fluorescence lifetimes were recorded as a function of the concentrations of oxygen as with the dextran conjugates and PBA in solution (section5.1.1).

It was observed that the fluorescence lifetimes recorded at 375 nm for PyDNP6 showed no significant (within experimental error) change between aerated and degassed solutions and all values were between 111 and 120 ns. This can be attributed to a shielding effect of the polyacrylamide nanoparticles and the possibility of their maintaining a higher local concentration of oxygen.

5.3.3. Coumarin-dextran in nanoparticles

The Coumarin-dextran (CoumDex) fluorophore was then incorporated into the polyacrylamide nanoparticles to give Coumarin based nanosensors (CoumDNP). The following section covers the photophysical properties of the resulting nanoparticles in comparison with the properties of the dye in solution.

The fluorescence spectra of the CoumDex nanoparticles below in Figure 5.24 show the characteristic bands of the coumarin fluorphore with the emission centred around 420 nm.

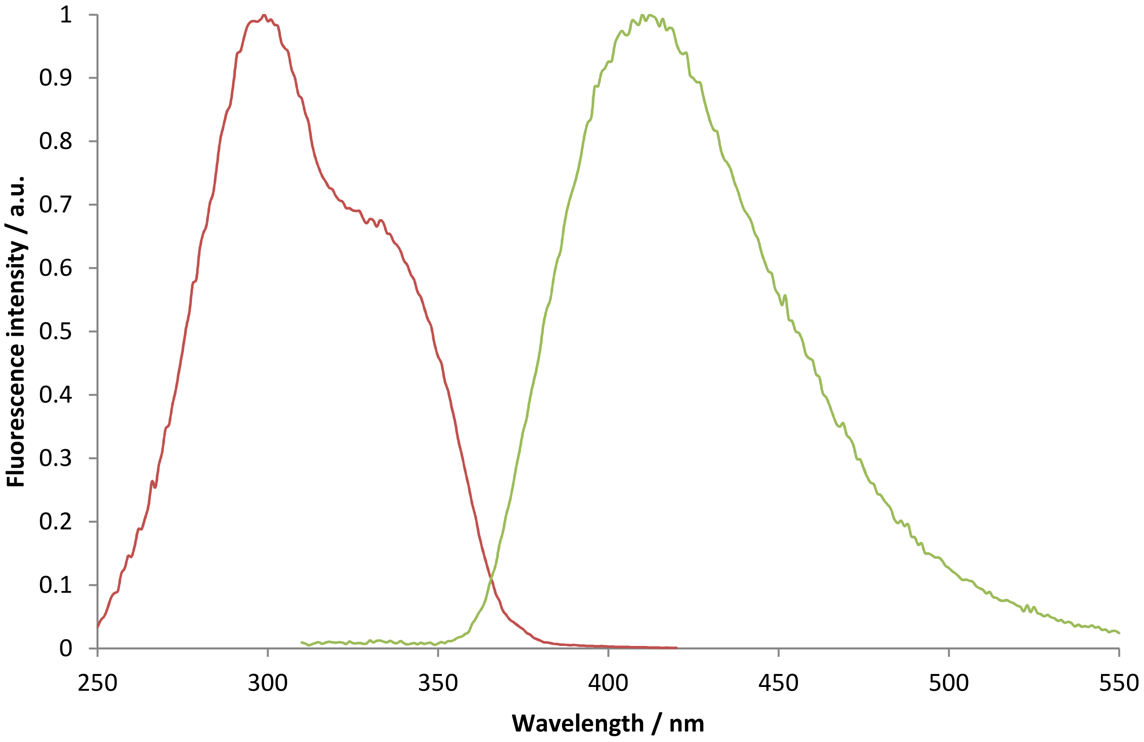

Figure 5.24 Normalized excitation and emission spectra of CoumDex in nanoparticles (CoumDNP) recorded in water, λ_{ex} = 300 nm and λ_{em} = 440 nm.

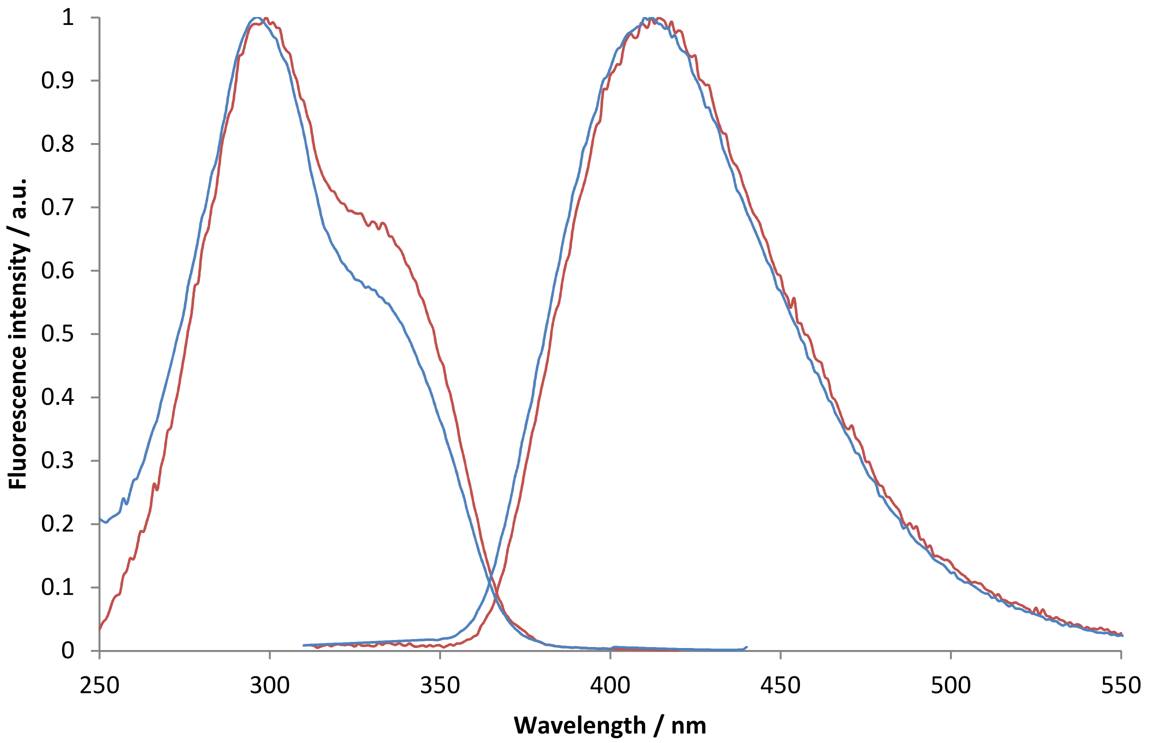

Figure 5.25 Normalized excitation and emission spectra of CoumDex in solution (blue) and CoumDex in nanoparticles (red), both recorded in PBS, λ_{ex} = 300 nm and λ_{em} = 440 nm for both molecules.

The overlaid fluorescence spectra in Figure 5.25 indicate that the fluorescence emission and excitation peaks remain the same upon incorporation of the dye into the polymer matrix. The shoulder seen in the excitation spectrum of the nanoparticles can be attributed to inner filter effects in the measurement.

Table 5.10 Data comparing fluorescence lifetimes of Coumdex and Coumdex in nanoparticles, both recorded in PBS.

	τ_f /n s
CoumDex	0.33 (± 0.02)
CoumDNP	0.35 (± 0.03)

The fluorescence spectra and lifetime data confirm that the spectral properties for CoumDex are maintained when incorporated into the nanoparticle matrix.

5.4. Concluding remarks

The data in this chapter show that it is possible to entrap lipophilic fluorophores as water soluble dextran conjugates. The conjugates themselves are soluble in aqueous environments but by incorporating them within the polyacrylamide matrix it is has been possible to develop nanosensors containing entrapped coumarin and pyrene derivatives.

The pyrene-1-butyric acid dextran conjugates were shown to be sensitive to the concentration of oxygen in solution, but when incorporated into the polyacrylamide nanoparticles the ability to monitor the concentration of oxygen present based on the fluorescence response was lost. An explanation for this is that the concentration of oxygen inside the nanoparticles, where the fluorophores reside, may differ from that outside the nanoparticles. Also it is likely that the rate of diffusion of oxygen through the nanoparticle is slower than in solution. Future attempts to find a method of conjugating the pyrene dyes to the exterior surface of the nanoparticle may give more to this conclusion. For example, it would confirm whether the rate of diffusion of oxygen is slower through the nanoparticle and whether the fluorophores work more efficiently on the exterior, e.g. brighter.

Further to this was the ability to also incorporate coumarin-3-carboxoylic acid dextran conjugates within polyacrylamide nanoparticles. The photophysical measurements showed that the fluorescence properties of the coumarin dye were maintained on incorporation into the nanoparticles. Some coumarin derivatives have been developed for pH sensing so it would seem logical to direct future work towards developing coumarin nanosensors responsive to environmental pH. Also, further work with the coumarin nanosensor employing more variations of the coumarin dye:dextran conjugate ratios would allow the assignment of the shoulder in the absorption spectrum, owing to aggregation or otherwise.

6. Photophysical properties of porphyrin based nanosensors

6.1. Porphyrins

As mentioned previously porphyrins have been extensively researched and studied for their use as an anti-cancer drug in the development of photodynamic therapy (PDT). PDT is a treatment that was developed for conditions that require destruction of cells that are damaged or malignant. It is a type of phototherapy that exploits the use of molecules that after light exposure become toxic to cells. One method by which this occurs is by the generation of reactive oxygen species (namely singlet oxygen) which leads to the subsequent destruction of cells that are targeted.

As singlet oxygen damages cells it is also considered that the initial onset of conditions such as cancer where cells mutate may be caused or initiated by reactive oxygen species.[41, 89, 90] It should, therefore, be possible in a controlled environment to generate singlet oxygen and observe the mechanism of cell death and understand how conditions that arise from this develop. The design in Chapter 4 explored the potential for this design and the studies on porphyrins within this chapter look at the importance that porphryin molecules have within the topic.

6.2. Free base water soluble porphyrin

The porphyrins studied in this section are derivatives of 5,10,15,20-Tetrakis(1-methyl-4-pyridinio)porphyrin (TMPyP). The derivative used replaces one of the 1-methyl-4-pyridinio groups with a hydroxyl succinimide ester.

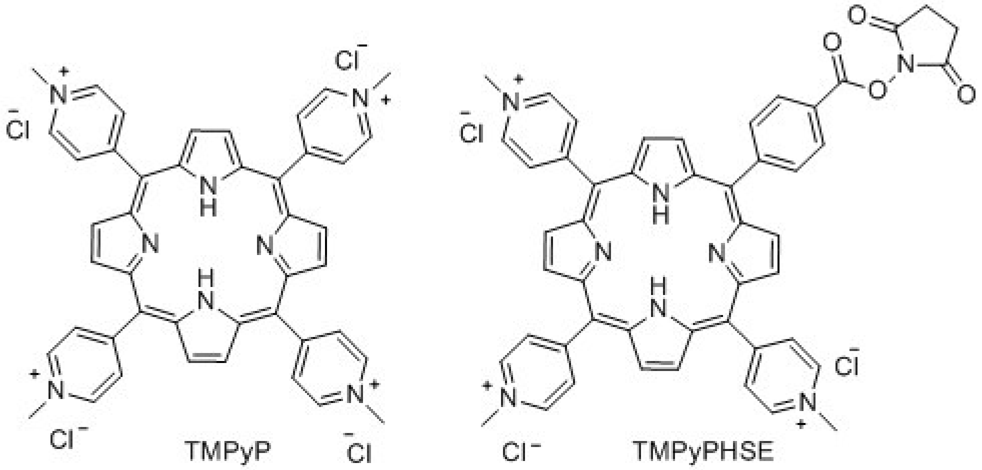

Figure 6.1 Molecular structures of free base water soluble porphyrins TMPyP and TMPyPHSE

Throughout, this molecule will be referred to as TMPyPHSE. These free base porphyrins are water soluble, due to the 3+ or 4+ charge, and so can be studied both conjugated to the nanoparticle matrix and in aqueous conditions. The derivative can then be coupled with amines bearing azide ($-N_3$) or alkyne ($-C\equiv CH$) functionality that can be conjugated by ‘click’ chemistry to nanoparticles bearing the opposite functionality.[91]

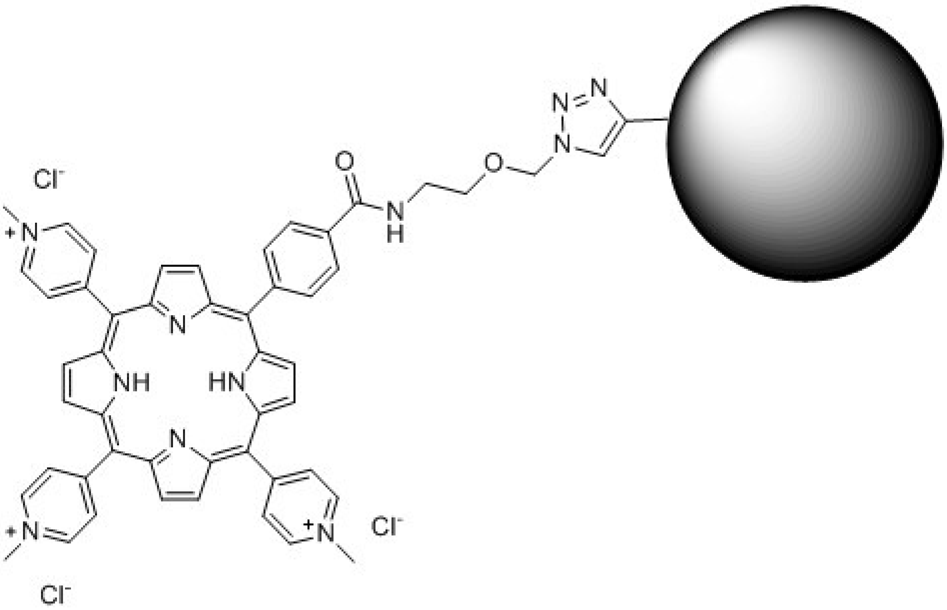

Figure 6.2 Diagram showing molecular structure of free base porphyrin, TMPyPHSE, conjugated to the surface of a nanoparticle

6.2.1. Previous reports

The photophysical properties of porphyrins, including the water-soluble, cationic TMPyP, has been extensively studied over the years by various research groups but conclusions regarding their behaviour have never been fully understood due to their complex nature. It is known that most charged porphyrins tend to aggregate or dimerise readily in solution due to π-stacking of the macrocyclic structures. [92, 93] However, the argument as to how or whether this case holds true for the multiply charged TMPyP family of porphyins has been under discussion for many years.

Pasternack *et al*[94, 95] have suggested by means of absorbance data that the positive charges on the peripheral pyridinium ions cause the delocalized π-electron cloud to be more diffuse over the surface of the molecule. Conversely, negative charges on the peripheral groups of porphyrins (anionic porphyrins) would lead to partial localization which would make the site more attractive to protons, increase basicity, and hence decrease acidity and cause stronger van der Waals interactions.

Kano *et al*[96, 97] previously reported that there are two forms of TMPyP in aqueous solution, one being the aggregate and the other the monomeric form. The suggestion that these were dependent upon concentration and temperature was examined by fluorescence and absorption spectroscopy with the evidence being that with the former there were changes in the emission profile dependent upon changes of concentration and temperature.

However, Kano *et al*[92, 98] later reassessed their former suggestion of aggregation, stating that despite the fact that it would be expected that TMPyP would form aggregates due to the π conjugated system, which would encourage van der Waals interactions, the positive charges on the periphery of the porphyrin seem to prohibit the formation of a dimer. This was presented along with supporting NMR and absorbance data.

Another contribution was from Vergeldt *et al*,[99] who proposed that TMPyP was monomeric in water and the emission profile that can be observed was due to mixing of the S_1 state and a close lying CT state in which an electron is transferred from the core of the porphyrin to a peripheral pyridinium group. This then results in a reduction in fluorescence lifetime and changes to fluorescence spectra, due to solvent polarity. This was supported by fluorescence spectra where they observed broad emission peaks in water and furthermore with temperature change.

More recent studies have shown that the photophysical properties of TMPyP are dependent on the interaction it has with its environment. It is understood that the tetrapyrrole ring has an important role to play in the formation of hydrogen bonds between the nitrogen and the water when in aqueous solvents and this association leads to the broadened emission that is seen.[30]

The aim here is to further define and understand the photophysical characteristics of free base porphyrins, especially in water, by the study of the derivative TMPyPHSE in comparison with TMPyP in solution and when conjugated to the surface of polyacrylamide nanoparticles.

6.2.2. Typical photophysics of a porphyrin

Tetraphenyl porphyrin (TPP) is a free base porphyrin with 4 phenyl ring substituents and can be considered as a ‘standard porphyrin’ to illustrate the characteristic photophysical properties generally observed for a molecule within the porphyrin family. TPP is not soluble in water and so the measurements shown below were made in toluene.

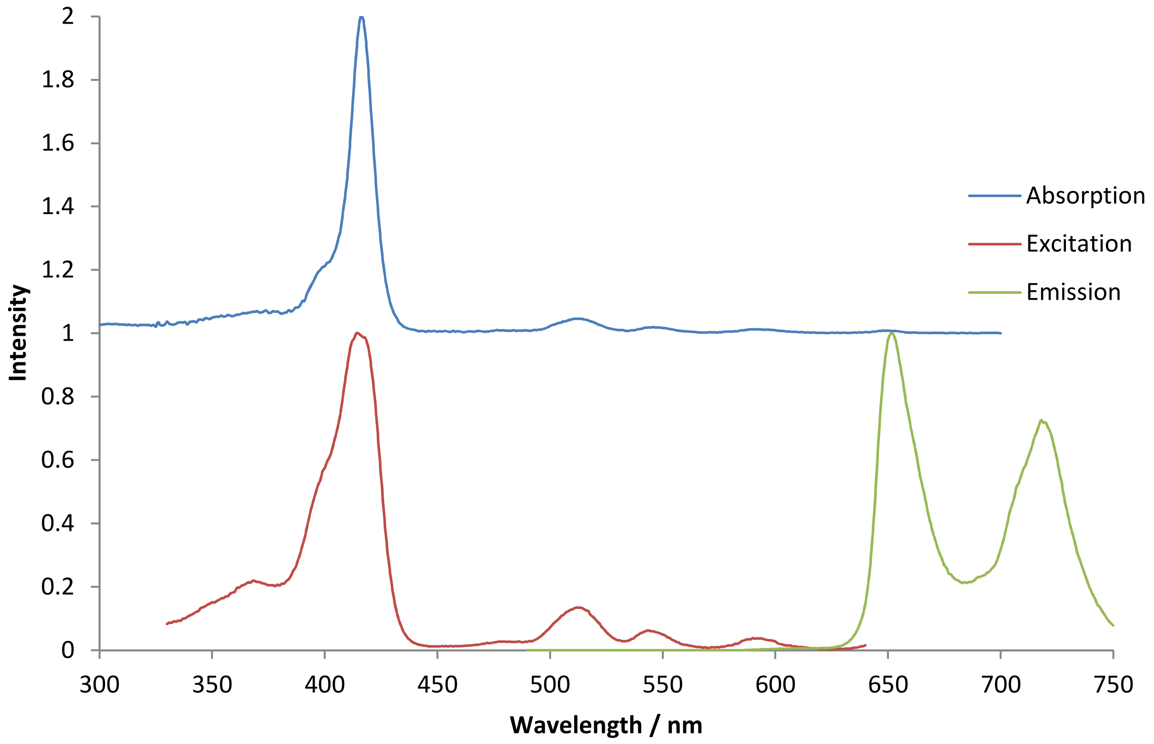

Figure 6.3 Photophysics of TPP in toluene, all spectra normalized and the absorption spectrum offset for clarity, λ_{ex} = 400 nm and λ_{em} = 650 nm

Figure 6.3 illustrates the absorption and fluorescence spectra for a standard free base porphyrin. In both the absorption and excitation spectra there is an intense peak, known as the Soret band, centred around 420 nm, accompanied by 4 less intense peaks, referred to as the Q-bands, extending into the red region of the spectrum. In the emission spectrum the profile observed is that of two clearly defined peaks.

The same emission spectrum is observed by excitation of either the Soret or Q-bands to illustrate that generally exciting the molecule anywhere within the absorption profile of the porphyrin yields the same emission spectrum. The only change is the intensity of the emission. This is because for the purpose of this measurement the same sample was used and, therefore, the absorbance differed dramatically depending on the band excited.

Due to the intense Soret band, a porphyrin normally exhibits a large extinction coefficient. The $S_1 \rightarrow S_0$ transition correlates to the Q-band which is normally of low intensity and hence oscillator strength is low which tends to yield a small PLQY in porphyrins.[100]

Owing to the fluorescent nature of the free base porphyrins the lifetime measured is typically in the order of nanoseconds. Here the lifetime of TPP in toluene was recorded as 10.2 ± 0.1 ns and the fluorescence quantum yield was 0.1 both of which are in agreement with literature values ($\Phi_f = 0.11$ ns[101] and $\tau_f = 9.3$ ns[102]). This yields a pure radiative lifetime, τ_0, = 100 ns, indicating a low oscillator strength for the S_1-S_0 transition.

6.2.3. Trimethylpyridinium porphyrin (TMPyPHSE)

As mentioned, free base porphyrins have gained much attention over the past three decades regarding their photophysical characteristics in water, particularly the observed change in the emission spectrum.

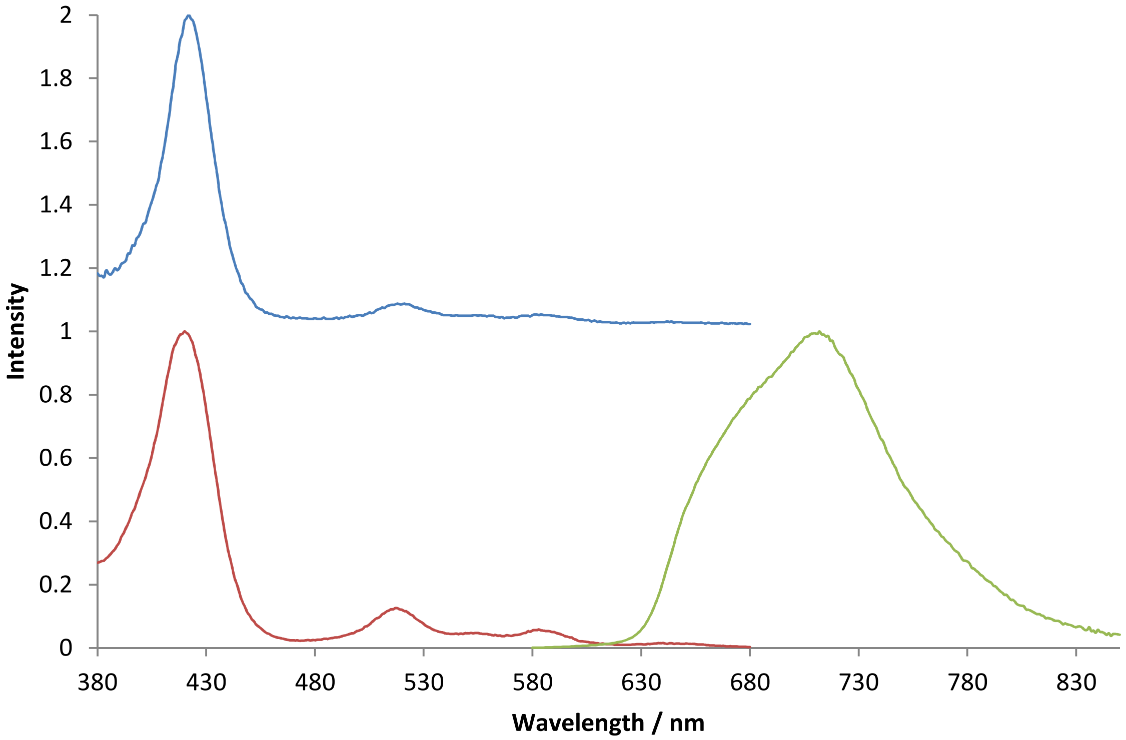

Figure 6.4 Normalized absorption and fluorescence spectra of TMPyPHSE in solution of PBS.

Figure 6.4 and Figure 6.5 show the fluorescence spectra for TMPyPHSE in an aqueous solution and then compared with other solvents, respectively. The main observation here being in the resulting emission profile from a free base porphyrin in water showing a broad 'single' peak spectrum whilst in other solvents (e.g. toluene, DCM) the emission spectrum is more structured with multiple defined vibrational bands. In this section, the results contribute to the debate of whether this phenomenon is due to aggregation or charge transfer effects of the molecule and its environment, as discussed earlier in this chapter.

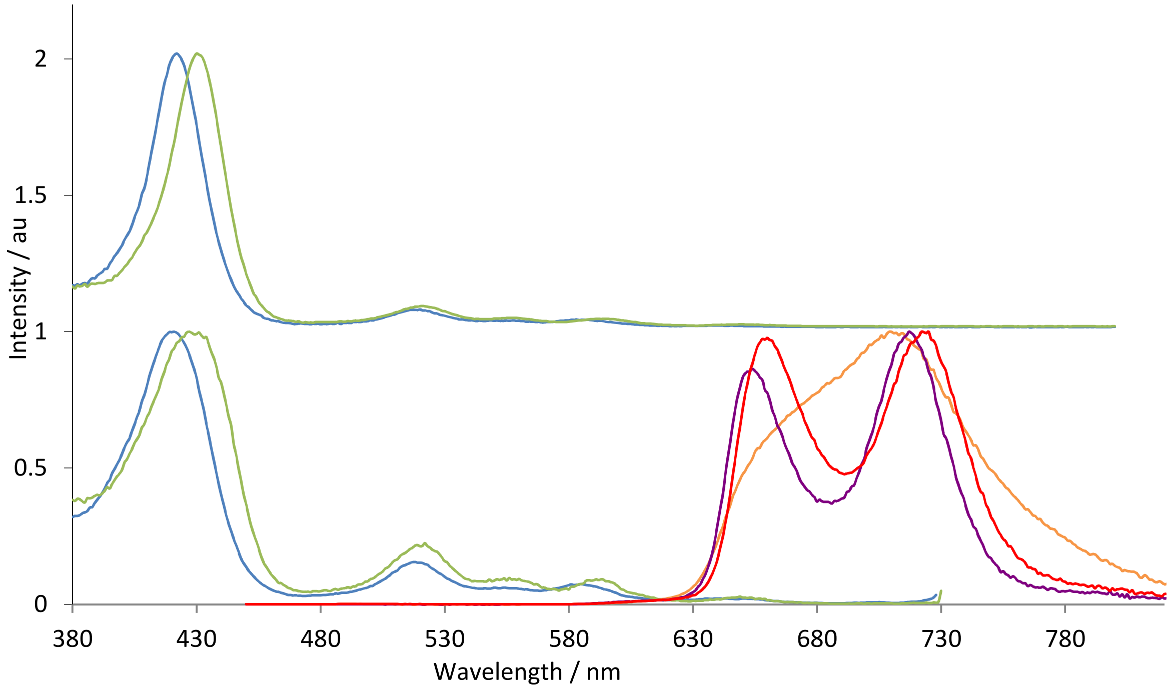

Figure 6.5 Normalized absorption and fluorescence spectra of TMPyPHSE recorded in various solvents. Absorption and excitation spectra colour key - Formamide (green); water, 0.1 M and 1.0 M NaCl, PBS, MeCN, EtOH, MeOH and DMSO (blue). Emission spectra colour key – water, 0.1 M and 1.0 M NaCl and PBS (orange); MeCN, DMSO and EtOH (purple); formamide and MeOH (red). λ_{ex} = 440 nm and λ_{em} = 740 nm.

Figure 6.5 highlights that the broad emission peak around 700 nm is only observed in aqueous solutions e.g. buffer solutions (PBS and both high and low concentrations of salt solutions. As mentioned, previous reports have attributed this to being due to charge transfer between the porphyrin and the environment, or the formations of a dimer or higher aggregates within the aqueous solution leading to peak broadening.

In aqueous solutions TMPyPHSE obeys the Beer-Lambert law over the range 2.6 – 19.5 µM, suggesting that it does not aggregate under these conditions. This is consistent with previous findings for the parent TMPyP.[103, 104]

Formamide has a dielectric constant of 110 whilst that of water is 80 hence this solvent should show similar stabilisation of a charge-transfer state and hence may give rise to the anomalous emission similar to that observed in water. The emission profile was measured in formamide to determine whether the change in dielectric constant would have an effect similar to that of water. The observed profile displays the characteristic double band which is observed in other organic solvents, but it is shifted ≈10 nm towards the red giving rise to solvatochromism. This observation suggests that the effect of charge transfer in the molecule may subtly influence the wavelength of the transition, and that the solvent does not have an effect on the emission profile or give rise to the loss of vibrational fine structure.

Table 6.1 Absorption and emission maxima (λ_{ex} = 440 nm) for TMPyPHSE in various solvents, extracted from Figure 6.5.

Solvent	Absorption / nm	Emission maxima / nm
Ethanol	422	654, 720
Methanol	422	660, 723
DMSO	422	654, 720
Acetonitrile	422	654, 720
Water	422	711
PBS	422	711
0.1 M NaCl	422	711
Formamide	431	660, 723

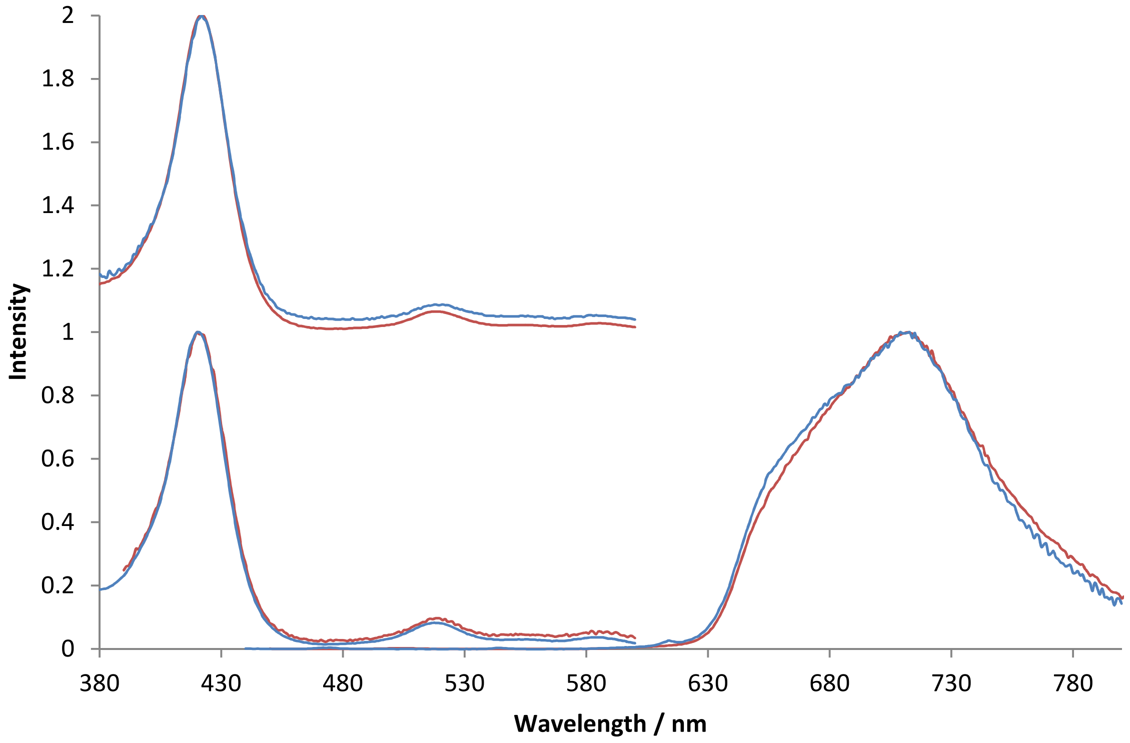

Figure 6.6 Normalized absorption and fluorescence spectra for TMPyP (red) and TMPyPHSE (blue) in PBS. λ_{ex} = 440 nm and λ_{em} = 740 nm

Figure 6.6 indicates that the presence of a chain containing a succinimidyl ester, attached to the porphyrin via a phenyl group in replace of a pyridinium, does not affect the fluorescence or absorption spectra of TMPyPHSE. The same can be said for the change in the charge (4+ to 3+) of the porphyrin.

Spectroscopic studies were then carried out in both an anionic (sodium dodecyl sulfate, SDS) and a cationic (cetyltrimethyl ammonium bromide, CTAB) surfactant to see if the interaction with the surfactant led to any changes in the emission profiles. Previous studies of TMPyP have shown that in anionic surfactants (e.g. SDS) the fluorescence properties of the porphyrin resemble that of an organic solvent rather than the characteristic broad band seen in aqueous environments. As previously discussed, research has shown that the photophysical properties of TMPyP are dependent upon the interaction it has with its environment. It is understood that the tetrapyrrole ring has an important role to play in the formation of hydrogen bonds between the nitrogen and the water when in aqueous solvents. In addition to this, the side chains and the charge they possess play a role in determining where the porphyrin is located.

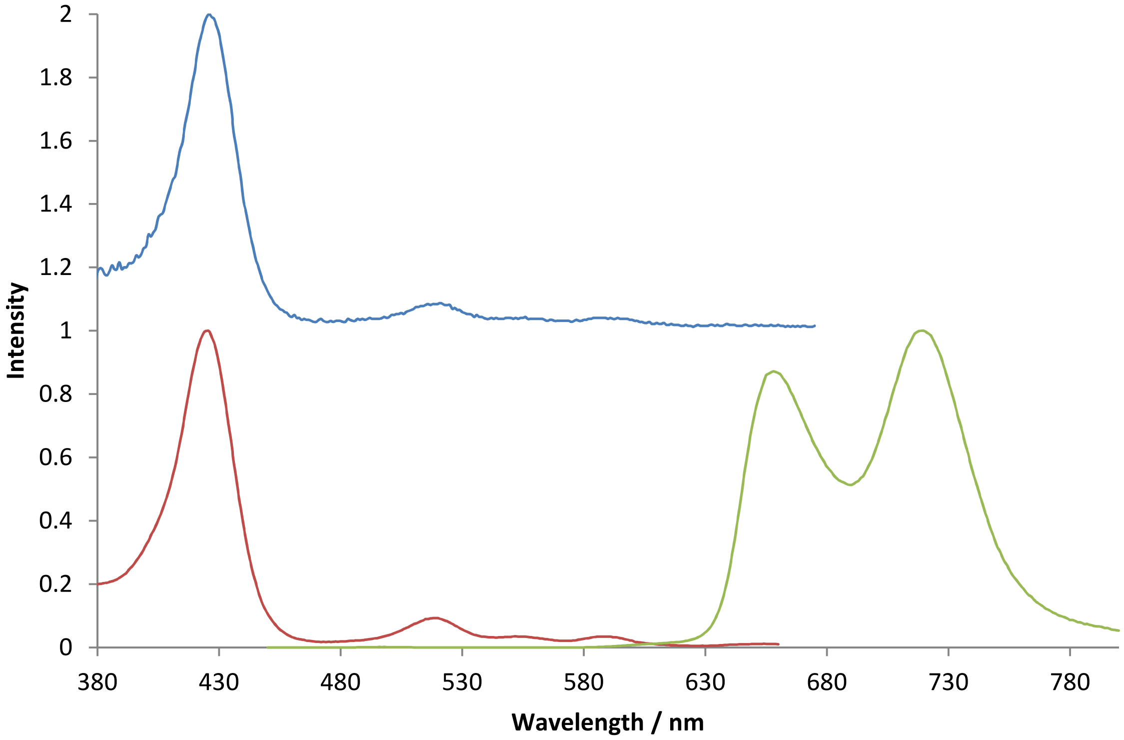

Figure 6.7 Normalized absorption and fluorescence spectra of TMPyPHSE in 0.1 M SDS, λ_{ex} = 430 nm and λ_{em} = 740 nm.

The fluorescence of TMPyPHSE was recorded in a 0.1 M solution of the anionic surfactant SDS which, as seen in Figure 6.7, gives rise to a double band emission spectrum centralised over the same region of the broad peak observed in pure water. As mentioned above, similar observations have been made for TMPyP in reporting that when dispersed in an anionic surfactant, such as SDS, the porphyrin fluorescence mimics that in organic solvents.[30, 105]

This can be attributed to the electrostatic interaction between the negative charge of the surfactant and a combination of the positive charge of the porphyrin and the two central hydrogen atoms found in the core of the porphyrin ring and a change in the local solvent microenvironment of the porphyrins in these solutions. The derivative of TMPyP used in these studies has a charge of 3+ attributed to the 3 peripheral pyridinium groups.

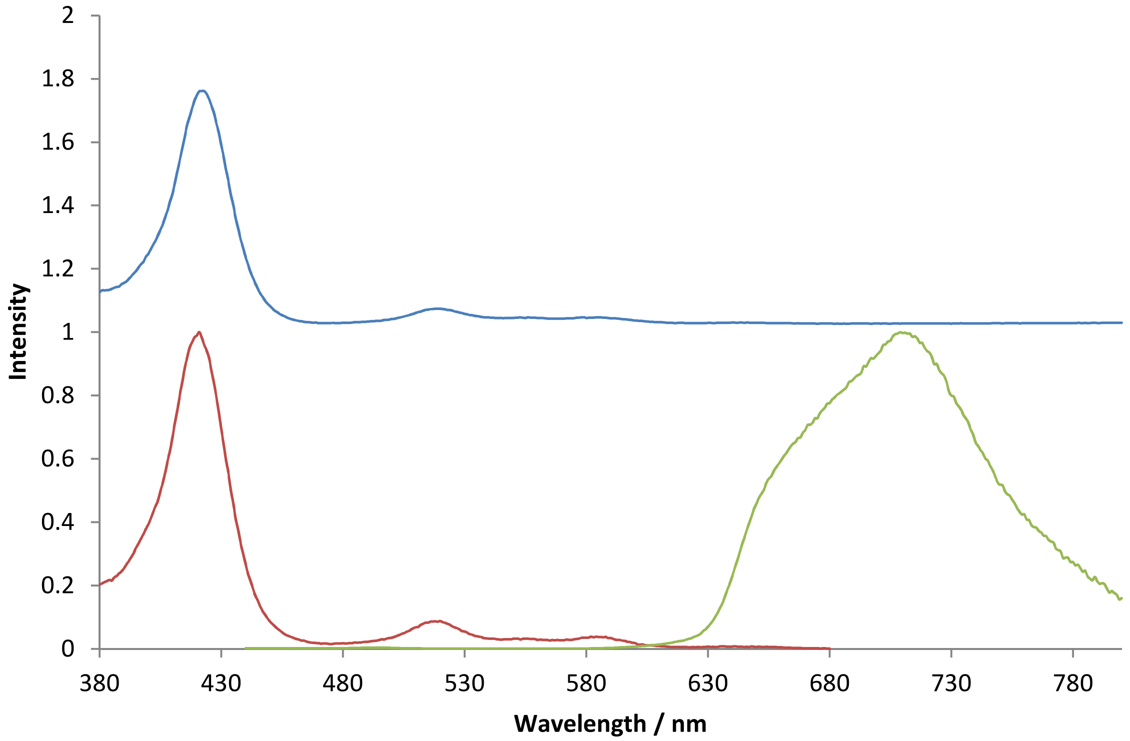

Figure 6.8 Normalized absorption and fluorescence spectra of TMPyPHSE in 0.1 M CTAB, λ_{ex} = 430 nm and λ_{em} = 740 nm.

In 0.1 M of the cationic surfactant CTAB, TMPyPHSE retains the broad fluorescence peak seen in pure water (Figure 6.8), attributed to the lack of interaction between the cationic molecule and cationic micelle. This supports the hypothesis that the interaction of the porphyrin with SDS is electrostatic in nature: the positive charge of CTAB causes no interaction with the central hydrogen atoms and repels the porphyrin due to its own positive charge.

The evidence of the porphyrin emission spectra in different surfactants supports the argument of dimerization as the porphyrin would be more inclined to aggregate or dimerise when surrounded by a similar charge, or aqueous conditions.

The negative charge associated with SDS causes the positive side pyridinium groups of the porphyrin to interact with the surfactant, weakening the formation of hydrogen bonds at the porphyrin core resulting in similar profiles as to the organic solvents.[30] This is consistent with previous findings for the fluorescence spectra of TMPyP. Whilst the porphyrin does not associate with the surfactant molecules in CTAB due to the positive charge, therefore, maintain the high affinity to the formation of hydrogren bonds as with measurements in water or neutral surfactants or buffers.

The fluorescence spectra for the tri-cationic free base porphyrin, TMPyPHSE, in both anionic and cationic surfactants are comparable with those of its tetra-cationic parent porphyrin, TMPyP.[30]

However, as seen by means of absorbance, TMPyPHSE obeys Beer's law indicating that there is no observed aggregation below concentrations 19.5 µM. Due to the intensity of the Soret band, $\varepsilon \sim 2.66\ 10^5\ M^{-1}\ cm^{-1}$, it is difficult to measure the extinction coefficient of this band at concentrations higher than ca. 20 µM, but it does make it possible to measure lower concentrations than most molecules.

Table 6.2 Fluorescence lifetime data recorded for TMPyPHSE in various aqueous solvents, λ_{ex} = 300 nm collecting the emission at 650 nm and for TMPyP reported in literature.[30]

Solvent	TMPyPHSE τ / ns	TMPyP τ / ns
Water	4.8 (±0.4)	5.4 (±0.5)
0.1 M SDS	10.1 (±1)	10.4 (±1)
0.1 M CTAB	4.3 (±0.5)	4.4 (±0.5)
0.1 M NaCl	4.6 (±0.4)	-

The other porphryin considered for conjugation to nanoparticles was ZnTMPyPHSE, so for comparison, the fluorescence spectra of the zinc-based porphyrin were recorded in both anionic and cationic surfactants to see if the emission behaviour resembled that observed with the metal free TMPyPHSE.

ZnTMPyPHSE with surfactant

In section 3.3, we saw the development of a calcium porphyrin nanosensor using ZnTMPyPHSE as the conjugated porphyrin. Zinc porphyrins are metalloporphyrins but unlike other transition metal containing porphyrins, the closed $3d^{10}$ shell of the zinc means that it does not couple significantly with the porphyrin. As a result some of the fluorescence characteristics of zinc containing porphyrins bear resemblance to that of the free base cationic porphyrins discussed above. Looking at the emission spectra for ZnTMPyPHSE this is evident from the broad emission peak seen ca. 700 nm, similar to that of TMPyPHSE.

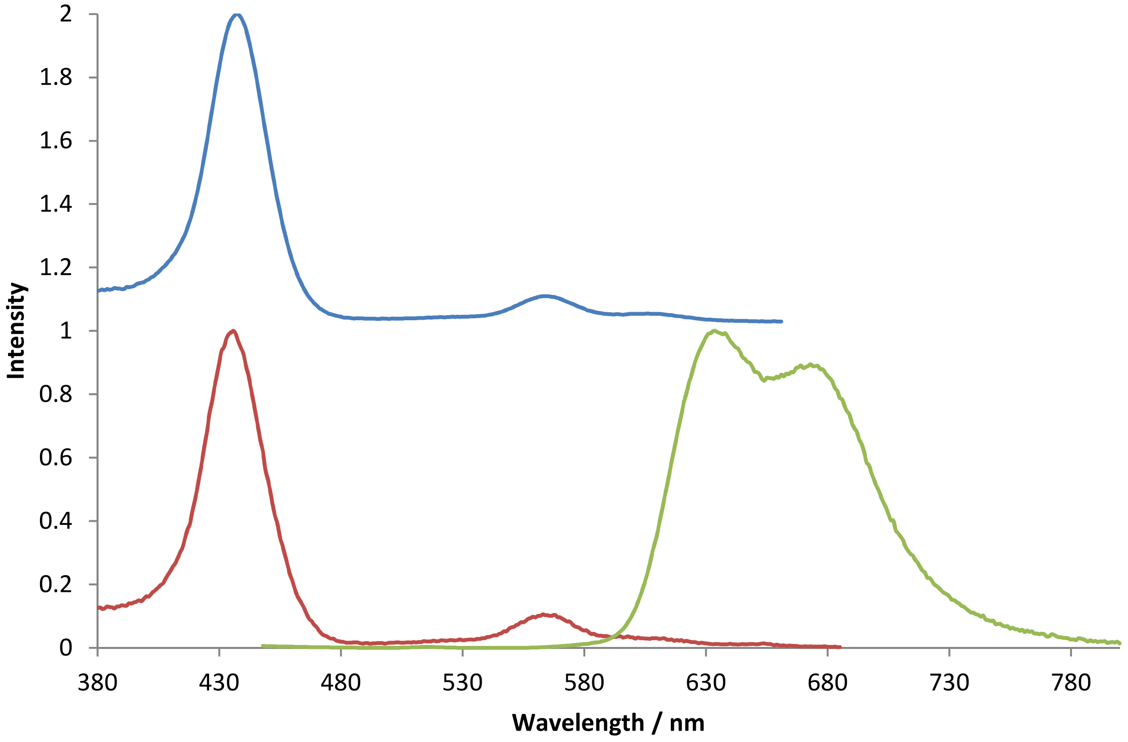

Figure 6.9 Normlalised absorption, emission and excitation spectra of ZnTMPyP in a solution of PBS buffer, λ_{ex} = 430 nm and λ_{em} = 700 nm

In the absorption spectrum in Figure 6.9 two peaks are seen in the Q-band region, reflective of the typical spectrum seen for metalloporphyrins. This is due to the d_{4h} symmetry found in metalloporphyrins whilst the d_{2h} symmetry of free base porphryins is responsible for the further splitting of the Q-bands into four peaks.[22]

Figure 6.10 shows the fluorescence spectra for ZnTMPyPHSE dissolved in both anionic and cationic surfactants. In both solutions, the fluorescence emission spectrum remains a broad band, much like in water and other aqueous solvents. This suggests that a contributing factor towards the characteristic fluorescence emission of TMPyP based porphyrins in water is their central hydrogen atoms as well as the argument for the porphyrin forming dimers in solution. These findings are consistent with previous research on the photophysical properties of ZnTMPyP.[106]

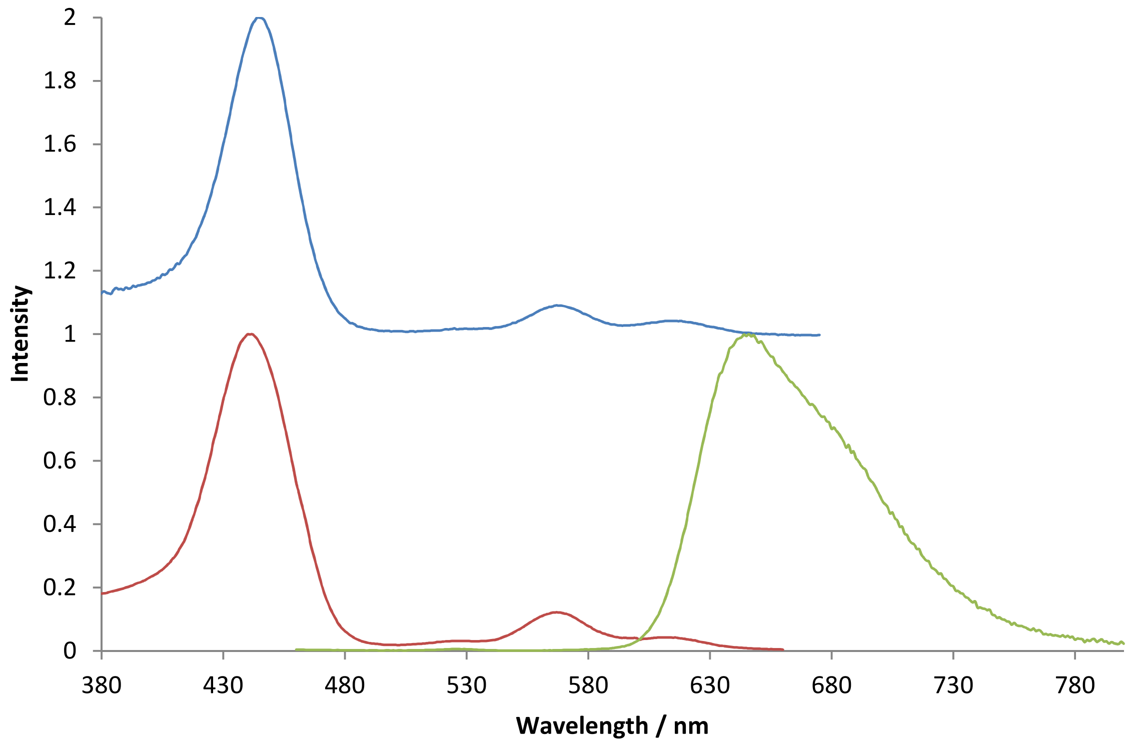

Figure 6.10 Normlalised absorption, emission and excitation spectra of ZnTMPyP in a solution of 0.1 M SDS and 0.1 M CTAB (appear as one spectrum as they were the same), λ_{ex} = 430 nm and λ_{em} = 740 nm.

6.2.4. TMPyPHSE conjugated to the nanoparticle surface

The next step after characterising the fluorescence of TMPyPHSE, was to conjugate the porphyrin to the surface of the polyacrylamide nanoparticles using the azide and alkyne functional groups to conjugate to the corresponding alkyne and azide functional groups on the nanoparticles via ‘click’ chemistry.

TMPyP was conjugated to the ‘surface’ of the PEBBLE nanostructure by click chemistry. In reality this is most likely not going to be a perfectly spherical particle with each porphyrin pointing out but a nanoparticle with uneven edges which may result in the porphyrin molecules pointing towards each other and to be trapped in clefts in the structure.

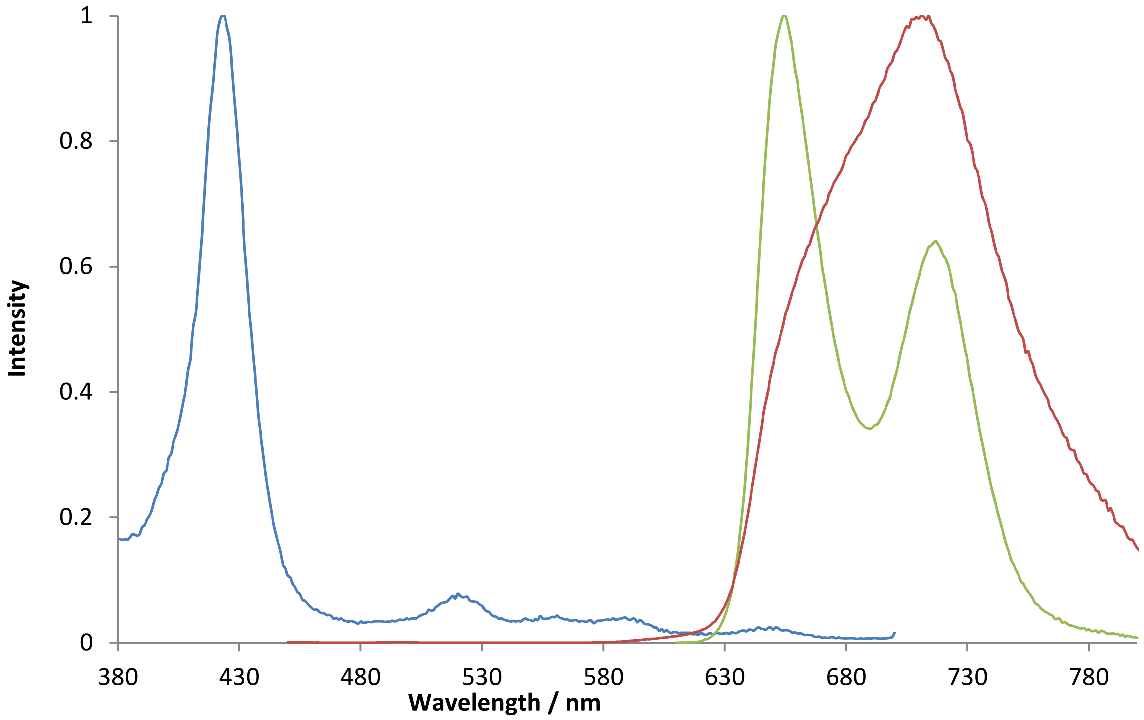

Figure 6.11 Normalized excitation (blue) and emission spectra of TMPyP (red) and NP-TMPyP (green) in PBS, λ_{ex} = 430 nm and λ_{em} = 740 nm.

Table 6.3 Tabulated fluorescence lifetime, emission and absorption data for TMPyP and NP-TMPyP in PBS

	Lifetime / ns	**Emission / nm**	**Absorption / nm**
Free TMPyP	4.8 ± 0.3 ns	716 (Broad)	425
NP-TMPyP	4.8 ± 0.3 ns	653, 715	425

When TMPyP is conjugated to the surface of the PEBBLE nanoparticle the double peak or band structured emission is observed much like in a non-aqueous environment, as seen in Figure 6.11. The overall emission spans the same region of the spectrum, 600 - 800 nm, but the broad band that is seen for the TMPyPHSE in all aqueous solvents or solutions reverts to the two band emission characteristic of most other poprhyrins or TMPyP in organic solvents. Another similarity in the emission spectrum for nanoparticle bound TMPyPHSE, is that of the porphyrin in a solution of the anionic surfactant, SDS.

6.2.4.1. Singlet oxygen: quantum yield measurements

Singlet oxygen ($^1\Delta_g$) measurements were run using D_2O as a solvent as the lifetime of singlet oxygen is longer in D_2O, 60µs, than in water, 4µs, making it easier to measure and monitor its quantum yield.

Table 6.4 Singlet oxygen quantum yields of TMPyP and NP-TMPyP in a solution of PBS

Sample	ΦΔ
TMPyP	0.64 ± 0.06
NP-TMPyP	0.30 ± 0.03

The singlet oxygen quantum yield value calculated for TMPyP in D_2O is comparable to the literature value of 0.74 in H_2O.[107]

The singlet oxygen quantum yield for the porphyrin attached to the nanoparticle is effectively half that of the porphyrin in solution. This can be attributed to the presence of the polymer matrix and the fact that it will enhance the non-radiative decay of the excited states due to dye-matrix interactions and limit access to the excited state of the porphyrin by the molecular oxygen.

6.3. Concluding remarks

The results obtained for TMPyP confirm more the notion that the porphyrin undergoes aggregation of some sort e.g. dimerization in an aqueous solution state. This is seen in the distinct emission bands observed when TMPyP is conjugated to the polyacrylamide nanoparticle.

As stated before, previous authors have reported the fluorescence properties of TMPyP and debated the effect seen as being either due to aggregation (or dimerization) or charge-transfer of the positively charged porphyrin.

An interesting addition to this is what was seen when conjugating the TMPyP derivative TMPyPHSE to the nanoparticle matrix. Figure 6.11 illustrates that this causes the porphyrin to revert back to the two peak emission band but in aqueous solutions which is also seen in a solution of anionic surfactant. Both of these situations would prevent aggregation or dimerization in solution as with the nanoparticles the porphyrins will be held in position, the possibility of their forming a dimer being very low. For the anionic surfactant this is also true as the anionic charge would reduce the chance for porphyin stacking and the formation of hydrogen bonds with the water molecules.

7. Nanoparticles for oxygen sensing

The next step in this project was to demonstrate further the versatility of the PEBBLE structure and nature by developing a different sensing system. The work in this chapter can be found in the paper published in April 2014.[108]

Regenerative medicine advancements have resulted in an increase in research for oxygen measurement and detection.[109] Cells need to have access to oxygen in order to regenerate tissue and therefore being able to know and sense the level of oxygen present is important for the regrowth of cells.[110] A common failure in cell regeneration being the development of hypoxic regions in the body.[110]

A variety of techniques have been developed, one which has gained much interest in recent times being optical imaging and sensing.[111, 112] Up until recently, the most popular method for detecting oxygen concentrations has been via amperometry.[113-115] An amperometric oxygen measurement using a Clark-type electrode monitors the reduction of oxygen at the cathode resulting in a current proportional to the concentration of oxygen. The disadvantage of this method is the life of the detector along with the slow response of the measurements. There is also significant signal drift due to the presence of other ions.[116]

The introduction of an optical sensor for oxygen measurements removes some of these disadvantages. This method relies on the quenching of the excited triplet state of phosphors by ground state molecular oxygen. In the absence of oxygen the molecules generally phosphoresce, and by monitoring changes in the triplet lifetime and emission intensity the rate of oxygen quenching and hence the oxygen concentration can be monitored.

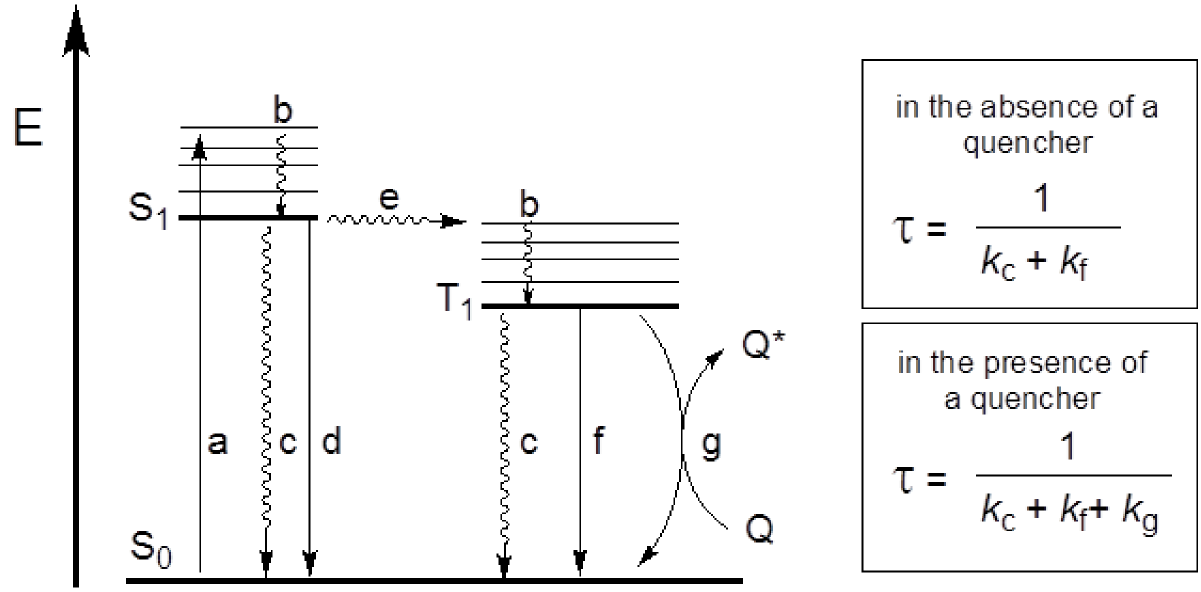

Figure 7.1 Modified Jablonski diagram: **S_0:** lowest energy singlet state (ground state); **S_1:** lowest excited singlet state; **T_1:** lowest excited triplet state; **Q:** ground state quencher; **Q*:** excited state quencher; **a:** absorption; **b:** internal conversion; **c:** non-radiative dissipation; **d:** fluorescence emission; **e:** inter-system crossing; **f:** phosphorescence emission; **g:** collisional triplet state deactivation; k_c, k_f, k_g: rate constants for processes **c**, **f**, and **g**, respectively.

Among various phosphors for oxygen sensing, which mainly fit into the category of organic transition metal complexes, the platinum and palladium porphyrin complexes are found to be highly efficient emitters that show good sensitivity towards oxygen.[117-120] Complexes of these metals are found to have high phosphorescent quantum yields, long triplet lifetimes and a large Stokes shift. These properties all lend themselves to being good oxygen sensors as they will be sensitive to the concentration of oxygen even at low concentrations.

A good biological oxygen sensor would be non-toxic and water soluble so as to be used safely and easily in a biological environment. A benefit to the design would also be for it to have adaptable functionality to conjugate to a support framework to introduce into the environment.

Previous work on PEBBLEs has shown that different functional group enable the attachment of other molecules to the surface of the nanoparticles. The work from collaborators in Hull showed the versatility of this, including the ability to attach two different molecules to one surface.[121] Due to this knowledge and research of attaching molecules, in particular porphyrins (photosensitising agents), to the surface of the nanoparticle matrix it was decided to develop probes containing palladium and platinum porphyrins, using their well-known phosphorescent properties to synthesise oxygen sensitive nanoparticles.

Further to this, the porphyrins would need to be water-soluble and the idea was to develop a range of palladium and platinum poprhyrins, with cationic and anionic functionality that could be bound to nanoparticles.

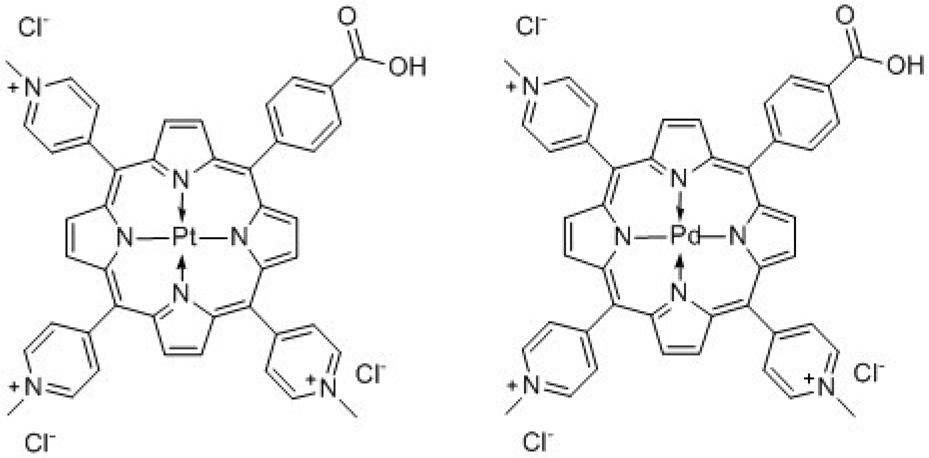

Figure 7.2 Chemical structures of cationic water soluble metalloporphyrins; platinum centred on the left and palladium on the right

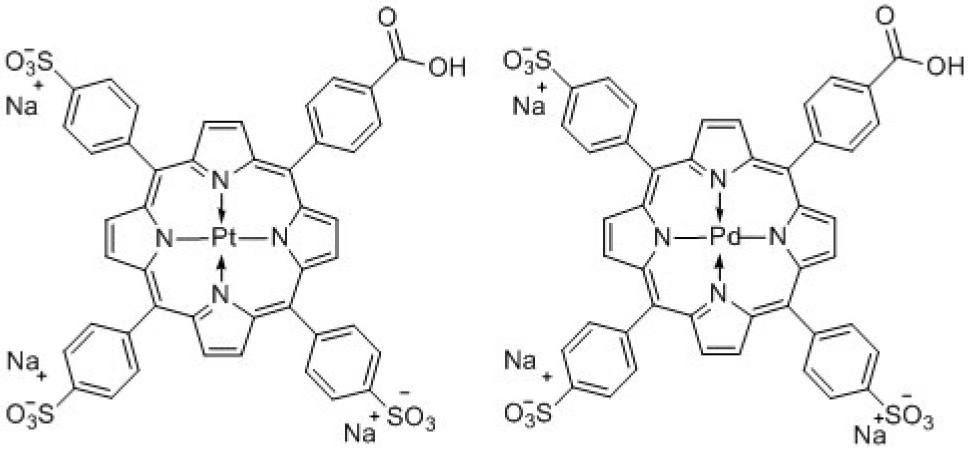

Figure 7.3 Chemical structures of anionic water soluble metalloporphyrins; platinum centred on the left and palladium on the right

The porphyrins designed and synthesised were to be water soluble with the means for efficient 'click' chemistry for attaching to either alkyne or azide functionalised PEBBLEs. This is the same method used for the conjugation of porphyrins to the nanoparticles as with the porphyrin nanosensors previously discussed in section 4.

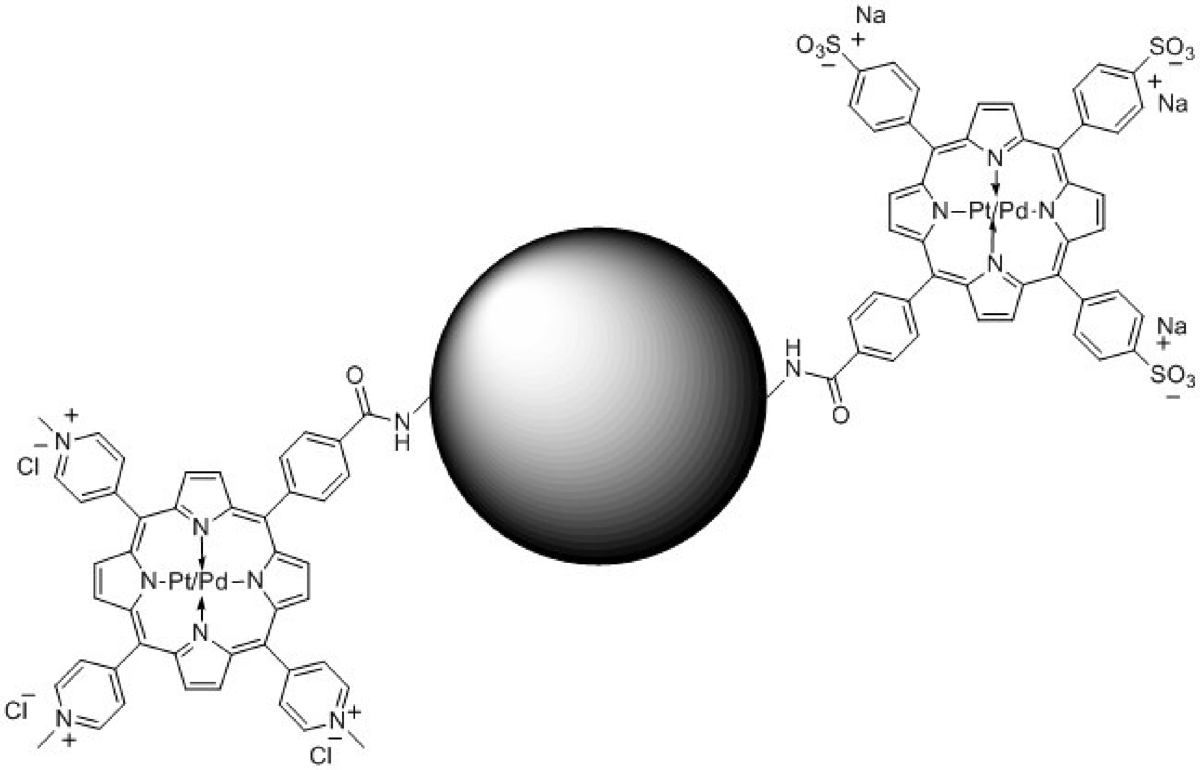

Figure 7.4 Diagram to show chemical structures of the anionic and cationic palladium and platinum porphyrins conjugated to the polyacrylamide nanoparticle

The photophysical properties of the porphyrins and their respective nanoconjugates in this section were studied concentrating specifically on their dependence on oxygen concentration. The collisional quenching of phosphorescence can be described by the Stern-Volmer relationship (Equation 7.1 and Equation 7.2); stating that the ratio between the triplet lifetime in both the absence and the presence of the quencher is proportional to that of the concentration of the quencher.[2]

$$\frac{F_0}{F} = \frac{\tau_0}{\tau} = K_{sv}\,[\mathrm{Q}] + 1 \text{ (where: } K_{sv} = \tau_0 k_{\mathrm{Q}})$$

Equation 7.1. Stern Volmer equation

Substitution of the lifetime input in the Stern-Volmer equation with that of the phosphorescence intensity recorded (I_0/I or F_0/F), where it also represents the quenching of the phosphorescence, is also possible for Stern-Volmer analysis.

$$\frac{1}{\tau} = \frac{1}{\tau_0} + k_{\mathrm{Q}}\,[\mathrm{Q}]$$

Equation 7.2 Stern-Volmer type analysis used to process the data to obtain the bimolecular quenching constants

The bimolecular quenching constant represents the efficiency of the quenching process of the accessibility the fluorophore has to the quencher. Lacowicz explains that typical values of k_{Q} for diffusion-controlled quenching in fluid solution are around the order of 1×10^{10} $\mathrm{M^{-1}\,s^{-1}}$.[2] Values of k_{Q} smaller than this can be a result of shielding of the fluorophore or a general low quenching efficiency.

The oxygen sensitive measurements throughout this section were processed and analysed by means of the Stern-Volmer relationship in order to determine the various molecules' efficiency as a quencher and thus a sensor of the concentration of oxygen. By obtaining a linear plot of the reciprocal of the measured phosphorescence lifetimes versus the relative oxygen concentration, the gradient of the graph allows the bimolecular quenching rate constant (k_{Q}) to be determined.

Thus, from both the above equations, the Stern-Volmer relationship can be determined by plotting the ratio of τ_0/τ and the ratio of I_0/I against the concentration of oxygen with the slope of the plot giving rise to the Stern-Volmer constant (K_{sv}). In addition to this the same data can be used to extrapolate the bimolecular quenching rate constant by plotting $1/\tau$ against the concentration of the quencher, oxygen.

7.1. 5-(4-Methoxycarbonylphenyl)-10,15,20-tris(4-methylpyridinium)porphyrinato palladium (II) trichloride (PdTMPyP)

This section contains the spectra of the cationic metalloporphyrin PdTMPyP (Figure 7.5). All measurements were recorded in both water and PBS buffer.

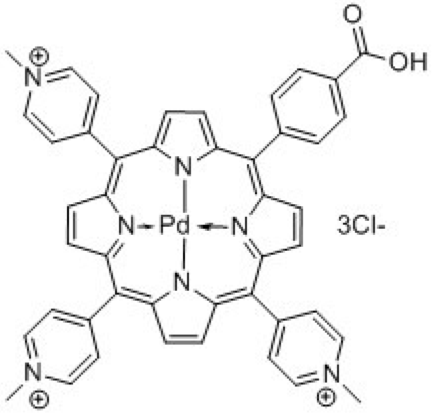

Figure 7.5 Chemical structure of PdTMPyP

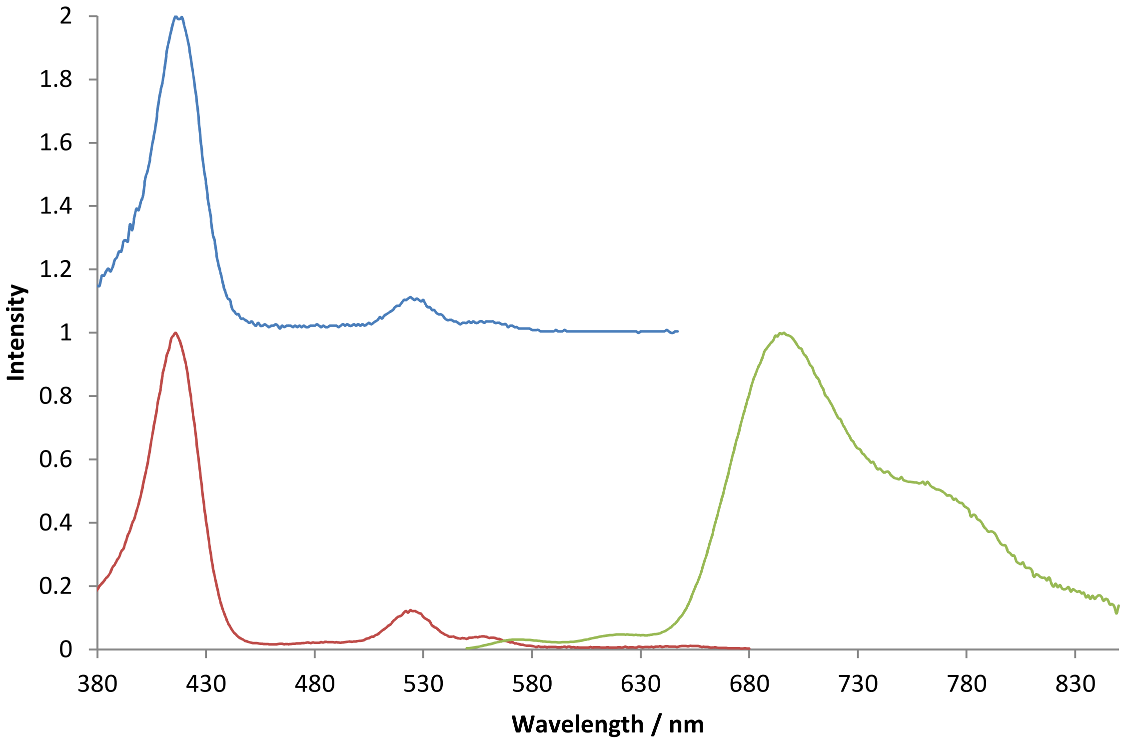

Figure 7.6. Normalized absorption, excitation and emission spectra of PdTMPyP recorded in PBS, λ_{ex} = 430 nm and λ_{em} = 700 nm.

The absorption, emission and excitation spectra in Figure 7.6 were recorded in a degassed solution of water illustrating both the water-soluble nature and phosphorescent characteristics of the porphyrin. In both the absorption and excitation spectra the characteristic intense Soret band between 400 and 420 nm is seen along with two Q-bands around 500 nm. The emission consists of a peak in the red around 700 nm with the typical shoulder further towards the red section of the spectrum ≈ 760 nm. The data for this are recorded in comparison with the other platinum and palladium porphyrins on Table 7.5 in section 7.5.

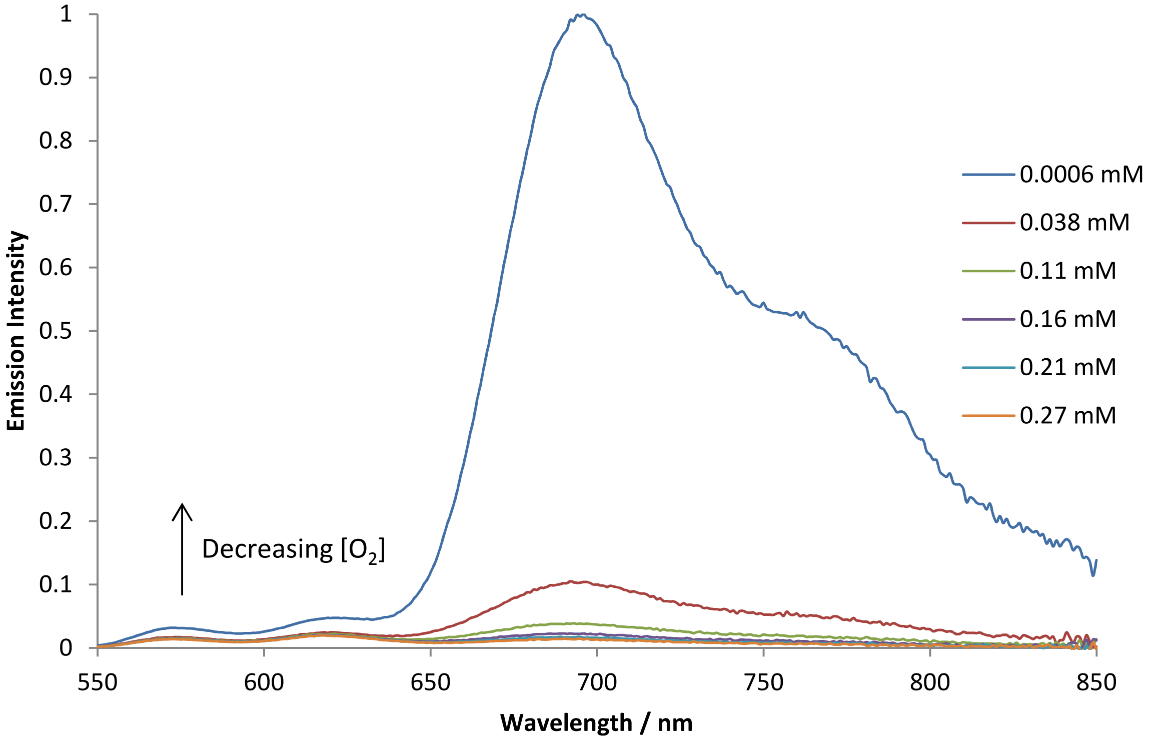

Figure 7.7. Normalised emission spectra of PdTMPyP at various concentrations of oxygen (shown in legend) and normalized to the measurement recorded in a degassed solution, recorded in PBS, λ_{ex} = 430 nm.

The potential oxygen sensing properties of PdTMPyP were recorded by measuring both the phosphorescence emission and lifetimes of the porphyrin at various concentrations of oxygen. Figure 7.7 shows the emission of the cationic palladium porphyrin measured at various oxygen concentrations, visually demonstrating its sensitivity to oxygen in aqueous solution between partial pressures of oxygen in the range 1.69 to 760 mmHg, corresponding to oxygen concentration of 0. 6 – 270 µM.

The phosphorescence lifetimes recorded show a linear relationship to the oxygen concentration as shown in the plot in Figure 7.8 with the gradient giving a value for k_Q of 2.5×10^9 M^{-1} s^{-1}.

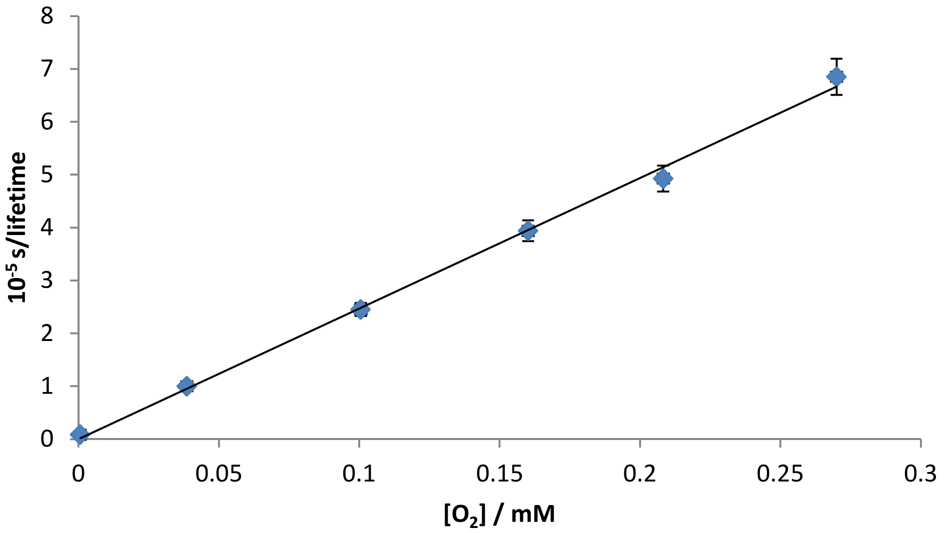

Figure 7.8 Scatter plot for the phosphorescent lifetimes of PdTMPyP, $10^{-6}/\tau$ plotted as a function of the concentration of oxygen present. 10^{-5}/lifetime = $24.6[O_2] + 0.01$.

The phosphorescence lifetime of PdTMPyP ranges from 1.5 µs to 120 µs in an air saturated and degassed solution respectively. These data are shown graphically in Figure 7.8 with $10^{-6}/\tau$ as a function of the concentration of oxygen in mM in the sample. Table 7.1 shows the raw lifetime values calculated from the measurements recorded at the different concentrations of oxygen.

The bimolecular quenching constant for PdTMPyP can be determined from the gradient of Figure 7.8 using Equation 7.2 on page 119 which is derived from the Stern-Volmer relationship (Equation 7.1 also on page 119).

Table 7.1. Recorded phosphorescence lifetime data for samples of PdTMPyP recorded in PBS containing various concentrations of oxygen.

$[O_2]$ / mM	τ / µs
0.0006	120.0
0.038	10.0
0.11	4.1
0.16	2.5
0.21	2
0.27	1.5

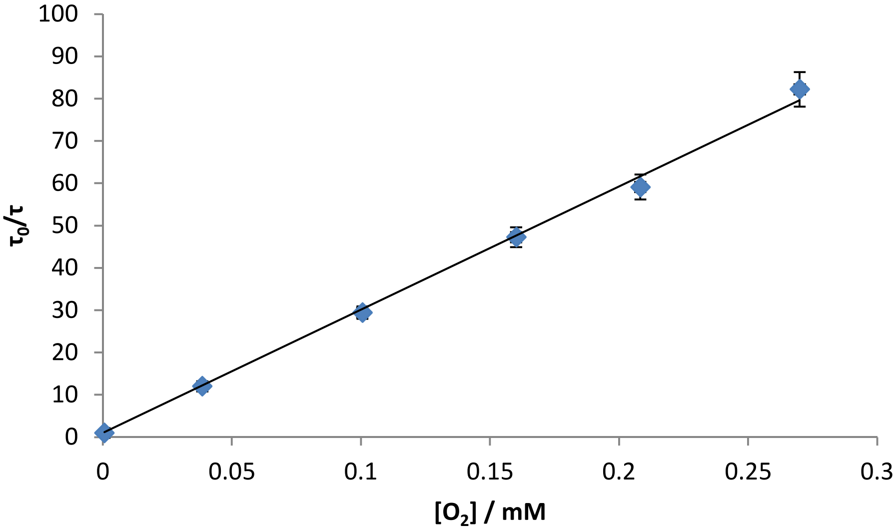

Figure 7.9 Stern-Volmer plot for the phosphorescent lifetimes of PdTMPyP, τ_0/τ plotted as a function of the concentration of oxygen present. $\tau_0/\tau = 295.3\ [O_2] + 1$.

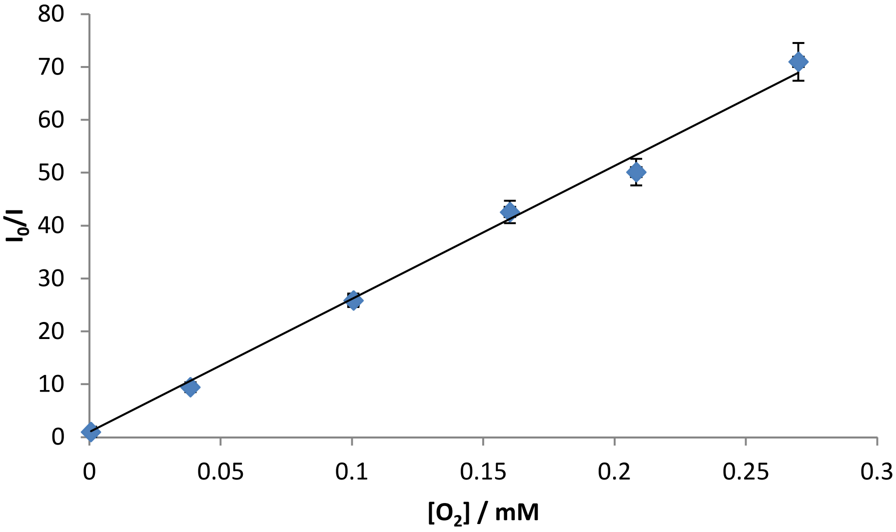

Figure 7.10 Stern-Volmer plot for the phosphorescent lifetimes of PdTMPyP, I_0/I plotted as a function of the concentration of oxygen present. $I_0/I = 278.2\ [O_2] + 1$.

Figure 7.9 and Figure 7.10 show the lifetime and intensity Stern-Volmer plots, respectively, where the value for K_{SV} can be obtained from each plot. They yield values which are in good agreement with each other (2.3×10^5 and 2.8×10^5 M^{-1} respectively). This indicates that the predominant pathway for relaxation from the triplet state for PdTMPyP is due to dynamic quenching of the phosphorescence by oxygen.

The data in this section indicate the useful oxygen sensing properties that would be expected for a palladium porphyrin. In addition to the oxygen sensing properties, its high solubility in water indicate the potential it holds as a water soluble oxygen sensor. All photophysical data are compared at the end of this section along with the other platinum and palladium metalloporphyrins.

7.2. 5-(4-Methoxycarbonylphenyl)-10,15,20-tris(4-methylpyridinium)porphyrinato platinum (II) trichloride (PtTMPyP)

The section contains the spectra of the cationic metalloporphyrin PtTMPyP (Figure 7.11). All measurements were recorded in both water and PBS and the same measurements as for PdTMPyP in section 7.1 were repeated for comparison. The peripheral functional groups on the porphyrin are identical to those for PdTMPyP in section 7.1 with only the central metal atom changed.

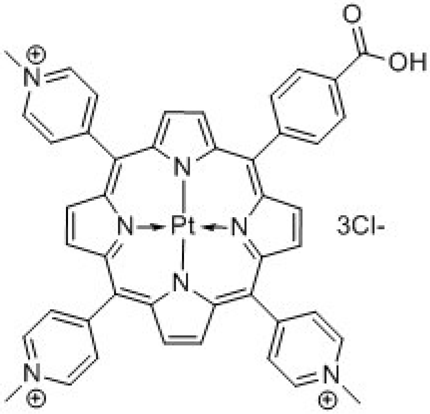

Figure 7.11 Chemical structure of PtTMPyP

As with PdTMPyP, the platinum derivative easily dissolved in both water and PBS buffer. The spectra recorded in PBS, Figure 7.12, indicate again the characteristic intense Soret band centred around 400 nm with two distinctive Q-bands attributed to metalloporphyrins. In the emission spectrum a central band ≈ 680 nm can be seen with a small shoulder towards the red around 720 nm.

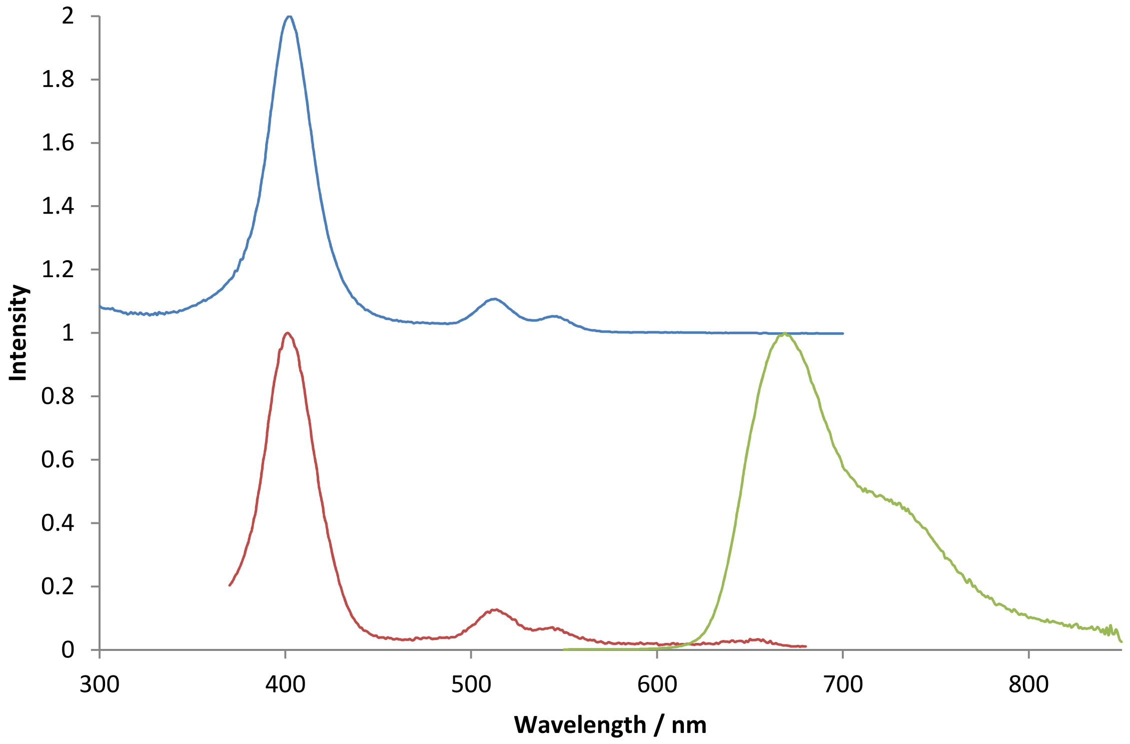

Figure 7.12 Normalized absorption, excitation and emission spectra of PtTMPyP recorded in PBS at atmospheric pressure, λ_{ex} = 440 nm and λ_{em} = 700 nm.

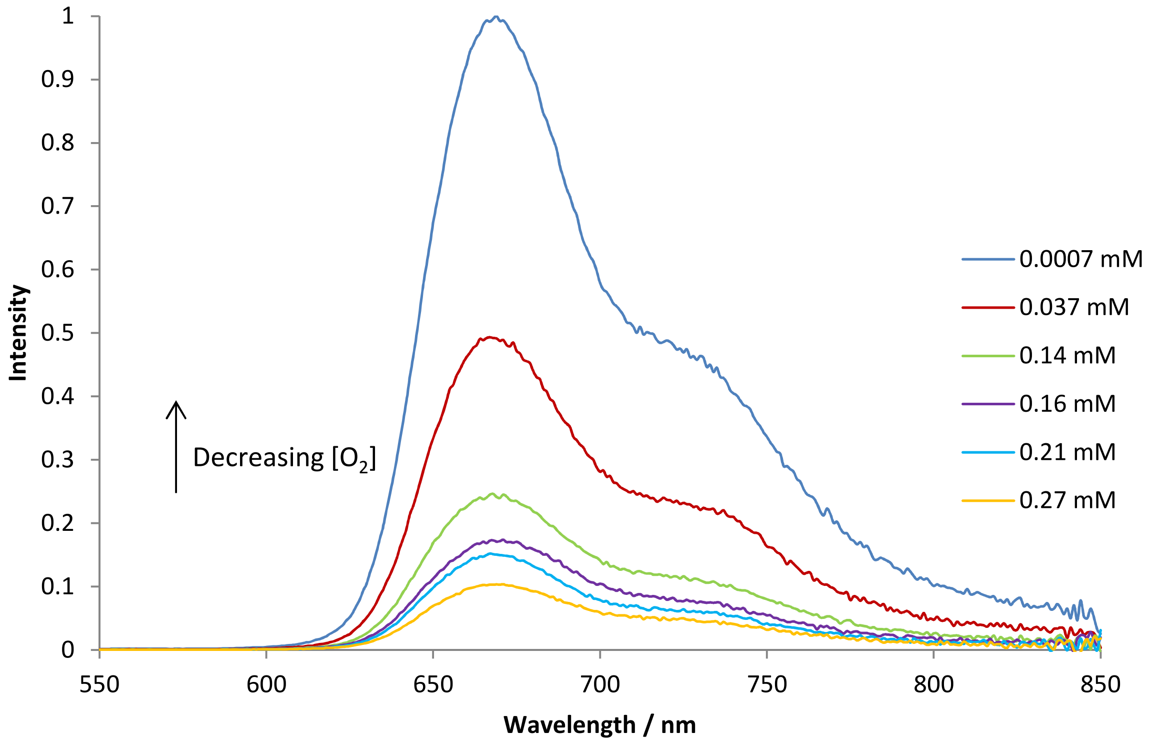

Figure 7.13 Normalised emission spectra of PtTMPyP at various concentrations of oxygen and normalized to the measurement recorded in a degassed solution, recorded in PBS, λ_{ex} = 440 nm.

Triplet lifetime measurements were carried out for PtTMPyP to calibrate its sensitivity to oxygen. Initial measurements indicated a much shorter phosphorescent lifetime than its corresponding palladium derivative. This reflects the metals in question as literature shows longer lifetimes observed for palladium porphyrin than the platinum equivalent derivative.[122]

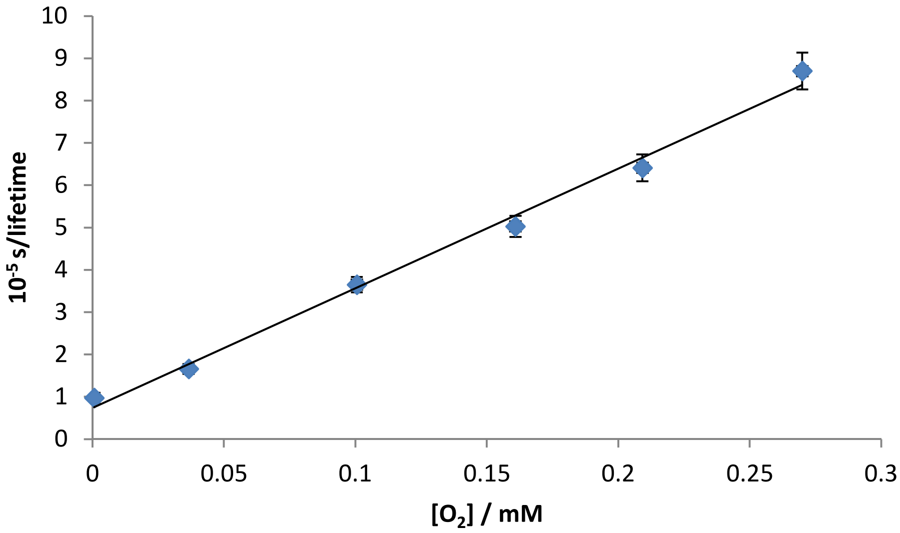

Figure 7.14. Scatter plot for the phosphorescent lifetimes of PtTMPyP, $10^{-6}/\tau$ plotted as a function of the concentration of oxygen present. 10^{-5}/lifetime = $28.2[O_2] + 0.07$.

A linear relationship was seen between the lifetime and the concentration of oxygen present shown in the 10^{-6}/lifetime vs $[O_2]$ Stern-Volmer plot in Figure 7.14. This enabled a quenching constant of 2.8×10^9 M^{-1} s^{-1} to be extrapolated. The lifetimes calculated shown in Table 7.2 confirms the shorter lifetimes (1.2 μs in aerated solution to 10.3 μs in a degassed solution) that were expected from the heavier platinum porphyrin in comparison to a palladium complex.

The phosphorescence lifetimes recorded show a linear relationship to the oxygen concentration as shown in the plot in Figure 7.14 with the gradient giving a value for k_Q of 2.8×10^9 M^{-1} s^{-1}.

Table 7.2. Recorded phosphorescence lifetime data for samples of PtTMPyP recorded in PBS containing various concentrations of oxygen.

$[O_2]$ / mM	τ / µs
0.0007	10.3
0.037	6.0
0.14	2.7
0.16	2.1
0.21	1.6
0.27	1.2

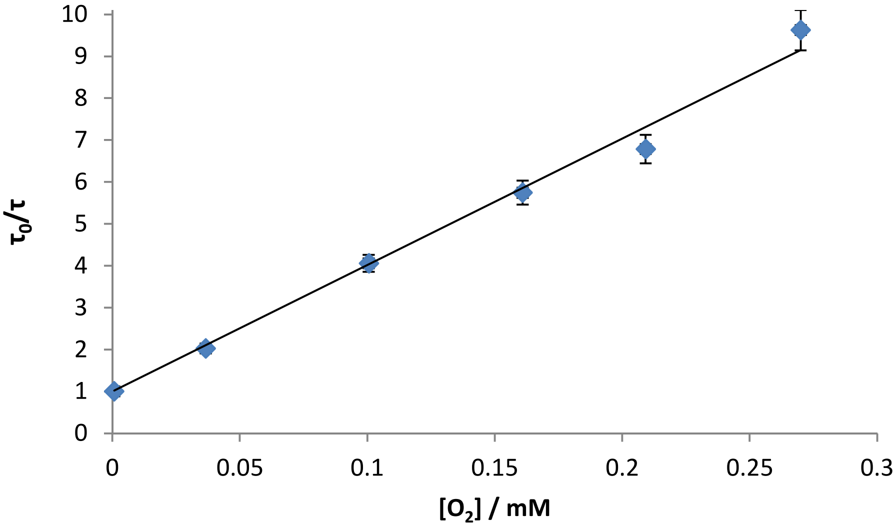

Figure 7.15 Stern-Volmer plot for the phosphorescent lifetimes of PtTMPyP, τ_0/τ plotted as a function of the concentration of oxygen present. $\tau_0/\tau = 30.4\,[O_2] + 1$.

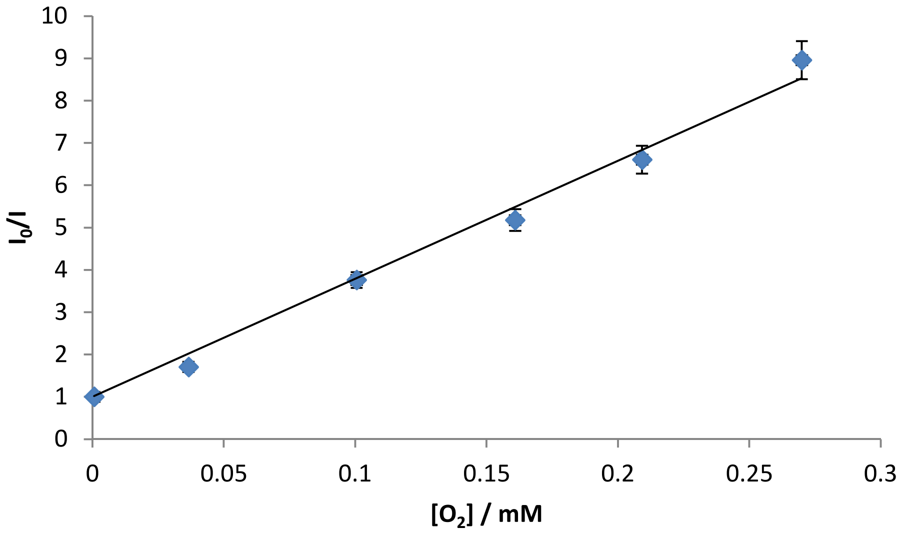

Figure 7.16 Stern-Volmer plot for the phosphorescent lifetimes of PtTMPyP, τ_0/τ plotted as a function of the concentration of oxygen present. $I_0/I = 29.0\ [O_2] + 1$.

The Stern-Volmer plots for PtTMPyP are shown with respect to the phosphorescent lifetime in Figure 7.16 and the emission intensity in Figure 7.15 where the value obtained in each for K_{SV} is in good agreement with the other (3.4×10^4 and 2.9×10^4 M^{-1} respectively). These results, along with the value obtained for k_Q of 2.8×10^9 M^{-1} s^{-1} indicate that the major pathway for triplet deactivation in the porphyrin PtTMPyP is caused from dynamic quenching of the phosphorescence by oxygen.

7.3. 5-(4-Carboxyphenyl)-10,15,20-tris(sulfonatophenyl) porphyrinato palladium (II) trisodium (PdTSP)

The section contains the spectra of the cationic metalloporphyrin PdTSPP (Figure 7.17). All measurements were recorded in both water and PBS and the same measurements as for PdTMPyP in section 7.1 were repeated for comparison.

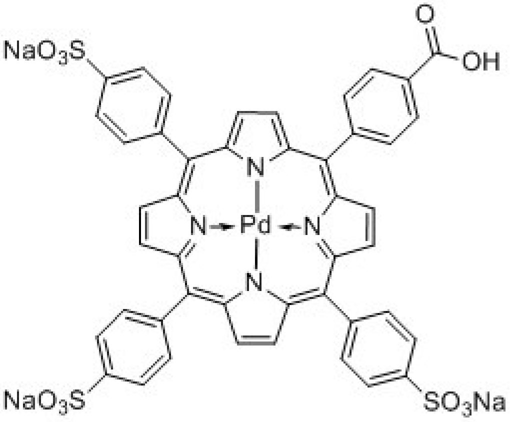

Figure 7.17 Chemical structure of PdTSPP

The palladium derivative of the anionic porphyrin (PdTSP) also dissolved readily in water and PBS buffer. The characteristic Soret band and two Q-bands for a metalloporphyrin are seen in Figure 7.18. The Soret band centred around 410 nm with the Q-bands in the 500 – 580 nm region. The emission band shows a strong peak at 700 nm with a shoulder further to the red at 765 nm. The emission profile recorded at varying concentrations is shown in Figure 7.19 which indicates the oxygen dependent phosphorescence.

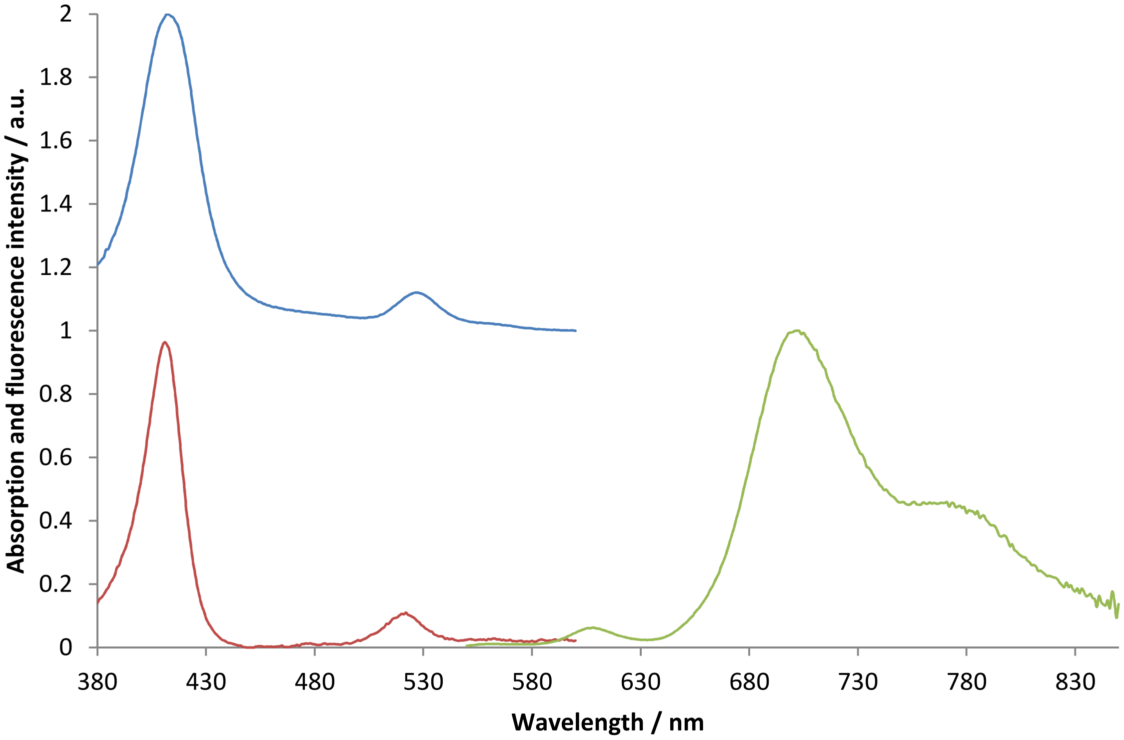

Figure 7.18 Normalized absorption, excitation and emission spectra of PdTSPP recorded in a degassed solution of PBS, λ_{ex} = 430 nm and λ_{em} = 680 nm.

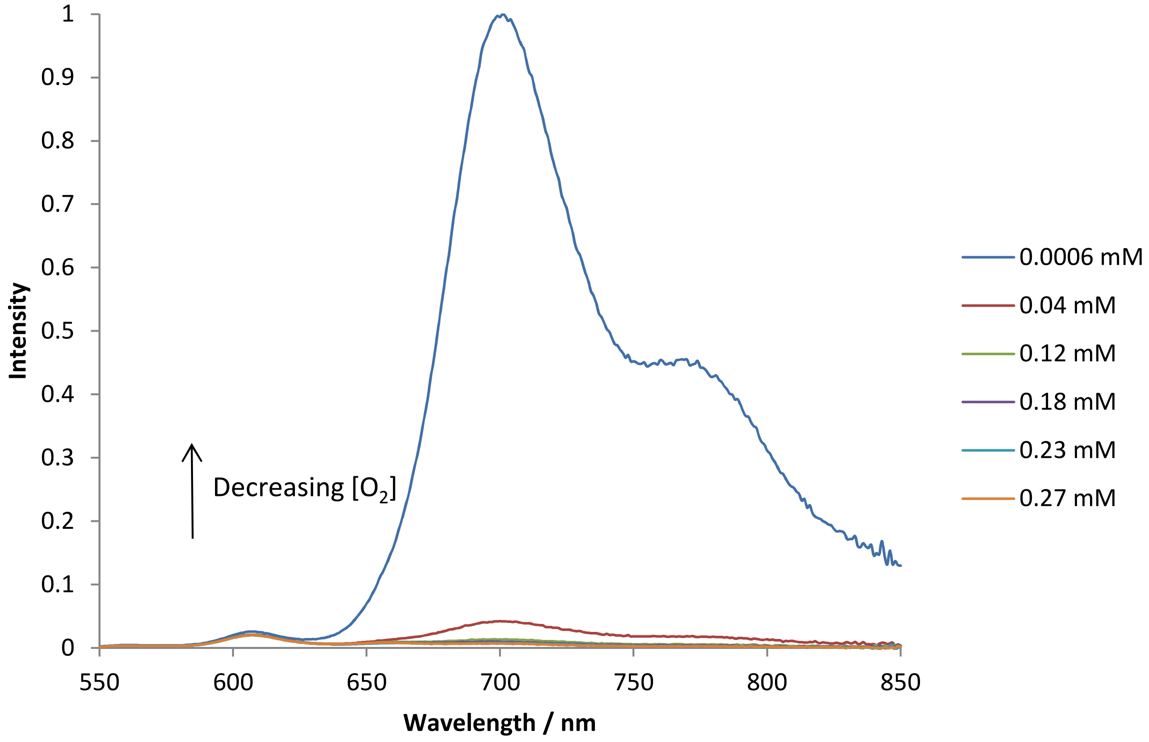

Figure 7.19 Normalised emission spectra of PdTSPP at various concentrations of oxygen and normalized to the measurement recorded in a degassed solution, recorded in PBS, λ_{ex} = 430 nm.

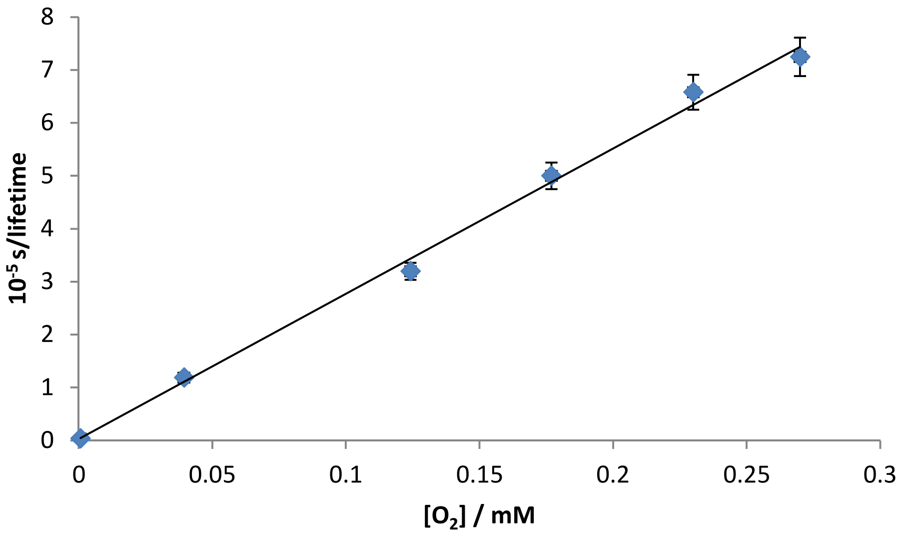

Figure 7.20 Scatter plot for the phosphorescent lifetimes of PdTSPP, $10^{-6}/\tau$ plotted as a function of the concentration of oxygen present. 10^{-5}/lifetime = 27.3[O_2] + 0.01.

Measurements shown in Figure 7.19 and Figure 7.20 illustrate the oxygen sensitive nature of the emission of PdTSPP. The data recorded in Table 7.3 shows that PdTSPP exhibits a long phosphorescent lifetime of 294 μs as with PdTMPyP in degassed solutions And a good linear relationship can be seen in Figure 7.20 for $10^{-6}/\tau$ vs $[O_2]$ giving a quenching constant of 2.7×10^{9} M^{-1} s^{-1}.

Table 7.3 Recorded phosphorescence lifetime data for samples of PdTSPP recorded in PBS containing various concentrations of oxygen.

$[O_2]$ / mM	τ / μs
0.0006	294.0
0.039	8.4
0.12	3.2
0.18	2.0
0.23	1.5
0.27	1.4

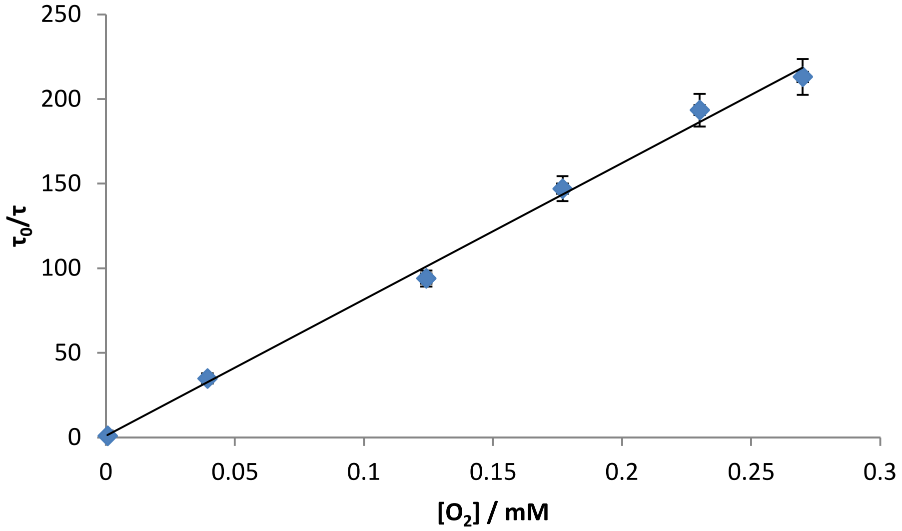

Figure 7.21 Stern-Volmer plot for the phosphorescent lifetimes of PdTSPP, τ_0/τ plotted as a function of the concentration of oxygen present. $\tau_0/\tau = 806.9\,[O_2] + 1$.

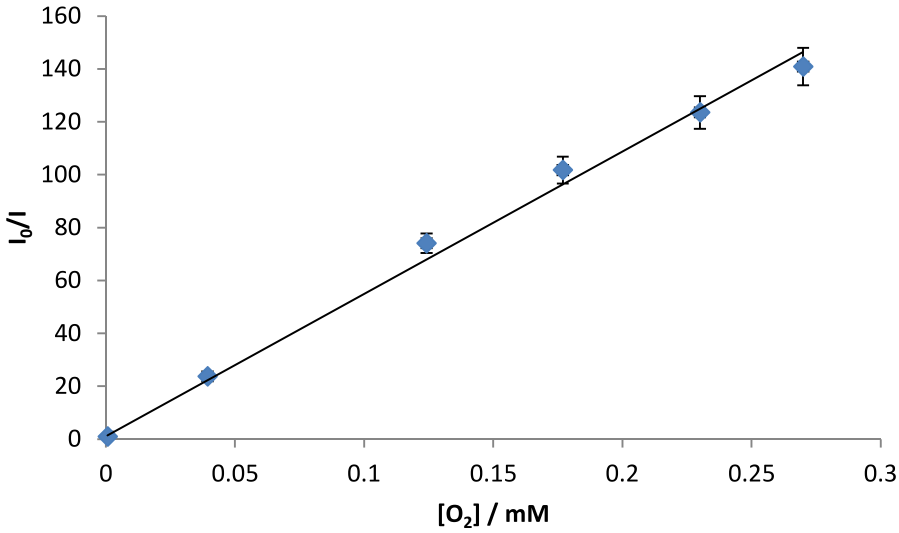

Figure 7.22 Stern-Volmer plot for the phosphorescent lifetimes of PdTSPP, I_0/I plotted as a function of the concentration of oxygen present. $I_0/I = 525.6\ [O_2] + 1$.

Figure 7.21 and Figure 7.22 show the lifetime and intensity Stern-Volmer plots, respectively, where the value for K_{SV} can be obtained from each plot. They yield values which are in relatively good agreement with each other (8.0×10^5 and $5.2 \times 10^5\ M^{-1}$ respectively). This indicates that the predominant pathway for relaxation from the triplet state for PdTSPP is due to dynamic quenching of the phosphorescence by oxygen.

7.4. 5-(4-Carboxyphenyl)-10,15,20-tris(sulfonatophenyl)porphyrinato platinum (II) trisodium (PtTSPP)

The section contains the spectra of the cationic metalloporphyrin PtTSPP (Figure 7.23). All measurements were recorded in both water and PBS and the same measurements as for PdTMPyP in section 7.1 were repeated for comparison.

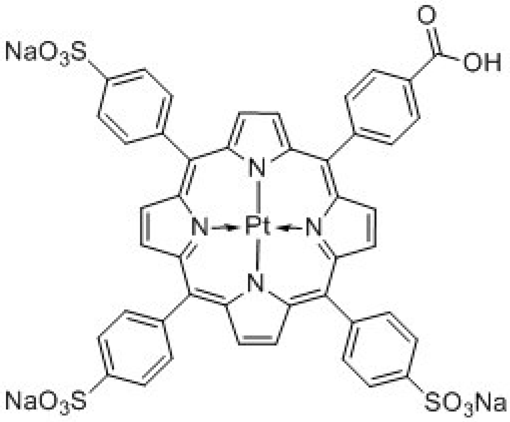

Figure 7.23 Chemical structure of PtTSPP

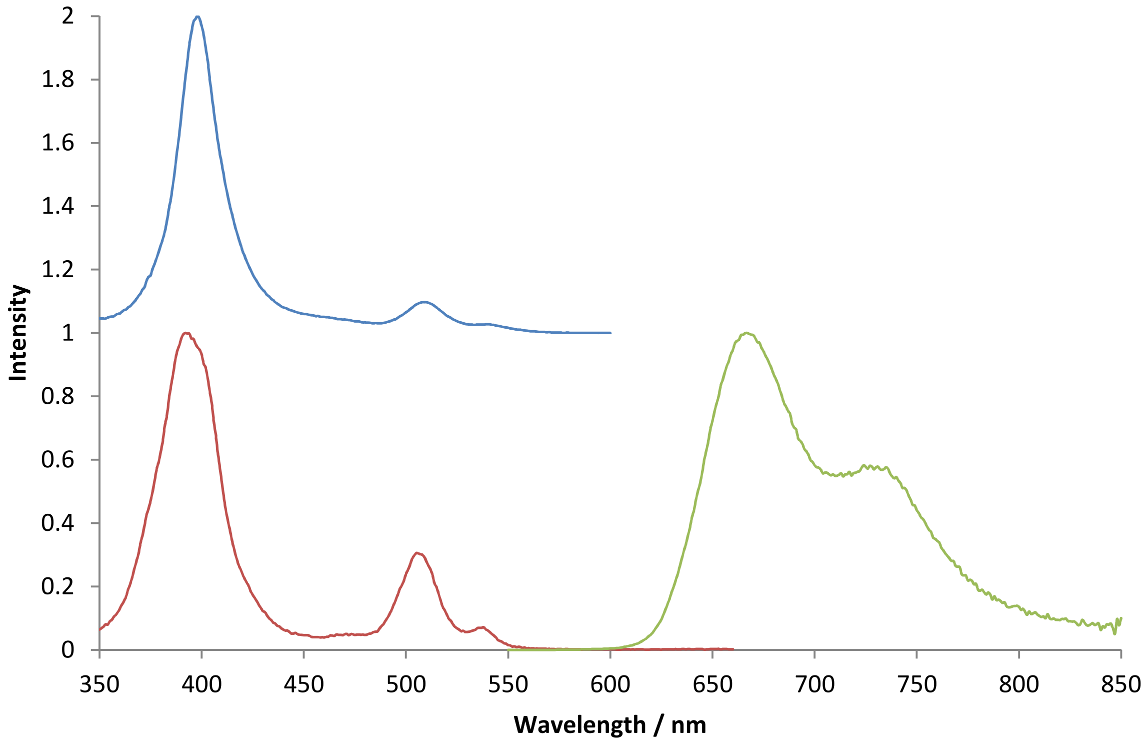

Figure 7.24 Normalised absorption, excitation and emission spectra of PtTSPP recorded in a degassed solution of PBS, λ_{ex} = 510 nm and λ_{em} = 660 nm.

The absorption spectra of PtTSPP in Figure 7.24 shows the characteristic strong Soret band centred around 400 nm with two weaker Q-bands around 500 nm that would expected for a platinum based porphyrin. Likewise the emission spectrum recorded in a degassed solution of PBS in Figure 7.24 shows a two-peak band with a stronger peak around 670 nm and a weaker shoulder around 720 nm as seen with PtTMPyP.

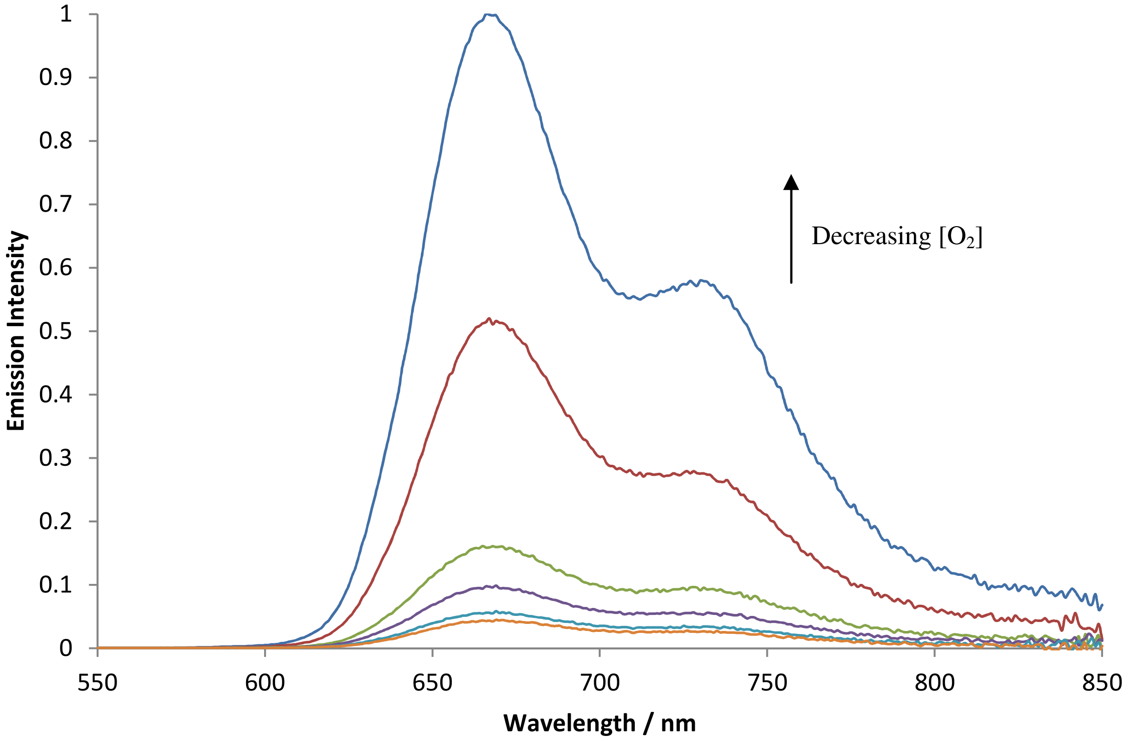

Figure 7.25 Nornalised emission spectra of PtTSPP at various concentrations of oxygen and normalized to the measurement recorded in a degassed solution, recorded in PBS, λ_{ex} = 510 nm.

The emission spectra recorded at varying oxygen concentration in Figure 7.25 indicates the oxygen sensitivity of the porphyrin and is consistent with the other poprhyrins in this chapter.

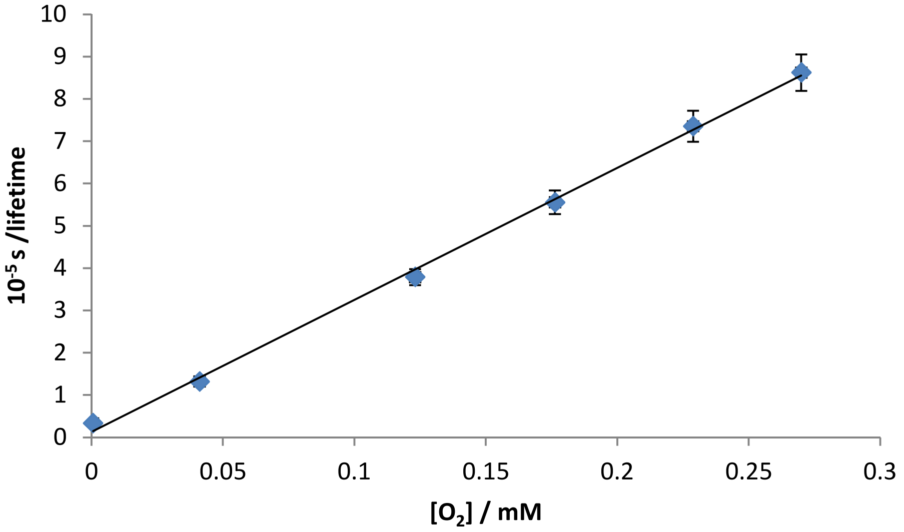

Figure 7.26 Scatter plot for the phosphorescent lifetimes of PtTSPP, $10^{-6}/\tau$ plotted as a function of the concentration of oxygen present. 10^{-5}/lifetime = 31.2[O_2] + 0.13.

Phosphorescence lifetime measurements were recorded at varying concentrations of oxygen in order to determine the sensitivity of the porphyrin to oxygen. The phosphorescent lifetime in degassed solution was recorded as being 29.9 μs which is similar to the measurements of PtTMPyP and previous findings for platinum porphyrins.[123] As with the other porphyrins in this chapter, good linearity is observed between the relationship of $10^{-6}/\tau$ vs $[O_2]$ in the sample which indicates good behaviour as an oxygen sensor and a value of 3.1×10^9 M^{-1} s^{-1} was determined for extrapolated for k_Q. The data for the phosphorescence lifetimes recorded at each concentration of oxygen can be seen below in Table 7.4.

Table 7.4 Recorded phosphorescence lifetime data for samples of PtTSPP recorded in PBS containing various concentrations of oxygen.

$[O_2]$ / mM	τ / μs
0.0006	29.9
0.04	7.6
0.12	2.6
0.18	1.8
0.23	1.4
0,27	1.2

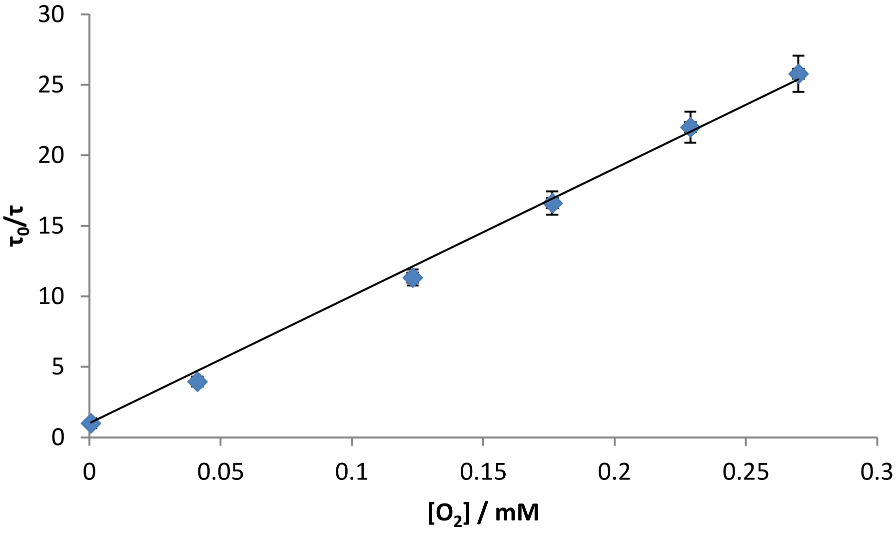

Figure 7.27 Stern-Volmer plot for the phosphorescent lifetimes of PtTSPP, τ_0/τ plotted as a function of the concentration of oxygen present. $\tau_0/\tau = 93.0\ [O_2] + 1$.

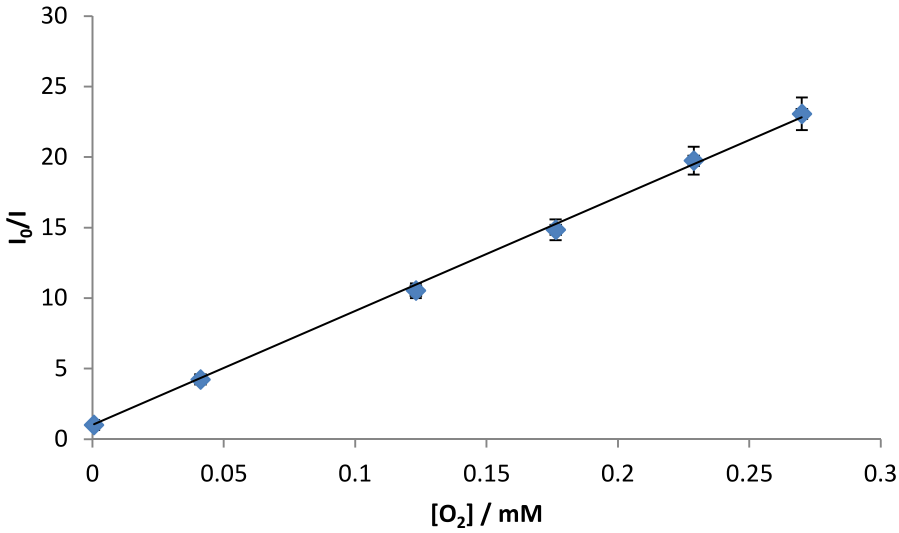

Figure 7.28 Stern-Volmer plot for the phosphorescent lifetimes of PtTSPP, I_0/I plotted as a function of the concentration of oxygen present. $I_0/I = 82.0\ [O_2] + 1$.

The Stern-Volmer plots for PtTSPP are shown with respect to the phosphorescent lifetime in Figure 7.27 and the emission intensity in Figure 7.28 where the value obtained in each for K_{SV} is in good agreement with the other (9.3×10^4 and 8.2×10^4 M^{-1} respectively). These results indicate that the major pathway for triplet deactivation in the porphyrin PtTSPP is caused from dynamic quenching of the phosphorescence by oxygen.

7.5. Overview of platinum and palladium porphyrins

Table 7.5 Absorption and emission spectral data for the platinum and palladium porphyrins in degassed cuvettes

Porphyrin	Absorption / nm	Emission / nm	λ_{ex} / nm	λ for lifetime / nm
PdTMPyP (Pd+)	416	692 (760)	430	700
PtTMPyP (Pt+)	398	665 (720)	440	670
PdTSPP (Pd-)	411	698 (770)	430	700
PtTSPP (Pt-)	396	662 (723)	510	670

Table 7.6 Phosphorescence data for the palladium and platinum porphyrins discussed in sections 7.1, 7.2, 0 and 7.4

Porphyrin	ΦΔ	τ_p/ μs (degassed)	k_Q (O_2) / M^{-1} s^{-1}	K_{sv} / M^{-1} (from τ_o/τ)	K_{sv} / M^{-1} (from I_0/I)
PdTMPyP (Pd+)	0.75 (±0.1)	120 (±3)	2.5×10^9 ($\pm 0.1 \times 10^5$)	3.0×10^5 ($\pm 0.1 \times 10^5$)	2.78×10^5 ($\pm 0.1 \times 10^5$)
PtTMPyP (Pt+)	0.72 (±0.1)	10.3 (±0.2)	2.8×10^9 ($\pm 0.2 \times 10^5$)	2.9×10^4 ($\pm 0.2 \times 10^4$)	3.0×10^4 ($\pm 0.2 \times 10^4$)
PdTSPP (Pd-)	0.76 (±0.1)	294 (±4)	2.7×10^9 ($\pm 0.1 \times 10^5$)	8.0×10^5 ($\pm 0.3 \times 10^5$)	5.3×10^5 ($\pm 0.2 \times 10^5$)
PtTSPP (Pt-)	0.74 (±0.1)	29.9 (±0.1)	3.1×10^9 ($\pm 0.1 \times 10^5$)	9.3×10^4 ($\pm 0.2 \times 10^4$)	8.2×10^4 ($\pm 0.9 \times 10^4$)

All four of the developed metalloporphyins in this section display oxygen-dependant phosphorescence with a good linear relationship between $1/\tau$ and the oxygen concentration. The values for k_Q for each of the four platinum and palladium based metalloporphyrins discussed in this chapter all lie between 2.5×10^9 and 3.1×10^9 M^{-1} s^{-1} indicating that as expected the process is diffusion limited.[2] These values are also consistent with previous research on quenching constants of platinum and palladium porphyrins.[107]

The values of K_{SV} obtained for all porphyrins all lie between 2.9×10^4 and 8.0×10^{5} M^{-1}. Despite the fact that steady-state measurements of quencher concentration are less sensitive than time-resolved measurements and more easily affected by environmental or experimental conditions, these recordings are consistent with the corresponding time-resolved measurements. Monitoring the concentration of oxygen by means of the emission intensity, as opposed to the phosphorescence lifetime, despite being less sensitive, is a cheaper method of detection but prone to experimental errors due to competing absorption chromophores or auto-fluorescence.

The porphyrins containing palladium as their central metal atom give rise to oxygen sensors with phosphorescent lifetimes of 120 µs for the cationic porphyrin with over double for the anionic palladium based porphyrin at 294 µs.

In comparison, the platinum porphyrin derivatives have significantly lower phosphorescent lifetimes of 10.3 µs and 29.9 µs for both the cationic and anionic porphyrins respectively. This is in agreement with previous studies on both palladium and platinum porphyrins, giving lower phosphorescent lifetimes to the platinum derivatives due to the greater spin-orbit coupling of the heavier platinum.

Synthesising porphyrins with either anionic or cationic charges will greatly enhance the use of the nanosensors. This is because it allows flexibilillity depending on the medium or matrix the nanosensor is required for i.e. the charge can help in the location of the nanosensor to a specific part of a cell or for solubility if a specific medium. This should lead to greater solubility or prevention of aggregation of the nanosensors.

Following the determination of the various photophysical properties for the palladium and platinum water soluble porphyrins, the next step was to conjugate the porphyrins to the polyacrylamide nanoparticles and determine the stability of their oxygen sensing properties as nanosensors. The method of conjugating the porphryins to the polyacrylamide matrix was via click chemistry.[91]

7.6. Oxygen nanosensors

As shown earlier, the three outer reactive functionalities of the nanoparticles that have been developed are amino (NH_2), alkyne (C≡C) and azido (N_3), the latter two being for use in click chemistry. Here, the porphyrins were synthesised with a carboxylic acid functional group and the nanoparticles with the amino functionality in order to synthesise the porphyrin based oxygen nanosensors. This was carried out in water by carbodiimide-mediated coupling in the presence of N-hydroxysuccinimide.

Due to the scattering nature of the nanoparticles solutions, absorption spectra were not recorded.

7.6.1. PdTMPyP based oxygen nanosensor

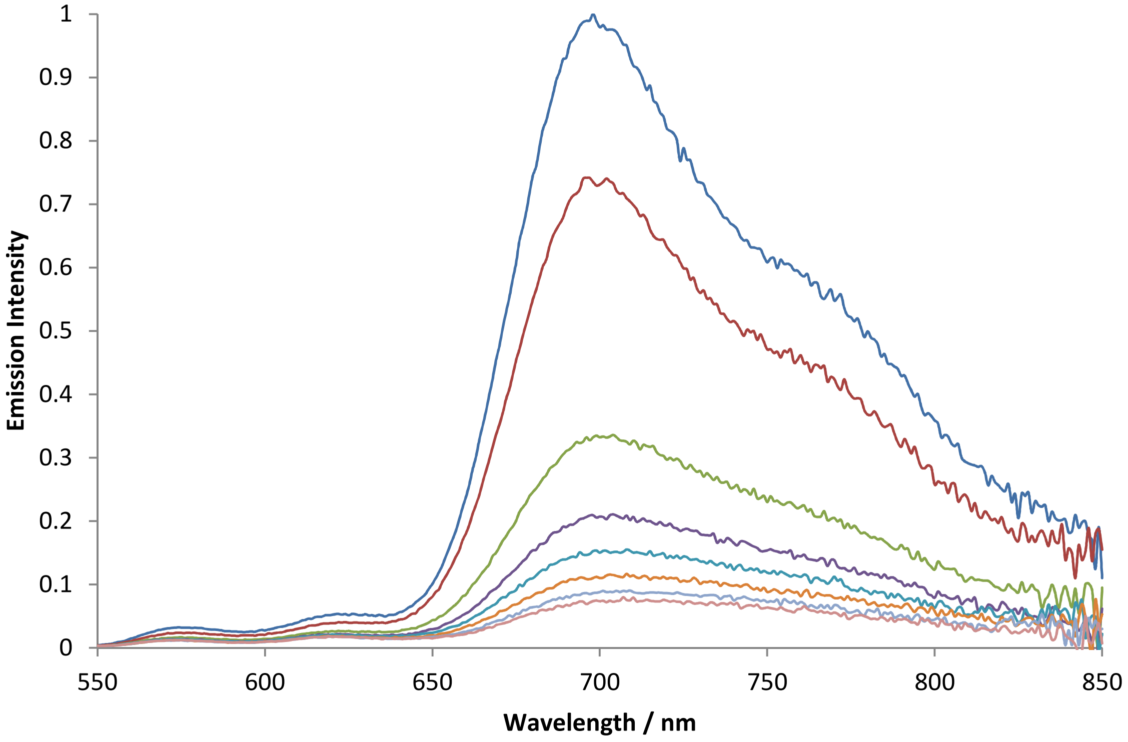

Figure 7.29 Normalised phosphorescence emission profiles of the PdTMPyP nanosensor at varying [O_2]. λ_{ex} = 430 nm.

The phosphorescence emission was recorded in a solution of PBS buffer at varying concentrations of oxygen, the resulting spectra can be seen in Figure 7.29. There is no notable change in the phosphorescence emission spectrum of PdTMPyP-NP when compared with the porphyrin in solution (see section 7.1).

In order to characterise the photophysics of the nanosensor, the phosphorescence lifetimes were recorded at varying [O_2].

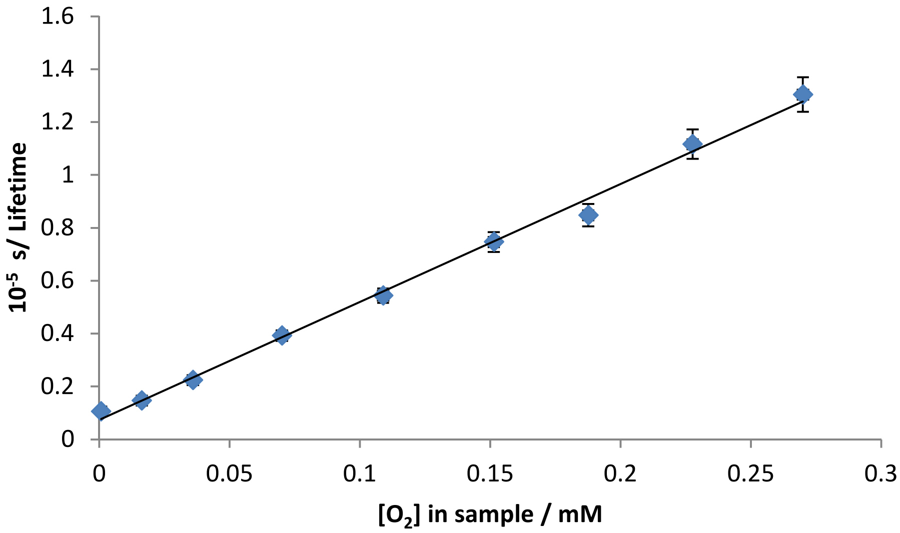

Figure 7.30 Scatter plot for the phosphorescent lifetimes of PdTMPyP-NP, 1/τ plotted as a function of the concentration of oxygen present. 10^{-5}/lifetime = 4.4[O_2] + 0.1.

Figure 7.30 shows the phosphorescent lifetime data plotted with its inverse as a function of the concentration of oxygen present within the sample cell. A good linear relationship is observed throughout the measurements giving a value for k_Q of 4.5×10^8 M^{-1} s^{-1}.

Table 7.7 Recorded phosphorescence lifetime data for samples of PdTMPyP-NP recorded in PBS containing various concentrations of oxygen.

[O_2] / mM	τ / μs
0.0008	95.1
0.04	44.6
0.11	18.4
0.15	13.4
0.19	11.8
0.27	7.7

Table 7.7 shows the raw lifetime data from the oxygen-controlled measurements showing the phosphorescent lifetime of the nanosensor in the degassed cuvette to be 95.1 µs and 7.7 µs in an aerated solution.

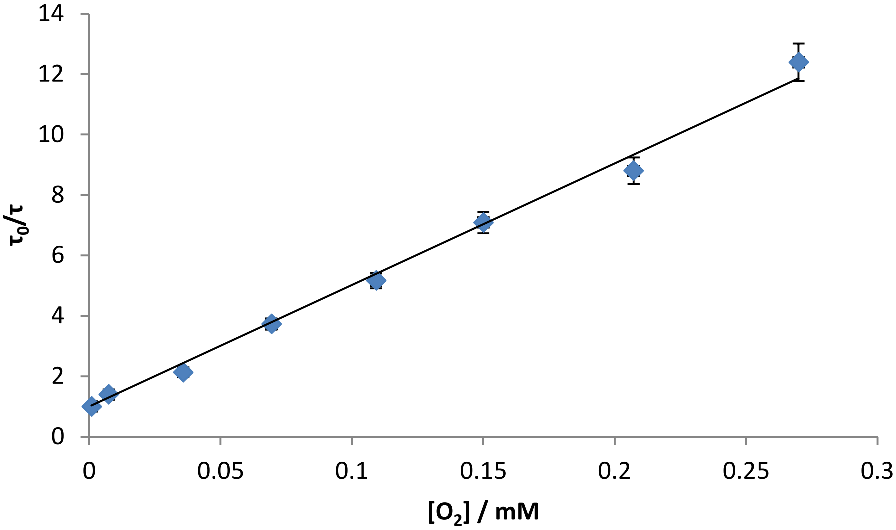

Figure 7.31 Stern-Volmer plot for the phosphorescent lifetimes of PdTMPyP-NP, τ_0/τ plotted as a function of the concentration of oxygen present. $\tau_0/\tau = 41.0\ [O_2] + 1$.

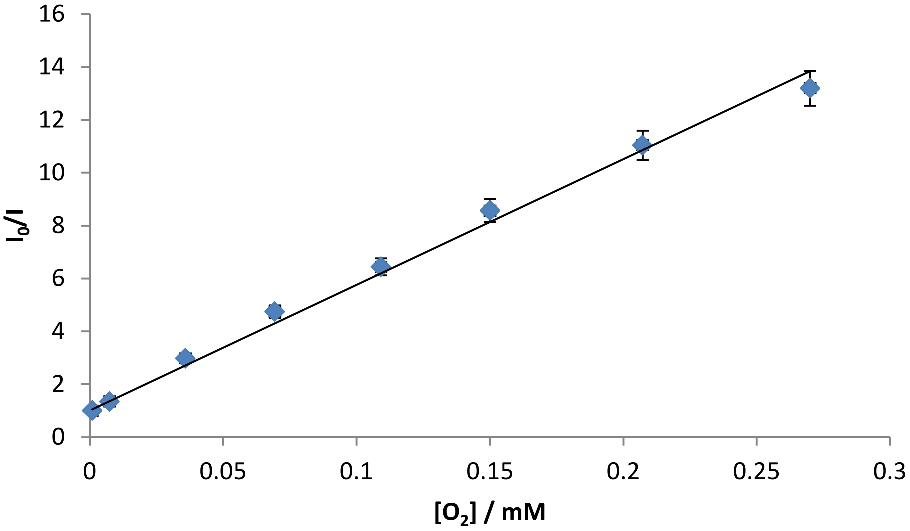

Figure 7.32 Stern-Volmer plot for the phosphorescent lifetimes of PdTMPyP-NP, I_0/I plotted as a function of the concentration of oxygen present. $I_0/I = 4.6 \times 10^0\ [O_2] + 1$.

The Stern-Volmer plots for PdTMPyP based nanosensors are shown with respect to the phosphorescent lifetime in Figure 7.31 and also the emission intensity in Figure 7.15 where the value obtained in each for K_{SV} is in good agreement with the other (4.1×10^4 and 4.6×10^4 M^{-1} respectively). These results indicate that the major pathway for triplet deactivation in the palladium porphyrin based nanosensor is caused from dynamic quenching of the phosphorescence by oxygen.

7.6.2. PtTMPyP based oxygen nanosensor

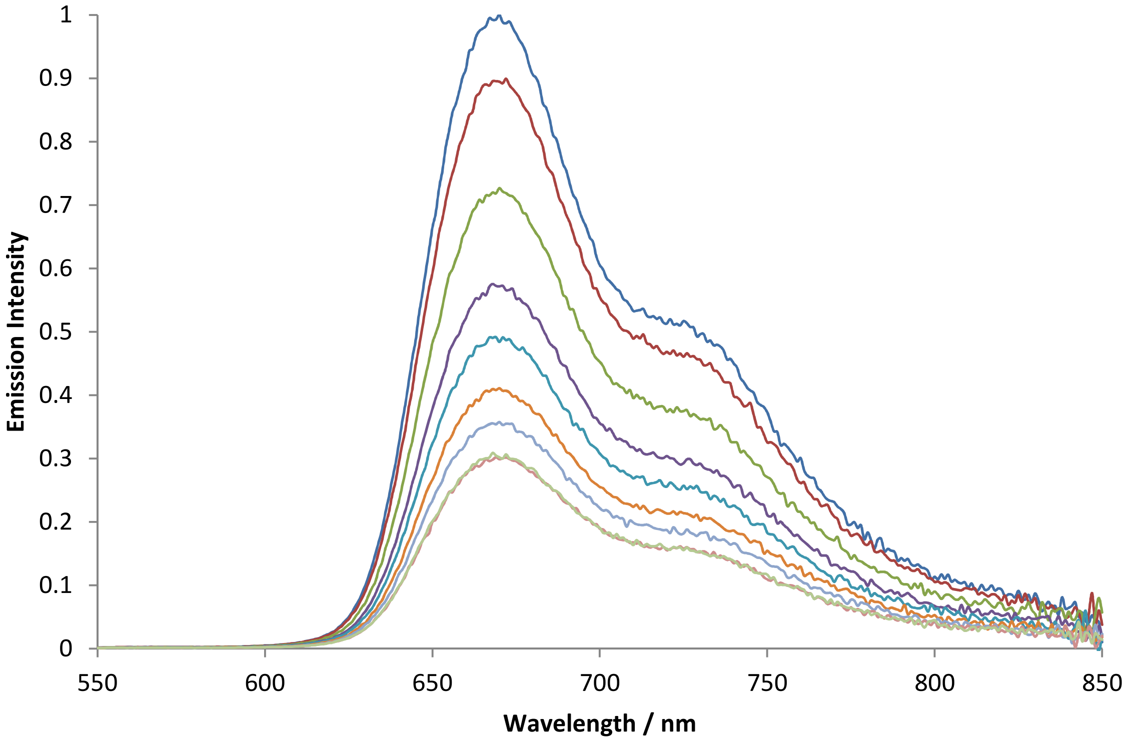

Figure 7.33 Normalised phosophorescence emission profiles of the PtTMPyP nanosensor at varying [O_2]. λ_{ex} = 440 nm.

The phosphorescence emission was recorded in a solution of PBS at varying concentrations of oxygen, the resulting spectra can be seen in Figure 7.33. There is no notable change in the phosphorescence emission spectrum of PtTMPyP-NP when compared with the porphyrin in solution (see section 7.2).

In order to characterise the photophysics of the nanosensor, the phosphorescence lifetimes were recorded at varying [O_2].

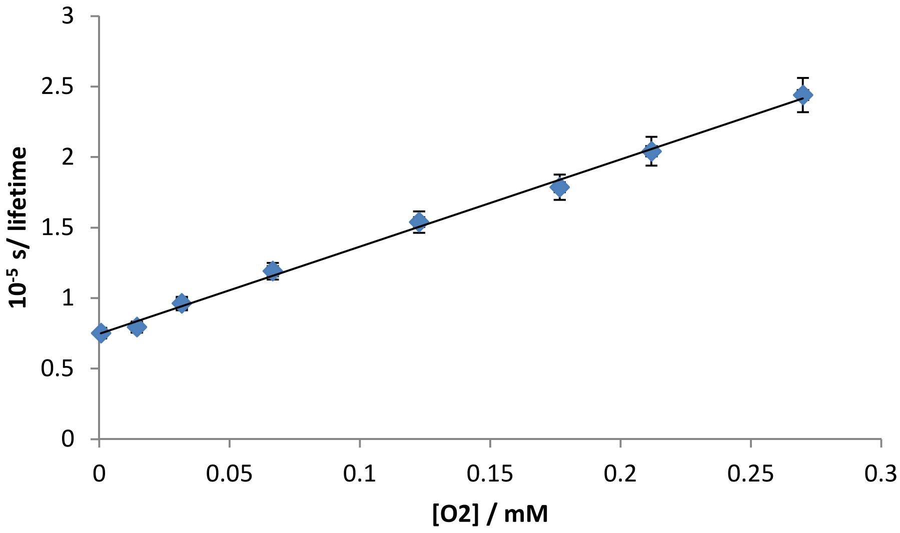

Figure 7.34 Scatter plot for the phosphorescent lifetimes of PtTMPyP-NP, 1/τ plotted as a function of the concentration of oxygen present. 10^{-5}/lifetime = 6.3[O_2] + 0.8.

Figure 7.34 shows the phosphorescent lifetime data plotted with its inverse as a function of the concentration of oxygen present within the sample cell. A good linear relationship is observed throughout the measurements giving a value for k_Q of 6.3×10^8 M^{-1} s^{-1}.

Table 7.8 shows the raw lifetime data from the oxygen-controlled measurements showing the phosphorescent lifetime of the nanosensor in the degassed cuvette to be 13.3 μs and 4 μs in an aerated solution.

Table 7.8 Recorded phosphorescence lifetime data for samples of PtTMPyP-NP recorded in PBS containing various concentrations of oxygen.

[O_2] / mM	**τ / μs**
0.0007	13.3
0.07	8.2
0.11	6.3
0.19	5.5
0.23	4.5
0.27	4.0

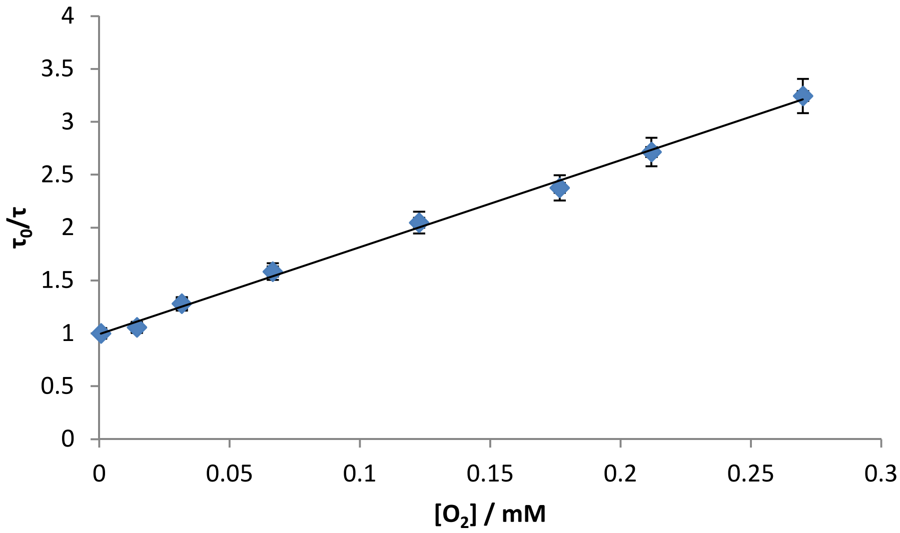

Figure 7.35 Stern-Volmer plot for the phosphorescent lifetimes of PtTMPyP-NP, τ_0/τ plotted as a function of the concentration of oxygen present. $\tau_0/\tau = 8.2\ [O_2] + 1.0$.

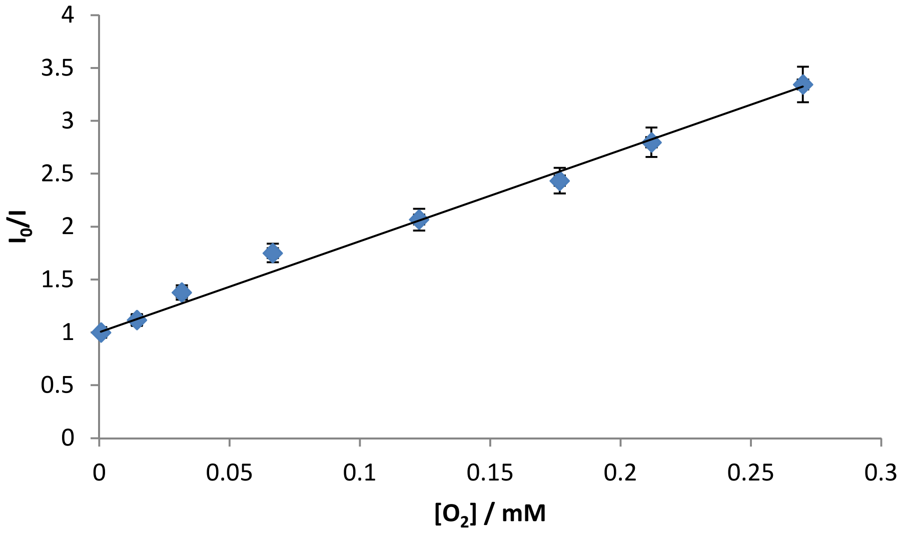

Figure 7.36 Stern-Volmer plot for the phosphorescent lifetimes of PtTMPyP-NP, I_0/I plotted as a function of the concentration of oxygen present. $I_0/I = 8.2\ [O_2] + 1$.

The Stern-Volmer plots for PtTMPyP based nanosensors are shown with respect to the phosphorescent lifetime in Figure 7.35 and also the emission intensity in Figure 7.36 where the value obtained in each for K_{SV} is in good agreement with the other (6.8×10^3 and $8.2 \times 10^3\ M^{-1}$ respectively). These results indicate that the major pathway for triplet deactivation in the platinum porphyrin based nanosensor is caused from dynamic quenching of the phosphorescence by oxygen.

7.6.3. PdTSPP based oxygen nanosensor

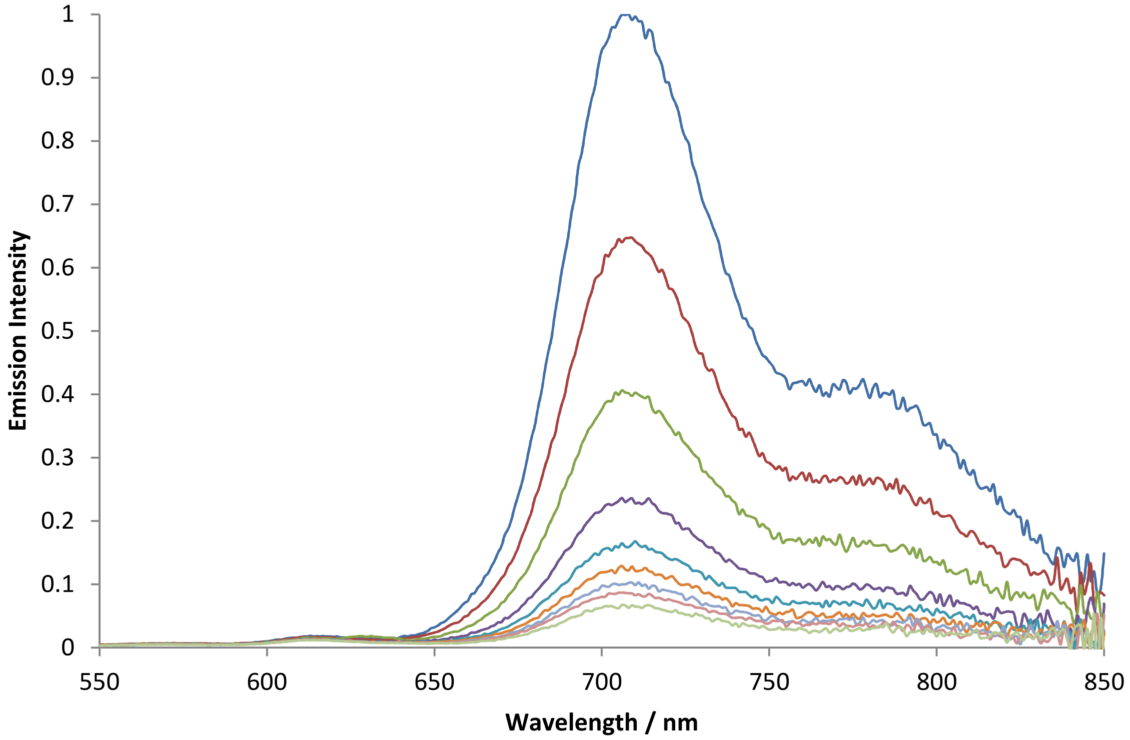

Figure 7.37 Normalised phosophorescence emission profiles of the PdTSPP nanosensor at varying [O_2]. λ_{ex} = 430 nm.

The phosphorescence emission spectra were recorded in a solution of PBS buffer at varying concentrations of oxygen, the resulting spectra are shown in Figure 7.33. There is no notable change in the phosphorescence emission spectrum of PdTSPP-NP when compared with the porphyrin in solution (see section 7.1).

In order to characterise the photophysics of the nanosensor, the phosphorescence lifetimes were recorded at varying [O_2].

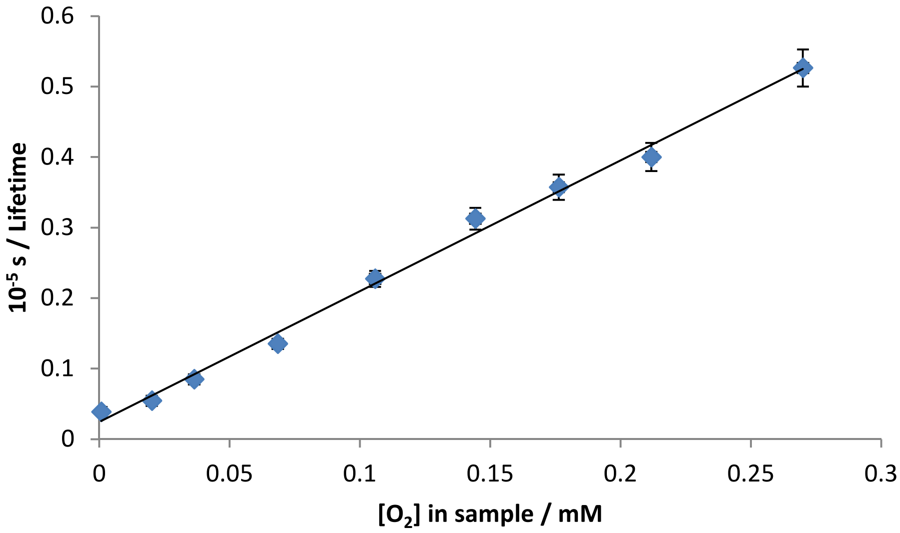

Figure 7.38 Scatter plot for the phosphorescent lifetimes of PdTSPP-NP, $10^{-6}/\tau$ plotted as a function of the concentration of oxygen present. 10^{-5}/lifetime = 1.9[O_2] + 0.02.

Figure 7.38 shows the phosphorescent lifetime data plotted with its inverse as a function of the concentration of oxygen present within the sample cell. A good linear relationship is observed throughout the measurements giving a value for k_Q of 1.9×10^8 M^{-1} s^{-1}.

Table 7.9 shows the raw lifetime data from the oxygen-controlled measurements showing the phosphorescent lifetime of the nanosensor in the degassed cuvette to be 260 μs and 19 μs in an aerated solution.

Table 7.9 Recorded phosphorescence lifetime data for samples of PdTSP-NP recorded in PBS containing various concentrations of oxygen.

[O_2] / mM	τ / μs
0.0008	260
0.037	118
0.11	44
0.14	32
0.21	25
0.27	19

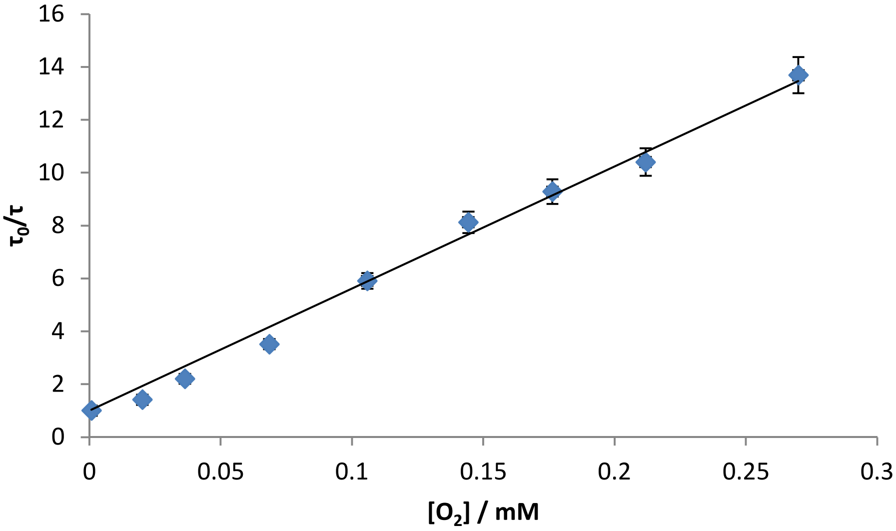

Figure 7.39 Stern-Volmer plot for the phosphorescent lifetimes of PdTSPP-NP, τ_0/τ plotted as a function of the concentration of oxygen present. $\tau_0/\tau = 48.2\ [O_2] + 1$.

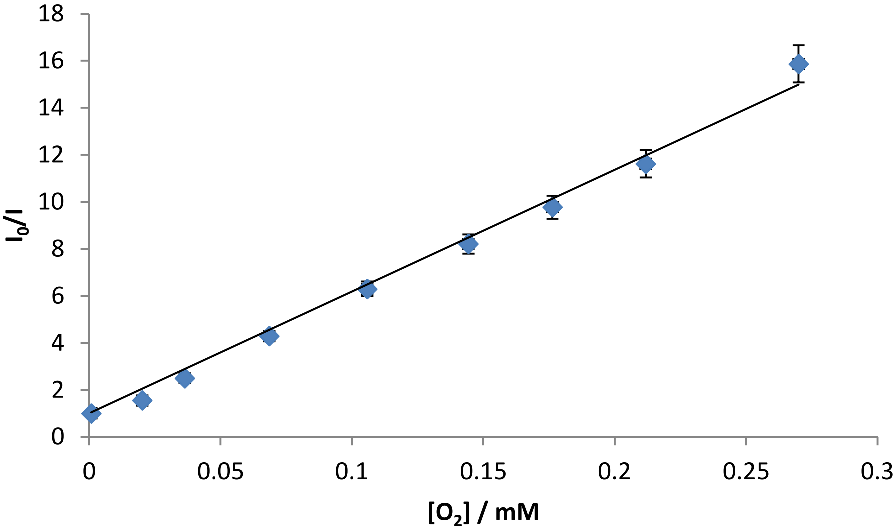

Figure 7.40 Stern-Volmer plot for the phosphorescent lifetimes of PdTSPP-NP, I_0/I plotted as a function of the concentration of oxygen present. $I_0/I = 54.3\ [O_2] + 1$.

The Stern-Volmer plots for PdTSPP based nanosensors are shown with respect to the phosphorescent lifetime in Figure 7.39 and also the emission intensity in Figure 7.40 where the value obtained in each for K_{SV} is in good agreement with the other (4.8×10^4 and 5.4×10^4 M^{-1} respectively). These results indicate that the major pathway for triplet deactivation in the palladium porphyrin based nanosensor is caused from dynamic quenching of the phosphorescence by oxygen.

7.6.4. PtTSPP based oxygen nanosensor

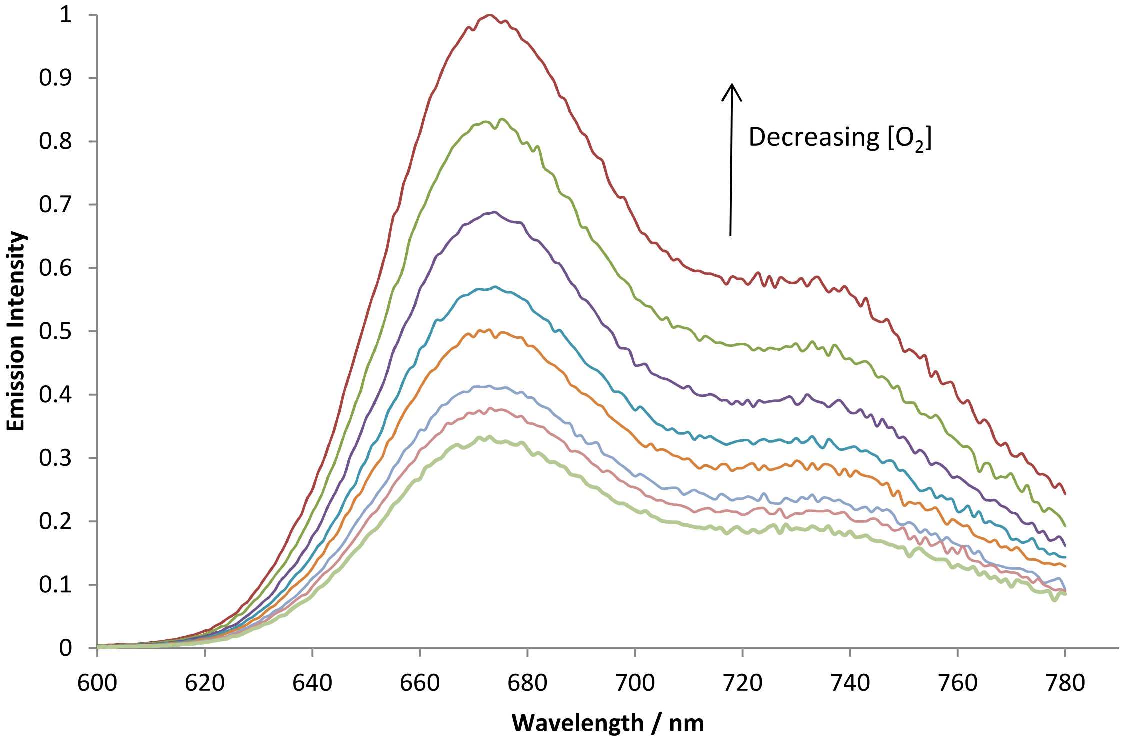

Figure 7.41 Normalised phosophorescence emission profiles of the PtTSPPnanosensor at varying $[O_2]$. λ_{ex} = 510 nm.

The phosphorescence emission was recorded in a solution of PBS at varying concentrations of oxygen; the resulting spectra can be seen in Figure 7.41. There is no notable change in the phosphorescence emission spectrum of PtTSP-NP when comapred with the porphyrin in solution (see section 7.4).

In order to characterise the photophysics of the nanosensor, the phosphorescence lifetimes were recorded at varying $[O_2]$.

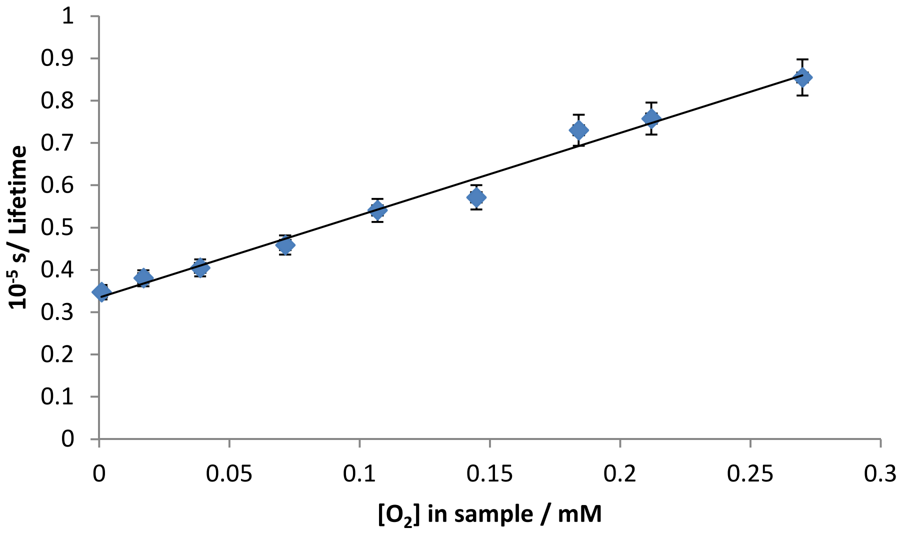

Figure 7.42 Scatter plot for the phosphorescent lifetimes of PtTSP-NP, $10^{-6}/\tau$ plotted as a function of the concentration of oxygen present. 10^{-5}/lifetime = $2.0[O_2] + 0.3$.

Figure 7.42 shows the phosphorescent lifetime data plotted with its inverse as a function of the concentration of oxygen present within the sample cell. A good linear relationship is observed throughout the measurements giving a value for k_Q of 2.0×10^8 M^{-1} s^{-1}.

Table 7.10 shows the raw lifetime data from the oxygen-controlled measurements showing the phosphorescent lifetime of the nanosensor in the degassed cuvette to be 28.8 μs and 11.7 μs in an aerated solution.

Table 7.10 Recorded phosphorescence lifetime data for samples of PtTSP-NP recorded in PBS containing various concentrations of oxygen.

$[O_2]$ / mM	τ / μs
0.0009	28.8
0.039	24.7
0.11	18.5
0.14	17.5
0.21	13.2
0.27	11.7

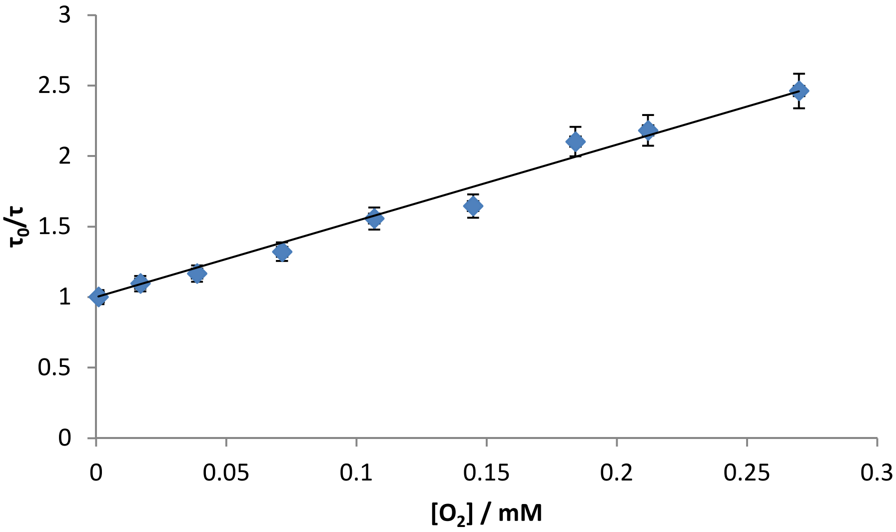

Figure 7.43 Stern-Volmer plot for the phosphorescent lifetimes of PsTSPP-NP, τ_0/τ plotted as a function of the concentration of oxygen present. $\tau_0/\tau = 5.6\ [O_2] + 1.0$.

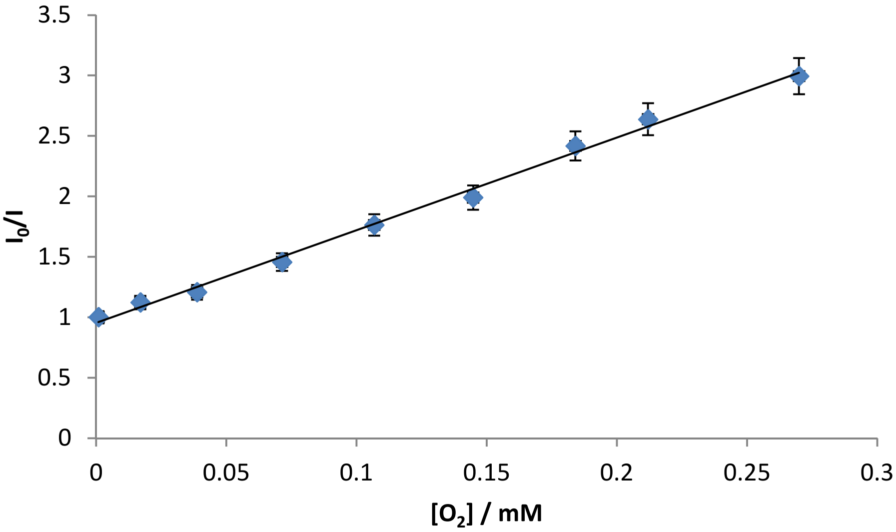

Figure 7.44 Stern-Volmer plot for the phosphorescent lifetimes of PtTSPP-NP, I_0/I plotted as a function of the concentration of oxygen present. $I_0/I = 7.7\ [O_2] + 1.0$.

The Stern-Volmer plots for PtTSPP based nanosensors are shown with respect to the phosphorescent lifetime in Figure 7.43 and also the emission intensity in Figure 7.44 where the value obtained in each for K_{SV} is in good agreement with the other (5.6×10^3 and 7.6×10^3 M^{-1} respectively). These results indicate that the major pathway for triplet deactivation in the platinum porphyrin based nanosensor is the dynamic quenching of the phosphorescent triplet state by oxygen.

7.6.5. Properties of platinum and palladium porphyrin nanoconjugates for oxygen sensing

All species, both plain metalloporphyrins and the corresponding nanoconjugates of the porphyrins display intense Soret bands within the spectral region 390 – 420 nm and two Q-bands within the region of 525 – 545 nm. The platinum derivatives display blue shifted Soret bands, characteristic of platinum porphyrins compared to the palladium derivatives.

Table 7.11 Phosphorescence data for the palladium and platinum porphyrin nanoparticles discussed in Sections 7.6.1, 7.6.2, 7.6.3 and 7.6.4

Nanosensor	ΦΔ	τ_p/ µs (degassed)	λ lifetime recorded/nm	k_Q (O_2) / M^{-1} s^{-1}	K_{sv} / M^{-1} (from τ_o/τ)	K_{sv} / M^{-1} (from I_0/I)
PdTMPyP (Pd^{+})	0.36 (± 0.03)	95 (± 2)	700	4.5×10^8 ($\pm 0.1 \times 10^8$)	4.1×10^4 ($\pm 0.2 \times 10^4$)	4.6×10^4 ($\pm 0.2 \times 10^4$)
PtTMPyP (Pt^{+})	0.30 (± 0.03)	13.3 (± 0.1)	670	6.3×10^8 ($\pm 0.3 \times 10^8$)	6.8×10^3 ($\pm 0.4 \times 10^3$)	8.2×10^3 ($\pm 0.3 \times 10^3$)
PdTSPP (Pd^{-})	0.35 (± 0.03)	260 (± 4)	700	1.9×10^8 ($\pm 0.1 \times 10^8$)	4.8×10^4 ($\pm 0.4 \times 10^4$)	5.4×10^4 ($\pm 0.1 \times 10^4$)
PtTSPP (Pt^{-})	0.32 (± 0.03)	28.8 (± 0.1)	675	2.0×10^8 ($\pm 0.1 \times 10^8$)	5.6×10^3 ($\pm 0.3 \times 10^3$)	7.7×10^3 ($\pm 0.8 \times 10^3$)

The conjugation of the porphyrins to the nanoparticles resulted in a noticeable decrease of the triplet state yields. Such behaviour has previously been seen with the conjugation of porphyrins to macromolecular and polymeric structures or carriers. This may be attributed to an increased potential for non-radiative decay of the porphyrin excited states due to the porphyrin-matrix/carrier interaction but may also be a result of free acrylamide sites that result in rapid quenching of the triplet state.

However, the triplet lifetimes in degassed solution show that the presence of the polyacrylamide matrix does not have a large effect on the lifetime of the emissive porphyrins. This suggests that in the absence of oxygen, the triplet decay is neither enhanced nor inhibited by the interaction between the porphyrin and the matrix for those that are not rapidly quenched.

The bi-molecular quenching constants and those obtained for K_{SV} for all nanoconjugates are reduced by one order of magnitude with respect to the corresponding porphyrins. This suggests that the conjugation of the porphyrins to the polyacrylamide matrix reduces the oxygen sensitivity of the porphyrin probes. The reason for this can be attributed to the fact that the polymeric support might partially shield the porphyrin from colliding with molecular oxygen resulting in a reduction in the quenching efficiency.

8. Overview and future work

The work detailed in this thesis addresses the following categories of luminescence sensing and applications with the overall aim of developing greater knowledge within the area of nanoparticles for bioimaging:

- Monitoring the pH of the environment
- Within the above, ratiometric sensing
- Monitoring the concentration of oxygen
- Monitoring the concentration of calcium
- Incorporation of hydrophobic fluorophores into a probe
- Generation of singlet oxygen

The wide applications of luminescence sensing throughout this thesis demonstrates the versatility of polyacrylamide based nanoparticles. The ability to sense the different luminescence properties highlights the fact that the inert matrix does not affect the overall role of the fluorophores. Previous reports have illustrated the different functional groups that can be synthesised on the exterior of the nanoparticle and recent reports have shown doubly functionalised nanoparticles, thus increasingly highlighting their versatility.[121]

The work discussed here details further developments within the area of polyacrylamide nanoparticles as luminescent sensors. The ability to sense and monitor a range of environments confirms the potential that nanotechnology could have in future applications given the time to continue to further the developments and understanding.

Following on from the incorporation of various fluorophores within the water soluble polyacrylamide matrix was the successful generation, followed by entrapment within the nanoparticle matrix, of two hydrophobic dyes derived from well-known parent molecules; pyrene and coumarin. This step in the development of PEBBLE nanosensors continues to widen the potential applications and use of this work. Further characterisation and research into other hydrophobic dyes could expand the applications of other limited but important fluorescent molecules. Monitoring the presence of any fluctuations in the properties of the fluorophores when subject to photobleaching studies could help to further support the argument for the protections offered by the polyacrylamide matrix.

The successful calibration of a calcium based nanosensor and also porphyrins attached to the same nanosensor confirms the ability to monitor these two different species; one to generate singlet oxygen and one to monitor the calcium concentration. Continuation in the characterisation of these nanoparticles, including cellular measurements could lead to further advancements in the understanding of cellular activity.

Chapter 7 details the phosphorescent properties of synthesised porphyrin based nanosensors for oxygen where further characterisation regarding the viability and biological activity of these would be beneficial to the applications described. As with PDT, further development using other photosensitisers would widen the use within oxygen sensing applications, namely biological imaging.

Continuing research into porphyrins and their singlet oxygen generating properties and monitoring the response from other fluorescent molecules would further deepen the knowledge for understanding the potential uses that the nanoparticles could have.

Leading on from the successful incorporation of a variety of fluorophores and porphyrins, an interesting area to investigate would be in the development of upconverting nanoparticles.

Overall, the measurements in this thesis continue to confirm the success and deepen the understanding we have of nanoparticles containing encapsulated fluorophores and molecules such as porphyrins conjugated to the exterior part of the nanoparticle. The polyacrylamide matrix consistently has an effect which marginally weakens the responses of the dyes or photosensitisers through a shielding effect but does not appear to cease the response entirely. This is again a benefit within optical imaging as it is offers the ability to sense and monitor low levels of luminescence and fluctuations within the responses.

9. Experimental

Experimental procedures for the synthesis of all species in this thesis are described or referenced below.

The following referenced experimental procedures were species synthesised by collaborators:

The general nanoparticle synthesis including the pH sensitive probes followed the procedure detailed by Aylott *et al* (specifically zinc porphyrin).[124]

The conjugation of porphyrins to the surface of nanoparticles followed the procedure detailed by Boyle *et al*.[121] The nanoparticles containing Calcium Green-1, and those with additional porphyrins bound to the surface were both synthesised following the same procedure.

The nanoparticles with oxygen sensing applications follow the procedures detailed by Boyle *et al*.[108]

The species detailed below in Sections 9.1 and 9.2 were synthesised in Durham.

Nanoparticles with porphyrins attached to the exterior of the nanoparticle surface yielded particles with an average diameter of 100 nm. Those synthesized without porphyrins attached yielded particles with an average diameter of 40 nm.

9.1. Hydrophobic dextran conjugates

The hydrophobic dextran conjugates were synthesised following the procedure of an EDC crosslinking reaction.

Equal masses of N-(3-Dimethylaminopropyl)-N′-ethylcarbodiimide hydrochloride (EDC) and the dye (either PBA or C3CA, see quantities below in Table 9.1 and Table 9.2) were combined in a flask with amino dextran (40 mg, 4 µmol) and DMSO (1.5 mL), then left to stir for 1 hour, until fully dissolved. The flask was surrounded by foil and the solution was then left overnight. Ethanol (≈20 mL) was added to the solution and left on ice for approx. 1 hour. The solid was then extracted by filtration and washed with DCM. This left a water soluble solid (white for PBA and white-yellow for C3CA).

Table 9.1 Quantities used for conjugations of aminodextran (10,000 MW) with PBA

Sample	**Aminodextran / mg (moles/µmol)**	**PBA / mg (moles/ µmol)**
PyDex 1	40 (4)	40 (139)
PyDex 2	40 (4)	20 (70)
PyDex 3	40 (4)	10 (35)
PyDex 4	40 (4)	2 (7)
PyDex 5	40 (4)	1 (3.5)
PyDex 6	40 (4)	0.5(1.7)

Table 9.2 Quantities used for various conjugations of aminodextran (10,000 MW) with C3CA

Sample	**Aminodextran / mg (moles/µmol)**	**C3CA / mg (moles/ µmol)**
CoumDex1	40 (4)	10 (53)
CoumDex2	40 (4)	5 (26)

9.2. Hydrophobic nanoparticles

Degassed hexane (42 mL) was added to a stirred solution of Brij®30 (3.08 g, 8.5 mmol) and dioctyl sulfosuccinate sodium salt (AOT, 1.59 g, 3.6 mmol). The mixture was allowed to stir under argon until the surfactants had completely dissolved. A solution of acrylamide

(527 mg, 7.6 mmol), dye-dextran conjugate (20 mg), and N,N'-methylenebisacrylamide (160 mg, 1.0 mmol) in water (1.8 mL) was added to the hexane mixture and left to stir under argon for 10 minutes. 10% aqueous ice-cold ammonium persulfate (30 mL) was added to the reaction vessel, followed by N,N,N',N'-tetramethylethylenediamine (15 mL), and the reaction mixture allowed to stir at room temperature under argon for two hours. Excess hexane was evaporated *in vacuo*, and the resulting white viscous liquid was washed with ethanol and centrifuged (7 times, 50 ml, 10 min, 4000 rpm). The solid was dried *in vacuo* to yield the desired nanospecies as a white solid.

References

1. G. Salvato-Sallverdu, *The perrin-jablonski diagram*, http://www.texample.net/tikz/examples/the-perrin-jablonski-diagram/.
2. J. R. Lakowicz, *Principles of Fluorescence Spectroscopy*, Springer, New York, 2006.
3. *The Nobel Prize in Chemistry 2014 - Press Release*, http://www.nobelprize.org/nobel_prizes/chemistry/laureates/2014/press.html.
4. K. Sasaki, Y. Shi Z, R. Kopelman and H. Masuhara, *Chem. Lett.*, 1996, **25**, 141-142.
5. H. A. Clark, S. L. R. Barker, M. Brasuel, M. T. Miller, E. Monson, S. Parus, Z. Y. Shi, A. Song, B. Thorsrud, R. Kopelman, A. Ade, W. Meixner, B. Athey, M. Hoyer, D. Hill, R. Lightle and M. A. Philbert, *Sens. Actuator B-Chem.*, 1998, **51**, 12-16.
6. S. M. Buck, Y. Koo Lee, E. Park, H. Xu, M. A. Philbert, M. Brasuel and M. Kopelman, *Current Opinion in Chemical Biology*, 2004, **8**, 540-546.
7. Y. Koo Lee, R. Smith and R. Kopelman, *Annu. Rev. Anal. Chem.*, 2009, **2**, 57-76.
8. S. M. Buck, H. Xu, M. Brasuel, M. A. Philbert and R. Kopelman, *Talanta*, 2004, **63**, 41-59.
9. H. A. Clark, R. Kopelman, R. Tjalkens and M. A. Philbert, *Anal. Chem.*, 1999, **71**, 4837-4843.
10. A. Webster, S. J. Compton and J. W. Aylott, *Analyst*, 2005, **130**, 163-170.
11. E. Park, M. Brasuel, C. Behrend, M. A. Philbert and M. Kopelman, *Anal. Chem.*, 2003, **75**, 3784-3791.
12. M. Brasuel, M. Kopelman, J. W. Aylott, H. A. Clark, H. Xu, M. Hoyer, T. J. Miller, R. Tjalkens and M. A. Philbert, *Sens. Mater.*, 2002, **14**, 309-338.
13. E. Brasolla, F. Mancin, E. Rampazzo, P. Tecilla and U. Tonellato, *Chemical Communications*, 2003, 3026-3027.
14. M. G. Brasuel, T. J. Miller, R. Kopelman and M. A. Philbert, *Analyst*, 2003, **128**, 1262-1267.
15. J. P. Sumner, J. W. Aylott, E. Monson and R. Kopelman, *Analyst*, 2002, **127**, 11-16.
16. R. A. Smith, *Journal of Chemical Education*, 1998, **75**, 420.
17. J. D. Coyle, R. R. Hill and D. R. Roberts, *Light, Chemical Change and Life: A Source Book in Photochemistry*, Open University, 1988.
18. J. D. Coyle, R. R. Hill and D. R. Roberts, *Light, Chemical Change and Life: A Source Book in Photochemistry*, Open University Press, 1982.
19. J. Moan, *Photochem. Photobiol.*, 1986, **43**, 681-690.
20. D. Bellus, M. Bohle, R. M. Borzilleri, D. Döpp, H. Döpp, R. J. Herr, R. H. Hutchings, C. Lindsley, N. B. McKeown and J. P. Meigh, *Science of Synthesis: Houben-Weyl Methods of Molecular Transformations Vol. 17: Six-Membered Hetarenes with Two Unlike or More than Two Heteroatoms and Fully Unsaturated Larger-Ring Heterocycles*, Thieme, 2014.
21. Y. Harel and J. Manassen, *Organic Magnetic Resonance*, 1981, **16**, 290-295.

22. R. Giovannetti, *The Use of Spectrophotometry UV-Vis for the Study of Porphyrins*, INTECH Open Access Publisher, 2012.
23. L. Josefsen and R. W. Boyle, *Theranostics*, 2012, **2**, 916-966.
24. Y. Koo Lee and R. Kopelman, *Wiley Interdiscip. Rev.: Nanomed. Nanobiotechnol.*, 2009, **1**, 98.
25. E. D. Sternberg and D. Dolphin, *Tetrahedron* 1998, **54**, 4151-4202.
26. J. R. Henderson, D. A. Fulton, C. J. McNeil and P. Manning, *Biosens. Bioelectron.*, 2009, **24**, 3608-3614.
27. J. M. Dąbrowski, M. M. Pereira, L. G. Arnaut, C. J. P. Monteiro, A. F. Peixoto, A. Karocki, K. Urbańska and G. Stochel, *Photochem. Photobiol.*, 2007, **83**, 897-903.
28. I. J. Macdonald and T. J. Dougherty, *Journal of Porphyrins and Phthalocyanines*, 2001, **5**, 105-129.
29. E. D. Sternberg, D. Dolphin and C. Brückner, *Tetrahedron*, 1998, **54**, 4151-4202.
30. P. J. Goncalves, P. L. Franzen, D. S. Correa, L. M. Almeida, M. Takara, A. S. Ito, S. C. Zilio and I. E. Borissevitch, *Spectroc. Acta Pt. A-Molec. Biomolec. Spectr.*, 2011, **79**, 1532-1539.
31. E. Sidi and J. Bourgeois-Gavardin, *The Journal of Investigative Dermatology*, 1952, **18**, 391-395.
32. N. Mohanty, M. D. Jalaluddin, S. Kotina, S. Routray and Y. Ingale, *J Clin Diagn Res.*, 2013, **7**, 1254-1257.
33. A. P. Castano, T. N. Demidova and M. R. Hamblin, *Photodiagnosis and Photodynamic Therapy*, 2004, **1**, 279-293.
34. A. P. Castano, T. N. Demidova and M. R. Hamblin, *Photodiagnosis and Photodynamic Therapy*, **1**, 279-293.
35. A. C. E. Moor, B. Ortel and T. Hasan, in *Photodynamic Therapy*, ed. T. Patrice, The Royal Society of Chemistry, 2003, vol. 2, pp. 19-58.
36. L. B. Josefsen and R. W. Boyle, *Theranostics*, 2012, **2**, 916-966.
37. G. O. Schenck, *Industrial & Engineering Chemistry*, 1963, **55**, 40-43.
38. G.-Y. Liou and P. Storz, *Free radical research*, 2010, **44**, 10.3109/10715761003667554.
39. D. B. Zorov, E. Kobrinsky, M. Juhaszova and S. J. Sollott, *Circ.Res.*, 2004, **95**, 239-252.
40. B. Kalyanaraman, V. Darley-Usmar, K. J. A. Davies, P. A. Dennery, H. J. Forman, M. B. Grisham, G. E. Mann, K. Moore, L. J. Roberts and H. Ischiropoulos, *Free radical biology & medicine*, 2012, **52**, 1-6.
41. P. R. Ogilby, *Chemical Society Reviews*, 2010, **39**, 3181-3209.
42. F. Wilkinson, W. P. Helman and A. B. Ross, *Journal of Physical and Chemical Reference Data*, 1995, **24**, 663-677.
43. A. A. Starkov, C. Chinopoulos and G. Fiskum, *Cell Calcium*, 2004, **36**, 257-264.
44. J. P. Keene, D. Kessel, E. J. Land, R. W. Redmond and T. G. Truscott, *Photochemistry and Photobiology*, 1986, **43**, 117-120.
45. W. Lei, J. Xie, Y. Hou, G. Jiang, H. Zhang, P. Wang, X. Wang and B. Zhang, *Journal of Photochemistry and Photobiology B: Biology*, 2010, **98**, 167-171.
46. A. J. W. G. Visser and O. J. Rolinski, *Basic Photophysics*, http://www.photobiology.info/Visser-Rolinski.html.
47. LifeTechnologies^{TM}, *Amino Dextran 10,000 MW Certificate of Analysis*, https://tools.lifetechnologies.com/content/sfs/COAPDFs/2015/1664830_D1860.pdf.
48. W. Becker, *Advanced Time-Correlated Single Photon Counting Techniques*, Springer, 2005.
49. A. Beeby, S. FitzGerald and C. F. Stanley, *Photochem. Photobiol.*, 2001, **74**, 566-569.

50. LifeTechnologies^{TM}, *Calcium Calibration Buffer Kits*, https://tools.lifetechnologies.com/content/sfs/manuals/CalciumCalibrationBufferKits_PI.pdf.
51. J. Janata, *Principles of Chemical Sensors*, Springer US, 2010.
52. A. Follenius and D. Gerard, *Photochem. Photobiol.*, 1983, **38**, 373-376.
53. S. R. Phillips, L. J. Wilson and R. F. Borkman, *Current Eye Research*, 1986, **5**, 611-620.
54. G. A. Crosby and J. N. Demas, *The Journal of Physical Chemistry*, 1971, **75**, 991-1024.
55. S. Globig and W. Hunter, *Current Research in Pharmaceutical Technology*, Apple Academic Press, 2011.
56. R. Sjöback, J. Nygren and M. Kubista, *Spectrochimica Acta Part A: Molecular and Biomolecular Spectroscopy*, 1995, **51**, L7-L21.
57. M. Kasha, H. R. Rawls and M. A. El-Byoumi, *Pure Appl. Chem.*, 1965, **11**, 371-392.
58. M. Kasha, *Reviews of Modern Physics*, 1959, **31**, 162-169.
59. D. Zhai, W. Xu, L. Zhang and Y.-T. Chang, *Chemical Society Reviews*, 2014, **43**, 2402-2411.
60. L. Marcu, P. M. W. French and D. S. Elson, *Fluorescence Lifetime Spectroscopy and Imaging: Principles and Applications in Biomedical Diagnostics*, Taylor & Francis, 2014.
61. LifeTechnologies^{TM}, *Fluorescent Ca^{2+} indicators*, https://www.lifetechnologies.com/uk/en/home/references/molecular-probes-the-handbook/indicators-for-ca2-mg2-zn2-and-other-metal-ions/fluorescent-ca2-indicators-excited-with-visible-light.html.
62. Y. Lu and M. Paige, *J. Fluoresc.*, 2007, **17**, 739-748.
63. P. Kloppenburg, W. R. Zipfel, W. W. Webb and R. M. Harris-Warrick, *The Journal of Neuroscience*, 2000, **20**, 2523-2533.
64. R. Yuste, A. Majewska, S. S. Cash and W. Denk, *The Journal of Neuroscience*, 1999, **19**, 1976-1987.
65. A. E. Oliver, G. A. Baker, R. D. Fugate, F. Tablin and J. H. Crowe, *Biophys J.* , 2000 **78**, 2116-2126.
66. K. Yoshiki, H. Azuma, K. Yoshioka, M. Hashimoto and T. Araki, *OPT REV*, 2005, **12**, 415-419.
67. Y. Zhou, J. W. Kim, M. J. Kim, W.-J. Son, S. J. Han, H. N. Kim, S. Han, Y. Kim, C. Lee, S.-J. Kim, D. H. Kim, J.-J. Kim and J. Yoon, *Organic Letters*, 2010, **12**, 1272-1275.
68. J. Kollár, P. Hrdlovič and Š. Chmela, *Journal of Photochemistry and Photobiology A: Chemistry*, 2010, **214**, 33-39.
69. J. Duhamel, *Langmuir*, 2012, **28**, 6527-6538.
70. N. J. Turro, *Modern Molecular Photochemistry*, University Science Books, 1991.
71. H. Li, L. Cai and Z. Chen, *Advances in Chemical Sensors*, 2012.
72. B. Wagner, *Molecules*, 2009, **14**, 210-237.
73. A. Pedone, E. Gambuzzi, V. Barone, S. Bonacchi, D. Genovese, E. Rampazzo, L. Prodi and M. Montalti, *Physical Chemistry Chemical Physics*, 2013, **15**, 12360-12372.
74. A.-C. Ribou, J. Vigo and J.-M. Salmon, *Photochem. Photobiol.*, 2004, **80**, 274-280.
75. W. M. Vaughn and G. Weber, *Biochemistry*, 1970, **9**, 464-473.
76. T. Rharass, J. Vigo, J.-M. Salmon and A.-C. Ribou, *Analytical Biochemistry*, 2006, **357**, 1-8.

77. LifeTechnologies^{TM}, *Certificate of Analysis for aminodextran 10,000 MW*, https://tools.lifetechnologies.com/content/sfs/COAPDFs/2015/1685595_D1860.pdf.
78. T. Förster and K. Kasper, *Zeitschrift für Elektrochemie, Berichte der Bunsengesellschaft für physikalische Chemie*, 1955, **59**, 976-980.
79. Y. Fujiwara and Y. Amao, *Sensors and Actuators B: Chemical*, 2003, **89**, 187-191.
80. B. J. Basu, A. Thirumurugan, A. R. Dinesh, C. Anandan and K. S. Rajam, *Sensors and Actuators B: Chemical*, 2005, **104**, 15-22.
81. Y. Fujiwara and Y. Amao, *Sensors and Actuators B: Chemical*, 2003, **89**, 58-61.
82. Y. Fujiwara, I. Okura, T. Miyashita and Y. Amao, *Analytica Chimica Acta*, 2002, **471**, 25-32.
83. M. Szadkowska-Nicze, M. Wolszczak, J. Kroh and J. Mayer, *Journal of Photochemistry and Photobiology A: Chemistry*, 1993, **75**, 125-129.
84. P. Lianos and G. Duportail, *Eur Biophys J*, 1992, **21**, 29-34.
85. Y. Matsushita and I. Moriguchi, *Journal of Pharmacobio-Dynamics*, 1989, **12**, 762-770.
86. B. Serban, S. Costea, O. Buiu, C. Cobianu and C. Diaconu, Semiconductor Conference (CAS), 2012 International, 2012.
87. A. Chatterjee and D. Seth, *Photochem. Photobiol.*, 2013, **89**, 280-293.
88. Y. Manevich, K. D. Held and J. E. Biaglow, *Radiat. Res.*, 1997, **148**, 580-591.
89. M. C. DeRosa and R. J. Crutchley, *Coordination Chemistry Reviews*, 2002, **233**, 351-371.
90. R. Schmidt, *Photochem. Photobiol.*, 2006, **82**, 1161-1177.
91. C. D. Hein, X.-M. Liu and D. Wang, *Pharmaceutical research*, 2008, **25**, 2216-2230.
92. K. Kano, H. Minamizono, T. Kitae and S. Negi, *The Journal of Physical Chemistry A*, 1997, **101**, 6118-6124.
93. M. Li, H.-J. Xu, K. Deng, Z. Shen, X.-Z. You, Q.-D. Zeng and C. Wang, *The Journal of Physical Chemistry C*, 2010, **114**, 1881-1884.
94. R. F. Pasternack, P. R. Huber, P. Boyd, G. Engasser, L. Francesconi, E. Gibbs, P. Fasella, G. Cerio Venturo and L. d. Hinds, *Journal of the American Chemical Society*, 1972, **94**, 4511-4517.
95. R. F. Pasternack, *Annals of the New York Academy of Sciences*, 1973, **206**, 614-630.
96. K. Kano, T. Miyake, K. Uomoto, T. Sato, T. Ogawa and S. Hashimoto, 1983, **12**, 1867-1870.
97. K. Kano, T. Sato, S. Yamada and T. Ogawa, *The Journal of Physical Chemistry*, 1983, **87**, 566-569.
98. K. Kano, K. Fukuda, H. Wakami, R. Nishiyabu and R. F. Pasternack, *Journal of the American Chemical Society*, 2000, **122**, 7494-7502.
99. F. J. Vergeldt, R. B. M. Koehorst, A. van Hoek and T. J. Schaafsma, *The Journal of Physical Chemistry*, 1995, **99**, 4397-4405.
100. F. Würthner, *SUPRAmolecular dye chemistry*, Springer, 2005.
101. S. M. Andrade and S. M. B. Costa, *Biophysical Journal*, 2002, **82**, 1607-1619.
102. M. Ghosh, A. K. Mora, S. Nath, A. K. Chandra, A. Hajra and S. Sinha, *Spectrochimica Acta Part A: Molecular and Biomolecular Spectroscopy*, 2013, **116**, 466-472.
103. H. Dezhampanah, A. K. Bordbar and S. Tangestaninejad, *J. Iran Chem. Soc.*, 2009, **6**, 686-697.
104. J.-O. Kim, Y.-A. Lee, B. H. Yun, S. W. Han, S. T. Kwag and S. K. Kim, *Biophysical Journal*, 2004, **86**, 1012-1017.
105. P. S. Santiago, D. d. S. Neto, S. C. M. Gandini and M. Tabak, *Colloids and Surfaces B: Biointerfaces*, 2008, **65**, 247-256.

106. P. J. Gonçalves, D. S. Corrêa, P. L. Franzen, L. De Boni, L. M. Almeida, C. R. Mendonça, I. E. Borissevitch and S. C. Zílio, *Spectrochimica Acta Part A: Molecular and Biomolecular Spectroscopy*, 2013, **112**, 309-317.
107. R. W. Redmond and J. N. Gamlin, *Photochem. Photobiol.*, 1999, **70**, 391-475.
108. F. Giuntini, V. M. Chauhan, J. W. Aylott, G. A. Rosser, A. Athanasiadis, A. Beeby, A. J. MacRobert, R. A. Brown and R. W. Boyle, *Photochemical & Photobiological Sciences*, 2014, **13**, 1039-1051.
109. S. K. Bhatia, *Engineering Biomaterials for Regenerative Medicine: Novel Technologies for Clinical Applications*, Springer, 2011.
110. K. Crossin, *Cell Adhesion & Migration*, 2012, **6**, 49-58.
111. S. P. Morgan, F. R. Rose and S. J. Matcher, *Optical Techniques in Regenerative Medicine*, CRC Press, 2013.
112. A. Solanki, J. D. Kim and K.-B. Lee, *Nanomedicine*, 2008, **3**, 567-578.
113. R. Ramamoorthy, P. K. Dutta and S. A. Akbar, *Journal of Materials Science*, 2003, **38**, 4271-4282.
114. L. C. Thomas and G. D. Christian, *Analytica Chimica Acta*, 1977, **89**, 83-91.
115. J. R. Stetter and J. Li, *Chemical Reviews*, 2008, **108**, 352-366.
116. J. Zhang, E. Nuebel, D. R. R. Wisidagama, K. Setoguchi, J. S. Hong, C. M. Van Horn, S. S. Imam, L. Vergnes, C. S. Malone, C. M. Koehler and M. A. Teitell, *Nat. Protocols*, 2012, **7**, 1068-1085.
117. S. M. Borisov, G. Zenkl and I. Klimant, *ACS Applied Materials & Interfaces*, 2010, **2**, 366-374.
118. M. Quaranta, S. M. Borisov and I. Klimant, *Bioanalytical Reviews*, 2012, **4**, 115-157.
119. K. Koren, S. M. Borisov and I. Klimant, *Sensors and Actuators. B, Chemical*, 2012, **169**, 173-181.
120. A. P. Demchenko, *Introduction to Fluorescence Sensing*, Springer, 2008.
121. F. Giuntini, F. Dumoulin, R. Daly, V. Ahsen, E. M. Scanlan, A. S. P. Lavado, J. W. Aylott, G. A. Rosser, A. Beeby and R. W. Boyle, *Nanoscale*, 2012, **4**, 2034-2045.
122. C. M. Lemon, E. Karnas, M. G. Bawendi and D. G. Nocera, *Inorganic chemistry*, 2013, **52**, 10.1021/ic4011168.
123. A. Mills and A. Mills, *PLATINUM METALS REVIEW*, 1997, **41**, 115-127.
124. A. S. Desai, V. M. Chauhan, A. P. R. Johnston, T. Esler and J. W. Aylott, *Frontiers in Physiology*, 2013, **4**, 401.